AN INVOLUTION SATISFYING PARTICLE-IN-CELL METHOD

By

Stephen Robert White

A DISSERTATION

Submitted to
Michigan State University
in partial fulfillment of the requirements
for the degree of

Computational Mathematics, Science, and Engineering—Doctor of Philosophy

2025

ABSTRACT

This thesis presents a new Particle-in-Cell method for numerically simulating plasmas under the Vlasov-Maxwell system. Maxwell's equations and the Newton-Lorentz force are both recast in terms of vector and scalar potentials under the Lorenz gauge. This results in a set of decoupled wave equations governing the potentials and a Hamiltonian system with a generalized momentum formulation governing the particles. The Particle-in-Cell framework for solving a plasma system requires two main components, a method for updating the fields and a method for updating the particles of the system.

The first part of this thesis introduces the Method of Lines Transpose, or MOLT, as a way of solving partial differential equations in general and the wave equation in particular. Additionally it introduces a new particle pusher, the Improved Asymmetrical Euler Method, that is a modification of a previously existing method. We deploy these two techniques in the Particle-in-Cell framework. In this section in particular MOLT employs a dimensional splitting algorithm, solving a set of one dimensional boundary value problems using a Green's function. This will all be done using one particular temporal discretization scheme, the first order Backward Difference Formula. Numerical results are shown to give evidence for the quality of these techniques, though it is noteworthy that the combination of this wave solver and particle pusher does not satisfy the Lorenz gauge condition, nor does it satisfy the involutions of Maxwell's equations, otherwise known as Gauss's laws.

The second part of this thesis fills this lacuna, suggesting two ways for doing so. First it will consider theory to connect satisfaction of the continuity equation with satisfaction of the Lorenz gauge. It will consider in particular a way of satisfying this theory with multi-dimensional Green's functions, eschewing the dimension splitting of the first part. It will additionally consider the solution of the boundary value problems via other numerical techniques such as the Fast Fourier Transform or Finite Difference approach, ultimately choosing these for simplicity. The second approach will consider a gauge correction technique. It will be shown that both of these preserve the gauge, but the first method will additionally satisfy the involutions of Maxwell's equations. In a similar manner to the first part, it will do so using the first order Backward Difference Formula as the temporal

discretization scheme. Numerical evidence will be given to support the theory developed.

The third part of this thesis will generalize the theory connecting the satisfaction of the continuity equation with satisfaction of the Lorenz gauge and, in most cases, with Gauss's Laws. It will extend this theory to not only all orders of the Backward Difference Formulation, but to a family of second order time centered methods, arbitrary stage diagonally implicit Runge-Kutta methods, and all orders of Adams-Bashforth methods. In all but the diagonally implicit Runge-Kutta methods, Gauss's laws will be shown to be satisfied if the Lorenz gauge is. Once again numerical evidence will be given to support this.

Finally some future projects will be suggested to capitalize on this work.

To those who wouldn't let me quit.

ACKNOWLEDGMENTS

It has been quite the journey. Five years ago in the height of a pandemic I began the long process that has resulted in what you are holding in your hands. It is a very safe thing to say that I would not be here without a number of people. First and foremost I would like to thank my advisor, Dr. Andrew Christlieb, whose mentorship, teaching, patience, and kindness have made my experience here at the CMSE better than I could have hoped.

I am additionally indebted to my committee members. Dr. Zhang taught my first plasma physics class under the extraordinary circumstances of remote education with poise and clarity. His encouragement that indeed I could understand this material when I was fairly certain I could not was not unappreciated. The techniques I picked up in Dr. O'Shea's computational astrophysics class have born fruit, but I would be remiss if I did not also express gratitude for his advice on finishing my PhD strong and without losing my sanity. Lastly, Dr. Verbonceour has provided numerous insights that have worked their way into this thesis, both through in-person conversations as well as his 2005 review paper, which probably reigns supreme as the paper to which I have returned the most.

Graduate school is hardly composed only of one's committee. I also am very grateful to my labmates and fellow CMSE graduate students, Nic, Cole, Zenas, Gina, Arash, Mandela, Carolyn, Alejandro, Bowen, as well as Jamal from over at ME, all of whom all have my gratitude for their company along this journey. Dr. Nathan Haut especially has my thanks for all the shared midday lunches our second and third year while students were still trickling back into the office. In particular I would like to thank Dr. William Sands, an alumni of the Christlieb group, who guided me through my first two years of graduate school and continued his support up to now. The work composing this thesis was done directly in collaboration with him and Dr. Christlieb, and it is not an exaggeration to say that his friendship and mentorship made this thesis possible. I am additionally grateful to Drs. Sining Gong and Shiping Zhou for their help in understanding the collision operators and finite element formulation of MOLT. Sungmin, whom I have met nearly every week since my third year to talk about everything from international politics to baseball, has my thanks for the many great lunches and conversations. My girlfriend, Cassie, whom I met here at the CMSE, has shown me

more patience and kindness throughout our time together than I deserve.

Outside the CMSE I also find myself surrounded by good people. My professors at Spring Arbor were not only my teachers, but role models and mentors. Dr. Wu, with whom I have fond memories of not only classes but also road trips to programming competitions; Dr. Wegner, who showed me just how beautiful and elegant math could be; Dr. Hill, whose friendship and mentorship have persisted even after college; and Dr. Brewer, whose memory I carry with me; thank you all.

My friends, fellow philosophy enthusiasts, and podcasters at *The Problem With Reading* (available on all your favorite podcast platforms), Brevin and Sam, whose friendship formed over a fellow love of ideas has been a constant source of joy. The weekly "philosophy nights," hosted by Livingston Garland, have resulted in yet another group of friends I have come to cherish. These, too, have my thanks for their constant encouragement along these last five years.

I am deeply thankful to my parents, Jerry and Polly White, who instilled in me both the love of learning and the willingness to face life's challenges that are required to tackle something like graduate school; to my brothers, Aaron and Justin, who never hesitate to offer a word of encouragement or ego-deflation, whichever the need may be; and to my grandparents, who have been a constant source of joy and warmth that I have had the rare gift of enjoying up to my early 30s.

I wanted to quit my first year; four people stopped me. The first was my then-roommate Livingston Garland, who, as he was finishing his own graduate school race, took the time to encourage me to keep going at the start of mine. The second was Brevin Anderson, would conduct daily video chats for lunch in which we would, for a half hour, attempt to forget our respective graduate school struggles and enjoy a bit of food and company. The third was Curtis Underwood, also a daily visitor for morning coffee, who when told I wanted to quit responded that there was no shame in being defeated by such a challenge, but there was shame in quitting. The best friends are the ones who tell you what you need to hear rather than what you wish to hear. Finally, there was "Ryan" Kyle Mero, who when told the same quoted Thucydides, "Surely the bravest among us is the one with the clearest vision of what lies ahead, danger and glory alike, yet notwithstanding goes forth."

It is a blessed man to have one friend such as the these. I have many.

Sic transit gloria mundi

PREFACE

A Canticle For Leibowitz [1] tells the haunting story of a world that has deliberately forgotten its scientific heritage in the aftermath of nuclear armageddon. In a world torn apart by the "flame deluge," the survivors turned on the scientists with the accusation that it was their hands that created these instruments of war, that they were the ones who scorched the world, and as such the world is better off without them. In the midst of the mindless carnage and destruction, the titular Leibowitz, himself a scientist at an unnamed lab in the American Southwest, founds an order of monks who are dedicated to preserving the scientific heritage of a world that no longer wants it. As time passes, the monastic order continues to faithfully transcribe the strange symbols and concepts of a knowledge they no longer understand, believing, with good reason, that these texts are important and even sacred. As such, they shelter them and await the arrival of someone who will understand their worth and treat them with the respect and care they deserve.

Thankfully, no such armageddon has taken place, but nonetheless this story serves as a meditation on the nature of science (a word that really just means knowledge, stemming from the Latin scientia) and the scientific enterprise, and how without some sort of reverence it is easy to forget its worth. As we begin this exploration into one (extremely) small component of the scientific venture, it is worth remembering just how long it has taken to get here. Millennia of philosophers and scientists have passed their flame on to us. Now it is our turn.

TABLE OF CONTENTS

CHAPTER 1

INTRODUCTION

1.1 Introduction

Charged particles in motion constitute a current. A current induces an electromagnetic field. An electromagnetic field accelerates and rotates charged particles. As one can imagine, this system becomes quite complicated with only a handful of particles, and the typical plasma system is composed of trillions of such particles. Modern study of this phenomenon is predicated upon being able to accurately and efficiently simulate these particles, no small challenge.

The purpose of this thesis is to consider a new method of simulating plasmas using a kinetic method known as Particle-in-Cell (PIC). In this chapter we will first briefly consider what a plasma is and why we are so interested in studying this phenomenon. We will then explore some of the physical laws governing it in greater detail. Once we have a better understanding of the problem space we are navigating, we will then go over a history of plasma science in general and PIC in particular, examining how these studies have evolved over time. The remainder of the thesis will be dedicated to the work with which I (alongside others) have been engaged.

In Chapter 2 we will develop a novel PIC method. This method considers Maxwell's equations under the Lorenz gauge, which considers the electric and magnetic fields in terms of a vector and scalar potential, and these decoupled into a set of heterogeneous wave equations. We approach these wave equations using the Method of Lines Transpose under the first order Backward Difference Formula. Having discretized in time, we then dimensionally split the spatial operator and solve the resulting one dimensional boundary value problem with a Green's function. The particles are updated using a modification of the Asymmetrical Euler Method. We will compare the numerical results of this method with the flagship PIC scheme that employs the Yee grid together with the Boris push, showcasing a number of improvements. It will be noted that, despite a number of advantages, this method does not preserve the Lorenz gauge condition, nor does it satisfy Gauss's laws for electricity and magnetism, unlike the Yee-Boris method.

In Chapter 3, we will take a look at how this method may be modified to fill this lacuna. Theory

will be developed to show that the charge conservation is intimately connected with satisfaction of the Lorenz gauge. Moreover, this theory will prove that satisfaction of the Lorenz gauge will in turn enforce satisfaction of Gauss's laws. Eschewing the one dimensional Green's function for reasons that we will discuss, we consider a multidimensional Green's function as well as other numerical techniques such as the Fast Fourier Transform or Finite Difference method. We will also consider a gauge correction technique that will manually keep the Lorenz gauge to machine precision without concern for the continuity equation. Numerical evidence will be given to support this theory.

In Chapter 4, we will generalize the properties established in Chapter 3 to a wider family of time discretizations. Not only will we generalize to all orders of the Backward Difference Formulation, but also to a family of second order time centered methods, arbitrary stage diagonally implicit Runge-Kutta methods, and all orders of Adams-Bashforth methods. All of these methods will be shown to satisfy the Lorenz gauge if the continuity equation is satisfied. All but the diagonally implicit Runge Kutta methods will be shown to satisfy Gauss's laws if the Lorenz gauge is satisfied. Numerical evidence will showcase this theory.

Finally, in Chapter 5 we will sketch out some future lines of inquiry this work unlocks. Chapter 6 will bring us home with some concluding remarks.

The three main chapters, 2, 3, and 4, are based on the works [2, 3, 4]. respectively, done by myself in collaboration with Dr. Andrew Christlieb and Dr. William Sands.

I have included a number of appendices that are dedicated to explaining in greater detail concepts that are already very well established. All too often when something is well established the details are brushed aside, putting the novice looking to understand it in a difficult position, so it is my hope that anyone looking to learn about this method will find these helpful. I have no wish to pass off this work as my own, but rather to provide an easily accessible source for those interested, as well as elaborate on some steps I personally found difficult to follow. I hope it helps the reader.

And now to the matter at hand.

1.2 A Very Brief History of Plasmas

1.2.1 Etymology

> The word "plasma" will be used to designate that portion of an arc-type discharge in which the densities of ions and electrons are high but substantially equal.

With these words, in a footnote no less [5], Irving Langmuir gave a label to the fourth state of matter and the vast majority of matter in the observable universe. His collaborator in this now famous paper, Lewi Tonks, would later go on to describe the interaction the two had that led to this term [6]:

> Langmuir came into my room in the General Electric Research Laboratory one day and said, "Say, Tonks, I'm looking for a word. In these gas discharges we call the region in the immediate neighborhood of the wall or an electrode a 'sheath,' and that seems to be quite appropriate; but what should we call the main part of the discharge?..."
>
> My reply was classic: "I'll think about it, Dr. Langmuir."
>
> The next day Langmuir breezed in and announced, "I know what we'll call it! We'll call it the 'plasma'" The image of blood plasma immediately came to mind; I think Langmuir even mentioned blood. In the light of the contemporary state of our knowledge, the choice seemed very apt.

The word itself, "plasma," is a Greek term meaning "something molded or created," itself coming from an older Greek word, "plassein," meaning "to mold" or "to spread thin." It then migrated to Latin and took on the meaning "mold or matrix in which anything is cast or formed to a particular shape," and then eventually came to be associated with blood, and finally with the phenomenon Langmuir and Tonks studied. But what is this state of matter?

1.2.2 State of Matter

There are four fundamental states of matter in the universe, these being solid, liquid, gas, and plasma. An intuitive way of understanding plasmas, as well as states of matter in general, is in understanding the strength of the bonds of their constituent particles [7]. A solid is a material in which the constituent molecules are bonded together, resulting in a rigid form. When energy is

applied to a solid, eventually it reaches its melting point, the bonds are broken, but attraction from intermolecular forces remains, and the material becomes a liquid. More energy applied results in its reaching its boiling point, in which the attraction between the neutral particles is insufficient to keep them in place, and the material becomes a gas. When further energy is injected into the system, the neutral particles themselves begin to come apart, the electrons leave their atoms, and the material becomes ionized, resulting, finally, in a plasma.

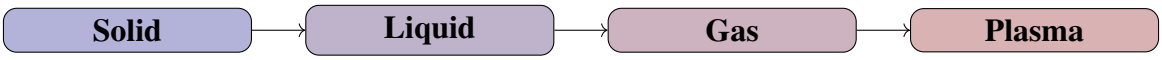

Figure 1.1 Changes in states of matter as energy is added.

It is in this last state of matter that we are most interested.

As Langmuir said, the ions and electrons are many, but they are for the most part equal, which results in macroscopic neutrality.[1] The distance at which this macroscopic neutrality breaks down is called the Debye length, and is denoted λ_D. A perturbation disturbing this macroscopic neutrality will cause electrons (the lighter of the two species) to rush to fill the void. Of course, in so doing they encounter each other, and the neutrality is broken yet again, causing them to rush away. This oscillation is called the plasma frequency, and is denoted ω_p. Collisions between electrons and neutral particles will reduce this oscillation amplitude over time. A much more thorough discussion of these parameters may be found in [7]. We will go over more details on those who derived these physical parameters in Section 1.4.2.

1.2.3 Motivation

Though perhaps not encountered by us humans in our day-to-day lives quite as much as the other three (after all, we walk upon solid earth, drink liquid water, and inhale gaseous air, but we do not encounter plasmas in an analogous manner), this phase of matter composes over 99% of the observable universe. One example we see every day, and depend upon for our very existence, the sun, is a plasma. The solar wind emitted therefrom is a plasma, as are the particles the earth's

[1] This is perhaps an oversimplification. Plenty of plasmas are not macroscopically neutral, in fact one of our examples in Section 2.4 will be a beam of particles of a single species. It is under the assumption of macroscopic neutrality that we get the following parameters.

magnetosphere catches from this wind. We observe the Aurora Borealis and Australis[2] because of the plasma that forms in the ionosphere when solar ultraviolet and x-ray radiation ionize the atmospheric particles. Beyond our solar system there are countless examples, and ones of a far more exotic nature, such as nebula, supernovae, pulsars, accretion disks about black holes contain plasmas, the list goes on [7].

This is all fascinating, and of course learning more about the universe is its own reward. However, what of the more practical applications of this material? One of the more urgent examples would be the Carrington event, in which a massive Coronal Mass Ejection (CME) struck the earth in 1859. The Aurora Borealis reached all the way down to the Caribbean, and multiple telegraph machines exploded. This is a relatively benign event in the mid 1800s (aside from some terrified telegraph operators), but it does not take a very active imagination to imagine the devastation a similar event would wreak upon the globe in the 2000s. It is of vital importance to have the capabilities to monitor and predict this sort of plasma phenomenon. And while PIC is a kinetic model more suited to smaller, bounded domains, there are a number of works that combine PIC with other methods such as magnetohydrodynamics (MHD) for modelling solar phenomena [8, 9].

One perhaps less urgent, though certainly no less exciting, use case would be plasma fusion energy. In December 2022 Lawrence Livermore successfully achieved the first igniting fusion plasma in a laboratory and produced 1.37 MJ of fusion energy [10, 11]. While there is still a long way to go to perfect the process and make it competitive with fossil fuel et al, this is a very significant step to more abundant, and more clean, energy.

Of more common, though admittedly less bombastic, examples there is a plethora. The manufacturing industry has come to rely heavily on plasmas, as they have the ability to modify materials and surfaces in very unique ways, such as being able to etch a .2-μm wide, 4-μm deep trench into a piece of silicon, which is an indispensable requirement for integrated circuits. Plasmas are also used to harden metals, which has increased the durability of the machine tools of the manufacting industry, also of which the medical industry has found useful for the creation of artificial joints [7, 12]. Hall

[2]Named for the Roman goddess of the dawn, Aurora, and the Greek gods of the North and South winds, Boreas and Auster, respectively.

thrusters [13], A6 magnetrons [14], next generation high power microwave sources [15, 16], and cross field amplifiers [17], all use plasmas, and all have nontrivial geometries that need resolving.

1.3 Problem Formulation

1.3.1 Introduction

We now have some understanding of what plasmas are and are motivated to consider more carefully how they behave. Thankfully this phenomena has been well studied for some time (to be explored further in Sections 1.4.1 and 1.4.2). First we will consider the laws governing a plasma, how electromagnetic waves propagate and how a charged particle behaves in these waves. We will then take a closer look at Particle-in-Cell (PIC) and consider how we may simulate plasmas using this method.

1.3.2 Problem Formulation

The laws governing a collection of particles of species α may be described as the evolution of the particle probability density function, f_α, in phase space, where phase space is both location in physical space and velocity. f_α is a seven dimensional function, consisting of three spatial, three velocity, and one temporal dimension. Of course, $\mathbf{x}$ and $\mathbf{v}$ are themselves functions of t. In the absence of collisions, the distribution does not change over time with regards to the total time derivative, $\frac{\mathcal{D}}{\mathcal{D}t}$. We apply this derivative, use the chain rule, and see

$$\begin{aligned}\frac{\mathcal{D}f_\alpha}{\mathcal{D}t} &= \frac{\partial f_\alpha}{\partial t} + \frac{\partial \mathbf{x}}{\partial t}\cdot\frac{\partial f_\alpha}{\partial \mathbf{x}} + \frac{\partial \mathbf{v}}{\partial t}\cdot\frac{\partial f_\alpha}{\partial \mathbf{v}} \\ &\equiv \frac{\partial f_\alpha}{\partial t} + \mathbf{v}\cdot\nabla f_\alpha + \mathbf{a}\cdot\nabla_v f_\alpha.\end{aligned} \tag{1.1}$$

Setting this equal to zero gives us the Vlasov equation,

$$\frac{\partial f_\alpha}{\partial t} + \mathbf{v}\cdot\nabla f_\alpha + \mathbf{a}\cdot\nabla_v f_\alpha = 0. \tag{1.2}$$

This is the Boltzmann equation in the absence of collisions:

$$\frac{\partial f_\alpha}{\partial t} + \mathbf{v}\cdot\nabla f_\alpha + \mathbf{a}\cdot\nabla_v f_\alpha = \left(\frac{\delta f_\alpha}{\delta t}\right)_{coll}. \tag{1.3}$$

See Appendix C for details on how to derive this from first principles.

Here $\mathbf{v}$ is velocity and $\mathbf{a}$ is acceleration of a particle species α. For our purposes we will be examining collisionless plasmas, ie (1.2).

Now, for the governing force we have the Lorentz equation of motion governing the motion of a particle in electric ($\mathbf{E}$) and magnetic ($\mathbf{B}$) fields:

$$\frac{d\mathbf{p}}{dt} = \mathbf{F} = q\left(\mathbf{E} + \mathbf{v} \times \mathbf{B}\right) \tag{1.4}$$

This is relativistically correct if $\mathbf{p} = \gamma m \mathbf{v}$. We have the relativistic form of Newton's second law:[3]

$$\mathbf{F} = \frac{d\mathbf{p}}{dt} = \gamma m \mathbf{a}. \tag{1.5}$$

With the Lorentz force we can rewrite the Vlasov equation as the Vlasov-Maxwell equation

$$\frac{\partial f_\alpha}{\partial t} + \mathbf{v} \cdot \nabla f_\alpha + \frac{q}{\gamma m}\left(\mathbf{E} + \mathbf{v} \times \mathbf{B}\right) \cdot \nabla_v f_\alpha = 0. \tag{1.6}$$

The electric and magnetic fields must satisfy Maxwell's equations:

$$\nabla \cdot \mathbf{E} = \frac{\rho}{\epsilon_0}, \tag{1.7a}$$

$$\nabla \cdot \mathbf{B} = 0, \tag{1.7b}$$

$$\nabla \times \mathbf{E} = -\frac{\partial \mathbf{B}}{\partial t}, \tag{1.7c}$$

$$\nabla \times \mathbf{B} = \frac{1}{c^2}\frac{\partial \mathbf{E}}{\partial t} + \mu_0 \mathbf{J}. \tag{1.7d}$$

Here ρ is the total charge density, $\mathbf{J}$ is the total current density, ϵ_0 is the free space permittivity, μ_0 is the free space permeability, and $c = \frac{1}{\sqrt{\epsilon_0 \mu_0}}$ is the speed of light.[4] For more details see Chapter 6 of [32], and Chapter 1 of [7]. For a more thorough history, see also Sections 1.4.1 and 1.4.2. Finally, see also Appendix A for nondimensionalizing both the field equations and the particle equations of motion. It is simulating the systems governed by the five above equations with which we are most concerned. The standard Yee-Boris scheme is well equipped to handle these equations, but the method we introduce in this thesis will require us to consider what they look like in terms of vector and scalar potentials.

[3] If γ is a function of t, which in most interesting cases it is, we need to apply the chain rule, seeing $\frac{d\mathbf{p}}{dt} = m\frac{d}{dt}\left[\gamma \mathbf{v}\right] = m\left(\frac{d\gamma}{dt}\mathbf{v} + \gamma\frac{d\mathbf{v}}{dt}\right)$. Conveniently, as $v \to c$, the first term dominates (eg a quick calculation shows that $v = .99995c$ yields $\gamma \approx 100$, many orders of magnitude lesser).

[4] SI units.

1.3.3 Maxwell's Equations Under the Lorenz Gauge

We will have need to have Maxwell's equations written in terms of a vector and scalar potential. As such, we follow the work of Jackson Chapter 6 [32] to convert them into this form.

We have Maxwell's equations, (1.7a) - (1.7d). From Gauss' Law we know $\nabla \cdot \mathbf{B} = 0$, and as such we also know $\mathbf{B} = \nabla \times \mathbf{A}$, given the vector identity $\nabla \cdot (\nabla \times \mathbf{A}) = 0$. We plug this into Faraday's Law (1.7c)

$$\nabla \times \left(\mathbf{E} + \frac{\partial \mathbf{A}}{\partial t} \right) = 0 \tag{1.8}$$

Another vector identity, $\nabla \times (\nabla \phi) = 0$ implies

$$\mathbf{E} + \frac{\partial \mathbf{A}}{\partial t} = -\nabla \phi \tag{1.9}$$

This gives us alternative definitions of the magnetic and electric fields in terms of vector and scalar potentials:[5]

$$\mathbf{B} = \nabla \times \mathbf{A}, \tag{1.10a}$$

$$\mathbf{E} = -\frac{\partial \mathbf{A}}{\partial t} - \nabla \phi. \tag{1.10b}$$

Using these definitions, Gauss's Law for Electricity becomes

$$\begin{aligned} \nabla \cdot \mathbf{E} &= \frac{\rho}{\epsilon_0} \\ \implies \nabla \cdot \left(-\frac{\partial \mathbf{A}}{\partial t} - \nabla \phi \right) &= \frac{\rho}{\epsilon_0} \\ \implies \Delta \phi + \frac{\partial}{\partial t} \left(\nabla \cdot \mathbf{A} \right) &= -\frac{\rho}{\epsilon_0} \end{aligned} \tag{1.11}$$

[5] These are in fact implicit in Maxwell's equations, and were derived by Maxwell in [23, 26, 28]. To be clear, $\mathbf{B} = \nabla \times \mathbf{A}$ is not original to him, it was already explored by Thomson, Neumann, Weber, and Kirchhoff in the early to mid 1800s, and he explicitly borrows this from Thomson [33]. It is unclear if $\mathbf{E} = -\nabla \phi - \frac{\partial \mathbf{A}}{\partial t}$ is a Maxwell original. In any case, they may be derived from physical principles or from Maxwell's equations.

Ampere's Law becomes

$$\begin{aligned}
&\nabla \times \mathbf{B} = \frac{1}{c^2}\frac{\partial \mathbf{E}}{\partial t} + \mu_0 \mathbf{J} \\
\implies &\nabla \times (\nabla \times \mathbf{A}) = -\frac{1}{c^2}\frac{\partial}{\partial t}\left(\frac{\partial \mathbf{A}}{\partial t} + \nabla\phi\right) + \mu_0 \mathbf{J} \\
\implies &\nabla(\nabla \cdot \mathbf{A}) - \Delta \mathbf{A} = -\frac{1}{c^2}\frac{\partial^2 \mathbf{A}}{\partial t^2} - \frac{1}{c^2}\frac{\partial}{\partial t}\nabla\phi + \mu_0 \mathbf{J} \\
\implies &-\Delta \mathbf{A} + \frac{1}{c^2}\frac{\partial^2 \mathbf{A}}{\partial t^2} + \nabla(\nabla \cdot \mathbf{A}) + \frac{1}{c^2}\frac{\partial}{\partial t}\nabla\phi = \mu_0 \mathbf{J} \\
\implies &\frac{1}{c^2}\frac{\partial^2 \mathbf{A}}{\partial t^2} - \Delta \mathbf{A} + \nabla\left(\nabla \cdot \mathbf{A} + \frac{1}{c^2}\frac{\partial \phi}{\partial t}\right) = \mu_0 \mathbf{J}
\end{aligned} \tag{1.12}$$

These are coupled, and as such quite gnarly to solve. However, there is an exploitable property in the definition of the potentials. Note if we define some other potentials $\mathbf{A}' \coloneqq \mathbf{A} + \nabla\psi$ and $\phi' \coloneqq \phi - \frac{\partial \psi}{\partial t}$, and consider $\mathbf{B}' \coloneqq \nabla \times \mathbf{A}'$ and $\mathbf{E}' \coloneqq -\nabla\phi' - \frac{\partial \mathbf{A}'}{\partial t}$, we see

$$\mathbf{B}' = \nabla \times (\mathbf{A} + \nabla\psi) = \nabla \times \mathbf{A} + \nabla \times \nabla\psi = \nabla \times \mathbf{A} = \mathbf{B}. \tag{1.13}$$

$$\mathbf{E}' = -\nabla\left(\phi - \frac{\partial \psi}{\partial t}\right) - \frac{\partial}{\partial t}\left[\mathbf{A} + \nabla\psi\right] = -\nabla\phi + \nabla\frac{\partial \psi}{\partial t} - \frac{\partial \mathbf{A}}{\partial t} - \nabla\frac{\partial \psi}{\partial t} = -\nabla\phi - \frac{\partial \mathbf{A}}{\partial t} = \mathbf{E}. \tag{1.14}$$

This means we have one remaining degree of freedom, which we pin down via the Lorenz[6] gauge

$$\nabla \cdot \mathbf{A} + \frac{1}{c^2}\frac{\partial \phi}{\partial t} = 0. \tag{1.15}$$

This leaves us with a set of decoupled heterogeneous wave equations:

$$\frac{1}{c^2}\frac{\partial^2 \phi}{\partial t^2} - \Delta\phi = \frac{\rho}{\epsilon_0} \tag{1.16}$$

$$\frac{1}{c^2}\frac{\partial^2 \mathbf{A}}{\partial t^2} - \Delta \mathbf{A} = \mu_0 \mathbf{J}. \tag{1.17}$$

It is important to remember that we have introduced the requirement of enforcing the Lorenz gauge condition, this acting as our connection back to Maxwell's equations. Now, of course the choice of this particular gauge condition is not necessary. We could have chosen the Coulomb gauge, $\nabla \cdot \mathbf{A} = 0$, the Weyl gauge, $\phi = 0$, or any other gauge, but we are interested in working with the Lorenz gauge and exploiting some of the properties that come with solving the above wave equations.

[6]Named after Danish physicist Ludvig Lorenz, not to be confused with the Dutch physicist, Hendrik Lorentz, after whom the Lorentz force, $\mathbf{F} = q\,(\mathbf{E} + \mathbf{v} \times \mathbf{B})$ is named. (A common mistake, even [32] makes it.)

1.3.4 The Particle Equations of Motion Under the Lorenz Gauge

We wish to derive the equations of motion in terms of the vector and scalar potentials. To do so, we have two options. We could first begin with the relativistic Lagrangians for a free particle and a particle interacting in a field and derive from there, obtained from Jackson [32]. Alternatively, we could simply take the Lorentz force and plug in the **E** and **B** fields and see what comes out, as does Sands [34]. The latter, though more tedious, follows the same logic as deriving the field equations from Maxwell's equations, so it makes sense for us to follow in its steps. See Appendix B for the derivation of the equations of motion from the relativistic Lagrangian.

Consider the Lorentz force, (1.4). We plug in the definitions and observe:

$$\begin{aligned} \mathbf{F} &= q\left(\mathbf{E} + \mathbf{v} \times \mathbf{B}\right) \\ &= q\left(-\nabla\phi - \frac{\partial \mathbf{A}}{\partial t} + \mathbf{v} \times \left(\nabla \times \mathbf{A}\right)\right) \end{aligned} \tag{1.18}$$

We use a vector identity to simplify things:

$$\mathbf{v} \times \left(\nabla \times \mathbf{A}\right) = \nabla\left(\mathbf{A} \cdot \mathbf{v}\right) - \left(\mathbf{v} \cdot \nabla\right)\mathbf{A}. \tag{1.19}$$

Plugging this in yields

$$\mathbf{F} = q\left(-\nabla\phi - \frac{\partial \mathbf{A}}{\partial t} + \left(\nabla\left(\mathbf{A} \cdot \mathbf{v}\right) - \left(\mathbf{v} \cdot \nabla\right)\mathbf{A}\right)\right). \tag{1.20}$$

We denote the total convective derivative

$$\frac{d\mathbf{A}}{dt} \coloneqq \frac{\partial A}{\partial t} + \left(\mathbf{v} \cdot \nabla\right)\mathbf{A}. \tag{1.21}$$

So we have

$$\mathbf{F} = q\left(-\nabla\phi - \frac{d\mathbf{A}}{dt} + \nabla\left(\mathbf{A} \cdot \mathbf{v}\right)\right). \tag{1.22}$$

Using Newton's second law (1.5), we shuffle some terms around and see

$$\frac{d}{dt}\left(\mathbf{p} + q\mathbf{A}\right) = q\left(-\nabla\phi + \nabla\left(\mathbf{A} \cdot \mathbf{v}\right)\right) \tag{1.23}$$

We use another vector identity to see

$$\nabla\left(\mathbf{A} \cdot \mathbf{v}\right) = \left(\nabla\mathbf{v}\right) \cdot \mathbf{A} + \left(\nabla\mathbf{A}\right) \cdot \mathbf{v}. \tag{1.24}$$

We know $\mathbf{v}$ is a function of time, so $\nabla\mathbf{v} = 0$. Denote the canonical momentum

$$\mathbf{P} \coloneqq \mathbf{p} + q\mathbf{A}. \tag{1.25}$$

We also know from Newton's second law and this definition

$$\mathbf{v} = \frac{1}{\gamma m}\left(\mathbf{P} - q\mathbf{A}\right) \tag{1.26}$$

Combining all of this yields

$$\frac{d\mathbf{P}}{dt} = q\left(-\nabla\phi + \frac{1}{\gamma m}\left(\nabla\mathbf{A}\right)\cdot\left(\mathbf{P} - q\mathbf{A}\right)\right). \tag{1.27}$$

Lastly, we know from $\frac{d\mathbf{x}}{dt} = \mathbf{v}$ and (1.26)

$$\frac{d\mathbf{x}}{dt} = \frac{1}{\gamma m}\left(\mathbf{P} - q\mathbf{A}\right) \tag{1.28}$$

Thus, for every particle i, evaluating ϕ and $\mathbf{A}$ at $\mathbf{x}_i$, we have arrived at our update equations:

$$\frac{d\mathbf{x}_i}{dt} = \frac{1}{\gamma_i m_i}\left(\mathbf{P}_i - q\mathbf{A}\right), \tag{1.29}$$

$$\frac{d\mathbf{P}_i}{dt} = q_i\left(-\nabla\phi + \frac{1}{\gamma_i m_i}\left(\nabla\mathbf{A}\right)\cdot\left(\mathbf{P}_i - q_i\mathbf{A}\right)\right). \tag{1.30}$$

We note

$$\gamma = \sqrt{1 + \frac{1}{(mc)^2}\left(\mathbf{P} - q\mathbf{A}\right)^2} \tag{1.31}$$

(Appendix B justifies this identity.) This yields our final set of update equations:

$$\frac{d\mathbf{x}_i}{dt} = \frac{c^2\left(\mathbf{P}_i - q\mathbf{A}\right)}{\sqrt{c^2\left(\mathbf{P}_i - q_i\mathbf{A}\right)^2 + \left(m_i c^2\right)^2}} \tag{1.32}$$

$$\frac{d\mathbf{P}_i}{dt} = \frac{c^2\left(\nabla\mathbf{A}\right)\cdot\left(\mathbf{P}_i - q_i\mathbf{A}\right)}{\sqrt{c^2\left(\mathbf{P}_i - q_i\mathbf{A}\right)^2 + \left(m_i c^2\right)^2}} - q_i\nabla\phi \tag{1.33}$$

1.3.4.1 Hamiltonian Systems

The above is a Hamiltonian system in disguise. Appendix B shows this explicitly by deriving the equations of motion first from a Lagrangian and then converting from a Lagrangian to a Hamiltonian, which turns out to be

$$\mathcal{H}(\mathbf{x}, \mathbf{P}) = \sqrt{c^2\left(\mathbf{P} - q\mathbf{A}\right)^2 + \left(mc^2\right)^2} + q\phi. \tag{1.34}$$

Here $\mathbf{A}$ and ϕ are functions of $\mathbf{x}$. This Hamiltonian represents the total energy in the system, and the updates to the $\mathbf{x}$ and $\mathbf{P}$ variables are computed as follows:

$$\frac{dx_i}{dt} = \frac{\partial \mathcal{H}}{\partial P_i}, \tag{1.35}$$

$$\frac{dP_i}{dt} = -\frac{\partial \mathcal{H}}{\partial x_i}. \tag{1.36}$$

If we plug our Hamiltonian in we find this produces the update equations (1.32)-(1.33). This Hamiltonian is noteworthy in particular due to the nature of the variables, in that it is a *non-separable* Hamiltonian. A Hamiltonian $\mathcal{H}$ is said to be *separable* if it can be written in the form

$$\mathcal{H}(\mathbf{x}, \mathbf{P}) = \mathcal{K}(\mathbf{P}) + \mathcal{U}(\mathbf{x}),$$

Where $\mathcal{K}$ and $\mathcal{U}$ denote the kinetic and potential energy of the system, respectively. In contrast, the Hamiltonian for the relativistic VM system considered in this work is *non-separable* because it contains a momentum-dependent potential of the form

$$\mathcal{H}(\mathbf{x}, \mathbf{P}) = \mathcal{K}(\mathbf{P}) + \mathcal{U}(\mathbf{x}, \mathbf{P}).$$

This causes challenges in preserving the symplectic nature of the Hamiltonian as it evolves over time. More of this will be discussed in Section 1.4.4.2.

1.3.5 The Particle-in-Cell Algorithm

Plasmas consist of many charged particles, all of which contributed to the fields which, in turn, contribute to the movement of the particles. This presents two problems. The first: the number of physical particles in any system of interest is far more than any computer could hope to simulate in a reasonable amount of time. The second: to model the movement of one particle amidst n, one must make n operations. Doing this n times yields an $O\left(n^2\right)$ operation for each timestep of the simulation, which is prohibitively expensive for large N. Particle-in-Cell (PIC), and its closely related cousin, Cloud-in-Cell (CIC), was developed in response to these challenges. In response to the first challenge, PIC eschews simulating each physical particle, instead grouping a large number

of particles into a single so-called macroparticle with a weight corresponding to the number of physical particles it represents.[7]

This answers the first challenge, but not the second. Even drastically reducing n physical particles to N macroparticles, where $N \ll n$, computing the interactions between each macroparticle would be computationally intractable. PIC answers the second challenge by mapping each particle to a k^d mesh, where $k \ll N$ and d is the number of spatial dimensions we are considering, and use this mesh to dictate the movements of the particles.[8] The interaction between the Eulerian mesh and the Lagrangian particles depends on the shape function S, which acts as a map between the two. The resulting scheme gives us a $O(k^2)$ or even $O(k \log(k))$ update scheme, depending on our wave solver.

There are some schemes in which we will place the the particle locations and velocities at staggered timesteps $\frac{\Delta t}{2}$, where Δt is our timestep (see Figure Figure 1.3). This allows us to leapfrog the velocity and position updates, using the fields to update velocities, velocities to update positions and fields, and so on (see Figure 1.2). Given an initial condition for both the fields and the particles, we interpolate the fields to the particles and use our particle update scheme to push the particles. This motion generates a current $\mathbf{J}$, and the new location provides us a new charge density ρ, which we interpolate back to the mesh, which in turn informs our wave solvers and we update accordingly.

We represent our particle distribution function as a summation of shape functions multiplied

[7]These two techniques are practically very similar, with their main difference residing in how they consider the macroparticle. PIC considers it as a discrete particle it interpolates to a mesh, while Cloud-in-Cell considers the particle as the center of a cloud of particles whose shape dictates the value given to the mesh. This, practically, results in a very similar algorithm, though it does result in some key differences, especially when considering nonuniform meshes and the weights of the particles near the boundary. If f is represented by a summation of δ functions over phase space, ie $\sum_{i=1}^{n} \delta(\mathbf{x} - \mathbf{x}_i)\, \delta(\mathbf{v} - \mathbf{v}_i)$, PIC interpolates the δ function in space using a shape function S, while CIC relaxes the δ function in space to a shape function S [35]. Both frameworks result a new distribution function with $N \ll n$ macroparticles and the substitution of a shape function for the spatial component of the distribution function.

[8]The reader may justifiably wonder why a k^2 operation is fine when an N^2 or n^2 is not. Each approximation represents an order of magnitude. Obviously this will vary with each simulation, this thesis is concerned with method development rather than application, and so N is often on the order of ten thousand while k is at most in the low hundreds. A code like EMPIRE [36] may have a mesh with thousands or millions of nodes, millions or billions of macroparticles, simulating trillions of physical particles. In short, if N particles give a computationally vexing amount of particles interactions to compute, n is practically impossible.

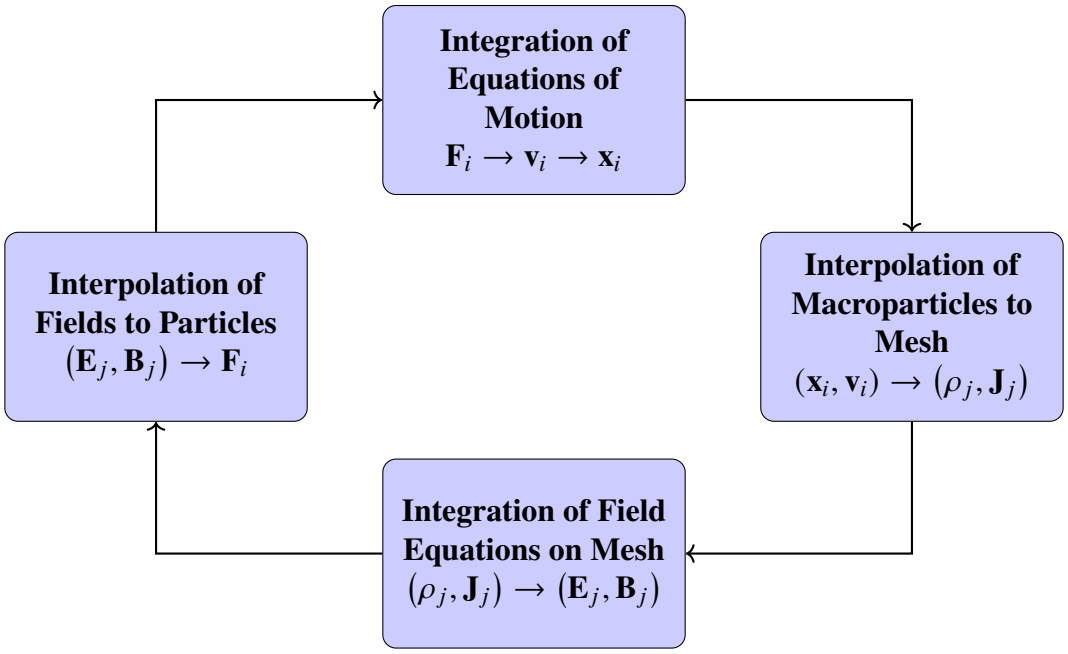

Figure 1.2 The basic Particle-in-Cell engine.

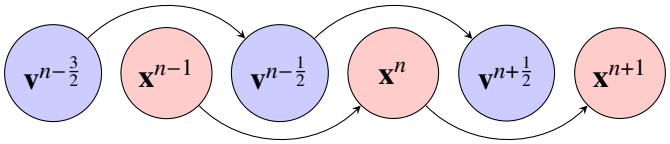

Figure 1.3 The basic Leapfrog scheme. $\mathbf{v}^{n+\frac{1}{2}}$ updates from $\mathbf{v}^{n-\frac{1}{2}}$ and $\mathbf{x}^n$, $\mathbf{x}^{n+1}$ updates from $\mathbf{x}^n$ and $\mathbf{v}^{n-\frac{1}{2}}$, and so on.

against a delta function (thus we are actually tracking macroparticles, not individual particles),

$$f_\alpha(\mathbf{x}, \mathbf{v}, t) = \sum_p^{N_\alpha} S(\mathbf{x} - \mathbf{x}_p)\delta(\mathbf{v} - \mathbf{v}_p). \tag{1.37}$$

We wish to acquire ρ and/or $\mathbf{J}$ to inform our wave solvers. Integrating over all of these gives us the number of particles:

$$N = \int_{\Omega_x}\int_{\Omega_v} f_\alpha(\mathbf{x}, \mathbf{v}, t) d\mathbf{v} d\mathbf{x}. \tag{1.38}$$

We can thus approximate ρ and $\mathbf{J}$:

$$\rho(\mathbf{x}) = \sum_{p=1}^{N} q_p S(\mathbf{x} - \mathbf{x}_p) \tag{1.39}$$

$$\mathbf{J}(\mathbf{x}) = \sum_{p=1}^{N} q_p \mathbf{v}_p S(\mathbf{x} - \mathbf{x}_p) \tag{1.40}$$

The shape function can be arbitrary, the most common being the linear spline function for a particle p at x_p:

$$S(x - x_p) = \begin{cases} 1 - \dfrac{|x - x_p|}{\Delta x}, & 0 \leq |x - x_p| \leq \Delta x, \\ 0, & |x - x_p| > \Delta x. \end{cases} \tag{1.41}$$

We must be careful here, if computing the current, a naive multiplication of charge by velocity at a particular timestep may lead to a violation of the continuity equation:

$$\frac{\partial \rho}{\partial t} + \nabla \cdot \mathbf{J} = 0. \tag{1.42}$$

Linear maps are not charge conserving for Yee, thus the shape functions of Villasenor and Buneman [37] are needed to preserve the continuity equation. See Appendix E for more details including the proof of charge conservation. For MOLT, no such modification is necessary, and linear weights are computed (see Figure 1.4 for a simplified 2D map). If we consider a particle at location $\mathbf{x}$, with the bottom lefthand node being at location $\mathbf{X}$, and the cell having dimensions $\mathbf{d}$, we let $w_i \coloneqq \frac{\mathbf{x}_i - \mathbf{X}_i}{d_i}$ and compute the weights as follows:

$$\begin{aligned}
Q_1 &= q_i(1 - w_1)(1 - w_2)(1 - w_3) \\
Q_2 &= q_i(w_1)(1 - w_2)(1 - w_3) \\
Q_3 &= q_i(1 - w_1)(w_2)(1 - w_3) \\
Q_4 &= q_i(w_1)(w_2)(1 - w_3) \\
Q_5 &= q_i(1 - w_1)(1 - w_2)(w_3) \\
Q_6 &= q_i(w_1)(1 - w_2)(w_3) \\
Q_7 &= q_i(1 - w_1)(w_2)(w_3) \\
Q_8 &= q_i(w_1)(w_2)(w_3).
\end{aligned}$$

We then compute $\rho = \frac{Q}{V}$, where V is the volume of the cell.[9] See Figure 1.4 for a 2D version of this. See also Appendix F for a more in depth exploration into high order interpolation schemes and

[9]This becomes a more complicated with a nonuniform mesh, which [38] derives. In Section 5.2 we briefly consider nonuniform meshes as the subject of future inquiry, but other than this the only mesh of interest is uniform, so the uniform mapping described above and in Appendix F will suffice.

B-splines.

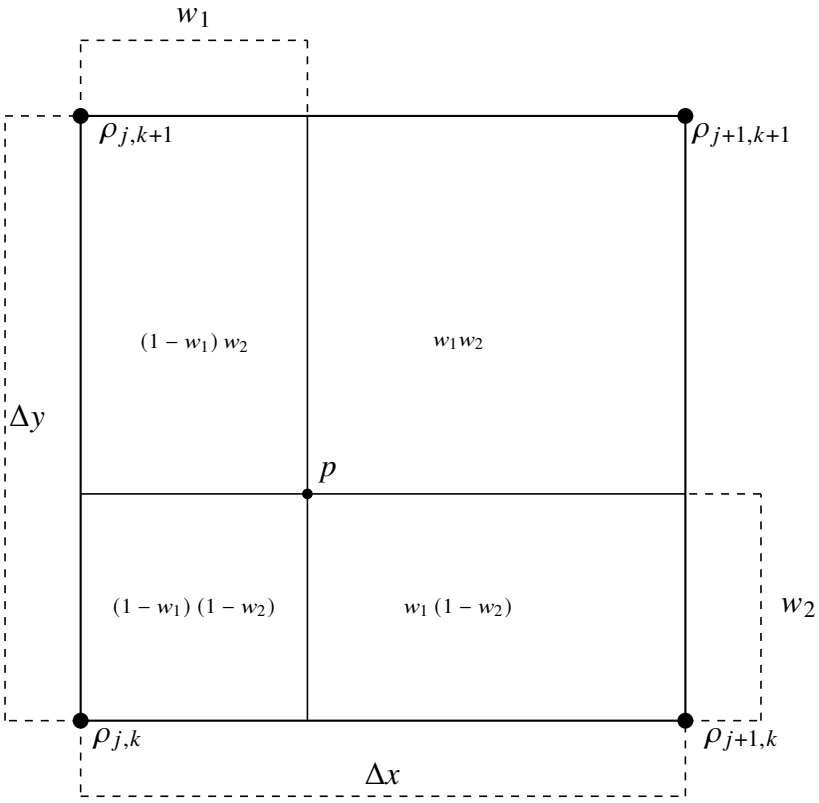

Figure 1.4 A linear interpolation of particle p.

Using the above method allows for an computationally efficient method for the modeling of plasmas. We have the framework, now we must start putting the pieces together.

1.3.6 Conclusion

In this section we considered first the basic equations governing a plasma. The Vlasov equation (1.6) governs the particle distribution function over phase space over time, evolving over the characteristics described by $\mathbf{v}$ and $\mathbf{a} = \frac{1}{\gamma m}\mathbf{F} = \frac{q}{\gamma m}(\mathbf{E} + \mathbf{v} \times \mathbf{B})$. This in turn indicates that we are interested in considering how the fields and particles themselves are evolved. The fields are governed by Maxwell's equations (1.7) and the particles are governed by the equations of motion described by Newton (1.5) and Lorentz (1.4). These were then cast in terms of vector and scalar potentials under the Lorenz gauge. Finally, we began considering the technique with which this dissertation is concerned, that of Particle-in-cell, or PIC, and how it takes both of these components, fields and particles, into consideration as it updates the plasma in question. Now that we have an idea of the

task at hand, we can begin a brief historical inquiry into the progress made thus far.

1.4 Literature Review

A classical problem confronting any historical inquiry is the question, "How far back do you wish to go?" Should we only consider PIC methods developed in the last ten years? This hardly seems just. Should we go back as far as Euclid developing his geometric theories? This hardly seems practical.[10] As such, we are in the unhappy position of having to choose where to begin and simply take what came before as a given. This hardly seems fair to the giants whose shoulders we are now taking for granted,[11] but time and paper command these constraints. As such, we will begin with a brief exploration into the work done on electromagnetics in the 1800s, and then move quickly into the early explorations into plasma science that occurred in the early 1900s. Without these two remarkable scientific achievements, we would having nothing to simulate. After this, we will begin a much more thorough inspection into the history of plasma simulations using PIC beginning in the 1940s and continuing to the present time.

1.4.1 Early Electromagnetics

It is impossible to study plasmas without at least briefly considering electromagnetics, the study of the underlying fields governing the particle equations of motion. Faraday's concept of expressing magnetism as lines of force, particularly in Part III of *Experimental Researches in Electricity* [20],[12,13] was one of the main inspirations for James Clerk Maxwell to begin considering

[10]Though David Foster Wallace somehow manages to accomplish this in his absolute tour de force historical inquiry into Georg Cantor in [39]. But he also had 300+ pages to do so and we do not.

[11]We will be effectively ignoring Newton, Coulomb, Ampère, Ohm, and reducing Faraday to a series of footnotes.

[12]Maxwell cites Series XXXVIII of the Experimental Researches as well as *Phil. Mag. 1852* in his *On Faraday's Lines of Force* [23]. There are two journals, *Philosophical Magazine and Journal of Science* and *Philosophical Transactions of the Royal Society of London*, both of which have articles by Faraday published in 1852 [21, 22]. The *Philosophical Magazine* article is a continuation of the *Transactions* article. The *Transactions* article itself is the 28th (XXVIII) of 29 articles compiled in the three volumes of *Experimental Researches in Electricity* [18, 19, 20]. Volume III is the last in the set and it only goes to series XXIX. Now, there are chapters in each series that were continuous throughout (eg series XXVI had chapters 32 and 33, series XXVII continued to chapter 33), but these leave off at 37, and besides, are labeled using Arabic numerals rather than Roman. There are some articles at the end of Volume III that are not a part of a series, the first three of which have to do with lines of magnetic force (the second of which is the *Philosophical Magazine* [21] that is the continuation of the *Transactions* article [22], ie Series XXVIII. I am somewhat hesitant to accuse Maxwell of even this small a typo, however, a number of typos have been cataloged, for example Boltzmann [40] did find a number of other errors in this work, so it is not beyond the pale that this may be an instance of one.

[13]Part III may get special attention, but he references throughout Faraday's corpus, and does so almost every other page. It is also worth noting he repeatedly cites Professor William Thomson (better known as Lord Kelvin) almost as

how magnetism, electricity, and charge and current density were intimately connected. Faraday had already developed the concept of magnetism as "lines of magnetic force as representations of magnetic power, not merely in the points of quality and direction, but also in quantity." This can be easily visualized by spilling some iron filings in the presence of a magnet, and, interestingly enough, an electric current. He takes pains to point out that this line of force means no more and no less than just that, giving the strength and direction of the magnetic force, as he is reluctant to tie this to a specific physics (§3175), though he does give a nod to the possibility of modeling this field as either a fluid or a magnetic center of action. In any case, Maxwell takes his lines of force with the analogy of an incompressible fluid[14] in *On Faraday's Lines of Force* [23], in which he considered magnetism as an array of infinitely tiny tubes through which a fluid flowed exerting force. The purpose of this paper was mostly to give a mathematical framework for what Faraday had discovered. In the section entitled "Electro-magnetism" of this paper he notes an interesting observation, that the law observed by Ampère, $\nabla \times \mathbf{H} = \mathbf{J}$, results in $\nabla \cdot \mathbf{J} = 0$, the continuity equation for closed circuits. Given the assumption of incompressibility, this limits the study of magnetism to steady currents, breaking down on the introduction of any variation over time.

It is in a series of papers in the 1860s that he fully develops a unified theory of light and electromagnetism [24, 25, 26, 27],[15] and it is in these papers that he solved this issue. Proposition XIV in [26] is where the correction to Ampère's law was made, he adds "a variation of displacement,"

much as Faraday. Ironically, though the two had sincere admiration for the other, Thomson was skeptical of Maxwell's conclusions to his death [33].

[14] Anticipated by Faraday as well in §3073.

[15] It is worth noting that Parts I and II both appear in the same volume of *Philosophical Magazine*, but Part II is itself split into two separate sections. The ending of the first part fails to mention this.

noting that this is the exact same as a current.[16] If

$$\nabla \times \mathbf{B} = \mu_0 \mathbf{J}, \tag{1.43}$$

then the identity $\nabla \cdot \nabla \times \mathbf{v} = 0 \, \forall \, \mathbf{v} \in \mathbb{R}^n$ is exploited to show

$$\nabla \cdot \mathbf{J} = 0. \tag{1.44}$$

This only satisfies the continuity equation if the current is constant, in other words $\frac{\partial \rho}{\partial t} = 0$. Maxwell in this proposition adds $\frac{1}{c^2} \frac{\partial \mathbf{E}}{\partial t}$ to the righthand side to get the electrodynamic version of Ampère's law:[17]

$$\nabla \times \mathbf{B} = \mu_0 \mathbf{J} + \frac{1}{c^2} \frac{\partial \mathbf{E}}{\partial t}, \tag{1.45}$$

From Gauss's Law for Electricity, $\nabla \cdot \mathbf{E} = \frac{\rho}{\epsilon_0}$ (also known at the time), when we apply the divergence to (1.45) we get

$$\nabla \cdot \mathbf{J} + \frac{\partial \rho}{\partial t} = 0. \tag{1.46}$$

This was all developed before the standardization of variables; there was no real use of vectors $\mathbf{E}$ or $\mathbf{B}$ to represent the electric and magnetic fields, nor was there any convenient notation such as $\nabla\cdot$ or $\nabla\times$ to represent the divergence or curl, and the units of Maxwell are somewhat difficult to track to the point where John Arthur advises, wisely, to not worry too much about it [43]. All work was done component-wise and with different variables even for components of the same fields. Thankfully Feynman makes very short and accessible work of this in Chapter 18 of [44], as does Jackson in Chapter 6 of [32], and Griffiths in Chapter 7 of [42].

[16] Despite an emphasis placed by many on the aesthetic nature of a more symmetric set of equations this change induced, Bork [41] finds no compelling evidence to suggest this was what motivated Maxwell, who was seemingly more interested in the satisfaction of the continuity equation and the nature of the displacement current as being as physical a current as the conduction current. Interestingly, Griffiths [42] claims that the satisfaction of the continuity equation was more accidental, a "happy dividend" rather than the actual intent. True, Maxwell does explicitly says in Prop. XIV, "To correct the equations (9) of electric currents for the effect due to the elasticity of the medium," with (9) being $\nabla \times \mathbf{H} = \mathbf{J}$, but then immediately shows that this satisfies the continuity equation, so it seems somewhat up for grabs if he was only motivated by the interpretation of $\frac{\partial \mathbf{D}}{\partial t}$ as another current or by satisfying the continuity equation. Griffiths cites Bork, but Bork himself lists the two reasons Maxwell had as satisfying the continuity equation and treating the variation of the displacement as a physical current, in that order, so it is unclear if Maxwell was more concerned in considering the displacement current as a physical current, correcting the continuity equation, or both equally.

[17] This is a somewhat simplified version of the events. For brevity we are smuggling in the assumption that the permittivity and permeability are respectively ϵ_0 and μ_0, which is the only scenario in which this current work is interested, though by no means the only interesting one.

It was in Part III of this work [26] as well that Maxwell derived the speed of propagation of electromagnetic waves through the aether (Proposition XVI), which he immediately noted was less than 1.5% off from the speed of light found by Fizeau. He was quick to identify this similarity and conclude, "we can scarcely avoid the inference that *light consists in the transverse undulations of the same medium which is the cause of electric and magnetic phenomena*" (emphasis in original).

Maxwell would go on to refine and compile this work into *A Dynamical Theory of the Electromagnetic Field* [28]. He finally expanded this into the two volume work *A Treatise on Electricity and Magnetism* [29]. A more thorough discussion on how this developed can be found in [41, 43]. Far from his only work, he published prolifically on a variety of topics, including gas dynamics, fluid mechanics, the nature of color and colorblindness, thermodynamics, and topics in philosophy including the nature of free will and paradox [30, 31]. He died at age 49 in 1879, and left the world with a treasure trove of scientific discovery.

The work of Maxwell sent waves throughout the scientific community, who wasted no time in dissecting this work and examining the implications it held. [43] does a good job discussing the history of this. Oliver Heaviside is credited with taking Maxwell's equations, written in [29] in quaternion form, and rewriting them in the vector notation with which we are familiar today, doing so in Article 30 of [45]. Willard Gibbs introduced the ∇ operator to vector calculus in [46].[18] Though he was mostly interested in discussing math rather than electromagnetics, it worth noting he briefly mentions Maxwell's curl equations on pages 195 and 196 in [47]. To emphasize the novelty of this, the first of the equations he emphasizes the equivalence by the following line:

$$\nabla \times \mathbf{E} = -\dot{\mathbf{B}}, \quad \operatorname{curl} \mathbf{E} = -\dot{\mathbf{B}}. \tag{1.47}$$

Amusingly enough, he is more brief with the other equation,

$$\nabla \times \mathbf{H} = 4\pi \mathbf{C}. \tag{1.48}$$

We see here the standardization of the electric and magnetic fields taking place, but the total current is still described, understandably enough, as $\mathbf{C}$.

[18] Maxwell did use the nabla in *A Treatise on Electricity and Magnetism*, but that was in the context of quaternions. He and Gibbs both define the nabla in the same exact way though, $\nabla = \mathbf{i}\frac{\partial}{\partial x} + \mathbf{j}\frac{\partial}{\partial y} + \mathbf{k}\frac{\partial}{\partial z}$.

Heinrich Hertz, a student of Helmholtz, is the next major player to consider Maxwell's theory. He got his start though by attempting to derive Maxwell's theory from a different foundation, attempting to avoid what was seen as a rickety argument justifying the addition of the displacement current $\frac{\partial \mathbf{D}}{\partial t}$ to Ampère's law. Taking a page from Ampère, who stated that the magnetic field induced by a current is the same nature as that generated by an "ordinary" magnet, otherwise known as the principle of the "unity of magnetic force," Hertz thought this wise and applied this principle to the electric field generated by a changing magnetic field, claiming it is of the same nature as that generated by electrostatic charges. This was the principle of the "unity of electric force." While brilliant, it was dependent on some assumptions on how current is induced that were far from secure. He then turned to what would inadvertently make him the legend in not only the scientific community, but would possibly have the greatest impact on communication technology to his time. He was the one who gave experimental verification of Maxwell's theory, detailed in his book [48].[19] It was in this work that he managed to not only prove that Maxwell's equations correct, as his identification with the speed of electromagnetic waves and the speed of light,[20] but he also effectively invented the radio [33].

A few years after Hertz gave physical proof for Maxwell's theory came Hendrik Lorentz, after whom the equation of motion of a charged particle in an electric and magnetic field is named. Though the now famous equation of motion is derivable directly from Maxwell's work, it would take some time for this force to be codified. Heaviside for example was able to identify the correct equation of motion for a magnetic field [50],[21] but it was not until Hendrik Lorentz in [52][22] that

[19]Dedicated to his advisor, Helmholtz, and with a forward by Lord Kelvin. It is quite astonishing seeing the relationships between these legends.

[20]Larmor said of this, "the discoveries of Hertz left no further room for doubt that the physical scheme of Maxwell... constituted a real formulation of the underlying unity in physical dynamics." [49], quoted in [33].

[21]This may be found in Chapter 50 of [51]. Interestingly, equations that looks awfully similar to the Lorentz factor begin appearing in this paper. Given a particle with charge q, velocity u along the z axis, then the tensor representing the magnetic force at distance r from this particle is $H = \frac{q}{r^2} u \sin(\theta) = cEu\nu$, with θ being the angle $\mathbf{r}$ makes with the axis, and $\nu = \sin(\theta)$. We are given $\mu_0 c V^2 = 1$, where c is the permittivity that enforces this in a medium such that V is the speed of propagation (V is v in the original text, here switched to the capital letter to reduce confusion between v (vee) and ν (nu)). We begin seeing a term $H = \frac{qu\nu}{r^2}\left(1 + \mu \frac{d}{d\mu}\right)\left(1 - \nu \frac{u^2}{V^2}\right)$, where $\mu = \cos\theta$, which has a term that looks eerily reminisce of $\gamma = \left(1 - \frac{u^2}{c^2}\right)^{-1/2}$. Even more interesting, he acknowledges that this only works for $u^2/V^2 \ll 1$, and that it all breaks down when $u^2/V^2 \to 1$.

[22]The translation of the title is *Attempt of a Theory of Electrical and Optical Phenomena in Moving Bodies*,

the full Lorentz force would be established:

$$\mathbf{F} = q\left(\mathbf{E} + \mathbf{v} \times \mathbf{B}\right). \tag{1.49}$$

It is also worth noting the Lorentz had been doing serious work with relativity, considering how a body moving relative to the stationary aether's frame of reference would change, developing what is now known as the Lorentz transform. He still considered the aether as the "true" frame of reference, with everything moving relative to it.

It was slightly over a decade until Einstein would take the work of Maxwell, including the work he had done in deriving the speed of light with regards to vacuum permittivity and permeability in (136) of [26], and revolutionize the world of physics with his theory of special relativity [53]. That connection between electromagnetism and light turns out to be more profound than anyone had anticipated. Maxwell's equations, like the speed of light, are true for any reference frame. There is something about the very nature of spacetime to which Maxwell's equations speak.

1.4.2 Early Plasmas

The above is concerned with abstract electromagnetic fields. But what happens when charged particles are placed in these fields? What about the fields generated by these particles, how do they impact the other particles within the system? Scientists were eager to explore this burgeoning field. We first go back slightly in time, Brown [54] identifies Crookes in the late 1800s as the prophet of plasmas. In an address delivered to the British Association for the Advancement of Science in 1879 [55], Crookes announced the onset of what he viewed as a fourth state of matter in a rather captivating way, "[w]e have actually touched the border land [sic] where Matter and Force seem to merge into one another." It is worth noting that he himself cites Faraday as the true forerunner of this fourth state of matter, quoting him,[23] "If we conceive a change as far beyond vaporisation [sic] as that is above fluidity, and then take into account also the proportional increased extent of alteration as the changes rise, we shall perhaps, if we can form any conception at all, not fall far short

and the full translation to English may be found online at `https://en.wikisource.org/wiki/Translation:Attempt_of_a_Theory_of_Electrical_and_Optical_Phenomena_in_Moving_Bodies`

[23] I am unable to find this quote directly in Faraday's corpus, Crookes cites Dr. Bence Jones's *Life and Letters of Faraday*.

of Radiant Matter; and as in the last conversion many qualities were lost, so here also many more will disappear." This assertion stemmed from his work with glow discharges that, when described in [56], sound quite similar to that which was described by Langmuir in [57].

Several scientists would continue this work. Lodge was the scientist who identified the cyclotron radius and frequency [58].[24] Lord Rayleigh began the conception of the plasma frequency in [59], that of a stationary set of ions among which an equal number of electrons oscillate, and this was codified in its modern form in [5]. Debye and Hückel in [60] identified the Debye length, interestingly enough referring to it by the inverse square: χ^2. Langmuir and Tonks would use both of these constants in their seminal work *Oscillations in Ionized Gases* [5], which coined the term, "plasma." While Boltzmann was the one who codified gaseous dynamics including collisions [61, 62] (English translation [63]), Landau developed what would become the standard operator for plasma collisions in the 1930s [64],[25] which is a simplified form of the Boltzmann collision operator, considering only grazing collisions with small angle deflections. Vlasov would take the works of Boltzmann, Langmuir, Tonks, Rayleigh, and Landau and, in 1938, publish what would become known as the Vlasov equation [69], translated to English later in 1967 [70].[26]

Presently we have a system of charged particles that, according the the laws of Maxwell (though

[24] In his *A Short History of Gaseous Electronics*, Brown [54] attributes Lodge as the one who identified the cyclotron frequency. In his bibliography, he specifically cites page 36 of [58]. It is unclear if he is attributing this page to where Lodge identifies the frequency, given page 36 contains a rather lovely description of the current conception of electrons, or "electrions" or "electrical ghosts", but nothing about a frequency or even a magnetic field. The next chapter, specifically page 42, is where he goes into a discussion of a charged particle in a static magnetic field and identifies the radius of this particle. Of course, contained in the radius is the frequency (see Chapter 2 of [7] for a clearer explanation). It is entirely possible Brown simply had a different edition of *Electrons* than the one I found, no edition is given in his bibliography.

[25] An English translation may be found in chapter 24 of [65] It's worth noting there is a 1937 article [66] published in a different journal, but the book simply cites both as the original work it is translating, and the titles are both extremely similar, one is in Russian and one is in German. Both (Google) translate to *The Kinetic Equation in the Case of Coulomb interaction*, which is close to the title of the chapter, the only difference being the "transport" is used in place of "kinetic." Needless to say I am no Russian or German speaker, but given the plethora of references to both "transport" and "kinetic" English translations of the term in the literature (eg Kunz uses "transport" [67] while Bobilev, Potapenko, and Chuyanov (themselves writing from Moscow) [68] use "kinetic" when citing Landau) and the similarity of the terms themselves in physics contexts, it seems safe to conclude these are referencing the same concept. Dr. Matthew Pauly at MSU has suggested that "kinetic" is indeed the better translation.

[26] Frustratingly, while there are many references to his 1945 monograph Теория колебательных свойств электронного газа и её приложения, or *Theory of Vibrational Properties of an Electron Gas and Its Applications*, as his allegedly more popular and thorough explanation of the subject. I am unable to locate this monograph and, despite several references to the title itself, unable to even find out what journal or publisher it was.

we now see that the discovery of these laws was a group effort), generate electromagnetic fields when they move, forming a current. By Lorentz we also know that a charged particle is accelerated and twisted by these fields. Truly a complicated system, and one that will require a considerable amount of effort to model. But, it was at this time that the first concepts of modern computing were beginning to be introduced to the scientific community. In 1936 Turing would introduce a formal language for discussing computing [71][27] and the problems that may be solved by this process.[28] As it turns out, the simulation of plasmas by a technique known as Particle-in-cell (PIC) is one such problem that may be computed. It is this topic, the main focus of the thesis, to which we now turn.

1.4.3 Early PIC

Birdsall [73] traces the first numerical simulations of plasmas as far back as the 1940s, citing Professor Hartree and Phyllis Nicolson who, using Coulomb's Law, computed the orbits of around 30 interacting electrons in a magnetron with a simplified 1D projection of the electric field in 1943 [74].[29] This was accomplished using only a hand calculator! This model included the electric and magnetic fields, as well as the effect of space charge. Hartree would later go on to study electron flow in a one-dimensional diode in a like manner in 1950 [75]. As such, the first physics computers were Hartree and Nicolson.

The first great breakthrough for what we now think of as computers occurred in 1956 by Tien and Moshman [76], simulating noise in a high-frequency diode. In the classic textbook by Hockney and Eastwood [77], they pay tribute to this paper in a manner worth quoting in full:

> At about the time the first digital computers became available, and perhaps the earliest simulation on such computers, was the study of noise in a high-frequency diode by Tien and Moshman of Bell Laboratories. They used a Univac I to simulate a one-dimensional diode with about 360 electrons sheets and a physical time step of 2 ps. About 3000

[27] Of course, at the time "computing" was only the act of calculation, the idea of our modern computers was completely foreign.

[28] He published roughly at the same time as Church [72], tackling the same problem from very different angles. He modified his paper to acknowledge this, proving the equivalence of their approaches ("computability" from Turing and "effective calculability" from Church).

[29] Birdsall cites Buneman and Dunn's 1966 work, specifically page 36. I have copied their citation, *Science J. vol. 2, pp 34-43*, but it is worth noting that I was only able to locate a NASA archived document of the same name. This work does discuss this remarkable accomplishment, but on page 21, not 36.

> time steps were taken, each of which required between 25 and 40 s of computer time. The total computing task must rank as one of the most impressive achievements of early device modeling, requiring as it did some 25 h of reliable computing on a first generation vacuum-tube computer with a mercury delay-line store of only about 1000 numbers.

These 1000 numbers (or words to use the language of the original paper) were only capable of storing 11 decimal digits plus the sign. 500 of these words were used to store the actual program, the rest of them were dedicated to storing position and velocity, with each word being split into two pieces, the first six digits containing the spatial information and the last containing the sign and magnitude of the velocity (recall this is 1D). If you squint at this, it is the first warm plasma simulation. Buneman, the student of Hartree, would write the first paper intentionally modeling a plasma in 1959 [78], which studied the cold two stream instability problem, the problem in which electrons are moved amongst immobile ions that are representing as a neutralizing background. Buneman found that instabilities would emerge if electron drift velocity rises above $.9k_BT$, where k_B is the Boltzmann constant and T is the absolute temperature. Shortly following this was Dawson [79], who set up a similar system in which electrons were injected into a neutralizing background of ions. He considered series of "sheets" of electrons and how they would act when perturbed, finding they behaved as harmonic oscillators if they didn't cross each other. In representing these sheets as perfectly elastic, upon colliding he would simply have the particles exchange velocities, and in so doing he could represent them as a sequence of pendulums. In his 2005 review paper, Verbonceour [80] also identifies these as being the root to what is now known as Particle-in-Cell (PIC). Dawson and Smith in 1963, in modeling two warm species obtained results confirming theory five years before a laboratory was able to do so [73, 81]. It is now that we begin to see the trend of computation emerging. Until now, labwork would be the manner in which theory was confirmed, now computation would begin both confirming and refining theory.

Until this point, Birdsall [73] identifies all the models as being one-dimensional, electrostatic, collisionless, mesh-free, and simulating "disk" particles, or particles with zero thickness. Now we

reach the part of the story in which these limitations begin to be shrugged.

Throughout the 1960s, we see the 1D model get pushed to its absolute limits, with 1 spatial dimension being complemented with 2 and 3 velocity dimensions, and this being done to great effect. However, eventually the need came to extend to multiple spatial dimensions. With this need came the grid based approach, as solving Coulomb's law became prohibitive with the increased domain and thus the increased count of particles (and even in 1D this can become prohibitively expensive). The domain is discretized into a finite set of grid nodes, and various techniques are used to compute the fields only at these locations (more on this later). It was the work of Hockney [82], his student Burger [83], as well as Dunn and Ho [84], that pushed this grid based method. In computing charge or current from particles, a nearest-grid-point method would be used, simply totaling up the number of particles that are in the vicinity of a node and counting that as the charge in the area.

It is important to note that these are all viewing the electric and magnetic fields as static, with the ions in the background creating enough of a neutralizing presence such that we can simply ignore the derivatives of the electric and magnetic fields. But this is obviously an approximation, and eventually the need to have electromagnetic codes became apparent. One of the first attempts at such was a 1D-3V code by Langdon and Dawson [85] in 1967, which computes the longitudinal field E_x by solving Poisson's equation, and finds the transverse fields through Maxwell's equations (see [35], chapter 6 for more details). This is a somewhat involved process, and still leaves the user in one spatial dimension.

The need to consider electromagnetic conditions in multiple dimensions gave rise to one of the heroes of our story, applied mathematician Kane Yee, who developed one of the leading methods of solving Maxwell's Equations over time in 1965 [86], which soon came to be known as the Yee scheme (see Appendix D.1 for more details). While Yee was only concerned with simulating Maxwell's equations without particles, soon the plasma community would put this scheme to good work, with Buneman [87] in 1968 and Morse and Nielson [88] in 1971. Later on Langdon would go on to develop an implicit field solver [89] in 1985.

PIC would become fully codified in the 1970s [80]. This decade began with another large step in

the right direction. It was Langdon and Birdsall who identified the idea of a "finite-particle shape" in which a particle was no longer understood as a point particle represented by charge multiplied by a Dirac delta function, $q\delta(\mathbf{x} - \mathbf{x}')$, but rather as a collection of particles, or cloud, and as such a shape function multiplied by a charge, so $qS(\mathbf{x} - \mathbf{x}')$ [90]. We are no longer representing individual particles, but rather clouds of particles bundled together in a single macroparticle that we evolve over time. This increases our capacity to simulate many particles, resulting in a flexible method. Additionally, being able to modify shape functions in different dimensions will be used to preserve the continuity equation, which will be of vital importance. While this is a CIC concept, as mentioned previously this is easily mappable to a PIC framework, where S is viewed as the interpolant of a discrete point charge rather than the physical nature of what the macroparticle represents.

Also during this time, a number of accurate 3d particle pushers were developed, the most famous of which was developed by Boris in 1970 [91], but another, less well known, was also developed by Buneman [92]. The Boris push is further explored in Appendix D.2. These methods, though accurate and reliable, are not implicit and thus have the setback of requiring a timestep of $\omega_p \Delta t < 2$. We must wait until the 80s for implicit particle integrators to come onto the scene and dodge this issue (though not without their own drawbacks, they required timesteps in proportion with their maximum wavelength, $kv\Delta t < 1$), when in 1981 several papers came out on this topic, Mason [93], Friedman, Landon, and Cohen [94], and Denavit [95]. Mason and Denavit both approached this problem by introducing fluid moment equations for mass and momentum, where Friedman, Langdon, and Cohen elected to explicitly approximate the future density, linearize it, and compute the its correction in the advanced field (described in more detail in [96]). See [97] for a good overview of the methods in 1985, [35], p 205 for a brief summary and [98], chapter 8 for a more exhaustive one. More will be said about implicit PIC in Section 1.4.4.1.

The 1970s saw the PIC field finally come together, the results of which produced the seminal texts of Hockney and Eastwood [77] and Birdsall and Langdon [35] being written in 1981 and 1985, respectively.[30] There was a rather large problem confronting the community, however, in that most

[30]Dr. John Verboncoeur at MSU noted that the work undergirding these texts was concurrent, with [35] being published later due to Langdon's efforts to complete the analysis of the implicit model.

of the literature was concerned with periodic boundary problems, which does not capture device simulation. This was the problem Lawson [99] sought to solve, providing the first paper discussing non-periodic boundary conditions, though he is quick to point out that many had been working on non-periodic boundaries and as such he is simply giving a voice to this work ([80] also points out that this paper was the result of The Plasma Device Workshop at Berkeley and featured Birdsall, Crystal, Kuhn, and Lawson).

We now see how most of the limitations Birdsall elucidated have been eliminated. All but one, that is, we still are relying on collisionless plasmas. Collisions remained beyond reach for these techniques, a fact which [35] has a rather frank take on:

> It has often been stated that to obtain "collisionless" behavior, the collision times must be longer than the length of the run. Fortunately this is overly pessimistic. What appears to be closer to the truth is that collision times should exceed, e.g., instability exponentiation times and trapping times.

Now, at first glance this indicates that we have no way of taking collisions into account. While strictly speaking this is true, as we are not including any sort of overt collision operator, at long range (ie $> \Delta x$) the fields induced by the particles will influence their trajectories, thus a sort of Coulomb "collision" will take place.

Finally, collisions were introduced using Monte Carlo methods (MC) by individuals such as Burger, Takizuka, Hirotada, Vahedi, Surendra, Morey, Birdsall, et al [100, 101, 102, 103, 104, 105]. For our purposes we are dealing with collisionless plasmas, so we will not be going into details, but as this represented the last of the hurdles Birdsall identified, it is worth at least noting the individuals who first leaped it. We will give collisions a slightly closer look as a future line of inquiry in Section 5.5, some more will be said then.

1.4.4 Later PIC

We have now come to the end of the histories provided by Birdsdall [73] in 1991 and Verboncoeur [80] in 2005. What does the field look like now? There have been a few recent developments that are worth looking over.

Any PIC solver has two challenges confronting it, solving the fields (represented by Maxwell's equations), and solving the particles (represented by the Newton-Lorentz system). As such we will first examine what has been done to push the particle solvers forward, and then turn to the field solvers.

1.4.4.1 Implicit PIC

An explicit method carries with it the requirement of keeping its timestep below whatever the Courant–Friedrichs–Lewy (CFL) limit of the method is. It is typically much more intuitive to implement and much less costly (per step at least), and therefore it is often the default approach, most textbooks will present the explicit approach to PIC as the PIC approach. Ripperda et al [106] do an excellent job comparing five classic explicit, semi-implicit, and implicit particle methods, one of which, the Boris method, we explore in some detail in Appendix D.2. In the historical discussion, the implicit field and particle solvers that began development in the 1980s were mentioned [93, 94], but these have serious drawbacks, as both technological and scholarly development was at a place such that approximations such as linearizing and lagging were required, which resulted in energy conservation errors, which in turn leads to numerical heating and cooling [107].

Lapenta and Markidis [108, 109] in 2011 developed a method, which is implicit, can have electromagnetic phenomena, and is energy conserving. While [108] is not charge conserving, [109] adds a correction step that regulates charge conservation, reducing error in Gauss's law. The error that comes with the lack of charge conservation can be reduced with a technique called divergence cleaning [110, 111] (see also [112] for a slightly more niche cleaning technique), however, there is still the issue of light wave dispersion errors [113]. Due to its semi-implicit nature, however, it still has a CFL to satisfy, and as such is struggles with speed, requiring careful optimization. Lapenta would later go on in 2017 [114] to combine the approaches of [96] and [115] which resulted in an energy conserving and unconditionally stable scheme that only increases computation time in the field solver, the particle solver remains the same as that of an explicit pusher. However, in so doing charge and momentum conservation were again sacrificed. Again, this can be mitigated by divergence cleaning, though of course this increases computation time, and, despite the increased

adherence to these particular physical laws, reduced accuracy on the whole. Also in 2017 Siddi, Lapenta, and Gibbon developed a mesh free method for a plasma that recovered the Darwin limit of Maxwell's Equations [116]. Out of this work came the asymmetrical Euler method (AEM) of pushing particles. This is a semi-implicit method which is of particular interest for our purposes, as it is a particle pusher in terms of the scalar and vector potential rather than the electric and magnetic fields, which will be of great use when we discuss solutions to Maxwell's equations in terms of these potentials (see Section 2.3.1).

Another line of inquiry began with Chacón, Chen, and Barnes in 2011 [107], in which they developed a fully implicit, energy and charge conserving, electrostatic PIC code using a Jacobian-free Newton-Krylov (JFNK) [117] solver and employing Cohen et al's substepping algorithm [118], which uses a small timestep to move particles and a larger timestep to solve the fields. They were not exactly momentum conserving; however, their adaptive particle substepping combined with spatial smoothing keep the errors small. They followed this up in 2013 [119], in which they extend this to general mapped meshes, still keeping electrostatic and 1D, but outlining how they may extend to multiple dimensions. In 2014, Chen and Chacón extend this to the Darwin model [120], bringing this to 2D in 2015 [121] and to curvilinear coordinates in 2016 [122]. Chen, Chacón et al [113] have more recently (2020) combined the leap-frog method for the fields and the Crank-Nicolson method for the particle equations, resulting in an exactly energy and charge conserving relativistic electromagnetic PIC scheme which also overcomes the light wave dispersion errors from which Lapenta's method suffers, bringing them back down to the levels that come with explicit PIC. In the same year, Ricketson and Chacón [123] developed an asymptotically preserving implicit Crank-Nicolson based method which not only tracks full-orbit motion on small timescales, but also recovers all first order guiding center drifts and the correct gyroradius on large timescales. Koshkarove et al [124] built upon this in 2022, noting that, though remarkable, it was done with a brute force generalized minimal residual method (GMRES) JFNK solver, which is rather expensive. They managed to remove the JFNK component and replace it with Picard iteration for a 3-4 times speedup. Chen and Chacón in 2023 developed an implicit, charge and energy conserving PIC method that

preserves all drifts, though at the sacrifice that it is back to electrostatic [125]. Very recently, these authors regained a significant amount of ground, developing a fully implicit *local* energy and charge conserving scheme for both the electrostatic and Darwin electromagnetic limit [126].[31]

1.4.4.2 Structure Preserving Particle Methods

Any Hamiltonian system, such as a charged particle in a field, acts on a symplectic manifold, so it is desireable for any numerical update scheme to preserve this symplectic structure [131, 132, 133, 134]. What is a symplectic update? Given a vector in phase space $\mathbf{z} \in \mathbb{R}^{2n}$, an update matrix $A \in \mathbb{R}^{2n\times 2n}$ is called volume preserving if its determinant is unity, a necessary but not sufficient condition for it being symplectic, which is when $A^T J A = J$,[32] where $J = \begin{pmatrix} 0 & I_n \\ -I_n & 0 \end{pmatrix}$.[33] This translates over to a Hamiltonian system when we combine the $\mathbf{x}$ and $\mathbf{P}$ (typically denoted $\mathbf{q}$ and $\mathbf{p}$, respectively) into a single $\mathbf{z} \coloneqq (\mathbf{p}, \mathbf{q})$ vector and writing

$$\frac{d\mathbf{z}}{dt} = J^{-1}\nabla\mathcal{H}(\mathbf{z}).$$

We see this perfectly captures the Hamiltonian behavior of (1.35)-(1.36). While symplecticity is not strictly speaking necessary for accurate behavior, it is certainly desirable, as it ensures one aspect of the physical nature of the plasma.

Several lines of inquiry have followed this direction of research. Squire et al [136] developed a single spacetime discrete Lagrangian using discrete exterior calculus. It is worth noting they also preserved Gauss's law through this, specifically by equating gauge invariance of the action with

[31] The Darwin model, developed by Charles Galton Darwin, (the grandson of the grandfather of modern evolutionary biology, Charles Robert Darwin) [127], first considered in a coding perspective by Nielson and Lewis in 1976 [128], effectively reduces Maxwell's equations to a set of elliptic equations. This is justified for quasistatic systems, where the characteristic length of the domain is far greater than the characteristic time, ie $\bar{v}/c \equiv \epsilon \ll 1$ such that ϵ is significant, but ϵ^2 is not. Effectively this results in the reduction of Maxwell's equations to a set of elliptic equations. [129] gives a good overview of how to derive this system, building on the work of [130].

[32] This is the symplectic equivalent to A being orthogonal, $A^T A = A^T I A = I$. Orthogonality implies the identity I is preserved, symplecticity that J is preserved.

[33] Note that $J^2 = -I$, which should bring to mind the imaginary unit. In fact, "symplectic" is simply "complex" with the Greek root "syn-" substituted for the Latin root "con-", both meaning "with," while the proto-European root "-plek" is where we get "to plait." Not to be confused with "simplex" with the Proto-Indo-European root "sem-" meaning "one" or "together with" (this all may be found in the Online Etymology Dictionary). Coined by Weyl in [135], "The name 'complex group' formerly advocated by me in allusion to line complexes, as these are defined by the vanishing of antisymmetric bilinear forms, has become more and more embarrassing through collision with the word 'complex' in the connotation of complex number. I therefore propose to replace it by the corresponding Greek adjective 'symplectic.'"

conserving Gauss's law *and* current conservation. Xiao et al [137] would also consider a Lagrangian that preserved symplectic structure while allowing for a variety of smoothing functions to minimize numerical noise. He et al [138, 139][34] would develop a Hamiltonian splitting method, decomposing the Hamiltonian functional into separate components (first five and then reducing it to four, though at the cost of preserving K-symplecticity rather than general symplecticity.), solving them in a manner preserving symplectic structure, and then recombining the results. Having laid this theoretical groundwork, they would move on to apply this to PIC in a finite element formulation in [142]. This was an explicit update done in non-canonical form, which Xiao et al then extended to a higher order in [143] and generalized it to relativistic settings in [144]. Qin et al [145] were able to obtain a discrete Hamiltonian formulation of the Vlasov-Maxwell system by discretizing a canonical Poisson bracket. Their approach used the symplectic Euler, which resulted in a semi-implicit method that required 3×3 matrix inversion for each particle, bordering on an explicit update time. Xiao and Qin have extended the non-canonical geometric PIC scheme to curvilinear coordinates in [146]. Wang et al [147] introduced a structure-preserving relativistic PIC code in canonical coordinates, generalizing the work of [145].[35]

Shadwick, Evstatiev, and Stamm have a sequence of papers in which they explore a variational approach of Low's Lagrangian [148] to develop a structure-preserving PIC code. They do so in a variety of ways deriving a non-canonical [149] and canonical [150] Hamiltonian, integrating the original Lagrangian in Cartesian [151] and cylindrical coordinates [152], and finally developing a symplectic integrator for a Fourier transformed canonical Hamiltonian [153]. In all cases, energy is conserved.

A research group out of Max Planck developed a finite element PIC code relying on the semi-discrete Poisson bracket they derived [154]. This is the generalization of [142]. This geometric solver was proven to conserve charge and conserve total energy just as well or better than the FDTD-Boris scheme. This line of inquiry was continued in [155] in which they developed a semi-implicit method

[34]These are both commonly cited as their arxiv preprints [140, 141] in the early literature, hence the anachronisms.

[35]It is worth noting throughout all this, within the "et al", with the exception of [147], Hong Qin is a constant (and even then, [147] explicitly says Qin's work is the basis).

that conserves energy but at the cost of not satisfying Gauss's law. They additionally developed as a second method that conserves both energy while satisfying Gauss's law, but requires nonlinear iteration to solve the coupled particle and field equations. This nonlinear iteration is, of course, more computationally expensive, but conserves charge and satisfies Gauss's laws for magnetism and electricity. This is further extended to allow for a wider variety of structure-preserving discretizations and particle shapes in [156]. Lastly, a geometric PIC method has been developed by Pinto and Pagés [157] that is known to conserve charge and energy, doing so by taking Lapenta's semi-implicit energy-conserving particle pusher [114] and adding a predictor/corrector step. This avoids the nonlinear solve required in [155].

An interesting capstone to this history is the work of Glasser and Qin in [158]. In this piece they discuss the relationship between gauge invariance and charge conservation in both the Lagrangian and Hamiltonian formulation of the Vlasov-Maxwell system, noting that much of the above research has noticed this phenomenon, but never proven it.

Symplectic integration methods for this non-separable Hamiltonians such as ours are generally limited to fully-implicit Runge-Kutta type methods [131, 159, 160], which can become prohibitively expensive for systems with many simulation particles. As an example, the simplest method among this class of algorithms is the second-order implicit midpoint rule. Recently, an explicit, symplectic approach with fractional time steps was presented by Tao in [161] that extends phase space by duplicating variables and prescribes a certain mixing operator to keep these copies "close" together; however, the numerical experiments they presented did not consider problems with self-fields, so over time, these copies can drift apart and can lead to certain non-physical behavior (see, e.g., Figures 4.4 and 4.5 in [34]). Additionally, the duplication of phase space variables also applies to the fields associated with each set of particle data. This makes the approach computationally demanding in terms of memory usage [162]. Qin et al have shown the possibility of explicit symplectic methods for product separable (as opposed to sum-separable) Hamiltonians [163, 164], with product separability defined as either $\mathcal{H}(\mathbf{q}, \mathbf{p}) = q_i \mathcal{K}(\mathbf{p})$ or $p_i \mathcal{U}(\mathbf{q})$.[36] This works fine for a non-relativistic Hamiltonian,

[36] It is important to note that a Hamiltonian can be composed of multiple sub-Hamiltonians. So if $\mathcal{H}(\mathbf{q}, \mathbf{p}) = \sum_i q_i \mathcal{K}(\mathbf{p}) + \sum_i p_i \mathcal{U}(\mathbf{q})$ this would qualify as product-separable.

but our relativistic Hamiltonian does not qualify. We will therefore attempt to find a balance between computational cost, numerical feasibility, and accuracy.

1.4.4.3 Finite Difference Time Domain

In order to represent the fields in this, or in any, method, we must use the curl equations to update the fields while satisfying the divergence equations. The former is a fairly straightforward task, the latter is the rub. A common technique for solving partial differential equations (PDEs) is the Finite Difference (FD) method, which employs Taylor expansions to discretize a domain over space and/or time, and solves this discretized problem using a variety of numerical techniques (see [165] for a more thorough examination).[37] We must take care, however, if we were to simply Taylor expand the curl equations in space and time we would find ourselves quickly violating the divergence equations. This is where the brilliance of the Yee scheme, mentioned above in Section 1.4.3 and discussed in more detail in Appendix D, comes to play, by staggering the fields and their components (see Figure D.1 in Appendix D) the divergence equations are automatically satisfied. Initially this was just used to model electromagnetic waves, but the applications to plasmas quickly became apparent, and the marriage of the Finite Difference Time Domain (FDTD) to PIC came swiftly. This was not without some struggle, however. While Yee preserves the divergence equations for electromagnetic waves, the standard shape functions for most PIC, when combined with Yee, do not satisfy the continuity equation, which leads to a violation of Gauss's Law. Now, this need not necessarily cause too much alarm. As will be shown in Chapter 2, errors in Gauss's Law do not necessarily result in a simulation's particles behaving nonphysically, especially if a bound remains on the error. Nonetheless, this is something we must be wary of, and in some cases must address. Villasenor and Buneman [37] developed a charge preserving map that reduces the order of the shape functions but in so doing preserves continuity (see Appendix E for proof of this feature). Divergence cleaning has already been mentioned [110, 111, 112] and is a good, albeit somewhat costly, manner of handling this.

[37] I am also indebted to Dr. Ameeya Kumar Nayak of the Indian Institute of Technology in Roorkee for his excellent Youtube series on the Finite Difference Method. This series was my first taste of numerical analysis of PDEs, and it is one I recommend all first year students review before their Numerical PDEs course.

Typical FDTD methods (see [166] for a thorough discussion) are second order in time and space, though Greenwood et al [167] put forward a fourth order extension to remove Cerenkov radiation, a numerical dispersion error resulting from high energy particles moving faster than the numerical waves can propagate. To be clear, they also stress that this is computationally more vexed, and as such an easier alternative is to just filter the erroneous waves out as shown in Godfrey [168], Friedman et al [169], and Rambo et al [170]. Hesthaven also has a good review of higher order methods [171].

One problem that arises with FDTD, and Yee in particular, is the grid's requirement of uniformity. While Δx can be different than Δy, changing the two values over space naïvely results in the staggering of the mesh being thrown off, which in turn results in the violation of the divergence equations. This means something as simple as rotating a 2d grid, keeping the x and y lines as they are, becomes a very thorny problem, as the question of what to do with the boundaries arises immediately. The more straightforward solution is to simply staircase the boundaries, which preserves the structure of the grid, but does introduce errors (see Section 5.2). The dispersion errors were studied by Cangellaris and Wright [172], while Verboncoeur [173] looked at the modal content. It is shown that this staircasing (or sugarcubing in 3d) introduces continuum waves that cannot be resolved on the mesh. The shorter frequency waves can be dispensed with, but the longer frequency waves are nontrivial to remove without knowledge of the physical modes. Even disregarding this phenomenon, with this representation you have an inaccurate grid for the domain if it is supposed to be a perfect rectangle. This inaccuracy, as well as the aliasing, can be mitigated by increasing the mesh refinement (though even so, problems will persist), but the CFL for the Yee scheme is such that doing so will make the simulation run for much longer.

There have been some attempts at remedying this, such as the Contour Path (CP-)FDTD, which recasts the FDTD algorithm in terms of surface and contour integrals, but this is plagued by late time instabilities. Railton and Schneider [174] examined a few different approaches have been made to fix this. Railton and Craddock [175] developed a method that removed the instability by adding a term to the electric field updates. Anderson et al [176] in 1996 developed a method in which cut

cells' values were modified in proportion to the fraction of their area that was part of the boundary. Lastly comes Dey, Mittra, and Chebolu in 1997. First in 2d [177] and subsequently in 3d [178], they found that stability was achieved by distorting cells to bring them within the domain, but only changing the magnetic update equations, leaving the electric alone. This does come at the price of reducing the timestep by roughly 70%. [174] found this to be the best alternative as of 1999. See [179] for an full discussion on CP-FDTD.

More recently Enquist et al [180] found that, by modifying the coefficients of the update equations, they could have both embedded boundaries and keep energy conservation, the structure of the Yee grid, and the normal CFL. This is only possible for angles of the nature arctan $(1/n)$ or arctan (n), where $n \in \mathbb{Z}$. They do rush to point out that one can extend this to arbitrary angles by approximating the boundary by piecewise sections keeping this angle requirement.

Within the last few years Law et al [181] developed a FDTD grid with embedded boundaries by implementing a fourth order Yee grid and a Correction Function Method (CFM), originally developed to solve Poisson problems with interface jumps [182]. This carries with it a serious computation cost, as the CFM is a minimization problem that must be solved. Additionally, the scheme, when directly applied for Perfectly Electrically Conducting boundary conditions would lead to an ill-posed minimization problem for the CFM, something Law and Nave would go on to address in [183].

1.4.4.4 Finite Element and PIC

FDTD is intuitive and fairly easy to code, but has several setbacks, among which reside geometry (discussed above, and note *this is just for a rotated rectangular grid*), the related difficulty with refining patches of your domain, the difficulty finite difference has in dealing with discontinuities (see [165], p 231 for a brief discussion of this), and a restrictive CFL that makes overall refinement difficult. The Finite Element Method (FEM) is an alternative to the more common FD method to solving PDEs. FEM, instead of discretizing by Taylor expanding and solving on a finite set of nodes, forms a variational problem of which it seeks to minimize the energy. From this setup it breaks the domain into an arbitrary set of subdomains called "elements," which themselves are typically

low-order piecewise polynomial, and approximates the solution on these elements by solving the resulting system of equations. The advantage here is that the domain may be subdivided as much as desired, moreover, the refinement need not be uniform. The geometric advantage lies not only in the nonuniform refinement capabilities, but also by the nature of the element shape. Finite difference requires its nodes to be organized in uniform lines along the Cartesian axes, whereas the elements in FEM may take any orientation or shape (triangles being the most common, but far from the only shape). Additionally, FEM gives a much clearer account of its error bounds. [184] gives a good examination of the method overall.

Much of the origins of FEM and PIC is wrapped up in Richard True's research into the so-called "electron gun" device [185, 186, 187, 188, 189, 190], in which FEM was employed to solve Poisson's equation in an electrostatic PIC scenario.[38] Additional work was done with Zaki et al [193, 194] for general Vlasov-Poisson problems in the 1D setting. This FEM work was extended to electromagnetics first for unstructured meshes around the boundaries (ie a uniform grid[39] other than the boundary elements themselves) [195, 196] and then extended to a general FEM formulation [197]. Sonnendrücker et al in 1995 [198] introduced a FEM approach to the Darwin limit. Gauss's Law for electricity is, however, not satisfied by this, and as such they employ both two divergence cleaning methods, one a projection in the spirit of the two that we have seen before [110, 111], and the other a hyperbolic divergence clean found in [199]. Under this scheme we are now solving elliptic equations, which have no CFL, and so the bound for solving the field equations is gone. They then combine this field solve with a Boris push. Eastwood et al [200] at the same time developed a more efficient FEM method that was easily parallelizable.

FEM would soon become a standard approach to PIC, with Discontinuous Galerkin (DG) becoming the standard bearer of this method (see [201] for a more thorough discussion of DG). In May 1999, the first international conference on DG was held in Rhode Island, during which the first paper on approximating Maxwell's equations was written by Kopriva, Woodruff, and Hussaini

[38] True's work has carried on in the MICHELLE codebase [191, 192].

[39] The motivation here is that a full unstructured requires more bookkeeping, which is memory intensive. The authors acknowledged in these works that the advent of high performance computing would eventually undo this requirement, and indeed it did.

[202]. After them, Hesthaven and Warburton in 2002 [203] continued to pioneer this particular technique. Hesthaven [171] gives a good summary of the state of FEM-PIC up to this point in 2003, including DG, though he is quick to lament the lack of progress made, attributing it to a combination of difficult technical questions (eg what elements to use, variation form) and the failure of the more simple FEM formulations. Since then, much work has been done with FEM in general and DG in particular. Jacobs and Hesthaven in 2006 [204] developed the first FEM-PIC combination not limited by the Darwin model (see [205] for their benchmarks). Movahhedi et al developed the first Finite Element Time Domain (FETD) Maxwell solver that implements both the alternating direction implicit (ADI) and Crank-Nicolson techniques in 2007, both of which are implicit in time and therefore unconditionally stable [206]. Cheng et al would developed a DG solver for the Vlasov-Maxwell system [207] which conserved mass and energy (though conservation of energy requires a careful choice of the numerical flux). Their setup was for semi-discrete total energy conservation, Cheng, Christlieb, and Zhong [208] developed solvers that in a fully discrete setting preserve mass and energy for arbitrary time and spatial DG discretizations for the Vlasov-Ampere system in 2014 and then generalize it back up to the Vlasov-Maxwell system [209]. Very recently Pinto et al [210] developed a generalized FEM-PIC method which is charge preserving on arbitrary grids. See Ramachandran et al [211] for a full review. [179] additionally gives a good discussion on FEM-PIC.

O'Connor, Crawford, et al [212, 213] developed a set of benchmark tests specifically for FEM-PIC (though it should be noted that these test cases may be abstracted for FDTD-PIC, and in fact we will see a few of them shortly).

As with all algorithms, there is no free cake, and while FEM does an excellent job handling geometry and establishing rigorous error bounds, it is noteworthy that it is computationally expensive, most FEM methods requiring the inversion of a mass matrix at each step. This can be mitigated by techniques such as preconditioning, but only so much can be done. DG does dodge this by allowing the elements to be discontinuous at the interfaces, instead taking a page from the Finite Volume Method (FVMs) and using a numerical flux function to transmit information between the surfaces.

It is also worth mentioning that it is difficult to implement, in the words of Hesthaven, "The success of the finite difference methods for many problems combined with its simplicity also made the finite element formulation less attractive" [171].

1.4.4.5 Miscellaneous Approaches to the Yee Grid

Zhen, Chen, and Zhang [214] introduced the first unconditionally stable numerical solver of Maxwell's equations using the alternating direction implicit (ADI) technique in 1999, stabilizing a traditional Yee grid. ADI was pioneered by Douglas, Gunn, Peaceman, Pearcy, and Rachford [215, 216, 217, 218, 219, 220] in the 1950s and 60s. Zhen, Chen, and Zhang swiftly followed this success up with a full 3d code in 2000 [221]. In their words, "the time step used in the simulation is no longer restricted by stability but by accuracy of the algorithm." Inspired by this success, Lee and Fornberg improved upon it by adding a Crank-Nicolson split-step (CNS) method in 2003 [222], following it up with another improvement in 2004 [223] by way of special time-step sequences [224], Richardson extrapolation [225], and deferred correction [226].

A different take on FDTD is the finite difference frequency domain (FDFD) is a Fourier transformed Yee grid. It is a flexible method, fairly intuitive, great for resolving fields with sharp resonances, accurate, and stable [227]. This technique has much of the strengths of the Yee grid, but instead of stepping forward in time, it solves a linear system in frequency space, Fourier transforming back to time after. For a full discussion, see [228]. While this completely avoids the issue of timesteps entirely, it is important to note that this does not necessarily equate to a speedup. The sparse linear system that results is massive. Additionally, while it incorporates all the strengths of Yee, it also carries with it its geometrical weaknesses.

1.4.4.6 The Method of Lines (Transpose)

We now come to another one of the heroes of our story, the Method of Lines Transpose (MOL^T),[40] a technique developed by Rothe in 1930 [229]. Of historical interest is the fact that Rothe referred to this as the Method of Lines (MOL), however, this is not the current situation. What is now referred to as MOL is a related technique which which dates back to at least the early 1960s in a

[40] As appropriate as MOL^T may be notationally speaking, we will be using MOLT from here on out.

paper published in the USSR by Sarmin and Chudov in 1963 [230]. The basic idea is, given a PDE that evolves over time, semidiscretize it in space and then solve each timeline as an initial value problem (IVP) using whatever method you wish, eg Runge-Kutta (as Sarmin and Chudov did with the wave equation). Cho [231] begins her history of MOL in 1998, in which Eyre used second-order centered FD in space to discretize the spatial domain of the Cahn Hilliard (CH) equation [232]. Liu and Shen [233] approach the CH and related Allen-Cahn (AC) equation, but instead opt to use a spectral deferred correction approach instead, resulting in unconditional stability. Christlieb et al [234] propose implicitly stepping in time, generating the solution with a conjugate gradient method. Jones [235] would go on to examine the functionalized CH equation with, among other things, MOL, applying exponential time differencing [236], which involves discretizing via Fourier spectral method (or, in the case of non-periodic boundaries, transforming to some other basis such as Chebyshev polynomials), decomposing the linear and nonlinear parts, transforming the nonlinear parts back to space, evaluating at the grid points, and then transforming back to spectral space. The resulting system of stiff ODEs may then be solved in a variety of methods. Further searching reveals a plethora of different techniques to solve whatever system of ODEs result from the spatial/spectral discretization, for example Yuan [237] in 1999 describes the parametric finite difference method, the Karantovitch method (the semi-discrete counterpart of the Ritz method), and the Finite Element method, developed in 1990 [238][41], which itself is derived from the Karantovitch method. See Yuan [237] for more details up to 1999, Cho [231] for up to 2016.

MOLT is, unsurprisingly, simply MOL except transposed, discretizing in time rather than space, solving each discrete timestep as a system of boundary value problems (BVP). The solution at this timestep will then act as a source term for the subsequent time step. In other words, our update equation becomes something akin to

$$\mathcal{L}\left[u^{n+1}\right](x) = \bar{S}(x,t), \tag{1.50}$$

where $\mathcal{L}$ is a linear differential operator and $\bar{S}$ is a linear combination of the source term $S(x,t)$ of the original PDE and the previous timesteps of u. This BVP may be solved in any manner provided

[41] Frustratingly, this paper is cited by Yuan as the progenitor of the FE approach, but is unavailable online

it leaves the solution stable and within desired accuracy.

There is a gap between Rothe's paper in 1930 and the 1970s when interest in this technique increased. Kačur published several papers on this in the 1970s [239, 240, 241], where his primary interest is in nonlinear parabolic problems. Martensen at the same time applied Rothe to a number of problems which are of interest to us, solving Maxwell's equations [242] and the wave equation in several dimensions [243]. Finally, both individuals presented on Rothe's technique at a conference in Berlin in 1986, Martensen using it to solve the Cauchy problem for Burger's equation [244] and Kačur staying true to form and primarily addressing nonlinear parabolic problems [245]. Amusingly, neither men appear in the other's bibliographies.

There is one technique worth discussing before we consider a Green's function approach to solving these BVPs, that of Bruno and Lyon's Fourier Continuation - Alternating Direction (FC-AD). Bruno and Lyon developed the FC-AD method in 2010 [246, 247]. This technique is based on the ADI method of approaching MOLT, combined with Fourier continuation, which was developed by Bruno, Boyd, Han, and Pohlman in the 2000s [248, 249]. ADI is used to semi-discretize in time, while the spatial domain is solved spectrally. Now, if the domain is nonuniform, this would result in Gibbs phenomenon. Adding Fourier continuation avoids this obstacle. This results in a least squares problem that [249] used a singular value decomposition to solve. However, noting the computational complexity of this, and that they are in a 1D context, they use a modification involving Gram polynomials that results in a faster algorithm. As such, FC-AD is able to handle complicated geometry while maintaining its unconditional stability. In addition, it has $O\left(N \log\left(N\right)\right)$ runtime and brings with it a very impressive order convergence, eg solving the wave equation with fourth-order in time, sixth-order in space accuracy and completely eliminating dispersion error. It is worth noting that ADI typically struggles with hyperbolic problems, but this FC(Gram) method enables them to do so with remarkable accuracy and efficiency. They extended this to handle nonuniform coefficients [250], and to compressible Navier-Stokes and non-linear acoustics [251]. [252] focused on waves, particularly electromagnetic phenomena, tweaking their method to consider a frequency and time hybrid integral equation method, and again finding they could eliminate numerical dispersion and

handle nontrivial geometries.[42] Additional emphasis was placed on parallelization possibilities. Recent work has been done to replace the Gram polynomials with Hermite polynomials, resulting in elimination of expensive precompute of the extension data and gives provable error bounds [253].[43] So the ADI method is employed to semi-discretize in time, and the Fourier Continuation by means of Gram polynomials is used to solve the BVPs. The main takeaway here though is that the dimensions are split in the ADI methodology, which brings with it its own errors, but greatly reduces the complexity of the problem. This key insight will yield dividends shortly.

Back to solving BVPs. For our purposes we are interested in solving this sequence of BVPs that come with MOLT via an analytic inversion of $\mathcal{L}$ with a Green's function G:

$$u^{n+1}(x) = \int_{\Omega} G(x;x')\bar{S}(x')dx'. \tag{1.51}$$

This technique has been used across a number of fields, including acoustics [254], fluid dynamics [255, 256, 257], diffusion, Allen-Cahn, and Cahn-Hilliard [258, 259, 231], and, of particular interest to us, electromagnetics [260]. In particular, we are interested in using this method to solve a set of wave equations described in Section 1.3.3.

Now, Cho [231] points out that, if we wished, we could simply form a linear system out of this using quadrature

$$u^{n+1}(x_j) = \int_{\Omega} G(x_j;x')\bar{S}(x')dx' \approx \sum_{i=1}^{N} G\left(x_j;x_i\right) f_i \Delta x_i, \, j = 1, ..., N. \tag{1.52}$$

However, though straightforward enough, this is computationally infeasible for even moderately sized grids, being $\mathcal{O}\left(N^2\right)$. There are two ways of approaching this challenge we will go over. The Fast Multipole Method (FMM) and the dimensional splitting approach.

The FMM was developed first by Greengard and Rokhlin [261] to evaluate the Coulomb potential and force fields in a system of particles. Greengard would later go on to extend this to other potential functions with Huang [262]. This method was used by Kropinksi and Quaife to evaluate the modified Helmholtz equation using a Green's function [263], which they would then go on to use in solving

[42] Frustratingly, the promised Part II has not been published as of April 2025.
[43] Under review as of April 2025.

diffusion problems [258] using the MOLT framework. Kropinski would go on to extend this to a Navier-Stokes solver in [257]. One issue with this method, however, is how it fits in with modern computing. FMM is predicated on receiving information from the entire domain, meaning parallel processing is a vexed challenge at best, as communication between processes will be intensive.

FC-AD introduced the idea of dimension splitting, however. The combination of operator splitting with an analytic inversion a la Green's function has been used extensively by the Christlieb group. Causley et al [264] and the thesis of Cho [231], both in the 2010s, explored its applications to parabolic problems. Hyperbolic problems were more thoroughly explored by Causley, Christlieb, Groningen, Ong, and Yaman. [265] introduced the method as a solution to the wave equation using ADI. [266] followed improved upon this by replacing the Lax correction it used by more accurate quadrature. [267] extended MOLT to a family of wave solvers of $2P$ order accuracy that run in $O\left(P^d N\right)$ steps per timestep, where N is the number of grid points in one direction and d is the number of dimensions, and explored its performance with complex geometries. Finally, [268] expanded the boundary conditions in 1 and 2D, including outflow. It also explored embedded boundaries for Neumann and Dirichlet boundary conditions. It is worth noting that this itself helps with computational efficiency, computing a sequence of one dimensional integrals is faster than computing a multi-dimensional system, however, even here improvements have been made. [269] developed a fast convolution algorithm that was not only computationally efficient, but also easily parallelizeable, requiring only the nearest neighbor (or "halo") nodes to pass information, unlike that of FMM. We will discuss this method more thoroughly in Section 2.2. We then see it extended to PIC methods in Wolf, Causley, Christlieb, and Bettencourt [270], going on to form the backbones of the dissertations of Wolf [271] and Sands [34]. One may also see a prototype of a MOLT-PIC code in [272, 273], both of which used a Green's function to solve Poisson's equation to acquire the potential and implemented this using a treecode. Very recently there has been work in comparing the simulations of the plasma simulations done by the FDTD-PIC and MOLT with Improved Asymmetrical Euler Method [2, 3, 4], using, among others, the toy problems developed in [212], and it is to this we will devote the bulk of the study.

1.5 Conclusion

In this chapter we considered first what a plasma is and why it is we are interested in this form of matter. We then turned to consider the basic equations governing a plasma. The Vlasov equation (1.6) governs the particle distribution function over phase space over time, and relies on particle location in phase space as well as field information to update itself. The fields are governed by Maxwell's equations, (1.7), and the particles are governed by the equations of motion described by Newton (1.5) and Lorentz (1.4). We discussed how all of these may be cast in terms of vector and scalar potentials under the Lorenz gauge. Finally, we began examining the technique with which this dissertation is concerned, that of Particle-in-Cell, or PIC, and how it takes both of these components, fields and particles, into consideration as it updates the plasma in question.

After this discussion, we turned to review what those who came before developed, as it is their shoulders upon which this thesis stands. It is clear that the study of plasmas and the computational simulation of them, despite only having existed for slightly over a century (less for the simulation science), has burgeoned into a rich field with an extensive history and literature.

We are now motivated by some practical examples of plasmas in nature, informed of the laws governing these plasmas we wish to accurately simulate, and inspired by the scholars that came before us. We now turn to consider a new PIC method.

CHAPTER 2

A NEW PARTICLE-IN-CELL METHOD

The above formulated PIC algorithm has two primary requirements: a wave solver and a particle pusher. In this chapter, we first give a very brief review of the equations we are interested in solving in Section 2.1. We then describe the algorithm used for wave propagation in Section 2.2 as well as the particle pusher in Section 2.3. After establishing these we will examine the numerical results in Section 2.4, comparing them to a standard PIC method which uses the Yee grid as a wave solver and the Boris push as the particle solver. Details on the Yee wave solver and Boris push may be found in Appendix D. We conclude with a brief summary in Section 2.5. This chapter is based on the work published by myself in collaboration with Dr. Andrew Christlieb and Dr. William Sands [2]. My contributions in this work was the development of the Yee-Boris code against which we compared our novel method, as well as the implementation of the sheath problem using our method.

2.1 Problem Review

The vector and scalar potential formulation of Maxwell's equations and the Lorentz force has already been discussed thoroughly in Section 1.3. Here we simply repeat the equations to save the reader from the hassle of flipping back and forth between chapters. Firstly, we have the Lorentz Force which governs the motion of a charged particle in an electric (**E**) and magnetic (**B**) field:

$$\frac{d\mathbf{p}}{dt} = \mathbf{F} = q\left(\mathbf{E} + \mathbf{v} \times \mathbf{B}\right) \tag{2.1}$$

This is relativistically correct if $\mathbf{p} = \gamma m \mathbf{v}$. We have the relativistic form of Newton's second law:

$$\mathbf{F} = \frac{d\mathbf{p}}{dt} = \gamma m \mathbf{a}. \tag{2.2}$$

The electric and magnetic fields must satisfy Maxwell's equations:

$$\nabla \cdot \mathbf{E} = \frac{\rho}{\epsilon_0}, \tag{2.3a}$$

$$\nabla \cdot \mathbf{B} = 0, \tag{2.3b}$$

$$\nabla \times \mathbf{E} = -\frac{\partial \mathbf{B}}{\partial t}, \tag{2.3c}$$

$$\nabla \times \mathbf{B} = \frac{1}{c^2}\frac{\partial \mathbf{E}}{\partial t} + \mu_0 \mathbf{J}. \tag{2.3d}$$

Under the Lorenz gauge, the above may be rewritten in terms of a scalar (ϕ) and vector ($\mathbf{A}$) potential:

$$\begin{cases} \dfrac{d\mathbf{x}_i}{dt} = \dfrac{c^2\left(\mathbf{P}_i - q_i\mathbf{A}\right)}{\sqrt{c^2\left(\mathbf{P}_i - q_i\mathbf{A}\right)^2 + \left(m_i c^2\right)^2}}, & (2.4) \\ \dfrac{d\mathbf{P}_i}{dt} = \dfrac{q_i c^2\left(\nabla\mathbf{A}\right)\cdot\left(\mathbf{P}_i - q_i\mathbf{A}\right)}{\sqrt{c^2\left(\mathbf{P}_i - q_i\mathbf{A}\right)^2 + \left(m_i c^2\right)^2}} - q_i\nabla\phi, & (2.5) \\ \dfrac{1}{c^2}\dfrac{\partial^2\phi}{\partial t^2} - \Delta\phi = \dfrac{\rho}{\epsilon_0}, & (2.6) \\ \dfrac{1}{c^2}\dfrac{\partial^2\mathbf{A}}{\partial t^2} - \Delta\mathbf{A} = \mu_0\mathbf{J}, & (2.7) \\ \dfrac{1}{c^2}\dfrac{\partial\phi}{\partial t} + \nabla\cdot\mathbf{A} = 0, & (2.8) \\ \dfrac{\partial\rho}{\partial t} + \nabla\cdot\mathbf{J} = 0. & (2.9) \end{cases}$$

Equations (2.4) and (2.5) are the particle equations of motion, (2.6) and (2.7) are the scalar and vector potential wave equations, (2.8) is the Lorenz gauge condition we must satisfy, and (2.9) is the continuity equation we will ideally satisfy as well. The nondimensionalization of these equations may be found in Appendix A.

Now that we are properly refreshed on the equations governing the system we wish to simulate, we now need two main components to do so, a wave solver and a particle pusher. We now turn to consider the wave solver.

2.2 Numerically Solving the Wave Equation

We begin with a brief discussion of integral equations in Section 2.2.1, which is helpful for introducing the dimensionally-split methods considered in this paper. The semi-discrete form of the solver considered in this work is presented in Section 2.2.2.1, and its stability is discussed in Section 2.2.2.2. A solution is formulated in terms of one-dimensional operators that can be inverted using the methods discussed in Section 2.2.3. We then discuss the methods used to obtain derivatives in 2.2.4 and demonstrate the application of boundary conditions in Section 2.2.5. These derivatives will be shown in Section 2.4.1 to have the same temporal and spatial convergence rates as the fields.

2.2.1 Integral Equation Methods and Green's Functions

Integral equation methods are a powerful class of techniques used to solve boundary value problems (BVPs) in a range of applications, and has been discussed in Section 1.4.4.6. Such methods allow one to write an explicit solution of a PDE in terms of a Green's function (see Appendix G for more details). While explicit, this solution can be difficult or impossible to evaluate, so numerical quadrature is used to evaluate these terms. Layer potentials can then be introduced in the form of surface integrals to adjust the solution to satisfy the prescribed boundary data [274]. We illustrate these features with an example that is the basis for the method presented in this work.

Suppose that we are solving the following modified Helmholtz equation

$$\left(\mathcal{I} - \frac{1}{\alpha^2}\Delta\right) u(\mathbf{x}) = S(\mathbf{x}), \quad \mathbf{x} \in \Omega, \tag{2.10}$$

where $\Omega \subset \mathbb{R}^n$ and $\mathcal{I}$ is the identity, Δ is the Laplacian in $\mathbb{R}^n$, S is a source, and $\alpha \in \mathbb{R}$ is a parameter. While this method can be broadly applied to other elliptic PDEs, equation (2.10) is of interest to us because it can be obtained from the time discretization of a parabolic or hyperbolic PDE. In this case, the source function can include additional time levels of u and the parameter $\alpha = \alpha(\Delta t)$ is connected to the time discretization of this problem.

To apply a Green's function method to equation (2.10), one first identifies the function $G(\mathbf{x}, \mathbf{y})$ that solves

$$\left(\mathcal{I} - \frac{1}{\alpha^2}\Delta\right) G(\mathbf{x}, \mathbf{y}) = \delta(\mathbf{x} - \mathbf{y}), \quad \mathbf{x}, \mathbf{y} \in \mathbb{R}^n, \tag{2.11}$$

over free-space, with $\delta(\mathbf{x} - \mathbf{y})$ being the Dirac delta distribution. The construction of fundamental solutions is extensively tabulated for many different operators, including the modified Helmholz operator [275].[1] For details on how this is derived for the modified Helmholtz equation, see Appendix G. The fundamental solution $G(\mathbf{x}, \mathbf{y})$, which solves (2.11) can be used to build a solution to the original problem (2.10). First, let u be a solution of the problem (2.10). Multiplying the equation (2.11) by u, integrating over Ω, and applying the divergence theorem (or integration by parts in the

[1] [275] has the Helmholtz operator, not the modified one, but the logic is the same.

one-dimensional case) leads to the integral identity

$$u(\mathbf{x}) = \int_{\Omega} G(\mathbf{x},\mathbf{y}) S(\mathbf{y})\, dV_{\mathbf{y}} + \frac{1}{\alpha^2} \int_{\partial\Omega} \left(G(\mathbf{x},\mathbf{y}) \frac{\partial u}{\partial \mathbf{n}} - u(\mathbf{y}) \frac{\partial G}{\partial \mathbf{n}} \right) dS_{\mathbf{y}}, \tag{2.12}$$

where we have used the assumption that the function u solves the PDE (2.10). Since the volume integral term does not enforce boundary conditions, the surface integral contributions involving u are replaced with an ansatz of the form

$$u(\mathbf{x}) = \int_{\Omega} G(\mathbf{x},\mathbf{y}) S(\mathbf{y})\, dV_{\mathbf{y}} + \int_{\partial\Omega} \left(\sigma(\mathbf{y}) G(\mathbf{x},\mathbf{y}) + \gamma(\mathbf{y}) \frac{\partial G}{\partial \mathbf{n}} \right) dS_{\mathbf{y}}, \tag{2.13}$$

where $\sigma(\mathbf{y})$ and $\gamma(\mathbf{y})$ are the single- and double-layer potentials, which are used to enforce the boundary conditions. The choice of names is reflected by the behavior of the Green's function associated with each of the terms. The Green's function itself is continuous, but its derivative will have a "jump." Based on the boundary conditions, one selects either a single or double layer form as the ansatz for the solution. The single-layer is used in the Neumann problem, while the double-layer is chosen for the Dirichlet problem.

The field solver considered in this work factors the multi-dimensional Laplacian into a product of one-dimensional operators, which are inverted in a dimension-by-dimension manner using the one-dimensional form of (2.13) [265]. The resulting methods solve for something that looks like a layer potential, with the key difference being that the linear system is now only a small, 2×2 matrix, which can be inverted by hand, rather than with an iterative method. Each integral over the one-dimensional line segment can be computed using a lightweight, recursive, fast summation method. This approach allows us to accommodate geometry with ease, as the domain can be represented using one-dimensional line segments whose termination points coincide with the geometry [276].

2.2.2 Description of the Wave Solver

Unlike the high-order time accurate methods from Causley et al [267], which are based on successive convolution, we discretize the time derivatives of the wave equation using a first-order accurate backward difference formula (BDF). Again, we wish to emphasize that the spatial discretization in the fully-discrete method is either fourth or fifth-order accurate, so we retain high-order spatial accuracy. Brief sections concerning the stability and phase error analyses of the semi-discrete method are

presented. We briefly discuss the splitting technique that reduces multi-dimensional problems into a sequence of one-dimensional updates and show how boundary conditions are applied.

2.2.2.1 The Semi-discrete BDF Scheme

To derive the BDF wave solver, we start with the equation

$$\frac{1}{c^2}\partial_{tt}u - \Delta u = S(\mathbf{x}, t), \tag{2.14}$$

where c is the wave speed and S is a source function. Then, using the notation $u(\mathbf{x}, t^n) = u^n$, we can apply a three-point backwards finite-difference stencil for the second derivative about time level t^{n+1} to obtain

$$\partial_{tt}u\Big|_{t=t^{n+1}} = \frac{u^{n+1} - 2u^n + u^{n-1}}{\Delta t^2} + O(\Delta t),$$

where $\Delta t = t^k - t^{k-1}$, for any k, is the grid spacing in time. Evaluating the remaining terms in equation (2.14) at time level t^{n+1}, and inserting the above difference approximation, we obtain

$$\frac{1}{c^2\Delta t^2}\left(u^{n+1} - 2u^n + u^{n-1}\right) - \Delta u^{n+1} = S^{n+1}(\mathbf{x}) + O\left(\Delta t\right),$$

which can be rearranged to obtain the semi-discrete equation

$$\left(\mathcal{I} - \frac{1}{\alpha^2}\Delta\right)u^{n+1} = \left(2u^n - u^{n-1}\right) + \frac{1}{\alpha^2}S^{n+1}(\mathbf{x}) + O\left(\frac{1}{\alpha^3}\right), \quad \alpha := \frac{1}{c\Delta t}. \tag{2.15}$$

We note that the source term is treated implicitly in this method, which creates additional complications if the source function S depends on u. This necessitates some form of iteration, which increases the cost of the method.

2.2.2.2 Stability and Dispersion Analysis of the Semi-discrete BDF Scheme

We now analyze the stability of the first-order semi-discrete BDF scheme given by equation (2.15). Suppose that the solution $u(\mathbf{x})$ takes the form of the plane wave given by

$$u^n(\mathbf{x}) = e^{i(\mathbf{k}\cdot\mathbf{x} - \omega t^n)} \equiv \lambda^n e^{i\mathbf{k}\cdot\mathbf{x}}.$$

Substituting this ansatz into equation (2.15) and ignoring contributions due to sources, we obtain the polynomial equation

$$\left(1 + z^2\right)\lambda^2 - 2\lambda + 1 = 0.$$

In the above equation, we have defined the real number $z^2 = |\mathbf{k}|^2/\alpha^2$ for simplicity. The roots of this polynomial are a pair of complex conjugates that can be written as

$$\lambda_\pm = \frac{1}{1+z^2}\left(1 \pm i\sqrt{z^2}\right),$$

which satisfy the condition $|\lambda_\pm| \leq 1$ for any Δt. This shows that the amplitude of the plane wave does not grow in time, so the scheme is unconditionally stable.

The phase error introduced by the semi-discrete scheme can also be determined by first noting that $t^n = n\Delta t$, so that

$$\lambda = e^{-i\omega\Delta t} \iff \omega = -\frac{1}{i\Delta t}\log(\lambda). \tag{2.16}$$

Then, we insert the factor λ_+ into equation (2.16) and expand the resulting expression into a series about $z = 0$, which gives

$$\begin{aligned}\omega_+ &= -\frac{1}{i\Delta t}\log(\lambda_+), \\ &= -\frac{1}{i\Delta t}\left(-iz - \frac{z^2}{2} + \frac{iz^3}{3} + \frac{z^4}{4} + O(z^5)\right), \quad z \ll 1.\end{aligned}$$

Since $z = |\mathbf{k}|/\alpha = c|\mathbf{k}|\Delta t$, the last expression can be further simplified to

$$\omega_+ = c|\mathbf{k}| - \frac{ic^2|\mathbf{k}|^2\Delta t}{2} - \frac{c^3|\mathbf{k}|^3\Delta t^2}{3} + \frac{ic^4|\mathbf{k}|^4\Delta t^3}{2} + O(c^5|\mathbf{k}|^5\Delta t^4).$$

Since the analytical dispersion relation for the plane wave solution is $\omega = c|\mathbf{k}|$, the phase error is

$$\omega - \omega_+ = \frac{ic^2|\mathbf{k}|^2\Delta t}{2} + O\left(c^3|\mathbf{k}|^3\Delta t^2\right).$$

Moreover, since the leading order term in the error is imaginary, this mode decays with time, which introduces dissipation into the scheme. Similar behavior is observed with the factor λ_-, so we exclude it from the discussion.

2.2.2.3 Splitting Method Used for Multi-dimensional Problems

The semi-discrete equation (2.15) is a modified Helmholtz equation of the form (2.10). Instead of appealing to (2.13), which formally inverts the multi-dimensional modified Helmholtz operator,

we apply a factorization into a product of one-dimensional operators. For example, the factorization used in two-spatial dimensions is given by

$$\begin{aligned}\alpha^2\mathcal{I} - \Delta &= \alpha^2\left(\mathcal{I} - \frac{1}{\alpha^2}\partial_{xx}\right)\left(\mathcal{I} - \frac{1}{\alpha^2}\partial_{yy}\right) + \frac{1}{\alpha^2}\partial_{xx}\partial_{yy}, \\ &\equiv \alpha^2\mathcal{L}_x\mathcal{L}_y + \frac{1}{\alpha^2}\partial_{xx}\partial_{yy},\end{aligned}$$

where $\mathcal{L}_x$ and $\mathcal{L}_y$ are one-dimensional operators and the last term represents the splitting error associated with the factorization step. Note that the coefficient of the splitting error is $1/\alpha^2 = O(\Delta t^2)$, which will not affect the global truncation error for the time discretization considered in this paper. However, for time discretizations higher than second-order accuracy, one must address the splitting error. Dropping the error terms, the semi-discrete equation (2.15) can be written more compactly as

$$\mathcal{L}_x\mathcal{L}_y\left[u^{n+1}\right](\mathbf{x}) = 2u^n(\mathbf{x}) - u^{n-1}(\mathbf{x}) + \frac{1}{\alpha^2}S^{n+1}(\mathbf{x}). \tag{2.17}$$

Next, we discuss the procedure used to invert the one-dimensional operators used in the above factorization.

2.2.3 Inverting One-dimensional Operators

The choice of factoring the multi-dimensional modified Helmholtz operator means we now have to solve a sequence of one-dimensional BVPs of the form

$$\left(\mathcal{I} - \frac{1}{\alpha^2}\partial_{xx}\right)w(x) = f(x), \quad x \in [a, b], \tag{2.18}$$

where $[a, b]$ is a one-dimensional line and f is a new source term that can be used to represent a time history or an intermediate variable constructed from the inversion of an operator along another direction. We will show the process by which one obtains the general solution to the problem (2.18), deferring the application of boundary conditions to Section 2.2.4. Further, this section also discusses the construction of spatial derivatives.

2.2.3.1 Integral Solution

Since the BVP (2.18) is linear, its general solution can be expressed using the one-dimensional analogue of equation (2.12):

$$w(x) = \int_a^b G(x,y) f(y)\, dy + \frac{1}{\alpha^2}\left[G(x,y)\partial_y u(y) - u(y)\partial_y G(x,y)\right]\Big|_{y=a}^{y=b}, \tag{2.19}$$

where the free-space Green's function in one-dimension (derived in Appendix G) is

$$G(x,y) = \frac{\alpha}{2} e^{-\alpha|x-y|}. \tag{2.20}$$

The solution (2.19) requires the derivatives of the Green's function near the boundary. Noting that

$$\partial_y G(x,y) = \begin{cases} \dfrac{\alpha}{2} e^{-\alpha(x-y)}, & x \geq y, \\ -\dfrac{\alpha}{2} e^{-\alpha(y-x)}, & x < y, \end{cases}$$

after taking limits, we find that

$$\lim_{y\to a} \partial_y G(x,y) = \frac{\alpha}{2} e^{-\alpha(x-a)},$$
$$\lim_{y\to b} \partial_y G(x,y) = -\frac{\alpha}{2} e^{-\alpha(b-x)}.$$

Combining these limits with (2.19), we obtain the general solution

$$w(x) = \frac{\alpha}{2}\int_a^b e^{-\alpha|x-y|} f(y)\, dy + Ae^{-\alpha(x-a)} + Be^{-\alpha(b-x)}. \tag{2.21}$$

The constants A and B are determined by boundary conditions and serve the same purpose as the layer potentials in (2.13). Further, we identify the general solution (2.21) as the inverse of the one-dimensional modified Helmholtz operator. In other words, we define $\mathcal{L}_x^{-1}$ so that

$$w(x) = \mathcal{L}_x^{-1}[f](x), \tag{2.22}$$
$$\equiv \frac{\alpha}{2}\int_a^b e^{-\alpha|x-y|} f(y)\, dy + Ae^{-\alpha(x-a)} + Be^{-\alpha(b-x)}, \tag{2.23}$$
$$\equiv \mathcal{I}_x[f](x) + Ae^{-\alpha(x-a)} + Be^{-\alpha(b-x)}. \tag{2.24}$$

Section 2.2.4 will make repeated use of definitions (2.22)-(2.24) in the construction of spatial derivatives and the application of boundary conditions. The integral operator $\mathcal{I}_x[f](x)$ is evaluated as

$$\mathcal{I}_x[f](x) = \frac{1}{2}\Big(\mathcal{I}_x^R[f](x) + \mathcal{I}_x^L[f](x)\Big). \tag{2.25}$$

where the integrals

$$\mathcal{I}_x^R[f](x) \equiv \alpha \int_a^x e^{-\alpha(x-y)} f(y)\, dy, \tag{2.26}$$

$$\mathcal{I}_x^L[f](x) \equiv \alpha \int_x^b e^{-\alpha(y-x)} f(y)\, dy, \tag{2.27}$$

are computed with a recursive fast summation method, to which we now turn.

2.2.3.2 Fast Convolution Algorithm

Computing the above integral may be accomplished in a very efficient manner, and has been well explored as discussed in Section 1.4.4.6. We exploit a useful property of both left and right moving convolutions:[2]

$$\mathcal{I}_x^L[u](x) = \mathcal{I}_x^L[u]\,(x-\delta_L)\, e^{-\alpha\delta_L} + \mathcal{J}_x^L\,[u]\,(x), \quad \mathcal{J}_x^L[u](x) \coloneqq \alpha \int_{x-\delta_L}^x u\,(y)\, e^{-\alpha(x-y)} dy, \tag{2.28}$$

$$\mathcal{I}_x^R[u](x) = \mathcal{I}_x^R[u]\,(x+\delta_R)\, e^{-\alpha\delta_R} + \mathcal{J}_x^R\,[u]\,(x), \quad \mathcal{J}_x^R[u](x) \coloneqq \alpha \int_x^{x+\delta_R} u\,(y)\, e^{-\alpha(y-x)} dy. \tag{2.29}$$

This is easily proven:

$$\begin{aligned}
\mathcal{I}_x^L[u](x) &= \alpha \int_a^x e^{-\alpha(x-y)} u(y) dy \\
&= \alpha \int_a^{x-\delta_L} e^{-\alpha(x-y)} u(y) dy + \alpha \int_{x-\delta_L}^x e^{-\alpha(x-y)} u(y) dy \\
&= \alpha \int_a^{x-\delta_L} e^{-\alpha(x-\delta_L-y)} u(y) e^{-\alpha\delta_L} dy + \alpha \int_{x-\delta_L}^x e^{-\alpha(x-y)} u(y) dy \\
&= \mathcal{I}_x^L[u]\,(x-\delta_L)\, e^{-\alpha\delta_L} + \mathcal{J}_x^L[u](x).
\end{aligned} \tag{2.30}$$

[2] It is worth mentioning different papers will put this in a slightly different way. For example [268] uses a change of variables to reorient the integrals to range from 0 to $\delta_{\{L,R\}}$. This takes the $\delta_{\{L,R\}}$ notation from [265], but leaves the integral oriented around x as in [270, 269]. Its coefficients are α rather than $\alpha/2$ due to how the original $\mathcal{I}$ operator is defined.

The right moving operator follows likewise. Typically δ_L and δ_R are quite small, in our case they are the Δx grid spacing. They need not be uniform, so long as all the vertices properly match up (ie the mesh is a tensor product of a line of non-necessarily uniform nodes). We discretize according to the grid nodes:

$$\mathcal{J}_j^L \coloneqq \alpha \int_{x_{j-1}}^{x_j} e^{-\alpha(x_j - y)} u(y) dy, \tag{2.31}$$

$$\mathcal{J}_j^R \coloneqq \alpha \int_{x_j}^{x_{j+1}} e^{-\alpha(y - x_j)} u(y) dy. \tag{2.32}$$

We compute $\mathcal{J}_j^{\{L,R\}}$ using quadrature as follows:

$$\mathcal{J}_j^L \approx Pu\left(x_j\right)) + Qu\left(x_{j-1}\right) - R\left(u\left(x_{j+1}\right) - 2u\left(x_j\right) + u\left(x_{j-1}\right)\right), \tag{2.33}$$

$$\mathcal{J}_j^R \approx Pu\left(x_j\right)) + Qu\left(x_{j+1}\right) - R\left(u\left(x_{j+1}\right) - 2u\left(x_j\right) + u\left(x_{j-1}\right)\right). \tag{2.34}$$

The coefficients are defined as follows, with $\nu \coloneqq \alpha \Delta x_j$ and $d = e^{-\nu}$:

$$P = 1 - \frac{1-d}{\nu}, \tag{2.35}$$

$$Q = -d + \frac{1-d}{\nu}, \tag{2.36}$$

$$R = \frac{1-d}{\nu^2} - \frac{1+d}{2\nu}. \tag{2.37}$$

For deriving these weights, see Appendix H.

Importantly, the only information needed is nearest-neighbor, or a "halo" of nodes. If we have an error tolerance $\epsilon \ll 1$, we need only constrain α such that $e^{-\alpha L_m} \leq \epsilon$, where $L_m = \min_i \left(\Delta \eta_i\right), \eta \in \{x, y, z\}$ is the smallest length between nodes. ie $-\alpha \leq \frac{\log(\epsilon)}{L_m}$. So long as this is preserved, we need only consider the halo of neighbors, making this easy to parallelize and even more efficient [269].

2.2.4 Methods for the Construction of Spatial Derivatives

To set the stage for the ensuing discussion, note that the semi-discrete update for the first-order BDF method, in one-spatial dimension, can be obtained by combining (2.21) with the semi-discrete equation (2.15). Defining the operand

$$R(x) = 2u^n(x) - u^{n-1}(x) + \frac{1}{\alpha^2} S^{n+1}(x),$$

we obtain the update

$$u^{n+1}(x) = \frac{\alpha}{2}\int_a^b e^{-\alpha|x-y|}R(y)\,dy + Ae^{-\alpha(x-a)} + Be^{-\alpha(b-x)}, \tag{2.38}$$

$$\equiv \mathcal{I}_x[R](x) + Ae^{-\alpha(x-a)} + Be^{-\alpha(b-x)}, \tag{2.39}$$

where we have used $\mathcal{I}_x[\cdot]$ to denote the convolution integral which is not to be confused with the identity operator.

In order to enforce conditions on the derivatives of the solution, we will also need to compute a derivative of the update (2.38) (equivalently (2.39)). For this, we observe that the dependency for x appears only on analytical functions, i.e., the Green's function (kernel) and the exponential functions in the boundary terms. To differentiate (2.38) we start with the definition (2.25), which splits the integral at the point $y = x$ and makes the kernel easier to manipulate. Then, using the fundamental theorem of calculus, we can calculate derivatives of (2.26) and (2.27) to find that

$$\frac{d}{dx}\left(\mathcal{I}_x^R[f](x)\right) = \frac{d}{dx}\left(\alpha\int_a^x e^{-\alpha(x-y)}f(y)\,dy\right) = -\alpha\mathcal{I}_x^R[f](x) + \alpha f(x), \tag{2.40}$$

$$\frac{d}{dx}\left(\mathcal{I}_x^L[f](x)\right) = \frac{d}{dx}\left(\alpha\int_x^b e^{-\alpha(y-x)}f(y)\,dy\right) = \alpha\mathcal{I}_x^L[f](x) - \alpha f(x). \tag{2.41}$$

These results can be combined according to (2.25), which provides an expression for the derivative of the convolution term:

$$\frac{d}{dx}\Big(\mathcal{I}_x[f](x)\Big) = \frac{\alpha}{2}\Big(-\mathcal{I}_x^R[f](x) + \mathcal{I}_x^L[f](x)\Big). \tag{2.42}$$

Additionally, by evaluating this equation at the ends of the interval, we obtain the identities

$$\frac{d}{dx}\Big(\mathcal{I}_x[f](a)\Big) = \alpha\mathcal{I}_x[f](a), \tag{2.43}$$

$$\frac{d}{dx}\Big(\mathcal{I}_x[f](b)\Big) = -\alpha\mathcal{I}_x[f](b), \tag{2.44}$$

which are helpful in enforcing the boundary conditions. The relation (2.42) can be used to obtain a derivative for the solution at the new time level. From the update (2.39), a direct computation reveals that

$$\frac{du^{n+1}}{dx} = \frac{\alpha}{2}\left(-\mathcal{I}_x^R[R](x) + \mathcal{I}_x^L[R](x)\right) - \alpha Ae^{-\alpha(x-a)} + \alpha Be^{-\alpha(b-x)}. \tag{2.45}$$

Notice that no additional approximations have been made beyond what is needed to compute $\mathcal{I}_x^R$ and $\mathcal{I}_x^L$. These terms are already evaluated as part of the base method. For this reason, we think of equation (2.45) as an analytical derivative. The boundary coefficients A and B appearing in (2.45) will be calculated in the same way as the update (2.39), and are discussed in the remaining subsections. This treatment ensures that the discrete derivative will be consistent with the conditions imposed on the solution variable.

2.2.5 Applying Boundary Conditions

The boundary coefficients A and B appearing in (2.45) will be calculated in the same way as the update (2.39), and are discussed in the remaining subsections utilizing the work of [266]. Our numerical experiments are only concerned with Dirichlet and Periodic boundary conditions, and so in the following sections we will derive the constants for these conditions, for Neumann and Outflow see [267, 268, 34].

2.2.5.1 Dirichlet Boundary Conditions

Suppose we are given the function values along the boundary, which is represented by the data

$$u^{n+1}(a) = g_a\left(t^{n+1}\right), \quad u^{n+1}(b) = g_b\left(t^{n+1}\right).$$

If we evaluate the BDF-1 update (2.39) at the ends of the interval, we obtain the conditions

$$\begin{aligned} g_a\left(t^{n+1}\right) &= \mathcal{I}_x[R](a) + A + \mu B, \\ g_b\left(t^{n+1}\right) &= \mathcal{I}_x[R](b) + \mu A + B, \end{aligned}$$

where we have defined $\mu = e^{-\alpha(b-a)}$. This is a simple linear system for the boundary coefficients A and B, which can be inverted by hand. Proceeding, we find that

$$\begin{aligned} A &= \frac{g_a\left(t^{n+1}\right) - \mathcal{I}_x[R](a) - \mu\left(g_b\left(t^{n+1}\right) - \mathcal{I}_x[R](b)\right)}{1-\mu^2}, \\ B &= \frac{g_b\left(t^{n+1}\right) - \mathcal{I}_x[R](b) - \mu\left(g_a\left(t^{n+1}\right) - \mathcal{I}_x[R](a)\right)}{1-\mu^2}. \end{aligned}$$

2.2.5.2 Periodic Boundary Conditions

Periodic boundary conditions are enforced by taking

$$u^{n+1}(a) = u^{n+1}(b), \quad \partial_x u^{n+1}(a) = \partial_x u^{n+1}(b).$$

Enforcing these conditions through the update (2.39) and its derivative (2.45), using the identities (2.43)-(2.44), leads to the system of equations

$$(1-\mu)A + (\mu-1)B = \mathcal{I}_x[R](b) - \mathcal{I}_x[R](a),$$
$$(\mu-1)A + (\mu-1)B = -\mathcal{I}_x[R](b) - \mathcal{I}_x[R](a),$$

with $\mu = e^{-\alpha(b-a)}$. The solution of this system, after some simplifications is given by

$$A = \frac{\mathcal{I}_x[R](b)}{1-\mu},$$
$$B = \frac{\mathcal{I}_x[R](a)}{1-\mu}.$$

2.3 Numerically Solving the Particle Equations of Motion

With the field solver in place, we now must consider the particle pusher component. We couple this field solver to a standard particle description of the particles using linear spline function representation, briefly discussed in Section 1.3.5 and more thoroughly explored in Appendix F. We then discuss a method developed by Gibbon et al [116] and an improvement to this method in Section 2.3.1. An algorithm which couples the time integration method for particles with the proposed field solvers is also presented. We conclude with a brief summary in Section 2.3.2.

2.3.1 The Base Method and an Improvement

2.3.1.1 The Asymmetrical Euler Method

A time integration method suitable for non-separable Hamiltonian systems was mentioned in Section 1.4.4, [116], which developed mesh-free methods for solving the Vlaxov-Maxwell system in the Darwin limit. Their adoption of a generalized Hamiltonian model for particles was motivated by the numerical instabilities associated with time derivatives of the vector potential in this particular

limit, which effectively sends the speed of light $c \to \infty$. The resulting approach for the particles, which is essentially identical to the system (2.4)-(2.5), trades additional coupling of phase space for numerical stability through the elimination of this time derivative. They proposed a semi-implicit method, dubbed the asymmetrical Euler method (AEM), which has the form

$$\begin{cases} \mathbf{x}_i^{n+1} = \mathbf{x}_i^n + \mathbf{v}_i^n \Delta t, & (2.46) \\ \mathbf{P}_i^{n+1} = \mathbf{P}_i^n + q_i \left(-\nabla \phi^{n+1} + \nabla \mathbf{A}^{n+1} \cdot \mathbf{v}_i^n \right) \Delta t, & (2.47) \\ \mathbf{v}_i^{n+1} \equiv \dfrac{c^2 \left(\mathbf{P}_i^{n+1} - q_i \mathbf{A}^{n+1} \right)}{\sqrt{c^2 \left(\mathbf{P}_i^{n+1} - q_i \mathbf{A}^{n+1} \right)^2 + \left(m_i c^2 \right)^2}}. & (2.48) \end{cases}$$

This method, which is globally first-order accurate in time, proceeds by, first, performing an explicit update of the particle positions using (2.46). Next, with the new positions $\mathbf{x}^{n+1}$ and the old velocity $\mathbf{v}^n$, we obtain the charge density ρ^{n+1} and an approximate current density $\tilde{\mathbf{J}}^{n+1}$ which are used to evolve the fields under the BDF-1 discretization. We note that the use of $\mathbf{v}^n$ in the construction of $\tilde{\mathbf{J}}^{n+1}$ is consistent with a first-order approximation of the true current density $\mathbf{J}^{n+1}$. Finally, once the fields are updated, the generalized momentum $\mathbf{P}^{n+1}$ and its corresponding velocity $\mathbf{v}^{n+1}$ are updated according to equations (2.47) and (2.48), respectively.

2.3.1.2 An Improved Asymmetrical Euler Method

One of the issues with the AEM, which was discussed in the previous section, concerns the explicit treatment of velocity in the generalized momentum equation for problems with magnetic fields. In such cases, this update resembles the explicit Euler method, which is known to generate artificial energy when applied to Hamiltonian systems. We offer a simple modification for such problems in an effort to increase the accuracy and reduce such energy violations. If the update for the generalized momentum equation (2.47) were treated implicitly with a backward Euler discretization, then we would instead compute

$$\mathbf{P}_i^{n+1} = \mathbf{P}_i^n + q_i \left(-\nabla \phi^{n+1} + \nabla \mathbf{A}^{n+1} \cdot \mathbf{v}_i^{n+1} \right) \Delta t.$$

Unfortunately, this approach necessitates iteration on $\mathbf{P}_i^{n+1}$ (through $\mathbf{v}_i^{n+1}$), which we are trying to avoid, given that the lion's share of the compute cost in typical PIC codes centers around particle

updates. Instead, with the aid of a Taylor expansion, we linearize the velocity about time level t^n so that

$$\begin{aligned}\mathbf{v}_i^{n+1} &= \mathbf{v}_i^n + \frac{d\mathbf{v}_i^n}{dt}\Delta t + O(\Delta t^2),\\ &\approx 2\mathbf{v}_i^n - \mathbf{v}_i^{n-1},\\ &\equiv \mathbf{v}_i^*.\end{aligned}$$

While this treatment is not symplectic, the numerical results presented in section 2.4.2 for a particle in a magnetic field indicate that the improved accuracy from the linear correction manages to tame the otherwise significant energy increase introduced by the AEM. Therefore, in problems with magnetic fields, we shall, instead, use the modified update

$$\begin{aligned}\mathbf{P}_i^{n+1} &= \mathbf{P}_i^n + q_i\left(-\nabla\phi^{n+1} + \nabla\mathbf{A}^{n+1}\cdot\mathbf{v}_i^*\right)\Delta t,\\ \mathbf{v}_i^* &= 2\mathbf{v}_i^n - \mathbf{v}_i^{n-1},\end{aligned}$$

as an improvement to the generalized momentum update (2.47). Since this approach is used to evolve particles in the electromagnetic examples considered in this work, its integration with the PIC lifecycle is presented in Algorithm 2.1. Henceforth, we shall call refer to this as the improved asymmetrical Euler method (IAEM).

2.3.2 Conclusion

In this section we proposed new PIC methods for the numerical simulation of plasmas. To this end, we combined methods for fields and their derivatives, which were introduced in section 2.2, with time integration methods for non-separable Hamiltonian systems. A high level description of the particle method was presented. In the next section, we present results from the numerical experiments conducted with Algorithm 2.1 in comparison with the Yee and Boris method. First, we establish the refinement properties of the field solver and methods for derivatives. Then, we demonstrate the performance of the proposed PIC methods in several key test problems involving plasmas with varying complexity.

Algorithm 2.1 Outline of the PIC algorithm with the improved asymmetric Euler method (IAEM)

Perform one time step of the PIC cycle using the improved asymmetric Euler method.

1: **Given**: $(\mathbf{x}_i^0, \mathbf{P}_i^0, \mathbf{v}_i^0)$, as well as the fields $\left(\phi^0, \nabla\phi^0\right)$ and $\mathbf{A}^0, \nabla\mathbf{A}^0$

2: Initialize $\mathbf{v}_i^{-1} = \mathbf{v}_i(-\Delta t)$ using a Taylor approximation.

3: **while** stepping **do**

4: Update the particle positions with

$$\mathbf{x}_i^{n+1} = \mathbf{x}_i^n + \mathbf{v}_i^n \Delta t.$$

5: Using the position data $\mathbf{x}_i^{n+1}$ and velocity data $\mathbf{v}_i^n$, compute the current density

$$\tilde{\mathbf{J}}^{n+1} = \mathbf{J}^{n+1} + O(\Delta t).$$

6: Using the position data $\mathbf{x}_i^{n+1}$, compute the charge density ρ^{n+1}.

7: Compute the potentials and their derivatives at time level t^{n+1} using the BDF-1 field solver.

8: Evaluate the Taylor corrected particle velocities

$$\mathbf{v}_i^* = 2\mathbf{v}_i^n - \mathbf{v}_i^{n-1}.$$

9: Calculate the new generalized momentum according to

$$\mathbf{P}_i^{n+1} = \mathbf{P}_i^n + q_i\Big(- \nabla\phi^{n+1} + \nabla\mathbf{A}^{n+1} \cdot \mathbf{v}_i^*\Big)\Delta t.$$

10: Convert the new generalized momenta into new particle velocities with

$$\mathbf{v}_i^{n+1} = \frac{c^2\left(\mathbf{P}_i^{n+1} - q_i\mathbf{A}^{n+1}\right)}{\sqrt{c^2\left(\mathbf{P}_i^{n+1} - q_i\mathbf{A}^{n+1}\right)^2 + \left(m_i c^2\right)^2}}.$$

11: Shift the time history data and return to step 4 to begin the next time step.

2.4 Numerical Results

This section presents numerical results that demonstrate the proposed methods for fields and particles that comprise the formulation adopted in this work. First, we establish the convergence properties of the BDF field solver and methods for evaluating spatial derivatives. The proposed methods are demonstrated using boundary conditions that will be considered in the applications involving plasmas. Once the refinement properties of the field solver are established, we focus on applications to plasmas. We begin with a single particle example involving cyclotron motion before moving to more complex problems involving self-fields. After benchmarking the time integration methods used for the generalized momentum formulation, we apply the proposed PIC methods to a

suite of electrostatic and electromagnetic test problems.

2.4.1 Numerical Experiments for Field Solvers

In this section we show results from the refinement studies involving the BDF-1 field solver and the proposed methods for computing spatial derivatives. Results for space and time refinement experiments are presented in the setting of two spatial dimensions. We only consider periodic and homogeneous Dirichlet boundary conditions, as these are relevant to the plasma examples considered in this work. In both examples, we consider the linear inhomogeneous scalar wave equation

$$\frac{1}{c^2}\frac{\partial^2 u}{\partial t^2} - \Delta u = S(x, y). \tag{2.49}$$

To study the convergence of the methods, we use the method of manufactured solutions.

2.4.1.1 Periodic Boundary Conditions

We first consider the case of the problem (2.49) subject to two-way periodic boundary conditions on the domain $[0, 2\pi]^2$. The manufactured solution for this problem is taken to be

$$u(x, y, t) = e^{-t}\sin(x)\cos(y), \tag{2.50}$$

which determines the initial condition, as well as the source function $S(x, y, t)$. From this solution, one can also obtain the corresponding partial derivatives in space. To initialize the multi-step method, we use the exact solution, since it is available.

For the space refinement experiment, we varied the spatial mesh in each direction from 16 points to 512 points. To keep the temporal error in the methods small during the refinement, we applied the methods for 10 time steps using a step size of $\Delta t = 10^{-4}$. The refinement plot presented in Figure 2.1a indicates fifth-order accuracy in space for the solution as well as the derivatives, which is the expected order of accuracy for the quadrature rule used by the methods. We note that the derivatives in the methods begin to level-off as the error approaches 10^{-11} due to a larger error constant arising from the differentiation process.

In the temporal refinement study, the solution is computed until a final time of $T_f = 1$ using a fixed 512×512 spatial mesh. We refine by successively doubling the number of time steps from $N_t = 8$ until $N_t = 2,048$. The results of the temporal refinement study are presented in Figure 2.1b,

in which all methods, including those for the derivatives, display the expected first-order convergence rate in time.

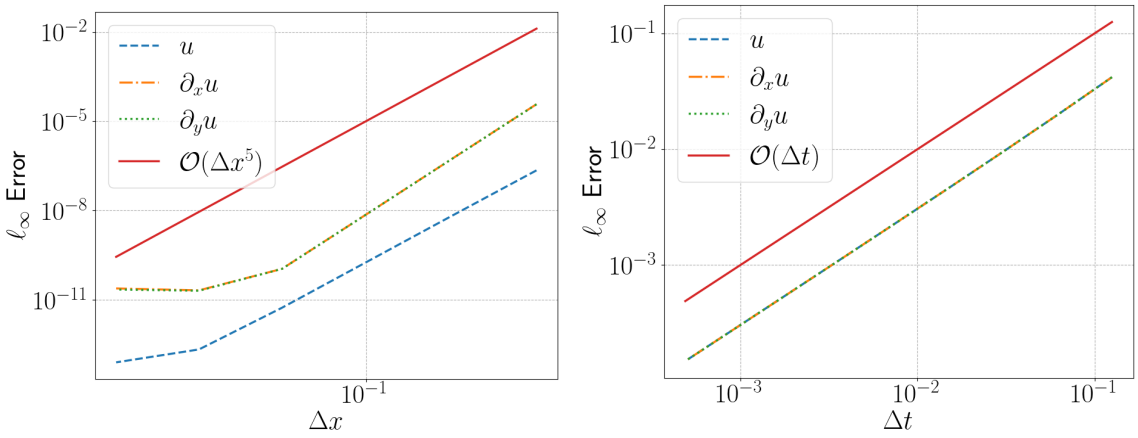

(a) Space refinement

(b) Time refinement

Figure 2.1 Refinement in space (left) and time (right) of the solution and its spatial derivatives for the two-dimensional periodic example 2.4.1.1 obtained with the BDF-1 method. Errors are measured using the ℓ_∞-norm. We observe fifth-order convergence in space and first-order accuracy in time for the solution and its derivatives. In each plot, we provide a reference corresponding to the expected rate of convergence.

2.4.1.2 Dirichlet Boundary Conditions

For the next test, we, again, consider the scalar wave equation (2.49) with homogeneous Dirichlet boundary conditions on the domain $[0, 2\pi]^2$. Here we use the manufactured solution

$$u(x, y, t) = e^{-t} \sin(x) \sin(y), \tag{2.51}$$

which is used to provide the initial data for the multi-step method.

We performed the spatial refinement study by varying the number of mesh points in each direction from 16 points to 512 points. Again, to keep the temporal error in the methods small while space is refined, we applied the methods for only 10 time steps with a step size of $\Delta t = 10^{-4}$. The same remark about small time step sizes mentioned in the space refinement experiment for the periodic case applies here, as well (see section 2.4.1.1). The space refinement plots in Figure 2.2a indicate that the methods refine to fourth-order in space rather than fifth-order in space. This is due to the

way in which we construct the stencil points in the ghost regions near the boundary of the domain. In our implementation, we use extrapolation with fourth-order accuracy to provide these stencil points.

In the temporal refinement study, the solution is computed until a final time of $T_f = 1$. We use a fixed 512×512 spatial mesh and the number of time steps in each case is successively doubled from $N_t = 8$ until $N_t = 2,048$. The results of the temporal refinement study are presented in Figure 2.2b, in which all methods, including those for the derivatives, display the expected first-order convergence rate. The behavior is essentially identical to the results obtained for the periodic problem presented in Figure 2.1b.

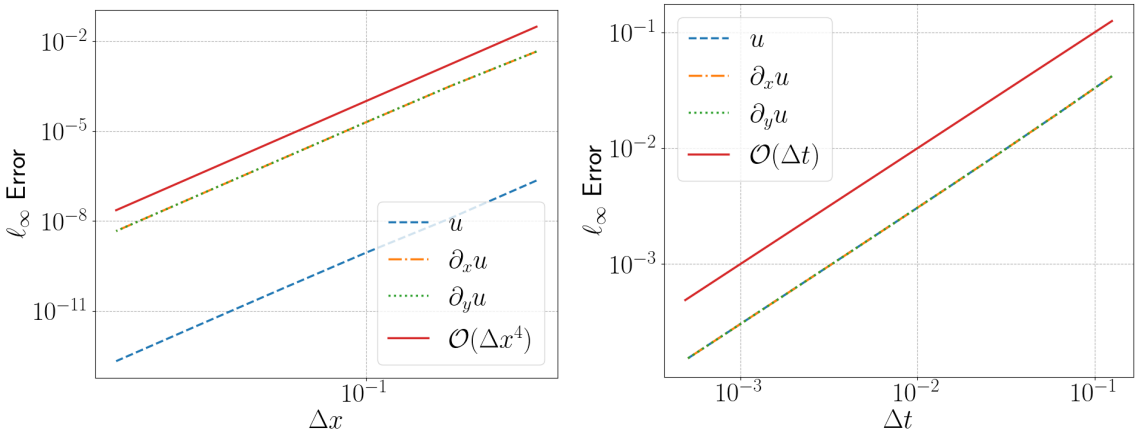

(a) Space refinement

(b) Time refinement

Figure 2.2 Refinement in space (left) and time (right) of the solution and its spatial derivatives for the two-dimensional Dirichlet problem 2.4.1.2 obtained with the BDF-1 method. Errors are measured using the ℓ_∞-norm. The methods refine to fourth-order accuracy in space, since we use fourth-order extrapolation to provide the ghost points. All methods refine to the expected first-order accuracy in time.

2.4.2 Plasma Test Problems

This section presents numerical results showcasing the proposed methods for fields in PIC applications. The benchmark PIC methods used in the comparisons implement conservative charge weighting for electrostatic problems and conservative current weighting [37] for electromagnetic problems. The electrostatic problems use the FFT to solve Poisson's equation, while the electromagnetic problems use the staggered FDTD grid introduced by Yee [86]. First, we consider a single particle moving through known fields. We then focus on applying the methods to problems involving

fields that respond to the motion of the particles, such as the two-stream instability as well as more challenging simulations of plasma sheaths and particle beams. In particular, the last problem we consider is the Mardahl beam problem [112], which is a popular benchmark problem for relativistic beams. The implementation used to obtain our results is based on the non-dimensionalization in Appendix A. All physical constants used in this non-dimensionalization are based on SI units, and, in all examples (with the exception of the heating tests), we show the results in normalized units. The relevant parameters used to set up each of the test problems are provided in dimensional form, so that the results can be more easily reproduced and compared with other methods.

2.4.2.1 Motion of a Charged Particle

We first compare the time integration methods for non-separable Hamiltonians with the well-known Boris method [91]. This is a natural first step before applying the method to problems with dynamic "self-fields" that respond to particle motion. Here, we consider a simple model for the motion of a single charged particle that is given by

$$\frac{d\mathbf{x}}{dt} = \mathbf{v}, \quad \frac{d\mathbf{v}}{dt} = \frac{q}{m}\left(\mathbf{E} + \mathbf{v} \times \mathbf{B}\right).$$

We use electro- and magneto-static fields here and suppose that the magnetic field lies along the $\hat{\mathbf{z}}$ unit vector

$$\mathbf{B} = B_0\hat{\mathbf{z}}, \quad \mathbf{E} = E^{(1)}\hat{\mathbf{x}} + E^{(y)}\hat{\mathbf{y}} + E^{(z)}\hat{\mathbf{z}},$$

where B_0 is a constant. Again, component-based definitions have been used for the fields $\mathbf{E} = \left(E^{(1)}, E^{(2)}, E^{(3)}\right)$ and $\mathbf{B} = \left(B^{(1)}, B^{(2)}, B^{(3)}\right)$. Consequently, we have that

$$\mathbf{v} \times \mathbf{B} = v^{(2)}B_0\hat{\mathbf{x}} - v^{(1)}B_0\hat{\mathbf{y}},$$

so the full equations of motion are

$$\begin{cases} \dfrac{dx^{(1)}}{dt} = v^{(1)}, & \dfrac{dv^{(1)}}{dt} = \dfrac{q}{m}\left(E^{(1)} + v^{(2)}B_0\right), \\ \dfrac{dx^{(2)}}{dt} = v^{(2)}, & \dfrac{dv^{(2)}}{dt} = \dfrac{q}{m}\left(E^{(2)} - v^{(1)}B_0\right), \\ \dfrac{dx^{(3)}}{dt} = v^{(3)}, & \dfrac{dv^{(3)}}{dt} = \dfrac{q}{m}E^{(3)}. \end{cases}$$

We can then use the linear momentum $\mathbf{p} = m\mathbf{v}$ to obtain

$$\begin{cases} \dfrac{dx^{(1)}}{dt} = \dfrac{1}{m}p^{(1)}, & \dfrac{dp^{(1)}}{dt} = q\left(E^{(1)} + \dfrac{1}{m}p^{(2)}B_0\right), \\ \dfrac{dx^{(2)}}{dt} = \dfrac{1}{m}p^{(2)}, & \dfrac{dp^{(2)}}{dt} = q\left(E^{(2)} - \dfrac{1}{m}p^{(1)}B_0\right), \\ \dfrac{dx^{(3)}}{dt} = \dfrac{1}{m}p^{(3)}, & \dfrac{dp^{(3)}}{dt} = qE^{(3)}. \end{cases}$$

Using the potentials ϕ and $\mathbf{A} \equiv \left(A^{(1)}, A^{(2)}, A^{(3)}\right)$, one can compute the electric and magnetic fields via (1.10). The time-independence of the magnetic field for this problem implies that $\partial_t \mathbf{A} = 0$, so that $\mathbf{E} = -\nabla\phi$. For this problem, we use

$$\phi = -E^{(1)}x - E^{(2)}y - E^{(3)}z.$$

Moreover, the magnetic field contains only a z-component, which implies that it can be written as

$$\mathbf{B} = (0, 0, B_0) = (0, 0, \partial_x A^{(2)} - \partial_y A^{(1)}).$$

As the choice of functions for gauges is not unique, it suffices to pick

$$A^{(1)} \equiv 0, \quad A^{(2)} = B_0 x, \quad A^{(3)} \equiv 0.$$

In summary, the non-zero values and required derivatives for the potentials are given by

$$-\partial_x\phi = E^{(1)}, \quad -\partial_y\phi = E^{(2)}, \quad -\partial_z\phi = E^{(3)}, \quad A^{(2)} = B_0 x, \quad \partial_x A^{(2)} = B_0,$$

which results in the simplified equations of motion for the Hamiltonian system

$$\begin{cases} \dfrac{dx^{(1)}}{dt} = \dfrac{1}{m}P^{(1)}, & \dfrac{dP^{(1)}}{dt} = qE^{(1)} + \dfrac{q}{m}\left[B_0\left(P^{(2)} - qB_0x^{(1)}\right)\right], \\ \dfrac{dx^{(2)}}{dt} = \dfrac{1}{m}\left(P^{(2)} - qB_0x^{(1)}\right), & \dfrac{dP^{(2)}}{dt} = qE^{(2)}, \\ \dfrac{dx^{(3)}}{dt} = \dfrac{1}{m}P^{(3)}, & \dfrac{dP^{(3)}}{dt} = qE^{(3)}. \end{cases}$$

The setup for the test consists of a single particle with mass $m = 1$ and charge $q = -1$ whose initial position is at the origin of the domain $\mathbf{x}(0) = (0, 0, 0)$. Initially, the particle is given non-zero

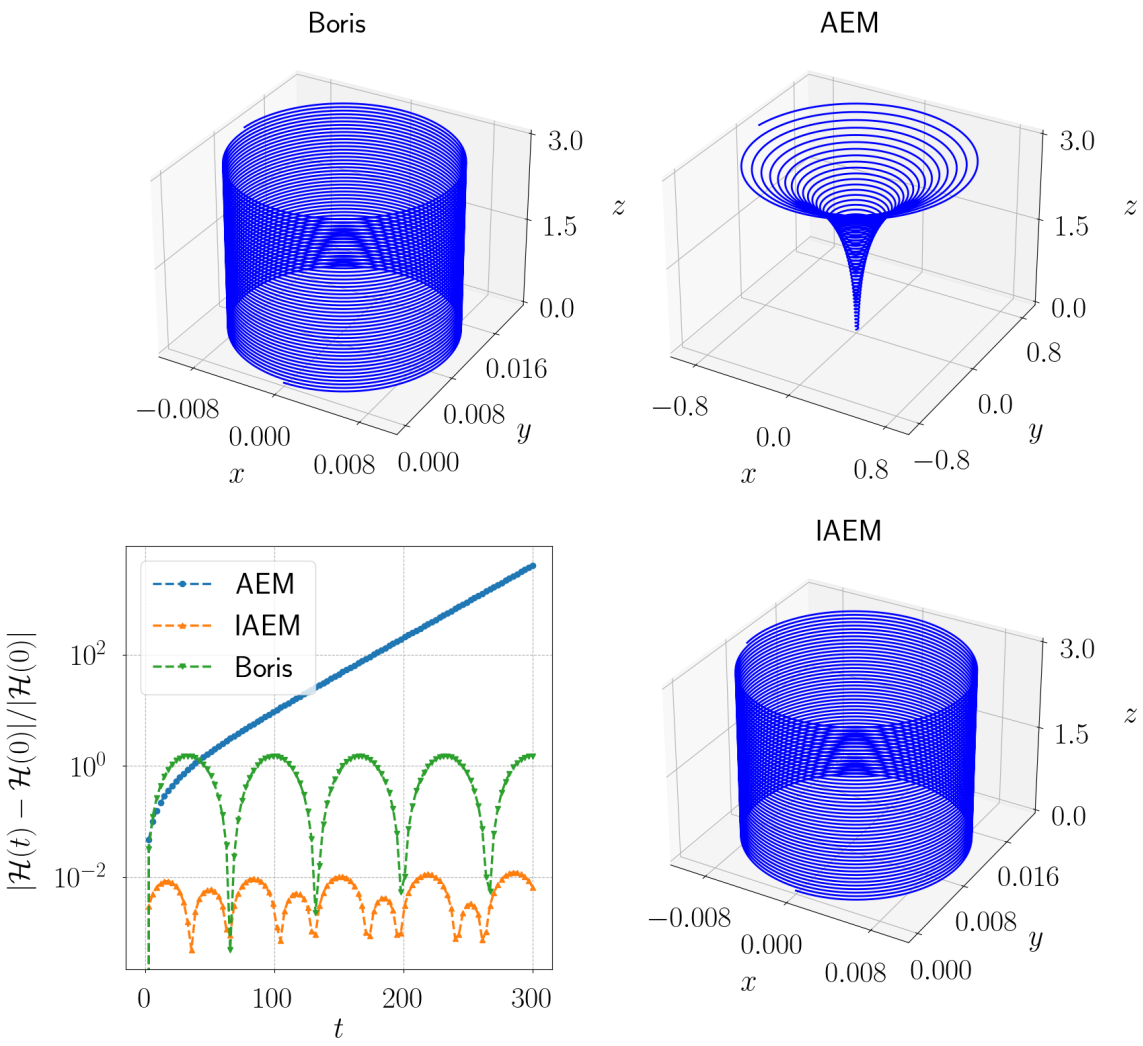

Figure 2.3 Trajectories for the single particle test obtained using the Boris method [91], the AEM [116], and the IAEM. The particle rotates about a static magnetic field which points in the z-direction. Also shown is the time history of the Hamiltonian generated by each of the methods which is measured relative to the initial data. In particular, the AEM shows a growth in the overall energy causing the gyroradius to increase. This behavior is not observed in the improved method.

momenta in the x and z directions so as to generate so called "cyclotron" motion. We choose the initial momenta to be $\mathbf{p}(0) = \mathbf{P}(0) = (0.01, 0, 0.01)$. The strength of the magnetic field in the z direction is selected to be $B_0 = 1$, and we ignore the contributions from the electric field, so that $\mathbf{E} = (0, 0, 0)$. Each method is run to a final time of $T_f = 300$, using a total of 10^4 time steps, so that $\Delta t = 0.03$. The position of the particle is tracked through time and plotted as a curve in three-dimensions. In Figure 2.3, we compare the particle trajectories and the relative error in the Hamiltonian obtained with each of the methods. We note that the gyroradius for the AEM increases

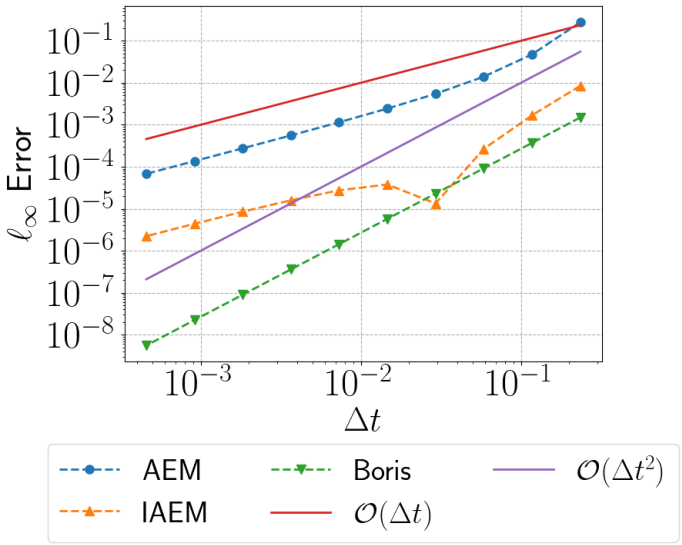

Figure 2.4 Refinement study for the trajectory of a single particle obtained using the Boris method [91], AEM [116], and the IAEM that uses a Taylor correction. Errors are measured in the ℓ_∞-norm against a reference solution obtained using the Boris method. Even though the AEM with the Taylor correction remains globally first-order accurate in time, its improvement over the AEM is quite apparent (roughly an order of magnitude).

over time because the method is not volume-preserving. Over time, this causes the total energy to increase, as substantiated by the growth of the Hamiltonian. In contrast, we see that the simple correction used in the IAEM reduces this behavior; however, the correction does not completely eliminate this growth in the case of longer simulations, as the truncation errors accumulate over time.

Next, we perform a refinement study of the methods to examine their error properties using the same experimental parameters from the cyclotron test. We reduce the final time to $T_f = 30$ and measure the errors with the ℓ_∞ norm using a reference solution computed with 10^6 time steps, so that $\Delta t = 3.0 \times 10^{-5}$. The test successively doubles the number of steps, starting with 100 steps and uses, at most, 1.28×10^4 steps. The results of the refinement study are shown in Figure 2.4. Despite the fact that both the base and improved versions of the AEM refine to first-order accuracy, we see that the Taylor correction decreases the error in the base method by roughly an order of magnitude. For coarser time step sizes, the improved method has errors that are (in some sense) comparable to the Boris method, which is second-order accurate. Of course, the second-order method will outperform both versions of the AEM as the time step decreases.

2.4.2.2 The Cold Two-stream Instability

We consider the motion of "cold" streams of electrons restricted to a one-dimensional periodic domain by means of a sufficiently strong (uniform) magnetic field in the two remaining directions. Ions are taken to be uniformly distributed in space and sufficiently heavy compared to the electrons so that their motion can be neglected in the simulation. The ions, which remain stationary, act as a neutralizing background against the dynamic electrons. The electron velocities are represented as a sum of two Dirac delta distributions that are symmetric in velocity space:

$$f(v) = \frac{1}{2}\delta(v - v_b) + \frac{1}{2}\delta(v + v_b). \tag{2.52}$$

The stream velocity $v_b > 0$ is set according to a drift velocity whose value ultimately controls the interaction of the streams. A slight perturbation in the electron velocities is then introduced to force a charge imbalance, which generates an electric field that attempts to restore the neutrality of the system. This causes the streams to interact or "roll-up," which corresponds to regions of trapped particles.

In order to describe the models used in the simulation, let us denote the components of the position and momentum vectors for particle i as $\mathbf{x}_i \equiv \left(x_i^{(1)}, x_i^{(2)}, x_i^{(3)}\right)$ and $\mathbf{P}_i \equiv \left(P_i^{(1)}, P_i^{(2)}, P_i^{(3)}\right)$, respectively. Then, the equations for the motion of particle i assume the form

$$\frac{dx_i^{(1)}}{dt} = \frac{1}{m_i}P_i^{(1)}, \quad \frac{dP_i^{(1)}}{dt} = -q_i\partial_x\phi.$$

The potential ϕ and its derivative $\partial_x\phi$ are obtained by solving a two-way wave equation for the scalar potential:

$$\frac{1}{c^2}\partial_{tt}\phi - \partial_{xx}\phi = \frac{\rho}{\epsilon_0}. \tag{2.53}$$

As this is an electrostatic problem, the gauge condition can be safely ignored. In the limit where the thermal velocity V of the particles become well-separated from the nondimensionalized speed of light ($\kappa = c/V \gg 1$), one instead solves the Poisson equation

$$-\partial_{xx}\phi = \frac{\rho}{\epsilon_0}. \tag{2.54}$$

Using asymptotic analysis, it can be shown that the error incurred by adopting the Poisson model for ϕ is $O\left(1/\kappa\right)$ [271].

We establish the efficacy of the proposed algorithms for time stepping particles and evolving fields by comparing with well-known methods. The setup for this test problem consists of a spatial mesh defined on the interval $[-10\pi/3, 10\pi/3]$, in units of the Debye length λ_D, which is discretized using 128 total grid points with periodic boundary conditions. The final time for the simulation is taken to be $T_f = 100$ in units of ω_{pe}^{-1} with 4,000 time steps being used to evolve the system. The plasma is represented with a total of 30,000 macroparticles, consisting of 10,000 ions and 20,000 electrons. As mentioned earlier, the positions of the ions and electrons are taken to be uniformly spaced along the grid. Ions remain stationary in the problem, so we set their velocity to zero. The construction of the streams begins by first splitting the electrons into two equally sized groups whose respective (non-dimensional) drift velocities are set to be ± 1 in units of the thermal velocity V. To generate an instability we add a perturbation to the electron velocities of the form

$$\delta v(x) = \epsilon \sin\left(\frac{2\pi k(x-a)}{L_x}\right).$$

Here, $\epsilon = 5.0 \times 10^{-4}$ controls the strength of the perturbation, $k = 1$ is the wave number for the perturbation, x is the position of the particle (electron), a is the left-most grid point, and L_x is the length of the domain. In a more physically realistic simulation, the perturbation would be induced by some external force, which would also result in a perturbation of the position data for the particles. Such a perturbation of the position data requires a self-consistent field solve to properly initialize the potentials. In our simulation, we assume that no spatial perturbation is present, so that the fields are identically zero at the initial time step. The plasma parameters used in the non-dimensionalization for this test problem are displayed in Table 2.1. Note that in this configuration, the normalized speed of light is $\kappa = 50$, and the corresponding normalized permittivity is $\sigma_1 = 1$. This configuration adequately resolves the plasma Debye length ($\approx$ 6 cells/λ_D), the angular plasma period ($\approx$ 40 steps/ω_{pe}^{-1}), and the particle CFL < 1, which are typically used to ensure stability in explicit PIC methods.

Parameter	Value
Average number density ($\bar{n}$) [m^{-3}]	7.856060×10^{1}
Average temperature ($\bar{T}$) [K]	2.371698×10^{6}
Debye length (λ_D) [m]	1.199170×10^{4}
Inverse angular plasma frequency (ω_{pe}^{-1}) [s/rad]	2.000000×10^{-3}
Thermal velocity ($v_{th} = \lambda_D \omega_{pe}$) [m/s]	5.995849×10^{6}

Table 2.1 Table of the plasma parameters used in the two-stream instability example.

We study the structure of the instability using the Poisson model (2.54) and the wave model (2.53) for the scalar potential using the AEM. We remark that the Taylor corrected version of the AEM was not considered in this problem because the contributions from the magnetic field are ignored. The particular initial condition for this problem leads to a special case in which the AEM is equivalent to leapfrog integration. Since the problem is initially charge neutral, there is no electric field at time $t = 0$. This further implies that there is no modification to the particle velocities in the step that normally generates the initial offset required by the leapfrog method. Plots comparing the evolution of the electron streams, obtained with both models, are presented in Figure 2.5. Each figure contains two colors which designate the groups of electrons in the initial condition (2.52). Here, the blue electrons move to the right, while those in red move to the left. We see that the behavior at early times is nearly identical, but the trapping regions at later times are quite different. In particular, the structures produced by the wave model tend to be more elongated than those of the Poisson model. This is a likely consequence of the finite speed of propagation in the wave model, where the potential responds more slowly to an imbalance in charge.

Next, we compare the growth rates in the electric fields produced by the Poisson and wave models against theoretically predicted growth rates. Applying basic linear response theory (see, e.g., Chapter 18 of [7]) with the distribution (2.52) one obtains the cold dispersion relation for the Vlasov-Poisson system

$$\omega^4 - 2\omega^2 \left(\omega_{pe}^2 + k^2 v_b^2\right) + k^2 v_b^2 \left(k^2 v_b^2 - 2\omega_{pe}^2\right) = 0. \tag{2.55}$$

While the dispersion relation for a warm problem could also be considered, its evaluation is slightly more complicated. We remark that cold problems cannot be not be adequately represented in

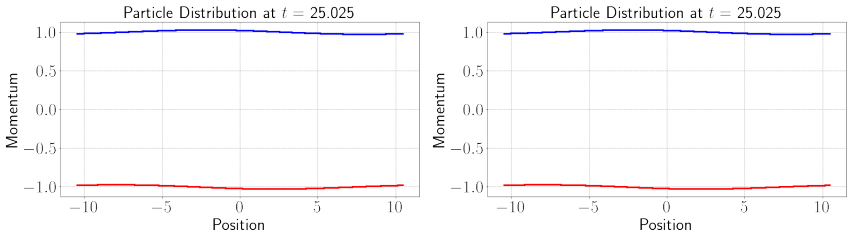

(a) AEM (Poisson) (b) AEM (Wave)

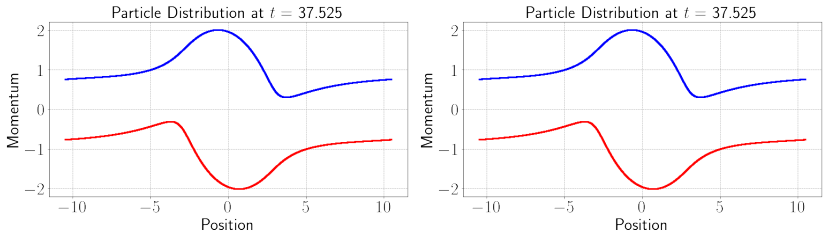

(c) AEM (Poisson) (d) AEM (Wave)

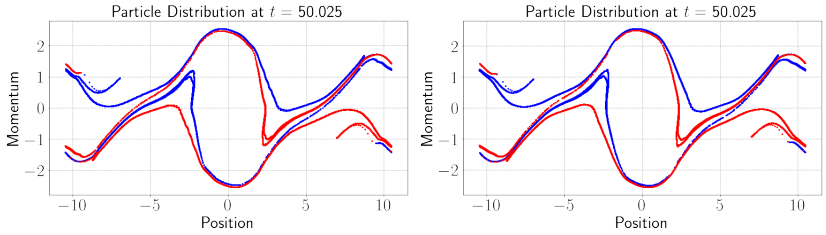

(e) AEM (Poisson) (f) AEM (Wave)

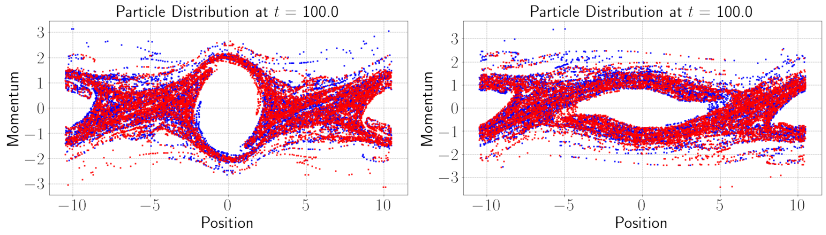

(g) AEM (Poisson) (h) AEM (Wave)

Figure 2.5 We plot the electrons in phase space obtained with the Poisson (left column) and wave (right column) model for the two-stream instability problem, at different times, in units of ω_{pe}^{-1}. The two colors represent the groups of electrons in the initial condition (2.52). The blue electrons move to the right, while those in red move to the left. Results were obtained using the AEM for time integration. The IAEM, which applies the Taylor correction, is not considered here because the contributions from the magnetic fields are ignored. The FFT is used to compute the scalar potential (as well as its derivative) in the Poisson model, while the BDF-1 field solver is used to compute the scalar potential (as well as its derivative) in the wave model. We see that there are clear differences in the structure of the trapping regimes at later times, with the wave model producing a more elongated trapping region due to the finite speed of propagation.

mesh-based discretizations, which is a key advantage offered by a particle method. Additionally, cold problems eliminate artifacts introduced by sampling methods during the initialization phase. Substituting the normalized quantities $v_b = 1$, $\omega_{pe} = 1$, and $k = 2\pi/L_x$ in the dispersion relation yields the growth rate $\mathrm{Im}(\omega) \approx 0.2760$. In Figure 2.6, we compare the growth rate of the electric fields produced by both methods using a variety of CFL numbers against the analytical growth rate. Again, we see identical results among both methods in the linear regime, but subtle differences at the later times when the assumptions of the linear response theory become invalid. This is true even when the CFL > 1 is used in the proposed BDF-1 method.

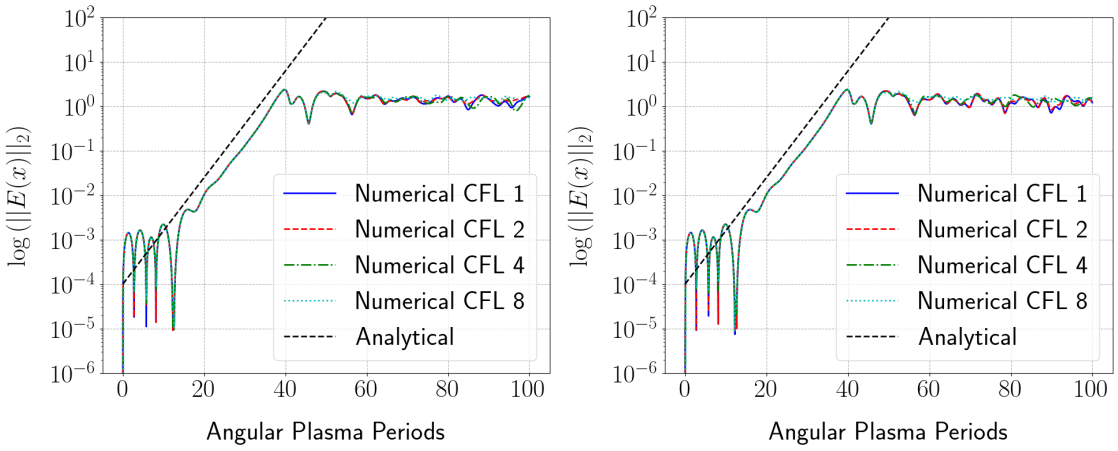

(a) AEM (Poisson) with variable CFL

(b) AEM (Wave) with variable CFL

Figure 2.6 We compare the growth rate in the ℓ_2-norm of the electric field for various methods against an analytical growth rate for the two-stream example obtained from linear response theory. Plot (a) combines the AEM with an FFT-based Poisson solver, while plots (b) and (c), instead, use a wave model for the scalar potential that is solved using the proposed BDF-1 approach. Plot (c) demonstrates the impact of the CFL number on the growth rate in the electric field. Using this particular experimental configuration, the analytical growth rate is given by $\mathrm{Im}(\omega) \approx 0.2760$. The AEM, when combined with each of the models, correctly follows the predicted growth rate. We also observe excellent agreement with the analytical growth rate even when a CFL > 1 is used for the proposed BDF-1 solver. At $t \approx 40$, the assumptions of the linearization become invalid, so the prediction becomes inaccurate.

2.4.2.3 Numerical Heating

We perform a numerical heating experiment to study the relationship between the Debye length λ_D and the mesh resolution Δx. A general rule of thumb for standard explicit PIC simulations is that the mesh spacing should satisfy $\Delta x < \lambda_D/4$ to slow the growth of the instability. Such artifacts can

be interpreted as an aliasing error, as the mesh cannot resolve the charge separation in the plasma. This can be problematic for purely dispersive field solvers, e.g., the FDTD method. In contrast, the BDF-1 field solver proposed in this work is more diffusive, which can be more effective at reducing the growth of these aliasing errors, especially over long time intervals. We remark that numerical heating effects can be suppressed by the use of high-order particle shape functions or even eliminated by an energy-conserving scheme [108, 109, 107, 277]. Since this problem is typically studied using periodic domains, the former approach creates no complication. However, we only consider low-order maps, such as the charge conserving map [37] and the linear shape function (1.41), as we are interested in the performance of the methods on bounded domains.

The setup for this problem is slightly different from the two-stream example discussed earlier. Here, we provide, as input, a Debye length λ_D and a thermal velocity v_{th}, which can be used to calculate the average number density $\bar{n}$ and macroscopic temperature $\bar{T}$ for the plasma. The remaining parameters can be derived from these values and are shown in Table 2.2. The normalized speed of light for both the electrostatic and electromagnetic problems is $\kappa = 50$, and the normalized permittivity is $\sigma_1 = 1$. For the electromagnetic problem, the normalized permeability obtained with these experimental parameters is $\sigma_2 = 4.0\times10^{-4}$. Here we consider both electrostatic (1D-1V/1D-1P) and electromagnetic (2D-2V/2D-2P) configurations that consist of ions and electrons in a periodic domain. The spatial domain for the electrostatic case is $[-25\lambda_D, 25\lambda_D]$, while the electromagnetic case uses $[-25\lambda_D, 25\lambda_D]^2$. In both cases, the spatial domain is refined by successively doubling the number of mesh points from 16 to 256 in each dimension. The simulations use 10^6 time steps with a final time of $T_f = 1,000$ angular plasma periods. Although the CFL number is quite small in the electrostatic case, where larger time steps can be used, we are primarily interested in a consistent comparison with the electromagnetic case. In this limit, the CFL must be ≤ 1 for the FDTD for stability. In the electrostatic simulation, we use $5,000$ macroparticles for each species, and increase this to $250,632$ for the electromagnetic simulation. As before, we assume that the ions remain stationary, since they are heavier than the electrons. Electrons are given uniform positions in space and their velocities are obtained by sampling from a Maxwellian distribution using the parameters

in Table 2.2. We make the problem current neutral by splitting the electrons into two equally sized groups whose velocities differ only in sign. A drift velocity is not used in these tests. To ensure consistency across the runs, we also seed the random number generator prior to sampling.

Parameter	Value
Average number density ($\bar{n}$) [m^{-3}]	1.129708×10^{14}
Average temperature ($\bar{T}$) [K]	2.371698×10^{6}
Debye length (λ_D) [m]	1.0×10^{-2}
Inverse angular plasma frequency (ω_{pe}^{-1}) [s/rad]	1.667820×10^{-9}
Thermal velocity ($v_{th} = \lambda_D \omega_{pe}$) [m/s]	5.995849×10^{6}

Table 2.2 Table of the plasma parameters used in the numerical heating examples.

We monitor heating during the simulations by computing the variance in the components of the electron velocities, since this is connected to the temperature of a Maxwellian distribution. In the one-dimensional case, the variance data at a given time step is converted to a temperature (in units of Kelvin) using the relation

$$\bar{T} = \frac{m_e V^2}{k_B} \mathrm{Var}(v^{(1)}),$$

where we have used "Var" to denote variance and V is the normalization used for velocity. Similarly, for the two-dimensional case, we compute the average of the variance for each component of the velocity, which is converted to a temperature (in units of Kelvin) using

$$\bar{T} = \frac{m_e V^2 \left(\mathrm{Var}(v^{(1)}) + \mathrm{Var}(v^{(2)}) \right)}{2 k_B}.$$

We use the superscripts in the above metrics to refer to the individual velocity components across all of the particles. The factor of two is used to average the variance among these components. When assessing the temperatures produced by different methods, we rescale the temperatures so they have the proper units of Kelvin. This allows us compare the different methods in a more realistic setting in which we might be interested in comparing the raw temperatures predicted by different methods.

The models used in the electrostatic tests are identical to the ones presented for the two-stream instability example, so we shall skip these details for brevity. In the case of the electromagnetic

experiment, the particle equations in the non-relativistic Hamiltonian formulation are

$$\begin{cases} \dfrac{dx_i^{(1)}}{dt} = \dfrac{1}{m_i}\left(P_i^{(1)} - q_i A^{(1)}\right), \\ \dfrac{dx_i^{(2)}}{dt} = \dfrac{1}{m_i}\left(P_i^{(2)} - q_i A^{(2)}\right), \\ \dfrac{dP_i^{(1)}}{dt} = -q_i \partial_x \phi + \dfrac{q_i}{m_i}\left[\left(\partial_x A^{(1)}\right)\left(P_i^{(1)} - q_i A^{(1)}\right) + \left(\partial_x A^{(2)}\right)\left(P_i^{(2)} - q_i A^{(2)}\right) \right], \\ \dfrac{dP_i^{(2)}}{dt} = -q_i \partial_y \phi + \dfrac{q_i}{m_i}\left[\left(\partial_y A^{(1)}\right)\left(P_i^{(1)} - q_i A^{(1)}\right) + \left(\partial_y A^{(2)}\right)\left(P_i^{(2)} - q_i A^{(2)}\right) \right]. \end{cases}$$

The contributions from the fields are obtained by solving a system of wave equations for the potentials, which take the form

$$\begin{cases} \dfrac{1}{c^2}\partial_{tt}\phi - \partial_{xx}\phi - \partial_{yy}\phi = \dfrac{1}{\epsilon_0}\rho, \\ \dfrac{1}{c^2}\partial_{tt}A^{(1)} - \partial_{xx}A^{(1)} - \partial_{yy}A^{(1)} = \mu_0 J^{(1)}, \\ \dfrac{1}{c^2}\partial_{tt}A^{(2)} - \partial_{xx}A^{(2)} - \partial_{yy}A^{(2)} = \mu_0 J^{(2)}. \end{cases}$$

To establish the heating properties of the proposed methods in an electromagnetic setting, an identical experiment is performed using a standard FDTD-PIC approach in which the equations of motion for the particles are expressed in terms of **E** and **B**. For this example, these equations take the form

$$\begin{cases} \dfrac{dx_i^{(1)}}{dt} = v_i^{(1)}, \quad \dfrac{dv_i^{(1)}}{dt} = \dfrac{q_i}{m_i}\left(E^{(1)} + v_i^{(2)} B^{(3)}\right), \\ \dfrac{dx_i^{(2)}}{dt} = v_i^{(2)}, \quad \dfrac{dv_i^{(2)}}{dt} = \dfrac{q_i}{m_i}\left(E^{(2)} - v_i^{(1)} B^{(3)}\right), \end{cases}$$

and are evolved in a leapfrog format through the Boris method [91]. Since we have restricted the system to two spatial dimensions, we retain the curl equations for the transverse electric (TE) mode, namely

$$\begin{cases} \partial_x E^{(2)} - \partial_y E^{(1)} = -\partial_t B^{(3)}, \\ -\partial_z B^{(2)} = \mu_0 J^{(1)} + \dfrac{1}{c^2}\partial_t E^{(1)}, \\ -\partial_x B^{(3)} = \mu_0 J^{(2)} + \dfrac{1}{c^2}\partial_t E^{(2)}, \end{cases}$$

which are discretized using the staggered FDTD mesh [86].

The results of the numerical heating experiments can be found in Figures 2.7 - 2.9. Figure 2.7 presents the result for the one-dimensional case, in which, we consider both Poisson and wave equation models for the scalar potential. Figure 2.8 shows the results for the electromagnetic heating experiment in which we compare the FDTD-PIC method and the IAEM. For the one-dimensional electrostatic experiments, we observe significant differences in the heating behavior due to the choice of models used for the scalar potential. We can clearly see the rate of heating is far more significant when the Poisson model is used instead of the wave equation. This is due to the finite speed of propagation offered by the wave model, which causes the potential to respond more slowly to variations in the charge density ρ. We find this to be true even in cases where the Debye length would normally be considered underresolved by practitioners, resulting in far less severe fluctuations in temperature. The use of the leapfrog time integration scheme produces nearly identical behavior, so we do not include these results. In the electromagnetic case, we see that the proposed method demonstrates mesh-independent heating properties, with notably smaller temperature fluctuations across the grid configurations, over many plasma periods. For example, over 1,000 plasma periods, the relative increase in temperature across all meshes is $< 0.1\%$. In contrast, the benchmark FDTD-PIC approach displays significant fluctuations in the temperature over a smaller time interval (100 versus $1,000$ angular plasma periods), even in cases where the grid spacing resolves the Debye length. These results indicate that the new method permits the use of a much coarser grid than current explicit particle methods for bounded domains. We also include some plots of conserved quantities for the electromagnetic case, namely, the total mass and the residual in the Lorenz gauge condition in Figure 2.9 obtained with the proposed method. We observe reasonable mass conservation and control of the gauge error over many plasma periods despite the fact that we are not enforcing the gauge condition. Figure 2.10 considers the same heating experiment for a variety of CFLs. We observe that larger CFL numbers slightly increase the sensitivity of heating with the mesh refinement. However, of the cases considered, we find that the coarsest mesh changes the electron temperature by $< 1\%$ after $1,000$ angular plasma periods when the CFL = 8.

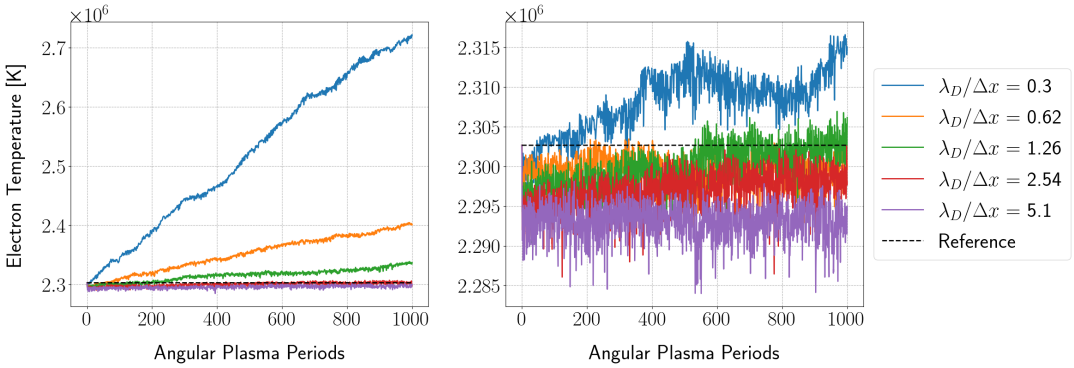

(a) AEM (Poisson) (b) AEM (Wave)

Figure 2.7 Average electron temperature as a function of the number of angular plasma periods for the electrostatic heating experiments with Poisson (left) and wave (right) models for the potential using the AEM [116]. Since the magnetic field is ignored in the model, the AEM and its improved version are identical. Fields and their derivatives in the Poisson model are constructed using the FFT, while the wave model uses the BDF-1 solver for the fields and their derivatives. The results for the Poisson model suggest that heating can be reduced if we use ≈ 2.54 grid cells per plasma Debye length. This is quite close to the usual rule of thumb which recommends ≈ 4 grid cells per Debye length. In contrast, the wave model shows less severe fluctuations in temperature, even in cases where the grid does not adequately resolve the Debye length.

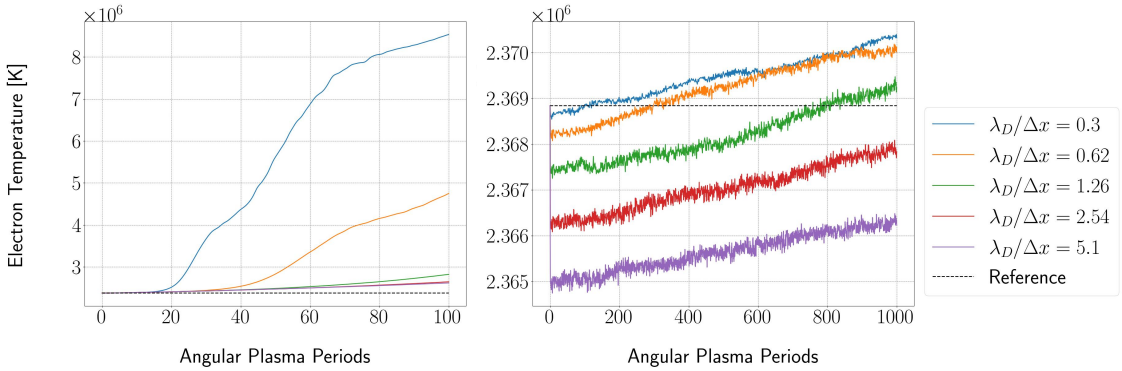

(a) FDTD-PIC (b) IAEM with BDF-1

Figure 2.8 Average electron temperature as a function of the number of angular plasma periods for the electromagnetic heating experiments. The plot on the left was obtained with the FDTD-PIC method, while the plot on the right uses the IAEM and the proposed BDF-1 field solver. Since the IAEM does not conserve energy, it will, over time, generate additional sources of energy causing the simulation to heat even if the plasma Debye length is sufficiently resolved; however, the results indicate that fluctuations in the temperature are not substantial, even in cases where the Debye length would normally be considered underresolved by the mesh. In contrast, the FDTD-PIC method displays more significant fluctuations over a smaller time window, even when the Debye length is resolved by the mesh. Note the differences in the magnitude of the electron temperature between the plots as well as the number of angular plasma periods in each case.

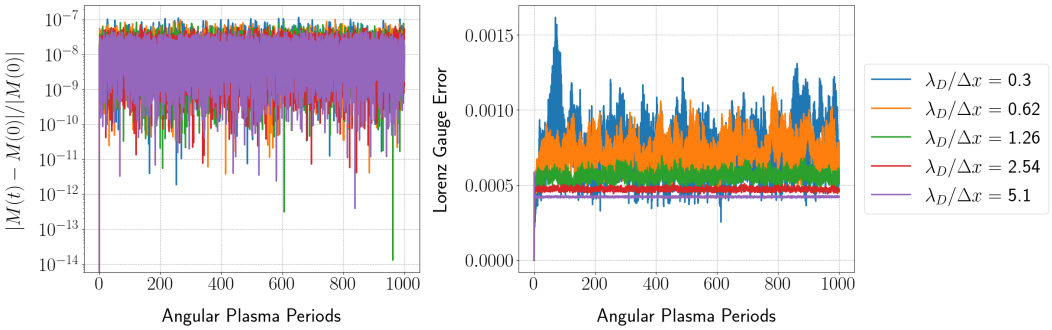

(a) Mass conservation

(b) Lorenz gauge error (ℓ_2)

Figure 2.9 Change in the total mass (left) and the error in the Lorenz gauge (right) for the BDF-1 field solver with the IAEM in the 2D-2V heating experiment. The change in the total mass is measured relative to its value at the initial time. Since the gauge condition is satisfied by the initial data for the problem, its value is initially zero, so we, instead, measure errors in the absolute sense using the ℓ_2-norm. The relative error in the Hamiltonian $\mathcal{H}$ (total energy) is not presented for brevity, as this information can be inferred from the temperature plot in Figure 2.8. The proposed method demonstrates reasonable mass conservation, and the gauge condition appears to be controlled over many plasma periods despite the absence of a cleaning method.

2.4.2.4 Plasma Sheath

Plasma sheaths are a fundamental concept in the physics of plasmas and can be simulated using PIC methods. The study of sheaths was pioneered by Langmuir [57], who described an ionized gas contained within a glass apparatus in a rather captivating manner:

> [W]hen a current of a few milliamperes from a hot cathode is flowing in a glass tube containing mercury vapor saturated at room temperature, the voltage being above about 20 volts, the tube is largely filled with the characteristic green-blue glow of the mercury discharge, but the glow does not quite reach the walls. A dark space separates the glow from the walls, as if the glow were being repelled by the glass.

The formation of sheaths is not an uncommon event, with two examples being the insertion of a conducting probe [7] and a basic matrix sheath with uniform ion charge density, which occurs in a DC discharge. Such discharges can be created using a pulsed negative electrode voltage during plasma immersion ion implantation [12].

In our computational model of a sheath, a macroscopically neutral plasma is deposited in a two-dimensional box with perfectly electrically conducting (PEC) walls, which have zero tangential

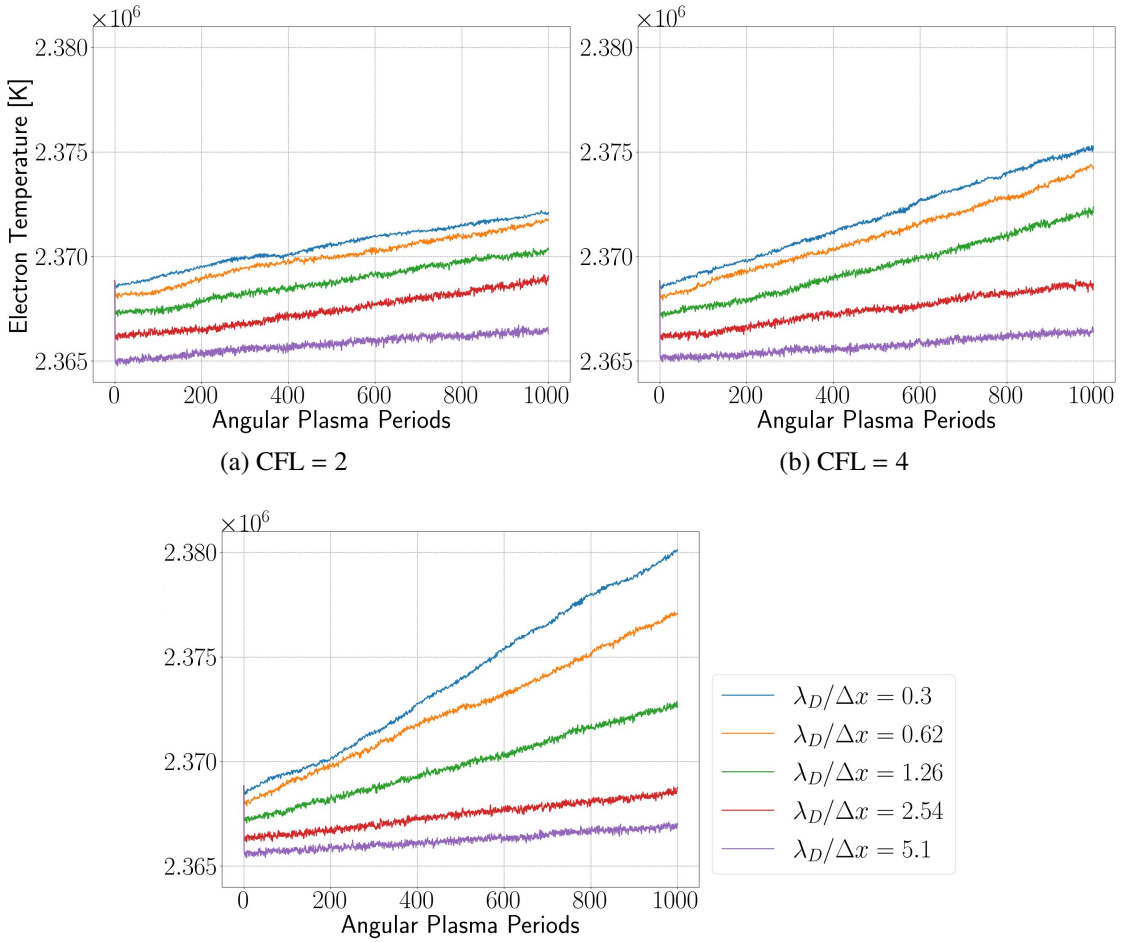

(a) CFL = 2

(b) CFL = 4

(c) CFL = 8

Figure 2.10 We note that increasing the CFL increases the sensitivity of heating to mesh refinement. A CFL of 2 demonstrates reasonable resilience to this sensitivity, close to the phenomenon to that of the refinement study with CFL 1 (Figure 2.8), though not quite as detatched. When a CFL of 4 or 8 is introduced, we see that the heating becomes sensitive to the mesh refinement, though even under worst case scenario of $\lambda_D/\Delta x = 0.3$ (16×16) with a CFL of 8 we observe approximately 0.6% increase in heat over the course of 1000 angular plasma periods.

components in their electric fields. As the problem is charge neutral, the electron drift velocity causes some of the electrons to move towards the wall. When an electron comes into contact with a PEC wall, it is effectively neutralized by its associated image charge (of opposite sign), which results in a cancellation of the electric field on the surface. Hence, it is removed from the simulation. Consequently, as the lighter and hotter electrons are eliminated from the domain, the charge imbalance forms a potential well that draws the electrons back in towards the heavier and cooler (stationary) ions. When the electrons rush back to the center of the box, they repel each

other, and the process begins anew, forming a "breathing" pattern over time. The loss of the hotter electrons to the wall results in the formation of a potential well, which, in turn, forms a sheath near the domain boundaries. In the domain of the sheath, quasi-neutrality no longer holds on the scale of the initial Debye length. In other words, the Debye length varies substantially between the quasi-neutral interior and the sheath region [278]. The results of the numerical heating experiment have clear computational implications to the study of sheaths, as one needs to ensure that the mesh appropriately resolves the smallest Debye length set by the high density regions. Therefore, methods that are less susceptible to (artificial) numerical heating would provide a clear advantage over those that suffer from heating effects because they permit the use of a coarser mesh. Of course, one needs to have adequate resolution of the sheath, but methods with high-order accuracy in space have the potential to resolve the sheath using fewer mesh points.

The procedure used to setup the simulation is nearly identical to the one used for the numerical heating experiment in section 2.4.2.3. Slight modifications to the plasma parameters are made to emphasize sheath formation (See Table 2.3). The resulting normalized speed of light for this problem is $\kappa = 7.700159 \times 10^2$. Additionally, the normalized permittivity and permeability for this problem are $\sigma_1 = 1$ and $\sigma_2 = 1.686555 \times 10^{-6}$, respectively. A neutral plasma consisting of ions and electrons is deposited within a two-dimensional box whose dimensions are $[-8\lambda_D, 8\lambda_D]^2$. The equations for the fields and particles in this experiment are identical to those used in the 2D-2V (2D-2P) electromagnetic heating experiment discussed in section 2.4.2.3. The proposed method was compared with the popular FDTD-PIC method, which (again) adopts the TE mode convention; however, this selection for the staggering with the FDTD mesh is motivated by the PEC boundary conditions for the fields, which, respectively, require $E^{(1)}$ to be zero along the x-axis and $E^{(2)}$ to be zero along the y-axis. Furthermore, since $B^{(3)}$ is cell-centered, its values along the boundary do not need to be specified. In our implementation of the FDTD-PIC method, we extend the $E^{(1)}$ field a half-cell in the x direction and the $E^{(2)}$ field a half-cell in the y direction. This ensures that $E^{(1)}$ and $E^{(2)}$ are positioned on the boundary and that $B^{(3)}$ remains on the interior of the domain. We note that this is not a requirement for the numerical heating problem, which uses periodic boundaries

and therefore has no such half-cell extensions.

Parameter	Value
Average number density ($\bar{n}$) [m^{-3}]	2.5×10^{12}
Average temperature ($\bar{T}$) [K]	1.0×10^{4}
Debye length (λ_D) [m]	4.364992×10^{-3}
Inverse angular plasma frequency (ω_{pe}^{-1}) [s/rad]	1.121147×10^{-8}
Thermal velocity ($v_{th} = \lambda_D \omega_{pe}$) [m/s]	3.893328×10^{5}

Table 2.3 Table of the plasma parameters used in the sheath problem.

In the first test, we perform a series of refinements to understand how the solution is impacted as a function of spatial resolution and the number of macroparticles. More specifically, we fix the total number of macroparticles and adjust the number of cells per dimension, taking $N_x = N_y = N$. During the refinement, N is successively doubled from 16 to 64. We use 250, 632 macroparticles for each species, for all meshes, which results in slightly more than 60 macroparticles of each species per mesh cell, in the case of a 64×64 mesh. We also fix $\Delta t = \text{CFL}\Delta x/c$, where $\text{CFL} = 1/\sqrt{2}$ for both the FDTD and BDF-1 field solvers. As noted, the initial positions for ions and electrons are sampled from a uniform distribution over the domain $[-8\lambda_D, 8\lambda_D]^2$ with a fixed random seed across all runs. The heavier ions are treated as stationary, so their velocities are set to zero in this test. Electrons velocities are obtained by sampling from a Maxwellian distribution using the parameters shown in Table 2.3. The problem is made current neutral by splitting the electrons into two equally sized groups whose velocities differ only in sign, and the simulation is run for 60 angular plasma periods. At each time step, we record the particle count, electron temperature, as well as the potentials and the corresponding fields on the mesh.

Figure 2.11 is a plot of the scalar potential for both methods at a time of 50 angular plasma periods using a 64×64 mesh. On the left, we plot the solution obtained with the Boris + FDTD method, while the plot on the right was obtained using the IAEM + BDF-1 approach. At 50 angular plasma periods, the transients arising from the sheath formation have mostly settled, and the fields become flat in the middle of the domain. What remains is a steady breathing mode, which we address in two ways. The first way is to choose a time snapshot were the field is flat on the interior,

as seen in Figure 2.11. The second is to time-average the fields, which is done in Figure 2.12 that follows. To get a sense of the sheath size, we can appeal to the well-known analytical theory of the matrix sheath [12]. Marked in red is the analytical solution to the 1D matrix sheath calculated from the plasma parameters from the simulation. We see that the predicted locations of the sheath obtained with both methods are in reasonable agreement with the analytical solution.

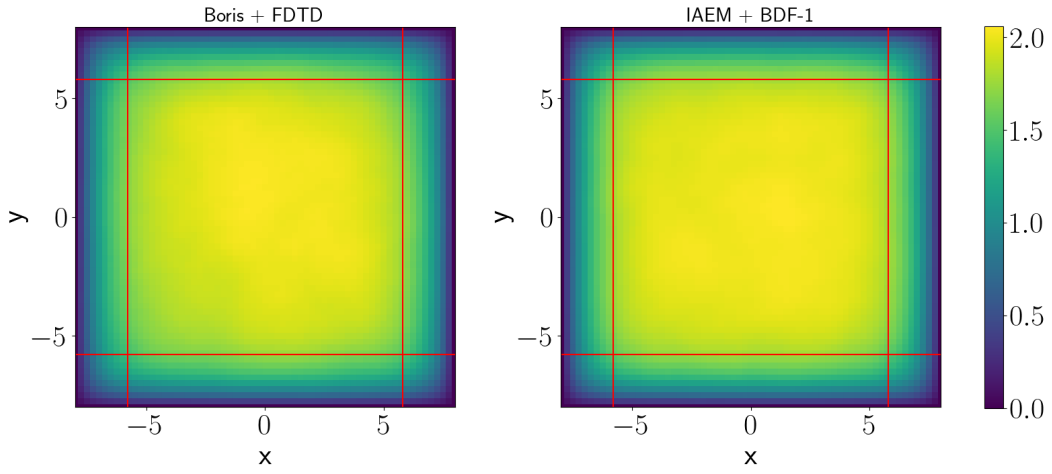

Figure 2.11 A comparison of the scalar potential obtained with the benchmark approach (Boris + FDTD) and the proposed scheme (IAEM + BDF-1). The formula for calculating the expected sheath width $s = \lambda_D \sqrt{2\phi_0/T_e}$, given in [12], is also included in the plot (marked with red lines). Here, ϕ_0 is the magnitude of the potential at the center of the domain, where the potential is flat. The sheaths produced by both methods agree with the width predicted from theory.

In Figure 2.12, we plot the time-averaged potentials and fields obtained with both methods using a 64×64 mesh. Solutions are time-averaged across the time interval ranging from $t = 40$ to $t = 60$ angular plasma periods. We observe more noise in the fields obtained with the Boris + FDTD approach when compared to the fields computed with the IAEM + BDF-1 method. Additionally, the Boris + FDTD method produces a clear asymmetry in the potential that is not present in the potential obtained with the IAEM + BDF-1 method. This suggests that the breathing mode is less adequately maintained with the Boris + FDTD method. If we look at the non-averaged solutions at a later time, this is indeed true. For this problem, one expects a symmetric solution, which indicates that the new method is an improvement to the benchmark approach.

In Figure 2.13, we plot the time-averaged center line potential about $y = 0$. As in Figure 2.12,

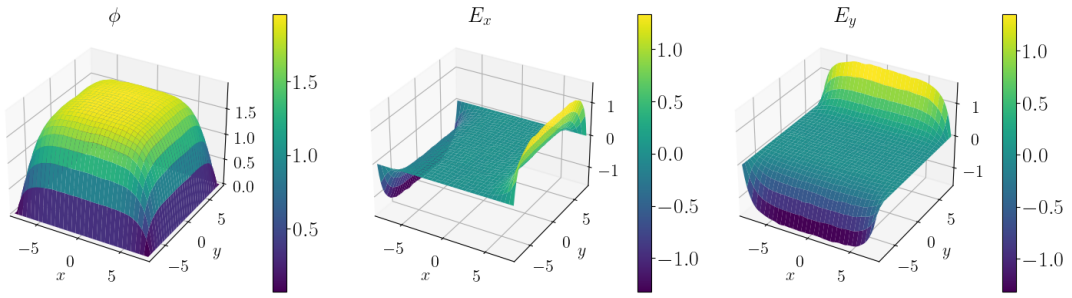

(a) IAEM + BDF-1

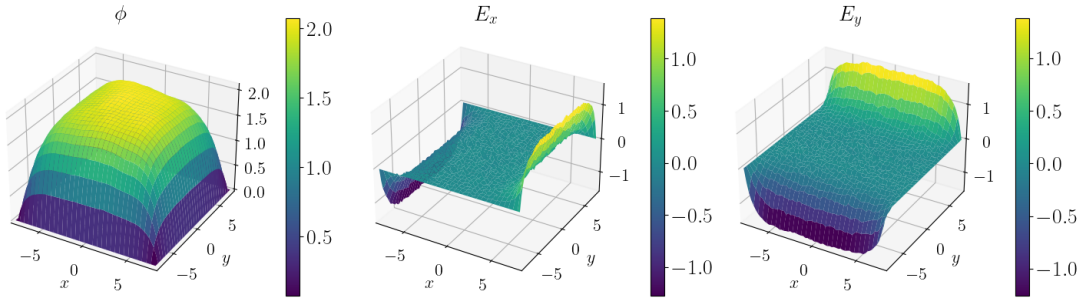

(b) Boris + FDTD

Figure 2.12 Time-averaged scalar potential along with the time-averaged x and y components of the electric fields for the sheath problem. The breathing mode is well established by $t = 40$, and the fields are averaged over the next 20 angular plasma periods. The potential and fields produced by the benchmark method (Boris + FDTD) are much rougher than those obtained with the proposed method (IAEM + BDF-1).

the solution is time-averaged from $t = 40$ to $t = 60$ angular plasma periods. The plot on the left is the IAEM + BDF-1 method and the one on the right is the Boris + FDTD method. The solid lines in both plots use a total of $250,632$ macroparticles, per species, for all mesh resolutions, while the dashed lines represent results with the number of macroparticles per cell set to 61. We see that the solution for the IAEM + BDF-1 approach shows notably smaller fluctuations across different mesh resolutions and is qualitatively more symmetric than the Boris + FDTD approach. These structural features in the potential also influence the convergence properties of the method. This aspect of the study is discussed in greater detail when we consider the time trace of the particle count and the temperature as the sheath forms and the problem settles into a breathing mode dynamic. In Figure 2.14 we consider the same results across a variety of CFL numbers, observing that these potentials also have superior smoothness to those from the Boris + FDTD method, but that the less refined

meshes do converge less quickly by CFL.

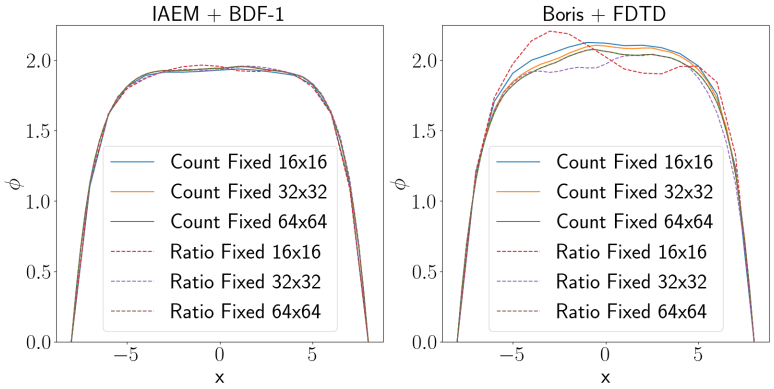

Figure 2.13 Cross-sections of the time-averaged potentials computed with both methods. Results obtained using a fixed total number of macroparticles per species ("Count Fixed") and a fixed number of particles per cell ("Ratio Fixed") are presented for comparison. Each simulation begins the time averaging procedure after 40 angular plasma periods, at which point both methods are well into the "breathing mode." The cross-sections are taken about $y = 0$ and are similar to those obtained by [12]. We note that the time-averaged potentials obtained with the Boris + FDTD approach are substantially "rougher" near the center.

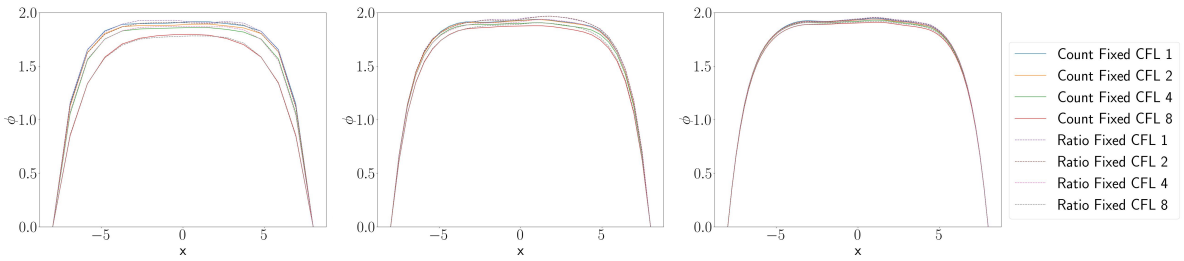

(a) 16×16 Potential Slice (b) 32×32 Potential Slice (c) 64×64 Potential Slice

Figure 2.14 We display the time averaged potentials sliced across the center of the y-axis, refining the IAEM + BDF-1 method by the CFL number. We see both ratio and count fixing have similar behavior. Refining by CFL has little impact with the more refined 64×64 grid, but has some impact on the less refined 16×16 and 32×32 grids, though it bears emphasizing that all refinements have superior smoothness across the potential than those of the Boris + FDTD method (Figure 2.13).

Next, in Figure 2.15, we show the electron temperature (left), the macroparticle count (middle) and electron count (right) for the range of spatial resolutions described earlier. In this study, the total macroparticle count for each species is initially 250, 632 for all runs. We see that the temperature and particle counts for the Boris + FDTD and IAEM + BDF-1 methods converge as the cell resolution increases. In particular, the Boris + FDTD method converges more slowly than the IAEM+BDF-1

method. We note that there are two mechanisms associated with the faster convergence of the IAEM + BDF-1 method. First, the IAEM+BDF-1 approach is high-order in space, so the sheath will be more resolved when compared to the Boris + FDTD approach on a similar computational mesh. Second, the Boris + FDTD approach contains a higher level of noise than the BDF-1 scheme because the latter is dissipative, while the former is dispersive. Additional noise in the Boris + FDTD approach is due to the current weighting scheme [37], which is used to enforce charge conservation. We might also expect that issues such as numerical heating could be impacting the Boris + FDTD results when the Debye length is not adequately resolved. In contrast, the IAEM + BDF-1 method displays more robust behavior even when the Debye length is "under-resolved." We repeat this experiment but we fix the number of macroparticles per cell to be 61. Similar phenomena is observed in Figure 2.16, namely, we see faster convergence in the number of electrons for the IAEM + BDF-1 method. Further, the results for the IAEM + BDF-1 approach on the 16×16 mesh and 61 macroparticles per cell are similar to those obtained with a 16 mesh and $250,632$ total macroparticles. This is also true for the 32×32 mesh in the case of the IAEM + BDF-1 method. In contrast, the results for the Boris + FDTD approach, while qualitatively similar, are not nearly as close together. These results, together with the data presented in Figures 2.12 and 2.13, seem to suggest that the IAEM + BDF-1 method can be used with far fewer simulation particles than the traditional Boris + FDTD method. Figure 2.14 further indicates that the CFL number can be increased without impacting the smoothness of this potential, though it does slightly impact the magnitude of the potential for the less refined meshes. These features will be the study of future work.

In Figure 2.17, we plot the electron temperatures as probability densities with a fixed total number of macroparticles set to $250,632$. From left to right in the figure, the plots correspond to data obtained using 16×16, 32×32, and 64×64 spatial meshes. The distribution function for IAEM + BDF-1 is in red and the distribution function for Boris + FDTD is in blue. In each case, the warmer tails of the IAEM + BDF-1 densities contain more simulation particles than the Boris + FDTD method. This is likely due to the high-order spatial resolution of the IAEM + BDF-1, as it

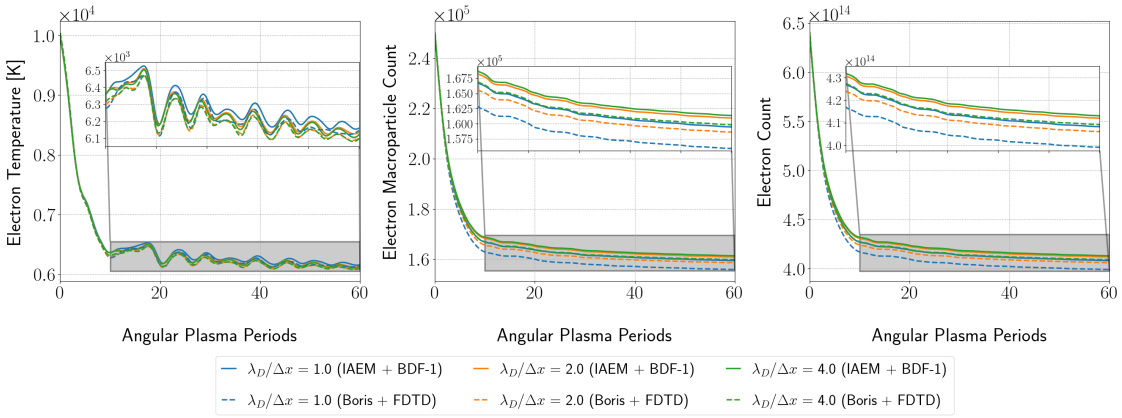

Figure 2.15 Electron temperature and particle counts collected for the sheath experiment using different grid resolutions and a fixed total number of macroparticles. As the mesh is refined, the number of macroparticles per cell decreases. However, the total number of physical particles is scaled so that the runs start in an identical manner. The data obtained with the new method (IAEM + BDF-1) is plotted using solid lines, while the results for the benchmark method (Boris + FDTD) are plotted on dashed lines. In the plot of the electron counts we focus on the region in which the potential begins to settle, highlighting the differences in the electron count. We see that the retention of the faster electrons with the new method results in a larger electron temperature when compared with the benchmark scheme. The observed electron temperatures in the proposed method are consistent with the results of the electromagnetic heating experiment in Figure 2.8. We note that the new method experiences less significant fluctuations in the temperature and physical particle counts than the benchmark scheme, despite the variations in the number of macroparticles per cell.

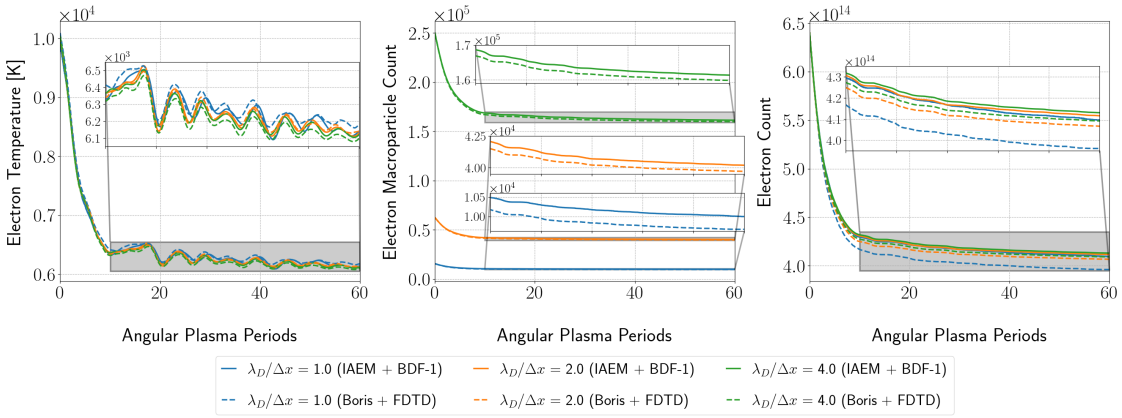

Figure 2.16 Electron temperature and count data collected for the sheath experiment with different grid resolutions. In contrast to the data presented in Figure 2.15, the number of macroparticles is increased as the mesh is refined so that the number of macroparticles per mesh cell is identical across the runs. The data obtained with the new method (IAEM + BDF-1) are plotted using solid lines, while the results for the benchmark method (Boris + FDTD) are plotted on dashed lines. The new method produces more qualitatively consistent results across the mesh resolutions than the benchmark scheme. In particular, these results suggest that the new method self-refines at a faster rate to the data obtained with the finest mesh than the benchmark scheme.

will be able to resolve the sheath with fewer points. It could also have to do with the reduced noise and improved symmetry observed in the solution to the fields from the IAEM + BDF-1 method, as noise or asymmetry in the breathing mode could easily push a warmer particle out of the domain.

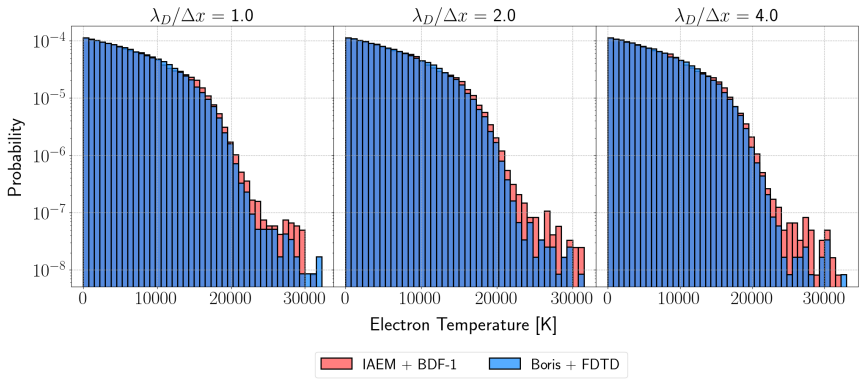

Figure 2.17 Stacked histograms of the particle temperature distributions, at the final time, obtained with both methods, for several different grid resolutions, with the total number of macroparticles held fixed. The bars in red correspond to the proposed method, and blue bars correspond to the FDTD-PIC method. While the bulk properties are similar among the approaches, the new method retains more of the warmer electrons than the benchmark scheme, contributing to a larger overall temperature.

Lastly, we check for any significant violations of the Lorenz gauge condition for the IAEM + BDF-1 method. Figure 2.18 plots the ℓ_2-norm of the gauge error as a function of time. We change the spatial resolution but keep the number of macroparticles fixed at $250,632$. In these experiments, the method maintains a bounded gauge error for all time. However, as the number of particles per cell decreases, we observe an increase in size of the Lorenz gauge error. We note that there is a sign to the gauge error, depending on whether it is ions or electrons. In a system that is truly equal, in the sense of number of particles, this error cancels. We believe the increase in the error with increased mesh resolution is simply a result of less local charge cancellation. This will also be explored as part of our future work.

2.4.2.5 Non-relativisitic Expanding Particle Beam

We now consider an application of the proposed methods to expanding particle beams [212]. This example is well-known for its sensitivity to issues concerning charge conservation, so it is typically considered when evaluating methods used to enforce charge conservation. While this

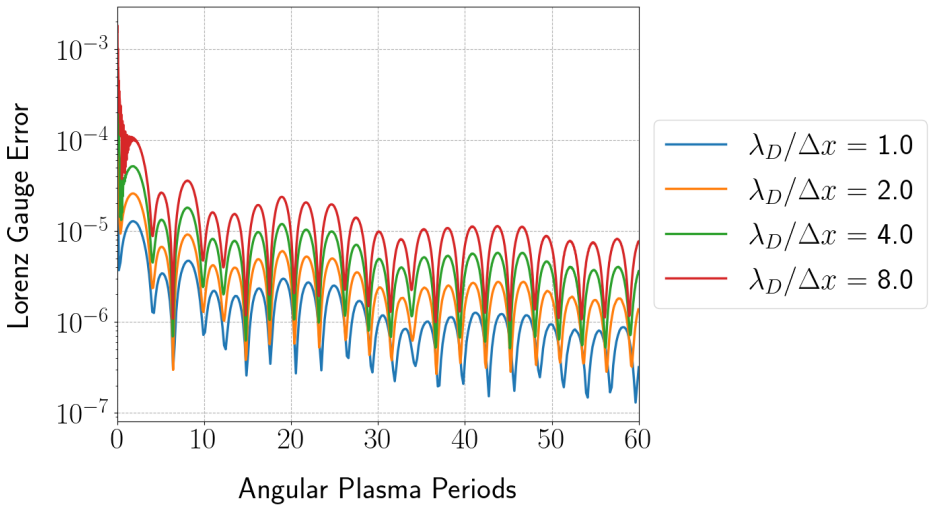

Figure 2.18 The ℓ_2-norm of the residual in the Lorenz gauge for the new method using a fixed total number of particles. Although the magnitude of the error increases as we refine the mesh, it is reasonable given that no method is used to enforce the gauge condition.

particular example is normally solved in cylindrical coordinates, the simulations presented in this work use a two-dimensional rectangular grid that retains the fields $E^{(1)}$ and $E^{(2)}$, as well as $B^{(3)}$. An injection zone is placed on one of the faces of the box and injects a steady beam of particles into the domain. The beam expands as particles move along the box due to the electric field and eventually settles into a steady-state. Similar to the sheath problem, particles are absorbed or "collected" once they reach the edge of the domain and are removed from the simulation. Along the boundary of the domain, the electric and magnetic fields are prescribed PEC boundary conditions, which, in two spatial dimensions, is equivalent to enforcing homogeneous Dirichlet boundary conditions on the potentials ϕ, $A^{(1)}$, and $A^{(2)}$. Since the problem is PEC, there can be no (tangential) currents or charge on the boundary.

As discussed earlier, the FDTD method is known to preserve the involutions for Maxwell's equations in the absence of moving charge [166, 279]. However, this is not applicable to the examples considered in this work. In order to update the fields in the FDTD approach, we need to map the current density components $J^{(1)}$ and $J^{(2)}$ to mesh points that are collocated with $E^{(1)}$ and $E^{(2)}$, respectively, according to the mesh staggering. As mentioned earlier, it is well known that the use of bilinear maps for depositing current to the mesh results in catastrophic errors due to violations of

charge conservation. The resulting fields cause the charged particles to "focus" in certain regions, leading to the appearance of striation patterns. An example of this phenomenon is presented in Figure 2.19, which shows the formation of non-physical striations after twenty particle crossings. However, indicators for such patterns can appear as early as two particle crossings. The FDTD method used in the comparison implements the charge conserving map for the current outlined by Villasenor and Buneman [37].

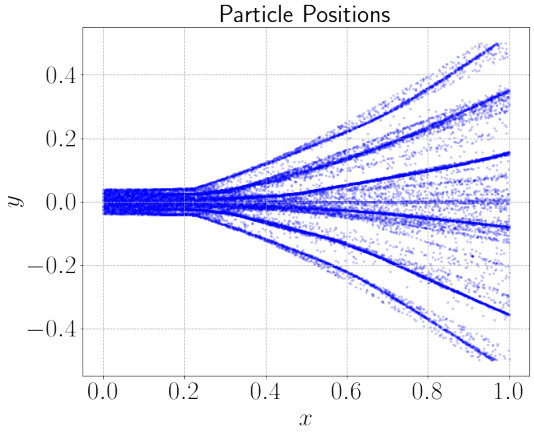

Figure 2.19 Striation patterns in a non-relativistic expanding beam simulation using the FDTD-PIC method with bilinear current mappings (area weighting). Irrotational errors in the electric field introduced by the mapping cause the particles to focus in regions of the domain.

To setup the simulation, we first create a box specified by the region $[0, 1] \times [-1/2, 1/2]$ that is normalized by the length scale L, which corresponds to the physical distance along the x-axis of the box. We assume that the beam consists only of electrons, which are prescribed some injection velocity $v_{\text{injection}}$ through their x-components. An estimate of the crossing time for a particle can be obtained from the injection velocity and the length of the domain, which sets the time scale T for the simulation. The duration of the simulation is given in terms of particle crossings, which are then used to set the time step Δt. In each time step, particles are initialized in an injection region specified by the interval $[-L_{\text{ghost}}, 0) \times [-R_b, R_b]$, where R_b is the radius of the beam, and the width of the injection zone L_{ghost} is chosen such that

$$L_{\text{ghost}} = v_{\text{injection}} \Delta t.$$

This ensures that all particles placed in the injection zone will be in the domain after one time step. The positions of particles in the injection region are set according to samples taken from a uniform distribution, and the number of particles injected for a given time step is set by the injection rate. In each time step, the injection procedure is applied before the particle position update, so that, at the end of the time step, the injection zone is empty. To prevent the introduction of an impulse response in the fields due to the initial injection of particles, a linear ramp function is applied to the macroparticle weights over one particle crossing. The methods were applied using both wide and narrow beam configurations, whose parameters can be found in Tables 2.4 and 2.5, respectively. The normalized speed of light in the simulations is $\kappa = 5.995849$. Using the wide beam configuration listed in Table 2.4, we obtain $\sigma_1 = 1.006865 \times 10^{-1}$ and $\sigma_2 = 2.762661 \times 10^{-1}$ for the normalized permittivity and permeability, respectively. For the narrow configuration provided in Table 2.5, these parameters change to $\sigma_1 = 5.061053 \times 10^{-1}$ and $\sigma_2 = 5.496139 \times 10^{-2}$, respectively.

Parameter	**Value**
Beam radius (R_b) [m]	8.0×10^{-3}
Average number density ($\bar{n}$) [m^{-3}]	7.8025×10^{14}
Physical domain length (L) [m]	1.0×10^{-1}
Injection velocity ($v_{\text{injection}}$) [m/s]	5.0×10^{7}
Injection rate ($r_{\text{injection}}$) [s^{-1}]	1×10^{2}
Crossing time (T) [s]	2.0×10^{-9}

Table 2.4 Parameters used in the setup for the non-relativistic expanding particle beam problems. Wide beam configuration.

Parameter	**Value**
Beam radius (R_b) [m]	8.0×10^{-3}
Average number density ($\bar{n}$) [m^{-3}]	1.5522581×10^{14}
Physical domain length (L) [m]	1.0×10^{-1}
Injection velocity ($v_{\text{injection}}$) [m/s]	5.0×10^{7}
Injection rate ($r_{\text{injection}}$) [s^{-1}]	1×10^{2}
Crossing time (T) [s]	2.0×10^{-9}

Table 2.5 Parameters used in the setup for the non-relativistic expanding particle beam problems. Narrow beam configuration.

The proposed method was compared against the Boris + FDTD method using the problem config-

urations specified in Tables 2.4 and 2.5. Each simulation was evolved to a final time corresponding to 3,000 particle crossings with a 128×128 mesh. A total of 4×10^6 time steps were used, which gave a CFL ≈ 0.576 for the fields. In Figure 2.20, we plot the particles in the beams generated using the IAEM + BDF-1 solver and the Boris + FDTD method. We observe excellent agreement with the benchmark FDTD PIC method despite the first-order time accuracy of the new method. Additionally, we find that the steady-state structure of the beam is well-preserved with the proposed method despite the fact that charge conservation is not strictly enforced. We find that the potentials and their spatial derivatives, which are computed using the BDF-1 wave solver are quite smooth and do not show signs of excessive dissipation even after 3,000 particle crossings. Plots of the scalar potential and its gradient obtained with the proposed methods are displayed in Figure 2.21. We show this data for the wide beam configuration provided in Table 2.4, and note that the results are quite similar for the narrow beam configuration provided in Table 2.5. While the goal of our work is to build higher-order field solvers for plasma applications, these results are interesting from the perspective of practicality, as they demonstrate that it is possible to obtain a solution of reasonable quality in a fairly inexpensive manner.

2.4.2.6 The Mardahl Beam Problem

We conclude the numerical experiments with the Mardahl beam problem, which is a benchmark relativistic beam problem proposed by Mardahl and Verboncoeur [112]. In this problem, electrons are injected into a PEC cavity with relativistic velocities ($v_{\text{injection}} = 0.967c$), and the number density is relatively small, so the beam moves across the domain mostly unperturbed. Once the electrons reach the boundary, they are removed from the simulation. A complete list of parameters for our experimental setup, which were derived from [112], is provided in Table 2.6. The normalized speed of light for this problem is $\kappa = 1.034126$, and the corresponding normalized permittivity and permeabilities are $\sigma_1 = 1.226639 \times 10^3$ and $\sigma_2 = 7.623181 \times 10^{-4}$ As with its non-relativistic counterpart, this problem is also sensitive to violations of charge conservation [270]. It also serves as as useful demonstration of the formulation presented in this work in the relativistic setting, which is the state space for applications that will be considered in future work.

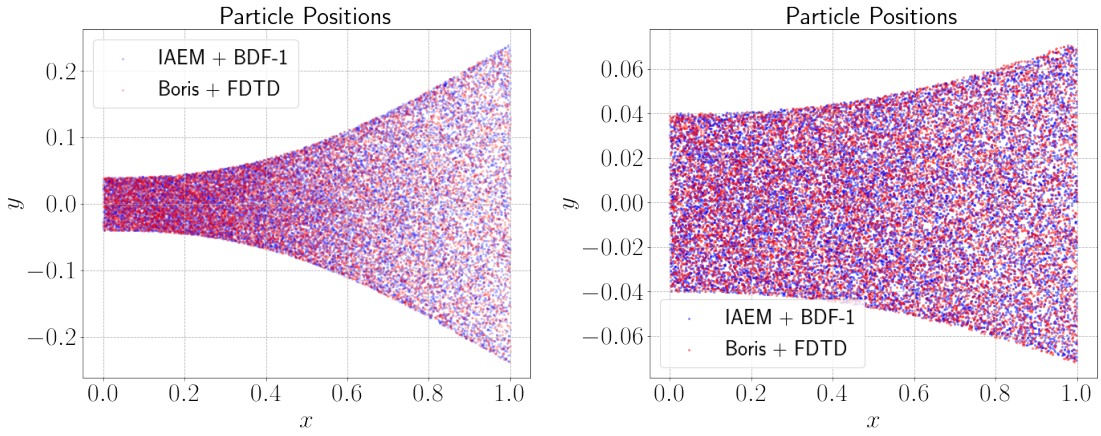

(a) (b)

Figure 2.20 We compare the proposed PIC method against the standard FDTD-PIC method for the non-relativistic expanding beam configurations specified in Tables 2.4 (shown on the left) and 2.5 (shown on the right). In each case, the electrons positions generated by the two methods after 3,000 crossings are plotted together to track the shape of the beam. The electrons from the proposed method are plotted in blue, while those of the FDTD-PIC method are plotted in red. We note that the beams produced using the proposed methods remain intact after many particle crossings without the use of a cleaning method. Moreover, the beams generated by the proposed methods show excellent agreement with the beam profiles from the benchmark FDTD-PIC method.

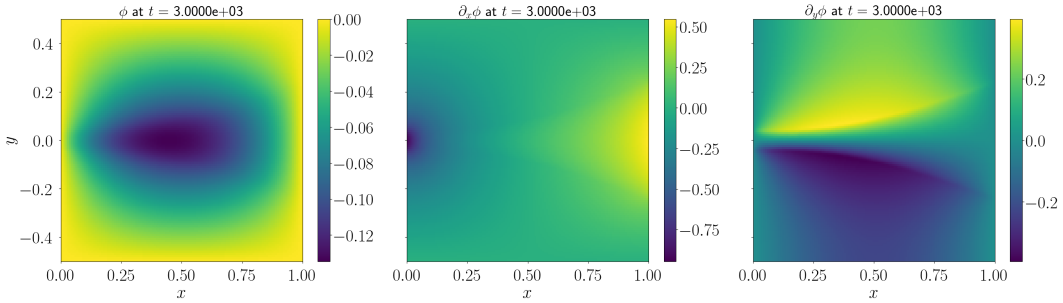

Figure 2.21 The scalar potential ϕ and its spatial derivatives for the non-relativistic expanding beam problem after 3,000 particle crossings. The fields shown above correspond to parameters listed in Table 2.4. No methods are used to enforce the gauge condition in this experiment. We can see that the proposed methods generate smooth fields for subsequent use in the particle update.

The setup for this test case is nearly identical to the non-relativistic expanding beam problems considered in the previous section, so we shall limit the discussion here for brevity. In the original presentation [112], the edge of the particle beam coincides with the boundary of the physical domain. Instead, we extend the normalized domain to $[0, 1] \times [-1, 1]$, so that the edge of the beam can be clearly seen. Furthermore, the original presentation showed simulation results up to 100 crossings of the beam. The final time of the simulation was set to $3,000$ particle crossings and used 4×10^6

Parameter	Value
Beam radius (R_b) [m]	5.0×10^{-1}
Average number density ($\bar{n}$) [m^{-3}]	$2.15299207054 \times 10^{10}$
Physical domain length (L) [m]	1.0×10^{0}
Injection velocity ($v_{\text{injection}}$) [m/s]	$2.89899306886 \times 10^{8}$
Injection rate ($r_{\text{injection}}$) [s^{-1}]	1×10^{2}
Crossing time (T) [s]	$3.44947358 \times 10^{-9}$

Table 2.6 Table of the parameters used in the setup for the Mardahl beam problem.

time steps, so the fields and particles have a CFL ≈ 0.01. We remark that this number is quite small for the BDF-1 field solver, which by the stability result shown in section 2.2.2.2, permits a much larger time step. As discussed earlier, the principle concern of this work is the development of a compatible formulation that can leverage the implicit wave solvers developed in previous work, e.g., [267, 268]. The exploration and integration of these solvers with the methods of this paper is an open area of research. As with the non-relativistic test case, the results of the proposed method show excellent agreement with the benchmark FDTD-PIC method, despite the fact that no method is used to explicitly enforce the gauge condition.

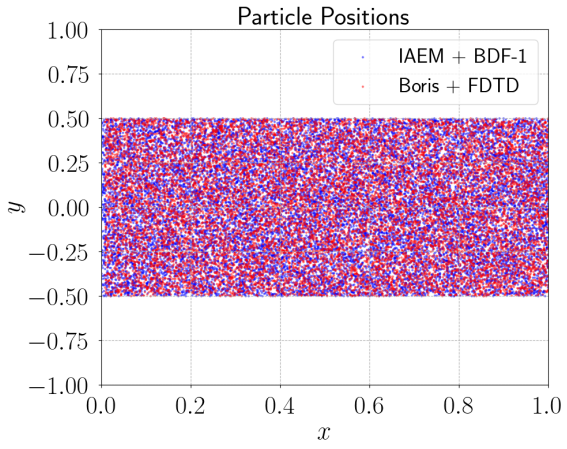

Figure 2.22 We compare the proposed PIC method against the standard FDTD-PIC method for the (relativistic) Mardahl beam problem whose configuration is specified in Table 2.6. The electron positions generated by the two methods are plotted together after 3,000 crossings to track the shape of the beam. The electrons from the proposed method are plotted in blue, while those of the FDTD-PIC method are plotted in red. The beam simulated with the proposed method remains intact after many particle crossings without the use of a cleaning method. Unlike the original paper [112], we extended the physical domain beyond the edge of the beam to investigate its structure. Similar to the non-relativistic problem, the beam structure obtained with the proposed method shows excellent agreement with the profile from the benchmark FDTD-PIC method.

In this section, we presented a collection of numerical results for the BDF wave solver, including applications to plasmas, where the wave solver is used to update fields in a new PIC method that is based on a Hamiltonian formulation. First, we analyzed the methods for evolving the potentials as well as the novel techniques for computing derivatives on the mesh. We considered several types of boundary conditions of relevance to the plasma examples presented in this work. In each case, the proposed methods for derivatives displayed space-time convergence rates that are identical to those of the wave solver used for the potentials. After establishing the convergence properties of the wave solver and the methods for derivatives, we then considered several applications involving plasmas using the new PIC method. The accuracy of the new PIC method was confirmed through a comparison of results obtained with standard PIC approaches. In particular, the new methods displayed superior numerical heating properties over the benchmark Boris + FDTD method used for electromagnetic problems. Additionally, the new method showed notable improvements in the sheath experiment, in terms of stability and preservation of symmetries. We found this to be true even in cases where the grid resolution is comparable to the plasma Debye length, which means that the new method permits coarser grids to be used in simulations. Additionally, the methods showed excellent agreement with the benchmark Boris + FDTD method for the relativistic and non-relativistic particle beam tests without resorting to the use of a method to explicitly enforce charge conservation. It is noteworthy, however, that the Lorenz gauge and Gauss's Law still exhibit nontrivial errors. These errors, though bound, are the reason why the Boris + FDTD is considered one of the staples in the PIC community, the Yee grid satisfies Gauss's law by very nature of its staggering.

2.5 Conclusion

The method we have developed has a number of desirable traits. The resilience to numerical heating, geometric flexibility, structure preserving behavior, and simple interpolation scheme all recommend this method. However, the errors in the Lorenz gauge and Gauss's law inherent MOTL + IAEM method are nontrivial. Though the numerical tests presented in this chapter are not impacted by these errors, this is far from guaranteed in other tests, not to say anything of real application

scenarios. The Lorenz gauge acts as our map back to Maxwell's equations, and Gauss's law for electricity is a fundamental involution that must be satisfied for the system to remain physically accurate. In the coming chapters we will explore how our method may approach this obstacle.

CHAPTER 3

ENFORCING THE LORENZ GAUGE

The above chapter introduced a novel PIC algorithm combining the MOLT wave solver with the Improved Asymmetrical Euler Method. This chapter extends the method by developing different approaches to enforce the Lorenz gauge condition in the context of co-located meshes. We start by establishing a certain time-consistency theorem, which shows, at the semi-discrete level, that enforcing the Lorenz gauge is equivalent to satisfying the continuity equation. Using the time-consistency result from this chapter, we first develop a map for the charge density that ensures we exactly satisfy a semi-discrete analogue of the Lorenz gauge condition on a non-staggered grid. This method utilizes the bilinear map of current density on the mesh, which is then coupled to a point-wise solution to the continuity equation to compute the charge density. In this time-consistent approach, the spatial derivatives are computed with high-order finite differences (e.g., sixth-order accuracy) or with a spectral method. A Lagrange multiplier is introduced to enforce charge conservation globally. When this charge density is used in the update of the scalar potential, both with and without the Lagrange multiplier, the method effectively satisfies the Lorenz gauge condition to machine precision. The second approach we propose is an exact map that enforces a semi-discrete continuity equation through a source term in the integral formulation of the field solver. A notable advantage offered by the integral solution with this particular map is that it allows for the removal of spatial derivatives that act on the particle current density. This quantity may be "rough" if too few simulation particles are used, as it is computed from linear combinations of low-order spline basis functions. The action of the spatial derivatives further amplifies this. Instead, we propose a new map that eliminates the spatial derivatives of the particle data by exploiting the structure of the integral solution for the scalar potential. The method is ideal for integral solutions that make use of the multi-dimensional Green's function as in [129]. The third method we consider is a gauge-correcting method in which bilinear mappings are used for both charge and current density on the mesh. Since the resulting fields will not satisfy the gauge condition, we treat the vector potential solution as exact and use the Lorenz gauge to compute a correction to the scalar potential. The vector potential and corrected

scalar potential are then guaranteed to satisfy the gauge condition to machine precision.

One of the major goals of this effort is to design fast algorithms that can address the challenges posed by the geometry of experimental devices. For this reason, we focus on simple mappings that are based on bilinear maps (or area weightings) which are more convenient in such circumstances and offer a good balance between accuracy and efficiency. Bilinear maps produce smoother representations of the particle data on the mesh compared to piece-wise constant maps, but still do no require support from nodes not immediately adjacent to the particle in question. For the gauge enforcing methods, the exact charge density mapping proposed in this work uses bilinear maps only for the current densities, and the continuity equation is used to identify the corresponding charge density. The gauge-correcting approach, on the other hand, uses bilinear maps for both the charge and current densities, but the gauge error is controlled through an equation that corrects the scalar potential.

This structure of this chapter is as follows. First, for convenience we will briefly review the equations that we will be using in Section 3.1. In Section 3.2, we establish some important properties of the semi-discrete formulation used for the potentials, including a time-consistency property of the field solver, which largely motivates the methods introduced in subsequent sections. We then introduce three techniques that enforce a semi-discrete gauge condition in Section 3.3. Some numerical results are presented in Section 3.4 to test the methods in periodic domains. In particular, we consider the relativistic Weibel instability and present a new test problem that is designed to amplify the errors in the gauge condition. A brief summary of the chapter is presented in Section 3.5. This chapter is based on the work published by myself in collaboration with Dr. Andrew Christlieb and Dr. William Sands [3]. My contribution in this work was the code development for our test problems, developing the so-called "moving cloud" problem, as well as assisting in the development of the theorems connecting satisfaction of the Lorenz gauge with satisfaction of the continuity equation and Gauss's law.

3.1 Problem Review

The vector and scalar potential formulation of Maxwell's equations and the Newton-Lorentz force have already been discussed thoroughly in Section 1.3, with the BDF-1 wave solver derived in Section 2.2. As such, we will not belabor the point, but will simply recall that the physical system we wish to simulate is as follows:

$$\begin{cases} \dfrac{d\mathbf{x}_i}{dt} = \dfrac{c^2\left(\mathbf{P}_i - q_i\mathbf{A}\right)}{\sqrt{c^2\left(\mathbf{P}_i - q_i\mathbf{A}\right)^2 + \left(m_i c^2\right)^2}}, & (3.1) \\ \dfrac{d\mathbf{P}_i}{dt} = \dfrac{q_i c^2\left(\nabla\mathbf{A}\right)\cdot\left(\mathbf{P}_i - q_i\mathbf{A}\right)}{\sqrt{c^2\left(\mathbf{P}_i - q_i\mathbf{A}\right)^2 + \left(m_i c^2\right)^2}} - q_i\nabla\phi, & (3.2) \\ \dfrac{1}{c^2}\dfrac{\partial^2\phi}{\partial t^2} - \Delta\phi = \dfrac{\rho}{\epsilon_0}, & (3.3) \\ \dfrac{1}{c^2}\dfrac{\partial^2\mathbf{A}}{\partial t^2} - \Delta\mathbf{A} = \mu_0\mathbf{J}, & (3.4) \\ \dfrac{1}{c^2}\dfrac{\partial\phi}{\partial t} + \nabla\cdot\mathbf{A} = 0, & (3.5) \\ \dfrac{\partial\rho}{\partial t} + \nabla\cdot\mathbf{J} = 0. & (3.6) \end{cases}$$

Equations (3.1) and (3.2) are the particle equations of motion, (3.3) and (3.4) are the scalar and vector potential wave equations, (3.5) is the Lorenz gauge condition we must satisfy, and (3.6) is the continuity equation we will ideally satisfy as well. Similar the the Lorenz gauge, we wish to satisfy Gauss's laws

$$\begin{cases} \nabla\cdot\mathbf{E} = \dfrac{\rho}{\epsilon_0}, & (3.7) \\ \nabla\cdot\mathbf{B} = 0. & (3.8) \end{cases}$$

(3.8) is satisfied by the definition of $\mathbf{A}$, so it is really (3.7) that we must work to satisfy.

The non-dimensionalization of these equations may be found in Appendix A. The particle equations of motion will remain constant throughout the rest of this thesis, we are only interested in modifying how the potentials are updated. In Chapter 2 we semi-discretized the waves using the BDF-1 method, dimensionally split the waves, and solved the resulting set of 1D boundary value problems using a Green's function. We will continue considering this discretization scheme, which

gives us the following system:

$$\begin{cases} \mathcal{L}\left[\phi^{n+1}\right] = 2\phi^n - \phi^{n-1} + \dfrac{1}{\alpha^2}\dfrac{\rho^{n+1}}{\epsilon_0}, & (3.9) \\ \mathcal{L}\left[\mathbf{A}^{n+1}\right] = 2\mathbf{A}^n - \mathbf{A}^{n-1} + \dfrac{\mu_0}{\alpha^2}\mathbf{J}^{n+1}, & (3.10) \\ \dfrac{\phi^{n+1} - \phi^n}{c^2\Delta t} + \nabla \cdot \mathbf{A}^{n+1} = 0, & (3.11) \end{cases}$$

The nondimensionalization of these equations may be found in Appendix A.

It is this system of two updates and an involution in which we are interested. However, we are making one vital change to our approach. As mentioned above, in Chapter 2 we would split the waves along dimensions and invert 1D operators. In this chapter, we will not be dimension splitting for reasons that will become clear presently, ie $\mathcal{L} \neq \mathcal{L}_x\mathcal{L}_y\mathcal{L}_z$. This means the integral solution will look differently than that given in Section 2.2.3.1. Given $\mathcal{L}[u] = S(\mathbf{x})$, the inverse to $\mathcal{L}$ will be as follows:

$$u(\mathbf{x}) = \int_\Omega G(\mathbf{x}, \mathbf{y})S(\mathbf{y})\, dV_\mathbf{y} + \int_{\partial\Omega} \left(\sigma(\mathbf{y})G(\mathbf{x}, \mathbf{y}) + \gamma(\mathbf{y})\frac{\partial G}{\partial \mathbf{n}}\right) dS_\mathbf{y}. \tag{3.12}$$

where $\sigma(\mathbf{y})$ is the single-layer potential and $\gamma(\mathbf{y})$ is the double-layer potential that are used to enforce boundary conditions on $u(\mathbf{x})$ [274]. Here, we use $G(\mathbf{x}, \mathbf{y})$ to denote the Green's function for the operator $\mathcal{L}$. This has several useful properties that will now be established.

The full algorithm is repeated, and slightly expanded, in Algorithm 3.1.

3.2 A Closer Look at the BDF-1 Wave Solver

3.2.1 Properties of the BDF-1 Wave Solver

In this section, we establish some structure preservation properties satisfied by the semi-discrete potential formulation, (3.9)-(3.11). This includes a lemma and two theorems which provide a connection relating the semi-discrete Lorenz gauge condition (3.11) to the semi-discrete continuity equation

$$\frac{\rho^{n+1} - \rho^n}{\Delta t} + \nabla \cdot \mathbf{J}^{n+1} = 0. \tag{3.13}$$

We also discuss the connection to the satisfaction of Gauss's Law, $\nabla \cdot \mathbf{E} = \frac{\rho}{\epsilon_0}$, in the semi-discrete sense.

Algorithm 3.1 Outline of the PIC algorithm with the improved asymmetric Euler method (IAEM)

Perform one time step of the PIC cycle using the improved asymmetric Euler method.

1: **Given**: $(\mathbf{x}_i^0, \mathbf{P}_i^0, \mathbf{v}_i^0)$, as well as the fields $\left(\phi^0, \nabla\phi^0\right)$ and $\mathbf{A}^0, \nabla\mathbf{A}^0$

2: Initialize $\mathbf{v}_i^{-1} = \mathbf{v}_i(-\Delta t)$ using a Taylor approximation.

3: **while** stepping **do**

4: Update the particle positions with

$$\mathbf{x}_i^{n+1} = \mathbf{x}_i^n + \mathbf{v}_i^n \Delta t.$$

5: Using $\mathbf{x}^{n+1}$ and $\mathbf{v}^n$, compute the current density $\mathbf{J}^{n+1}$ using a bilinear mapping.

6: Using $\mathbf{x}^{n+1}$, compute the charge density ρ^{n+1} using a bilinear mapping.

7: Compute the potentials, ϕ and $\mathbf{A}$, at time level t^{n+1} using the semi-discrete BDF method.

8: Compute the spatial derivatives of the potentials at time level t^{n+1} using the semi-discrete BDF method.

9: Evaluate the Taylor corrected particle velocities

$$\mathbf{v}_i^* = 2\mathbf{v}_i^n - \mathbf{v}_i^{n-1}.$$

10: Calculate the new generalized momentum according to

$$\mathbf{P}_i^{n+1} = \mathbf{P}_i^n + q_i\Big(- \nabla\phi^{n+1} + \nabla\mathbf{A}^{n+1} \cdot \mathbf{v}_i^*\Big)\Delta t.$$

11: Convert the new generalized momenta into new particle velocities with

$$\mathbf{v}_i^{n+1} = \frac{c^2\left(\mathbf{P}_i^{n+1} - q_i\mathbf{A}^{n+1}\right)}{\sqrt{c^2\left(\mathbf{P}_i^{n+1} - q_i\mathbf{A}^{n+1}\right)^2 + \left(m_i c^2\right)^2}}.$$

12: Shift the time history data and return to step 4 to begin the next time step.

3.2.1.1 Time-consistency of the Semi-discrete Lorenz Gauge Formulation

We will now prove a theorem that establishes a certain time consistency property of the Lorenz gauge formulation of Maxwell's equations (3.3)-(3.5) under the semi-discrete BDF-1 discretization. By time-consistent, we mean that the semi-discrete system (3.9)-(3.11) for the potentials induces an equivalence between the gauge condition and continuity equation at the semi-discrete level. In the treatment of the semi-discrete equations, we shall ignore effects of dimensional splittings and instead consider the more general inverse induced by the integral solution (3.12). Note that space is treated in a continuous manner, which means that effects due to the representation of particles on the mesh are ignored.

We show that this semi-discrete system is time-consistent in the sense of the semi-discrete Lorenz gauge. To simplify the presentation, we first prove the following lemma that connects the discrete gauge condition (3.11) to the semi-discrete equations for the potentials given by equations (3.9) and (3.10).

Lemma 3.2.1. *The semi-discrete Lorenz gauge condition* (4.48) *satisfies the recurrence relation*

$$\epsilon^{n+1} = \mathcal{L}^{-1}\left[2\epsilon^n - \epsilon^{n-1} + \frac{\mu_0}{\alpha^2}\epsilon_2^{n+1}\right], \tag{3.14}$$

where we have defined the semi-discrete residuals

$$\epsilon_1^n = \frac{\phi^n - \phi^{n-1}}{c^2\Delta t} + \nabla\cdot\mathbf{A}^n, \tag{3.15}$$

$$\epsilon_2^n = \frac{\rho^n - \rho^{n-1}}{\Delta t} + \nabla\cdot\mathbf{J}^n. \tag{3.16}$$

Proof. Again, we note that the modified Helmholtz operator $\mathcal{L}$ can be formally "inverted" with the integral solution given by equation (3.12). From this, we can calculate the terms involving the potentials in the residual (3.15). Proceeding, the equation for the scalar potential is found to be

$$\phi^{n+1} = \mathcal{L}^{-1}\left(2\phi^n - \phi^{n-1} + \frac{1}{\alpha^2\epsilon_0}\rho^{n+1}\right), \tag{3.17}$$

which can be evaluated at time level n to yield

$$\phi^n = \mathcal{L}^{-1}\left(2\phi^{n-1} - \phi^{n-2} + \frac{1}{\alpha^2\epsilon_0}\rho^n\right). \tag{3.18}$$

Likewise, we take the divergence of $\mathbf{A}$ in equation (3.10) and invert $\mathcal{L}$ to see

$$\nabla\cdot\mathbf{A}^{n+1} = \mathcal{L}^{-1}\left(2\nabla\cdot\mathbf{A}^n - \nabla\cdot\mathbf{A}^{n-1} + \frac{\mu_0}{\alpha^2}\nabla\cdot\mathbf{J}^{n+1}\right). \tag{3.19}$$

Substituting equations (3.17), (3.18), and (3.19) into (3.15) at time level $n+1$, we find it becomes

$$\begin{aligned}\epsilon_1^{n+1} = {}& \frac{1}{c^2}\frac{1}{\Delta t}\mathcal{L}^{-1}\left[2\phi^n - \phi^{n-1} + \frac{1}{\alpha^2}\frac{\rho^{n+1}}{\epsilon_0}\right] \\ & -\frac{1}{c^2}\frac{1}{\Delta t}\mathcal{L}^{-1}\left[2\phi^{n-1} - \phi^{n-2} + \frac{1}{\alpha^2}\frac{\rho^n}{\epsilon_0}\right] \\ & + \mathcal{L}^{-1}\left[2\nabla\cdot\mathbf{A}^n - \nabla\cdot\mathbf{A}^{n-1} + \frac{\mu_0}{\alpha^2}\nabla\cdot\mathbf{J}^{n+1}\right].\end{aligned}$$

The linearity of the operator $\mathcal{L}$ may be exploited to rewrite this as

$$2\mathcal{L}^{-1}\left[\frac{1}{c^2}\frac{\phi^n-\phi^{n-1}}{\Delta t}+\nabla\cdot\mathbf{A}^n\right]-\mathcal{L}^{-1}\left[\frac{1}{c^2}\frac{\phi^{n-1}-\phi^{n-2}}{\Delta t}+\nabla\cdot\mathbf{A}^{n-1}\right]+\frac{\mu_0}{\alpha^2}\mathcal{L}^{-1}\left[\frac{\rho^{n+1}-\rho^n}{\Delta t}+\nabla\cdot\mathbf{J}^{n+1}\right]$$

Note that we have used the relation $c^2 = 1/(\mu_0\epsilon_0)$. It is clear the first two terms are ϵ_1^n and ϵ_1^{n-1}, and the second is the residual of the continuity equation at time $n+1$, ϵ_1^{n+1}. We conclude

$$\epsilon_1^{n+1} = 2\epsilon_1^n - \epsilon_1^{n-1} + \frac{\mu_0}{\alpha^2}\epsilon_2^{n+1}.$$

This completes the proof. QED

With the aid of Lemma 3.2.1, we are now prepared to prove the following theorem that establishes the time-consistency of the semi-discrete system.

Theorem 3.2.1. *The semi-discrete Lorenz gauge formulation of Maxwell's equations* (3.9)-(3.11) *is time-consistent in the sense that the semi-discrete Lorenz gauge condition* (3.11) *is satisfied at any discrete time* t^{n+1} *if and only if the corresponding semi-discrete continuity equation* (3.13) *is also satisfied.*

Proof. We use a simple inductive argument to prove both directions. In the case of the forward direction, we assume that the semi-discrete gauge condition is satisfied at any discrete time t^n such that the residual $\epsilon_1^n = 0\,\forall\, n$. Combining this with equation (3.14), established by Lemma 3.2.1, it follows that the next time level satisfies

$$0 = \mathcal{L}^{-1}\left[\frac{\mu_0}{\alpha^2}\epsilon_2^n\right].$$

Applying the operator $\mathcal{L}$ to both sides leads to $\epsilon_2^n = 0$, which establishes the forward direction.

A similar argument can be used for the converse. Here, we show that if the residual for the semi-discrete continuity equation (3.13) is satisfied for any time level n, then the residual for the discrete gauge condition also satisfies $\epsilon_1^{n+1} = 0$. First, we assume that the initial data and starting values satisfy $\epsilon_1^{-1} = \epsilon_1^0 = 0$. Appealing to equation (3.14) with this initial data, it is clear that after a single time step, the residual in the gauge condition satisfies

$$\epsilon_1^1 = \mathcal{L}^{-1}\left[2\epsilon_1^0 - \epsilon_1^{-1} + \frac{\mu_0}{\alpha^2}\epsilon_2^0\right] = \mathcal{L}^{-1}\left[2(0) - (0) + \frac{\mu_0}{\alpha^2}(0)\right] = \mathcal{L}^{-1}\left[0\right] = 0.$$

This argument can also be iterated n more times to obtain the result, which finishes the proof. QED

Theorem 3.2.1 motivates, to a large extent, our choice in presenting a low-order time discretization for the fields. By repeating the calculations above with a higher-order time discretization for the fields, one can easily see that the residual for the gauge is non-vanishing, so additional modifications will be needed. The extension to higher-order time accuracy is the subject of on-going work and will be presented in a subsequent paper. While we have neglected the error introduced by the discrete maps that transfer particle data to the mesh, the results we present for the numerical experiments in Section 4.3 suggest that these effects are not significant. We will be using Theorem 3.2.1 to construct maps for the charge density which satisfy the semi-discrete form of the gauge condition.

3.2.1.2 Satisfying Gauss's Law

A benefit that comes with satisfying the semi-discrete Lorenz gauge (3.11) is the corresponding satisfaction of Gauss's law, $\nabla \cdot \mathbf{E} = \frac{\rho}{\epsilon_0}$. We summarize this with the following theorem:

Theorem 3.2.2. *If the semi-discrete Lorenz gauge* (3.11) *is satisfied, then Gauss's law,* $\nabla \cdot \mathbf{E} = \frac{\rho}{\epsilon}$*, is also satisfied.*

Proof. Consider the backward Euler discretization of the Lorenz gauge condition in time:

$$\frac{1}{c^2}\frac{\phi^{n+1} - \phi^n}{\Delta t} + \nabla \cdot \mathbf{A}^{n+1} = 0.$$

We know from the definition (1.10) that

$$\mathbf{E}^{n+1} = -\nabla\phi^{n+1} - \frac{\mathbf{A}^{n+1} - \mathbf{A}^n}{\Delta t}.$$

Applying the divergence operator to both sides yields

$$\begin{aligned}
\nabla \cdot \mathbf{E}^{n+1} &= -\Delta\phi^{n+1} - \frac{\nabla \cdot \mathbf{A}^{n+1} - \nabla \cdot \mathbf{A}^n}{\Delta t} \\
&= -\Delta\phi^{n+1} - \frac{\left(-\frac{1}{c^2}\frac{\phi^{n+1} - \phi^n}{\Delta t}\right) - \left(-\frac{1}{c^2}\frac{\phi^n - \phi^{n-1}}{\Delta t}\right)}{\Delta t} \\
&= -\Delta\phi^{n+1} + \frac{1}{c^2}\frac{\phi^{n+1} - 2\phi^n + \phi^{n-1}}{\Delta t^2}.
\end{aligned}$$

From the semi-discrete update (3.9) for the scalar potential, the last line is equal to ρ^{n+1}/ϵ_0, which completes the proof. QED

It is worth noting that the above argument requires that the discrete time derivative operator applied to the Lorenz gauge be the same as the one applied to the scalar potential wave equation.

3.3 Enforcing the Lorenz Gauge

Enforcing the Lorenz gauge is an important step to keeping the system physical. As long as errors exist in this gauge, the vector and scalar wave equations will not map back to Maxwell's equations, which is the original system we wish to simulate. In this section we present three methods to enforce this condition: in section 3.3.1 a charge map exploiting the theorems proven in section 3.2, in section 3.3.2 an extension to this charge map implementing multi-dimensional Green's functions, and finally in section 3.3.3 a gauge correcting method.

3.3.1 A Charge Map Utilizing Numerical Derivatives

We seek to create a map for the charge density that is consistent with a semi-discrete continuity equation (3.13). Our goal is that this map enforce the Lorenz Gauge condition. The semi-discrete properties established in Theorem 3.2.1 requires that the method satisfy (3.13) point-wise on the mesh. From a practical perspective, if one goes through the derivation of Lemma 3.2.1, an important observation is that if this Lemma is going to hold in the discrete setting, the discrete divergence operators used to compute the solution to (3.13) must be the same discrete operator used to compute the divergence of $\mathbf{A}$. The remark in Section 3.3.1.1, which is presented later, provides further clarification on this matter.

To create our map for the charge density, we will solve for ρ^{n+1} using an update of the semi-discrete continuity equation (3.13). The current density $\mathbf{J}^{n+1}$ used in this update is obtained from the particles using a bilinear map. To compute the discrete divergence operator, we will utilize either the fast Fourier transform (FFT) or the sixth-order centered finite difference method (FD6). Additionally, to make the point-wise map conservative, we introduce a Lagrange multiplier, which we now discuss. In the construction, we make the following observation: Starting from the non-corrected point-wise

update

$$\rho_{i,j}^{n+1} = \rho_{i,j}^{n} - \Delta t \nabla \cdot \mathbf{J}_{i,j}^{n+1},$$

after summing over the periodic domain, we obtain

$$\sum_{i,j} \rho_{i,j}^{n+1} = \sum_{i,j} \rho_{i,j}^{n} - \Delta t \sum_{i,j} \left(\nabla \cdot \mathbf{J}^{n+1} \right)_{i,j}. \tag{3.20}$$

To ensure charge conservation, we require

$$\sum_{i,j} \rho_{i,j}^{n+1} = \sum_{i,j} \rho_{i,j}^{n},$$

which further implies the condition

$$\sum_{i,j} \left(\nabla \cdot \mathbf{J}^{n+1} \right)_{i,j} = 0.$$

We introduce the Lagrange multiplier, γ, to enforce this condition. For 2D, we define

$$\gamma \coloneqq -\frac{1}{N_x N_y} \sum_{i,j} (\nabla \cdot \mathbf{J})_{i,j}, \quad \mathbf{F} \coloneqq \frac{1}{2} \gamma \mathbf{x},$$

and let $\mathbf{J}^* \coloneqq \mathbf{J} + \mathbf{F}$ be the adjusted current density. In 3D, the $\frac{1}{2}$ would become a $\frac{1}{3}$. Correspondingly,

$$\begin{aligned} \sum_{i,j} \left(\nabla \cdot \mathbf{J}^{n+1,*} \right)_{i,j} &= \sum_{i,j} \left(\nabla \cdot \mathbf{J}^{n+1} + \nabla \cdot \mathbf{F} \right)_{i,j} \\ &= \sum_{i,j} \left(\nabla \cdot \mathbf{J}^{n+1} - \frac{1}{N_x N_y} \sum_{l,k} \left(\nabla \cdot \mathbf{J}^{n+1} \right)_{l,k} \right) \\ &= \sum_{i,j} \left(\nabla \cdot \mathbf{J}^{n+1} \right)_{i,j} - \sum_{i,j} \left(\nabla \cdot \mathbf{J}^{n+1} \right)_{i,j} = 0. \end{aligned} \tag{3.21}$$

We now use ρ^{n+1} and $\mathbf{J}^{n+1,*}$ in the update of ϕ^{n+1} and $\mathbf{A}^{n+1}$.

As noted earlier, in the above expressions, the divergence $\nabla \cdot \mathbf{J}_{i,j}^{n+1,*}$ is computed using either an FFT or a sixth-order finite difference. For the FFT, we have the identity

$$\partial_x u = \mathcal{F}_x^{-1} \left[i k_x \mathcal{F} \left[u \right] \right],$$

where k_x is the wavenumber. Derivatives in y can be calculated using identical formulas. For FD6, we use the following centered finite-difference stencil

$$\partial_x u_{i,j} = -\frac{1}{60} u_{i-3,j} + \frac{3}{20} u_{i-2,j} - \frac{3}{4} u_{i-1,j} + \frac{3}{4} u_{i+1,j} - \frac{3}{20} u_{i+2,j} + \frac{1}{60} u_{i+3,j},$$

with an analogous set of coefficients for the y derivative. It should be mentioned that in numerical experiments, the schemes preserve the gauge condition to machine precision, with and without the Lagrange multiplier, using either the FFT or FD6 in the update of ρ^{n+1} (see Section 3.4).

In summary, Algorithm 3.1 is modified in two ways. Line 6 is changed by eliminating the bilinear interpolation of particles to obtain ρ^{n+1}. Instead, ρ^{n+1} is computed from the semi-discrete continuity equation (3.13), with line 5 supplying the value of $\mathbf{J}^{n+1}$ for whatever discrete derivative operator has been decided. Line 8 computes the derivatives acquired from line 7, which remains unchanged, and it does so using the same discrete derivative operator, for reasons we now move on to explain.

3.3.1.1 A Remark on the Derivatives

It is worth commenting upon the nature of the way the $\nabla\mathbf{A}$ and $\nabla\phi$ values are obtained in the context of the IAEM method (Section 2.3.1.2). As stated above, the BDF method does have the ability to analytically compute the derivatives of $\mathbf{A}^{n+1}$ and ϕ^{n+1} from the values of their previous timesteps, combined with the sources $\mathbf{J}$ and ρ, respectively. There is a difficulty in this approach, however. The proof of Theorem 3.2.1, which connects the gauge condition to the continuity equation, is predicated upon Lemma 3.2.1, the proof of which assumes the derivative operator used on $\mathbf{A}$ and $\mathbf{J}$ are the same. In order to assert (3.14), the following relationship must hold:

$$\mathbf{A}^{n+1} = \mathcal{L}^{-1}\left[2\mathbf{A}^n - \mathbf{A}^{n-1} + \frac{\mu_0}{\alpha^2}\mathbf{J}^{n+1}\right] \implies \nabla\cdot\mathbf{A}^{n+1} = \mathcal{L}^{-1}\left[2\nabla\cdot\mathbf{A}^n - \nabla\cdot\mathbf{A}^{n-1} + \frac{\mu_0}{\alpha^2}\nabla\cdot\mathbf{J}^{n+1}\right].$$

Of course, in the continuous case, this is trivial. However, should we, for example, update ρ based on a discrete Fourier transform of $\nabla\cdot\mathbf{J}$, then this theorem does not hold unless the spatial derivative applied to $\mathbf{A}$ is likewise obtained using a discrete Fourier transform. In the fully discrete setting, Lemma 3.2.1 requires that the discrete derivative operators used to compute $\nabla\cdot\mathbf{A}$ and $\nabla\cdot\mathbf{J}$ have the same form.

3.3.2 A Charge Map for the Multi-dimensional Boundary Integral Solution

The map used to construct ρ^{n+1} in the previous section has a natural extension to boundary integral formulations that evolve the potentials using multi-dimensional Green's functions. The solutions for the potentials in terms of the boundary integral representation (3.12) leads to the

equations

$$\phi^{n+1}(\mathbf{x}) = \int_\Omega G(\mathbf{x},\mathbf{y}) \left(2\phi^n - \phi^{n-1} + \frac{1}{\alpha^2}\frac{\rho^{n+1}}{\epsilon_0}\right)(\mathbf{y})\, dV_\mathbf{y} + \int_{\partial\Omega} \left(\sigma_\phi(\mathbf{y}) G(\mathbf{x},\mathbf{y}) + \gamma_\phi(\mathbf{y})\frac{\partial G}{\partial \mathbf{n}}\right) dS_\mathbf{y}, \tag{3.22}$$

$$\mathbf{A}^{n+1}(\mathbf{x}) = \int_\Omega G(\mathbf{x},\mathbf{y}) \left(2\mathbf{A}^n - \mathbf{A}^{n-1} + \frac{\mu_0}{\alpha^2}\mathbf{J}^{n+1}\right)(\mathbf{y})\, dV_\mathbf{y} + \int_{\partial\Omega} \left(\sigma_\mathbf{A}(\mathbf{y}) G(\mathbf{x},\mathbf{y}) + \gamma_\mathbf{A}(\mathbf{y})\frac{\partial G}{\partial \mathbf{n}}\right) dS_\mathbf{y}. \tag{3.23}$$

When particles are introduced, maps to the mesh for ρ^{n+1} and $\mathbf{J}^{n+1}$ generally do not satisfy the semi-discrete continuity equation (3.13), which, by Lemma 3.2.1, also means that the semi-discrete Lorenz gauge condition will be violated; however, if the map for ρ^{n+1} can be connected to the map for $\mathbf{J}^{n+1}$, then this constraint will indeed be satisfied. Following the observation of the previous section, we shall construct this map by solving equation (3.13) for the charge at the new time level according to

$$\rho^{n+1} = \rho^n - \Delta t\, \nabla \cdot \mathbf{J}^{n+1}.$$

This discretization, which is first-order in time, is consistent with the BDF field solver considered in this work. An obvious extension to higher-order is to include additional stencil points for the approximation of time derivative, which will be considered at a later time. Note that at the initial time $t^0 = 0$, the particle data is known, and therefore, the charge and current densities ρ^0 and $\mathbf{J}^0$ are also known.

The primary objective is to define the volume integral term

$$\int_\Omega G(\mathbf{x},\mathbf{y})\rho^{n+1}(\mathbf{y})\, dV_\mathbf{y} = \int_\Omega G(\mathbf{x},\mathbf{y})\rho^n(\mathbf{y})\, dV_\mathbf{y} - \Delta t \int_\Omega G(\mathbf{x},\mathbf{y})\nabla_y \cdot \mathbf{J}^{n+1}(\mathbf{y})\, dV_\mathbf{y}. \tag{3.24}$$

so that it is compatible with the low regularity charge and current data produced by particle simulations. In PIC, we construct $\mathbf{J}^{n+1}$ by scattering the current density of the particles to the mesh using particle shape functions that typically have low regularity. In most cases, especially in bounded domains, these maps are either piece-wise constant or linear functions, or combinations of these, so we would like to avoid taking derivatives of this term. With the aid of the divergence theorem, we can move the derivatives from the less regular particle data to the Green's function G whose

derivatives can be evaluated analytically. This allows us to write

$$\int_\Omega G(\mathbf{x},\mathbf{y})\nabla_y \cdot \mathbf{J}^{n+1}(\mathbf{y})\, dV_\mathbf{y} = \int_{\partial\Omega} G(\mathbf{x},\mathbf{y})\, \mathbf{J}^{n+1}(\mathbf{y}) \cdot \mathbf{n}\,(\mathbf{y})\ dS_\mathbf{y} - \int_\Omega \nabla_y G(\mathbf{x},\mathbf{y}) \cdot \mathbf{J}^{n+1}(\mathbf{y})\, dV_\mathbf{y},$$

which can be combined with equation (3.24). This yields the map

$$\begin{aligned}\int_\Omega G(\mathbf{x},\mathbf{y})\rho^{n+1}(\mathbf{y})\, dV_\mathbf{y} = &\int_\Omega G(\mathbf{x},\mathbf{y})\rho^{n}(\mathbf{y})\, dV_\mathbf{y} \\ &- \Delta t\left[\int_{\partial\Omega} G(\mathbf{x},\mathbf{y})\, \mathbf{J}^{n+1}(\mathbf{y}) \cdot \mathbf{n}\,(\mathbf{y})\ dS_\mathbf{y} - \int_\Omega \nabla_y G(\mathbf{x},\mathbf{y}) \cdot \mathbf{J}^{n+1}(\mathbf{y})\, dV_\mathbf{y}\right],\end{aligned} \tag{3.25}$$

which, by Theorem 3.2.1, will be charge-conserving and enforce the Lorenz gauge condition in the semi-discrete sense.

The charge map given by equation (3.25) can then be substituted into the boundary integral solution (3.22) to give the update

$$\begin{aligned}\phi^{n+1}(\mathbf{x}) = &\int_\Omega G(\mathbf{x},\mathbf{y})\left(2\phi^n - \phi^{n-1} + \frac{1}{\alpha^2}\frac{\rho^n}{\epsilon_0}\right)(\mathbf{y})\, dV_\mathbf{y} + \int_{\partial\Omega}\left(\sigma_\phi(\mathbf{y})G(\mathbf{x},\mathbf{y}) + \gamma_\phi(\mathbf{y})\frac{\partial G}{\partial \mathbf{n}}\right) dS_\mathbf{y} \\ &+ \frac{\Delta t}{\alpha^2\epsilon_0}\left[\int_\Omega \nabla_y G(\mathbf{x},\mathbf{y}) \cdot \mathbf{J}^{n+1}(\mathbf{y})\, dV_\mathbf{y} - \int_{\partial\Omega} G(\mathbf{x},\mathbf{y})\, \mathbf{J}^{n+1}(\mathbf{y}) \cdot \mathbf{n}\,(\mathbf{y})\ dS_\mathbf{y}\right].\end{aligned} \tag{3.26}$$

Expressions for the gradients of the scalar potential $\nabla\phi^{n+1}(\mathbf{x})$ can then be obtained by differentiating equation (3.26). Since the derivatives are in $\mathbf{x}$, they are transferred directly onto analytical functions. We remark that the modifications required to achieve compatibility with dimensionally-split solvers is non-trivial, since the divergence of the current density effectively couples the boundary conditions between different directions. However, the map (3.26) would be well-suited for solvers that use the full boundary integral solution [129].

Whereas in the previous approach we explicitly computed ρ^{n+1} from ρ^n and $\mathbf{J}^{n+1}$ using (3.13), thus modifying line 6 and correspondingly 8, this approach circumnavigates this by, instead, replacing computing ρ^{n+1} entirely, cutting out line 6. We then modify lines 7 and 8 in Algorithm 3.1 both by computing ϕ^{n+1} using a combination of ρ^n, ϕ^n, ϕ^{n-1}, and $\mathbf{J}^{n+1}$ in the BDF method, and likewise with the spatial derivatives. It should be noted that the computation of $\mathbf{A}^{n+1}$ remains unchanged.

3.3.3 Correcting ϕ Using the Gauge Condition

As an alternative approach to solving the continuity equation, we assume that a bilinear map of $\mathbf{J}^{n+1}$ is exact and use the gauge condition itself to create a correction to ϕ^{n+1}. To do this, we first use a bilinear map to construct both the ''exact'' $\mathbf{J}^{n+1}$ and an approximate ρ^{n+1} called ρ_A^{n+1}. These are used to construct the "exact" vector potential $\mathbf{A}^{n+1}$ and the approximate scalar potential ϕ_A^{n+1}. The correction to the scalar potential, ϕ_C^{n+1}, that we propose makes use of the analytical derivatives as discussed in Section 2.2.4 in the evaluation of the divergence of $\mathbf{A}^{n+1}$. To start, we update the vector potential and scalar potential using bilinear maps for the particle data, which gives

$$\mathbf{A}^{n+1}(x,y) = \mathcal{L}_y^{-1}\mathcal{L}_x^{-1}\left[2\mathbf{A}^n - \mathbf{A}^{n-1} + \frac{1}{\alpha^2}\mu_0\mathbf{J}^{n+1}\right](x,y),$$
$$\phi_A^{n+1}(x,y) = \mathcal{L}_y^{-1}\mathcal{L}_x^{-1}\left[2\phi^n - \phi^{n-1} + \frac{1}{\alpha^2}\frac{\rho_A^{n+1}}{\epsilon_0}\right](x,y),$$

where ϕ^n and ϕ^{n-1} are the corrected values such that $\mathbf{A}^n$, $\mathbf{A}^{n-1}$, ϕ^n and ϕ^{n-1} satisfy the gauge condition. We decompose the scalar potential as

$$\phi^{n+1} \coloneqq \phi_A^{n+1} + \phi_C^{n+1}, \tag{3.27}$$

where ϕ_A^{n+1} is the approximate potential and ϕ_C^{n+1} is its correction. We also assume that $\mathbf{A}^{n+1}$ and ϕ^{n+1} satisfy the gauge condition in the sense that

$$\frac{1}{c^2}\frac{\phi^{n+1}-\phi^n}{\Delta t} + \nabla\cdot\mathbf{A}^{n+1} = 0.$$

Since this is designed to be a correction method, the discrete divergence can be evaluated using a variety of methods, including the analytical differentiation techniques developed in Section 2.2.4. Rearranging the expression for the gauge error, we obtain the correction

$$\phi_C^{n+1} = \phi^n - \phi_A^{n+1} - c^2\Delta t\left(\partial_x A^{(1),n+1} + \partial_y A^{(2),n+1}\right).$$

Once the correction ϕ_C^{n+1} is obtained, we then form the total potential according to the definition (3.27) and compute its numerical derivatives for the particle advance used in the algorithm (no significant difference was seen between FFT and FD6). The use of a numerical derivative in the particle advance is because the terms that make up ϕ_C^{n+1} do not sit under the operator $\mathcal{L}^{-1}[\cdot]$.

This is the least intrusive of all our methods, being accomplished by simply adding a line after 8, in which we compute the correction to ϕ and its numerical derivatives. As will be seen in the numerical results, by construction, this method satisfies the gauge error to machine precision. Also, it is worth noting that if one needs the correct ρ, one can set up a iterative method that can compute ρ^{n+1} from ϕ^{n+1}. By Lemma 3.2.1, ρ^{n+1} and $\mathbf{J}^{n+1}$ will satisfy (3.13) because ϕ^{n+1} and $\mathbf{A}^{n+1}$ satisfy (4.48). Doing so would allow the use of analytical derivatives for ϕ^{n+1}, as in 2.2.4, in the particle update and would be useful in exploring problems with geometry. This will be explored in future work.

3.3.4 Summary

In this section, we presented gauge-conserving maps that use Theorem 3.2.1 in a direct manner to enforce the Lorenz gauge in the semi-discrete sense. The first map computes the current density $\mathbf{J}^{n+1}$ using a standard bilinear map, then computes ρ^{n+1} as the solution of a semi-discrete continuity equation. A Lagrange multiplier was also used to make certain that the continuity equation was enforced globally, though numerical experiments suggest this may not be necessary. The second map we proposed is based on the multi-dimensional Green's function and is well-suited for solvers that leverage a boundary integral formulation, and will be investigated in future work. These maps, which are based on semi-discrete theory, do not account for errors introduced by the spatial discretization. Additionally, we introduced a third approach which identifies a correction to ϕ based on the discrete gauge condition. The changes made to Algorithm 3.1 for all three methods are summarized in Table 3.1. In the next section, we investigate the capabilities of the first and third methods in problems defined on periodic domains. We note that in all cases, developing appropriate boundary conditions for bounded domains for inflow and outflow of charge that is consistent with gauge preservation is the next important step, and this will be the subject of future work.

3.4 Numerical Results

This section contains the numerical results for the PIC method using the exact and approximate methods to enforce the Lorenz gauge condition. We consider two different test problems with dynamic and steady state qualities. We first consider the Weibel instability, which is a streaming

Method	Summary of Changes	Label
Baseline method from Chapter 2	-	Bilinear Map
Numerical Derivatives FFT (or FD6)	Lines 5 and 8	Charge Conserving, FFT (or FD6)
Multi-dimensional Boundary Integral	Lines ~~6~~, 7, and 8	-
Gauge correction for ϕ	Correct ϕ after Line 8	Gauge Correcting

Table 3.1 A summary of the methods considered in this paper. We use the method from our previous work Chapter 2 as the baseline method in addition to three new methods. In each case, we provide a summary of changes to Algorithm 3.1 required to implement the methods as well as the corresponding label used to refer to each approach in the numerical results. Note that the multi-dimensional boundary integral method is not given a label because it is not considered in the numerical results.

instability that occurs in a periodic domain. The second example we consider is a simulation of a non-relativistic drifting cloud of electrons against a stationary cluster of ions. In each example, we compare the performance of the different methods by inspecting the fully discrete Lorenz gauge condition and monitoring its behavior as a function of time. We conclude the section by summarizing the key results of the experiments.

3.4.1 Relativistic Weibel Instability

The Weibel instability [280] is a type of streaming instability resulting from an anistropic distribution of momenta, which is prevalent in many applications of high-energy-density physics including astrophysical plasmas [281] and fusion applications [282]. In such circumstances, the momenta in different directions can vary by several orders of magnitude. Initially, the strong currents generated from the momenta create filament-like structures that eventually interact due to the growth in the magnetic field. Over time, the magnetic field can become quite turbulent, and the currents self-organize into larger connected networks. During this self-organization phase, there is an energy conversion mechanism that transfers the kinetic energy from the plasma into the magnetic field, which attempts to make the distribution of momenta more isotropic. The resulting instability creates the formation of magnetic islands and other structures which store massive amounts of energy. In such highly turbulent regions, this can lead to the emergence of other plasma phenomena such as magnetic reconnection, in which energy is released from the fields back into the plasma [283].

The setup for this test problem can be described as follows. The domain for the problem is a

periodic box defined on $[-L_x/2, L_x/2] \times [-L_y/2, L_y/2]$ in units of the electron skin depth c/ω_{pe}. The particular values of L_x and L_y are carefully chosen using the dispersion relation and will be specified later. Here, c is the speed of light and ω_{pe} is the electron angular plasma frequency. The system being modeled consists of two groups of infinite counter-propagating sheets of electrons and a uniform background of stationary ions. The electrons in each group are prescribed momenta from the ‘‘waterbag" distribution

$$f(\mathbf{P}) = \frac{1}{2P_\parallel}\delta\left(P^{(1)} - P_\perp\right)\left[\Theta\left(P^{(2)} - P_\parallel\right) - \Theta\left(P^{(2)} + P_\parallel\right)\right], \tag{3.28}$$

where $\Theta(x)$ is the unit step function, and we choose $P_\perp > P_\parallel > 0$ to induce an instability. Along the x direction, electrons are prescribed only a drift corresponding to $P_\perp$, and are linearly spaced in the interval $[-P_\parallel, P_\parallel)$ in the y direction. We make the problem charge neutral by setting the positions of the electrons to be equal to the ions. Electrons belonging to the first group are initialized according to the distribution (3.28), and those belonging to the second group are defined to be a mirror image (in momenta) of those in the first. This creates a return current that guarantees current neutrality in the initial data. For simplicity, we shall assume that the sheets have the same number density $\bar{n}$, but this is not necessary. In fact, some earlier studies explored the structure of the instability for interacting streams with different densities and drift velocities [284]. The particular values of the plasma parameters used in this experiment are summarized in Table 3.2. We remark that during the initialization phase of our implementation, we prescribe the velocities of the particles and then convert them to conjugate momenta using $\mathbf{P}_i = \gamma m_i \mathbf{v}_i$, since $\mathbf{A} = 0$ at the initial time. The electron velocities used to construct the distribution (3.28) are equivalently given in units of c by $v_\perp = 1/2$ and $v_\parallel = 1/100$. When these values are converted to conjugate momenta, we obtain $P_\perp \approx 5.773888 \times 10^{-1}$ and $P_\parallel \approx 1.154778 \times 10^{-2}$, respectively, which are given in units of $m_e c$. Lastly, we note that the normalized permittivity and normalized permeability are given by $\sigma_1 = \sigma_2 = 1$, and the normalized speed of light is $\kappa = 1$.

In other papers, which numerically simulate the Weibel instability, e.g., [284, 120, 88], the particle velocities are obtained using specialized sampling methods that mitigate the effects of noise in the starting distribution. As pointed out in [88], this can lead to electrostatic effects, such as

Parameter	Value
Average number density ($\bar{n}$) [m^{-3}]	1.0×10^{10}
Average electron temperature ($\bar{T}$) [K]	1.0×10^{4}
Electron angular plasma period (ω_{pe}^{-1}) [s/rad]	1.772688×10^{-7}
Electron skin depth (c/ω_{pe}) [m]	5.314386×10^{1}
Electron drift velocity in x ($v_\perp$) [m/s]	$c/2$
Maximum electron velocity in y ($v_\parallel$) [m/s]	$c/100$

Table 3.2 Plasma parameters used in the simulation of the Weibel instability. All simulation particles are prescribed a drift velocity corresponding to $v_\perp$ in the x direction while the y component of their velocities are sampled from a uniform distribution scaled to the interval $[-v_\parallel, v_\parallel)$.

Landau damping, which will alter the growth of the instability. This motivates the consideration of the distribution (3.28), as it is easy to compare with theory and control effects from sampling noise. For such distributions, the growth rate in the magnetic field can be calculated from the dispersion relation [285]

$$1 - \frac{c^2 k_\parallel^2}{\omega^2} - \frac{\omega_{pe}^2}{\omega^2 \gamma}\left[G(\beta_\parallel) + \frac{\beta_\perp^2}{2\left(1-\beta_\parallel^2\right)}\left(\frac{c^2 k_\parallel^2 - \omega^2}{\omega^2 - c^2 k_\parallel^2 \beta_\parallel^2}\right)\right] = 0.$$

Here, $k_\parallel$ is the wavenumber in the y direction, ω_{pe} is the electron plasma frequency and

$$\gamma := \sqrt{1 + \frac{P_\perp^2}{m_e^2 c^2} + \frac{P_\parallel^2}{m_e^2 c^2}}, \quad \beta_\perp := \frac{P_\perp}{\gamma m_e c}, \quad \beta_\parallel := \frac{P_\parallel}{\gamma m_e c}, \quad G(\beta_\parallel) := \frac{1}{2\beta_\parallel}\ln\left(\frac{1+\beta_\parallel}{1-\beta_\parallel}\right),$$

with m_e being the electron mass. In particular, Yoon and Davidson [285] showed that an instability occurs if and only if the condition

$$\frac{\beta_\perp^2}{2\beta_\parallel^2} > (1-\beta_\parallel)\, G(\beta_\parallel),$$

is satisfied, and that its corresponding growth rate can be directly calculated using the equation

$$\mathrm{Im}(\omega) = \frac{1}{\sqrt{2}}\left[\left(W_1^2 + W_2\right)^{1/2} - W_1\right]^{1/2}, \tag{3.29}$$

where we have introduced the definitions

$$W_1 := c^2 k_\parallel^2 \beta_\parallel^2 + \frac{\omega_{pe}^2 \beta_\perp^2}{2\gamma\beta_\parallel^2} - c^2\left(k_0^2 - k_\parallel^2\right), \quad W_2 := 4c^4 k_\parallel^2 \beta_\parallel^2\left(k_0^2 - k_\parallel^2\right),$$

$$k_0 := \frac{\omega_{pe}^2}{\gamma c^2}\left(\frac{\beta_\perp^2}{2\beta_\parallel^2\left(1-\beta_\parallel^2\right)} - G(\beta_\parallel)\right).$$

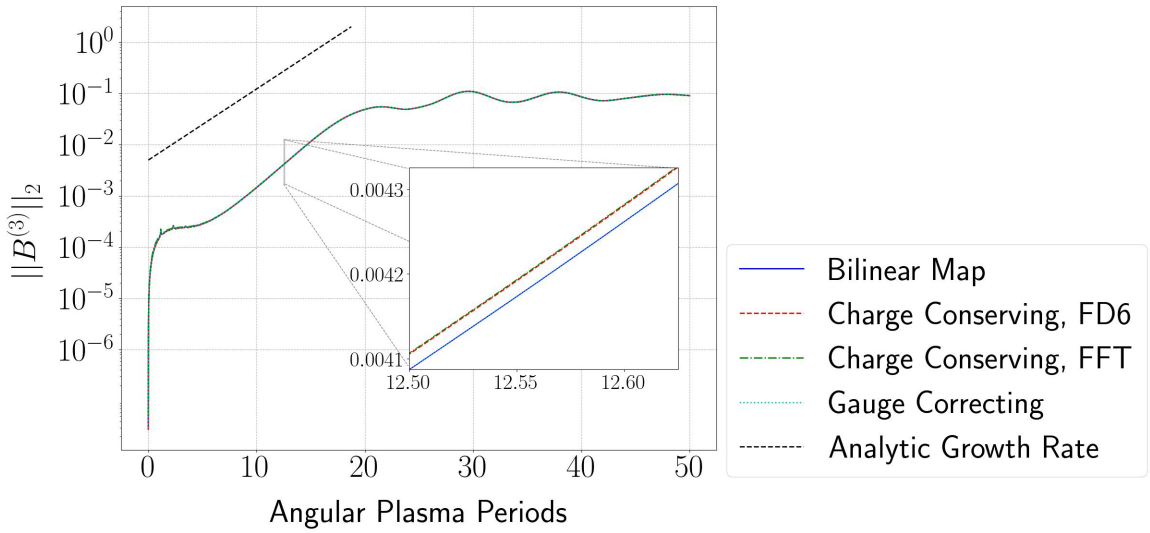

Figure 3.1 Growth in the magnetic field energy for the Weibel instability. We compare the growth rate in the ℓ_2-norm of the magnetic field $B^{(3)}$ for different methods against an analytical growth rate predicted from linear response theory [285]. The analytical growth rate for this configuration is determined to be $\mathrm{Im}(\omega) \approx 0.319734$. We observe good agreement with the theoretically predicted growth rate for each of the methods.

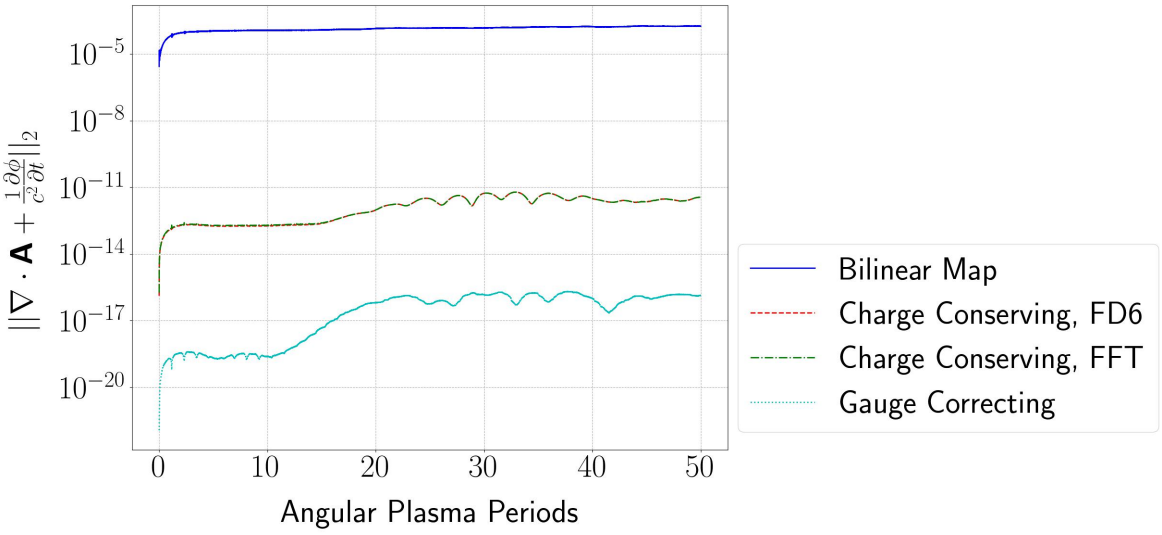

Figure 3.2 The gauge error for the different methods applied to the Weibel instability test problem. Naive interpolation introduces significant gauge error, whereas the maps based on the continuity equation or gauge correction result in substantial improvement. It should be noted that while FFT and FD6 appear identical, they differ by $O(10^{-14})$. The gauge-correcting approach produced the smallest gauge error among the methods we considered.

Finally, we remark that the range of admissible values of $k_\parallel$ for the instability is $0 < k_\parallel^2 < k_0^2$.

Using the parameters derived from Table 3.2 in an appropriately rescaled equation of the growth rate (3.29), we find the value of $k_\parallel$ that achieves the maximum growth is $k_\parallel \approx 5.445191$. Based on

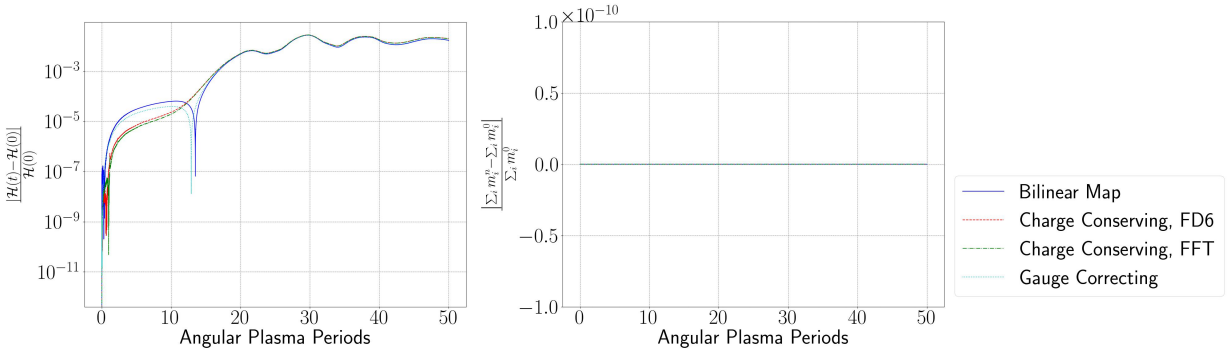

(a) Relative Energy Error

(b) Relative Mass Error

Figure 3.3 The relative energy error for the different methods applied to the Weibel instability test problem. All methods show reasonably good energy conservation, though far from machine precision, and the total mass is conserved in each approach. It is worth noting that that the start the two charge-conserving methods do a slightly better job at preserving energy than the bilinear map or gauge-correcting method, though all end up in the same order of accuracy.

this value, we scale the size of the (normalized) simulation domain so that $L_x = L_y = 1.153896$ in units of c/ω_{pe}. The corresponding theoretical growth rate in the magnetic field associated with this problem is $\mathrm{Im}(\omega) \approx 0.319734$. We ran the simulation to a final time of $T = 50$ in units of ω_{pe}^{-1} with a 128×128 mesh. The total number of simulation particles used in the experiment was set to 1×10^6 and was split equally between ions and electrons. Each electron group, therefore, consists of 2.5×10^5 particles, and the number of particles per cell was approximately 61. In Figure 3.1, we compare the growth rates in the ℓ_2-norm of the magnetic field $B^{(3)}$ obtained with different methods. We find that each of the methods, including the naive approach, show good agreement with the theoretical growth rate predicted from equation (3.29). Additionally in Figure 3.2, we plot the error in the gauge condition obtained with each of the methods, as well as the relative error in energy and mass in Figure 3.3. The naive approach, which uses bilinear maps for the charge and current densities introduces significant gauge error and increases over time. In contrast, the maps which use either the continuity equation or the gauge correction technique show significant improvement in reducing these errors when compared to the naive implementation. Most notably, the gauge correction technique ensures the satisfaction of the gauge condition at the level of machine precision. All methods conserve energy with roughly the same accuracy and mass is conserved exactly. It is worth noting that the two charge-conserving methods conserve energy slightly better during the initial

period of growth, though all show similar deviations in energy at the end of the simulation. While all methods conserve charge globally, only the hybrid FFT, FD6, and gauge-correcting methods conserve charge in a local sense.

3.4.2 Drifting Cloud of Electrons

Given the task of minimizing the gauge error, a test problem that tends to have a high gauge error was needed. When charged particles move through neutral space, the system is prone to gauge errors unless properly managed. As such, we take a periodic domain and induce a potential well by placing a grouping of ions, which are normally distributed with a standard deviation of $1/100$ of the domain length, in space and stationary, at its center. The electrons are given an identical distribution in space, but are given a drift velocity equal to $c/100$. With such a drift, the electrons are able to escape the potential well created by the ions and move throughout the domain (see Figure 3.4). The domain, itself, is a periodic square $[-1/2, 1/2]^2$ given in units of λ_D, and we run the simulation to a final time of $T = 1/2$ in units of ω_{pe}^{-1}. The specific values for the simulation parameters used in our experiment are specified in Table 3.3. The normalized permittivity and normalized permeability are given by $\sigma_1 = 1$ and $\sigma_2 = 1.686555 \times 10^{-6}$, respectively, and the normalized speed of light is $\kappa = 7.700159 \times 10^2$.

Parameter	**Value**
Average number density ($\bar{n}$) [m^{-3}]	1.0×10^{13}
Average electron temperature ($\bar{T}$) [K]	1.0×10^4
Debye length (λ_D) [m]	2.182496×10^{-3}
Electron angular plasma period (ω_{pe}^{-1}) [s/rad]	5.605733×10^{-9}
Electron drift velocity ($v_d^{(1)} = v_d^{(2)}$) [m/s]	$c/100$
Electron thermal velocity ($v_{th} = \lambda_D \omega_{pe}$) [m/s]	3.893328×10^5

Table 3.3 Plasma parameters used in the simulation of the drifting cloud of electrons.

In Figure 3.5, we plot the relative errors for conservation of total energy and total mass for different methods using a 64×64 grid. It is noteworthy that the relative energy error is superior to that of the Weibel instability problem, though both are above machine precision. It is worth considering that the relative energy error of the Weibel instability plateaus alongside the magnetic

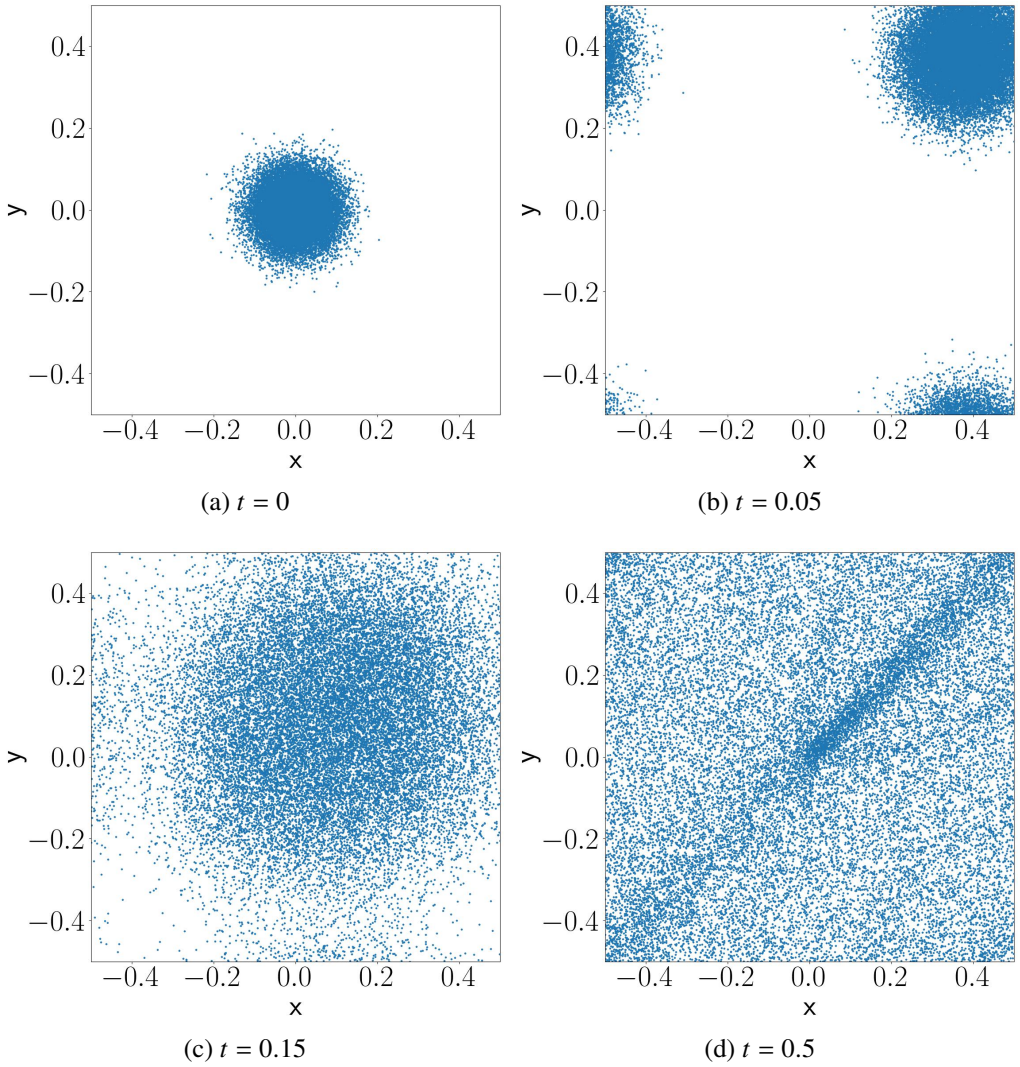

(a) $t = 0$ (b) $t = 0.05$

(c) $t = 0.15$ (d) $t = 0.5$

Figure 3.4 A Maxwellian distribution of electrons and ions are placed on a periodic domain. The electrons are given a thermal velocity in addition to a drift velocity $\mathbf{v}_d = (v_d^{(1)}, v_d^{(2)})^T$, where $v^{(1)} = v^{(2)} = c/100$, that is the speed is $\|\mathbf{v}_d\| = \sqrt{2}c/100$. We see the particles escape the well only to fall back in later. By $t = 0.15$ the electrons, beginning their second such traversal, have become quite dispersed throughout the domain, though the remnants of the original drift velocity can be found in a slight beam along the diagonal ($t = 0.5$).

magnitude, stabilizing at approximately $t = 0.20$ plasma periods, whereas the relative energy error of the moving cloud stays in the range of $O(10^{-10})$ throughout. Again, all methods globally conserve the total mass.

In Figure 3.6, we plot the gauge error for the drifting cloud problem and compare the proposed methods against a naive implementation that uses bilinear maps for both the charge density and

current density. In each of the methods, we examined the gauge error on spatial meshes with different resolution, with the coarsest mesh being 16×16 and the finest being 64×64. Aside from the naive approach, we note that the gauge error for a given method increases proportionally with the resolution of the spatial discretization. One explanation for this is that coarser spatial discretizations are less likely to resolve the gauge error, which is generally small, compared to more refined meshes. Using bilinear interpolation for both the charge density and current density results in a gauge error that starts at $O\left(10^{-5}\right)$ and quickly shrinks to $O\left(10^{-7}\right)$. On the other hand, we find that using a continuity equation to define the charge density, in combination with a bilinear mapping for the current density, results in a much lower error which is $O\left(10^{-13}\right)$. This is true for methods which compute the numerical derivatives using either the FFT or the FD6 method. We remark that the method used for differentiation must be identical to the one used for the potentials, following the discussion in section 3.3.1.1. In practice, solving the system with this technique results in an accumulation of error that is close to machine precision, yielding $O(10^{-13})$ accuracy. The gauge correction technique, on the other hand, does not accumulate this error, so we observe a much smaller error of $O(10^{-18})$.

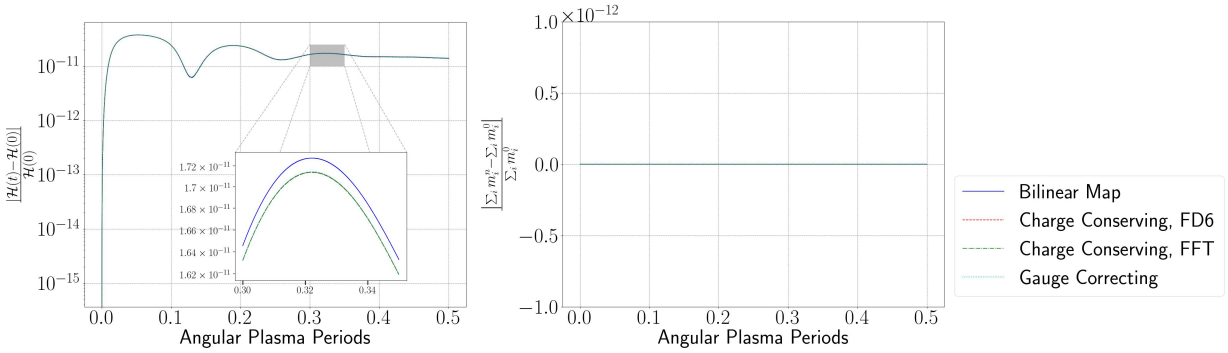

(a) Relative Energy Error

(b) Relative Mass Error

Figure 3.5 The relative energy error for the different methods applied to the Moving Cloud test problem along with the relative mass error. Both of these plots are for a simulation with a 64×64 grid. The relative energy error is significantly better than that found in the Weibel instability, and like the Weibel instability, the relative mass error is zero throughout.

3.5 Conclusion

This chapter constitutes a tactical step backwards from the remarkable method of Chapter 2. We now, akin to the Yee grid, automatically satisfy the semi-discrete Lorenz gauge and Gauss's law by

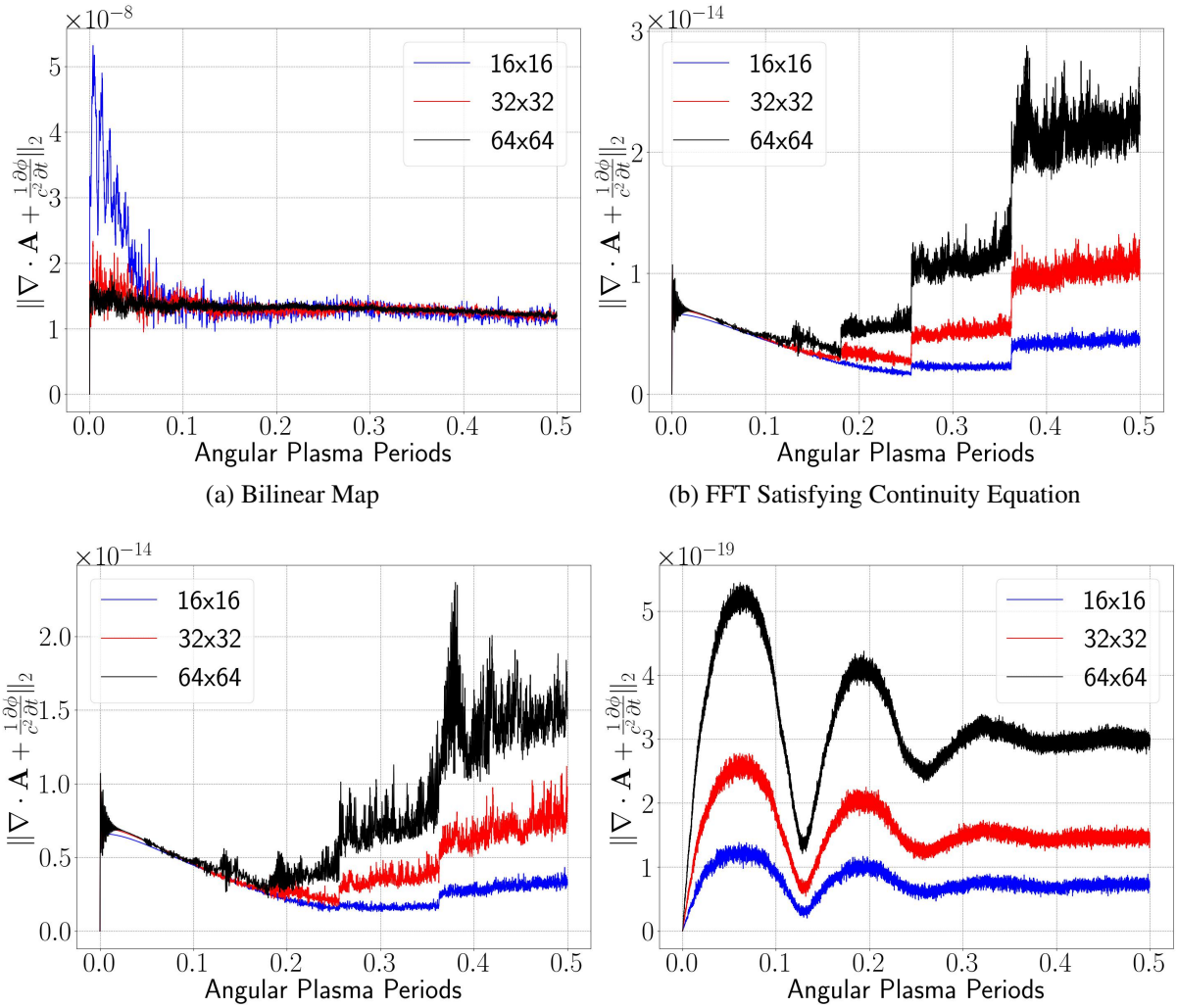

(a) Bilinear Map

(b) FFT Satisfying Continuity Equation

(c) FD6 Satisfying Continuity Equation

(d) Gauge-correcting

Figure 3.6 The gauge error of a cloud of electrons drifting into and out of a potential well. Naively interpolated such that the charge and current densities are not consistent, we see a significant gauge error. However, if the charge density is computed from the current density using the continuity equation and a high order method (eg FFT) to compute the divergence of $\mathbf{J}$, we see a much better gauge error over time.

simply satisfying the semi-discrete continuity equation, but at the cost of the geometric flexibility that comes with the Green's function solvers. The next chapter is concerned with generalizing this result to a variety of time discretizations. Once this is established, we will be fully regrouped, and may consider how to retake the ground of geometry and boundaries.

CHAPTER 4

GENERALIZATION

The exploration in Chapter 3 was done entirely using a first-order BDF time discretization method for the fields. In this chapter we seek to achieve higher-order temporal accuracy using a variety of techniques, including BDF methods, central discretizations, and diagonally implicit Runge-Kutta (DIRK) methods, and we prove that many of these methods satisfy the same properties established in Section 3.2. For the general BDF and central difference methods, this will be fully achieved. For the DIRK methods, we will prove that charge conservation implies satisfaction of the Lorenz gauge. We will additionally establish that the two-stage method holds in the other direction, suggesting that higher-order DIRK methods will also satisfy this property.

Our primary objective in this work is to prove the time-consistency property for a family of wave solvers. As such, we restrict ourselves to problems with periodic boundary conditions, which allows us to use a spectral discretization that can be rapidly evaluated using the FFT rather than the fast convolution operator considered in Chapter 2. Additionally, the restriction to periodic boundary conditions allows us to utilize high-order particle interpolation schemes, as is commonly done with high order non-diffusive wave solvers [286, 287, 288, 289]. All wave solvers we implement will be fully-implicit, with the source term $\mathbf{J}^{n+1}$ being computed using an updated particle location $\mathbf{x}^{n+1}$ and old velocity $\mathbf{v}^n$.

The remainder of the chapter is structured as follows. Section 4.1 gives a brief review of the problem formulation for convenience. More details may be found in Section 1.3. More attention will be paid to the various wave solvers we employ and proofs of the aforementioned properties in Section 4.2, which occupies the bulk of the chapter. The particle method has already been discussed in detail in Section 2.3.1.2, as such we will leave that out for brevity. Section 4.3 will present the numerical experiments confirming our findings, concentrating on the same periodic problems as in Section 3.4, and finally Section 4.4 will wrap things up with some concluding remarks. This chapter is based on the work submitted by myself in collaboration with Dr. Andrew Christlieb and Dr. William Sands [4]. My contribution in this work was the generalization of the theorems

presented in Chapter 3 to BDF-k methods, DIRK-s methods, and the Adams-Bashforth methods, as well as the implementation of all the code.

4.1 Problem Review

To prevent the hassle of flipping back and forth between chapters to look up equations, here we once more list out the equations with which we will be working. From Section 1.3.3 we know Maxwell's equations under the Lorenz gauge become

$$\begin{cases} \dfrac{1}{c^2}\dfrac{\partial^2\phi}{\partial t^2} - \Delta\phi = \dfrac{\rho}{\epsilon_0}, & (4.1) \\ \dfrac{1}{c^2}\dfrac{\partial^2\mathbf{A}}{\partial t^2} - \Delta\mathbf{A} = \mu_0\mathbf{J}, & (4.2) \\ \dfrac{1}{c^2}\dfrac{\partial\phi}{\partial t} + \nabla\cdot\mathbf{A} = 0. & (4.3) \end{cases}$$

Charge should be conserved, codified in the continuity equation

$$\frac{\partial\rho}{\partial t} + \nabla\cdot\mathbf{J} = 0. \tag{4.4}$$

The involutions of Maxwell's equations are Gauss's laws:

$$\begin{cases} \nabla\cdot\mathbf{E} = \dfrac{\rho}{\epsilon_0}, & (4.5) \\ \nabla\cdot\mathbf{B} = 0. & (4.6) \end{cases}$$

From Section 1.3.4 we know the particle equations of motion under the Lorenz gauge become

$$\begin{cases} \dfrac{d\mathbf{x}_i}{dt} = \dfrac{1}{\gamma_i m_i}\left(\mathbf{P}_i - q\mathbf{A}_i\right), & (4.7) \\ \dfrac{d\mathbf{P}_i}{dt} = q_i\left(-\nabla\phi + \dfrac{1}{\gamma_i m_i}\left(\nabla\mathbf{A}\right)\cdot\left(\mathbf{P}_i - q_i\mathbf{A}\right)\right). & (4.8) \end{cases}$$

The nondimensionalization of these equations may be found in Appendix A.

The particle motion will be accomplished by the Improved Asymmetrical Euler Method, described in Section 2.3. It is in solving the wave equations while enforcing the Lorenz gauge via conserving charge that we have interest. The precedent was set in Section 3.2, we now move to generalize.

4.2 Generalizing the Properties

This section is concerned with generalizing the theorems proven in Section 3.2.1.1 to a variety of time discretizations. First, in Section 4.2.1 we generalize from BDF-1 to BDF-k. In Section 4.2.2 we extend to a family of time centered second order discretizations. In Section 4.2.3 we extend this to s-stage Adams-Bashforth methods. Finally, in Section 4.2.4 we partially extend this to s-stage DIRK methods.

4.2.1 The General Semi-Discrete Formulation for BDF Methods Under the Lorenz Gauge

In Section 3.2.1, we introduced a lemma and two theorems that showcased properties associated with the first-order BDF method in a semi-discrete setting. That is, conservation of charge is satisfied if and only if the semi-discrete Lorenz gauge condition is satisfied, and that Gauss's law for electricity is satisfied if said gauge condition is. In this section, we generalize these properties to any BDF methods constructed with uniform step sizes. Vital to the original is the consistent nature of the temporal derivatives, that is, applying the first order derivative BDF method twice results in the second order derivative BDF method in the sense that $D_t[D_t[\cdot]] = D_t^2[\cdot]$; the generalization will also take advantage of this. We start with a time-consistent k-step BDF formulation

$$\frac{du}{dt} = \frac{1}{\Delta t}\sum_{i=n-k}^{n} a_{n-i}u^i + O(\Delta t^p), \tag{4.9}$$

$$\frac{d^2u}{dt^2} = \frac{1}{\Delta t^2}\sum_{i=n-k}^{n} a_{n-i}\sum_{j=i-k}^{i} a_{i-j}u^j + O(\Delta t^p). \tag{4.10}$$

Note that BDF-1 through BDF-6 have this form.

For purposes of bookkeeping later on, we now prove a lemma regarding the structure of the coefficients in the method, which, absorbing the Δt terms into the coefficients, we write as

$$\sum_{i=n-k}^{n} a_{n-i}\sum_{j=i-k}^{i} a_{i-j}u^j \equiv \sum_{i=n-2k}^{n} C_i u^i. \tag{4.11}$$

This term arises in the right hand side of the implicit solution to semi-discrete Maxwell's equations. It is important that we sort out this term first, as it is embedded inside of other backwards differences we encounter when doing the constructive proof for the theorems regarding preservation of the gauge condition, continuity equation, and Gauss's law.

Lemma 4.2.1. *We consider the BDF-k method applied to u^n twice:*

$$\sum_{i=n-k}^{n} a_{n-i} \sum_{j=i-k}^{i} a_{i-j} u^j. \tag{4.12}$$

Considering (4.11)*, the coefficient C_i for a term u^i at the corresponding $(n-i)$th time level below n takes the form*

$$C_i \coloneqq \begin{cases} \sum\limits_{j=0}^{n-i} a_j a_{n-i-j}, & n-i \le k, \\ \sum\limits_{j=0}^{2k-(n-i)} a_{k-j} a_{n-i-k+j}, & n-i > k. \end{cases} \tag{4.13}$$

Proof. We prove by induction. The base case $k = 1$ results in the sum

$$a_0 a_0 u^n + (a_0 a_1 + a_1 a_0) u^{n-1} + a_1 a_1 u^{n-2}. \tag{4.14}$$

This clearly has the form given in equation (4.13).

For the inductive step, we assume the hypothesis is true for $k \le m$. Next, let us consider $k = m+1$ for which we have the summation

$$\sum_{j=n-(m+1)}^{n} a_{n-j} \sum_{\ell=j-(m+1)}^{j} a_{j-\ell} u^{\ell}. \tag{4.15}$$

We can easily peel the outer $(m+1)$-th term out, which gives

$$\left(\sum_{j=n-m}^{n} a_{n-j} \sum_{\ell=j-(m+1)}^{j} a_{j-\ell} u^{\ell} \right) + \left(a_{m+1} \sum_{j=n-2(m+1)}^{n-(m+1)} a_{n-(m+1)-j} u^j \right). \tag{4.16}$$

Similarly, we then peel the inner $(m+1)$-th term out to obtain

$$\left(\sum_{j=n-m}^{n} a_{n-j} \sum_{\ell=j-m}^{j} a_{j-\ell} u^{\ell} \right) + \left(a_{m+1} \sum_{j=n-2(m+1)}^{n-(m+1)} a_{n-(m+1)-j} u^j \right) + \left(a_{m+1} \sum_{j=n-m}^{n} a_{n-j} u^{j-(m+1)} \right). \tag{4.17}$$

To prove the lemma, we must consider three cases, namely, $n - i < m + 1$, $n - i = m + 1$, and $n - i > m + 1$.

Consider C_i for $n - i < m + 1$. We know from the inductive hypothesis that the first nested sum is equal to

$$\sum_{\substack{j=0 \\ n-i<m+1}}^{n-i} a_j a_{n-i-j}.$$

The second summation contains u^j for $n - 2(m+1) \leq j \leq n - (m+1)$. Since $n - (m+1) < i$, this summation cannot contain u^i. The third summation contains u^j for $n - m \leq j \leq n$, and therefore contains u^i when $j - (m+1) = i$, or $j = i + (m+1)$. So

$$\begin{aligned} C_i &= \sum_{\substack{j=0 \\ n-i<m+1}}^{n-i} a_j a_{n-i-j} + a_{n-i-(m+1)} a_{m+1}, \\ &= \sum_{j=0}^{n-i} a_j a_{n-i-j}. \end{aligned}$$

Next, consider C_i for $n - i = m + 1$. Again, from the inductive hypothesis, the first nested sum is equal to

$$\sum_{\substack{j=0 \\ n-i<m+1}}^{n-i} a_j a_{n-i-j}.$$

In the second summation, the term containing u^i occurs when $j = i$ or $j = n - (m+1)$. Therefore, the coefficients in second sum reduce to

$$a_{m+1} \sum_{j=n-2(m+1)}^{n-(m+1)} a_{n-(m+1)-j} = a_{m+1} a_0.$$

Similar, we find that the terms containing u^i in third summation reduce to

$$\sum_{j=n-m}^{n} a_{n-j} a_{m+1} u^{j-(m+1)} = a_0 a_{m+1}.$$

Combining these terms, we find that this is equivalent to

$$\begin{aligned} C_i &= \sum_{\substack{j=0 \\ n-i<m+1}}^{n-i} a_j a_{n-i-j} + a_{m+1} a_0 + a_0 a_{m+1}, \\ &= \sum_{j=0}^{n-i} a_j a_{n-i-j}, \end{aligned}$$

when $n - i = m + 1$.

Consider C_i for $n - i > k = m + 1$. We know from the inductive hypothesis that the first nested sum is equal to $\sum_{j=0}^{2m-(n-i)} a_{m-j} a_{n-i-m+j}$ for $n - i \geq m$. We can adjust this index by one without any change to the actual value:

i	$n-i$	C_i
n	0	a_0a_0
$n-1$	1	$a_1a_0 + a_0a_1$
$n-2$	2	$a_2a_0 + a_1a_1 + a_0a_2$
$\vdots$	$\vdots$	$\vdots$
$n-k$	k	$a_ka_0 + a_{k-1}a_1 + \cdots + a_1a_{k-1} + a_0a_k$
$\vdots$	$\vdots$	$\vdots$
$n-2k+1$	$2k-1$	$a_{k-1}a_k + a_ka_{k-1}$
$n-2k$	$2k$	a_ka_k

Table 4.1 Table of coefficients for ith time level of the kth order Backward Difference method for timestep n.

$$\sum_{j=0}^{2m-(n-i)} a_{m-j}a_{n-i-m+j} = \sum_{j=1}^{2m-(n-i)+1} a_{m+1-j}a_{n-i-(m+1)+j} \tag{4.18}$$

Given $i < n-k = n-(m+1)$, we know the corresponding u^j term is in both the second and third summation term and have the coefficients $a_{m+1}a_{n-(m+1)-i}$ and $a_{m+1}a_{n-i-(m+1)}$, respectively. The former corresponds to $a_{m+1-j}a_{n-i-(m+1)+j}$ for $j = 2(m+1)-(n-i)$, the latter corresponds to $j = 0$. We thus fill in our summation and see

$$C_i = \sum_{j=0}^{2(m+1)-(n-i)} a_{m+1-j}a_{n-i-(m+1)+j}. \tag{4.19}$$

In all cases we see the nested sum takes the following structure.

$$C_i \coloneqq \begin{cases} \sum_{j=0}^{n-i} a_j a_{n-i-j}, n-i \leq k, \\ \sum_{j=0}^{2k-(n-i)} a_{k-j}a_{n-i-k+j}, n-i > k. \end{cases} \tag{4.20}$$

The base case and inductive step have been demonstrated, completing the proof. QED

An immediate consequence is the following corollary:

Corollary 4.2.1. *The following identity holds:*

$$\sum_{i=n-k}^{n-1} a_{n-i} \sum_{j=i-k}^{i} a_{i-j}u^j + a_0 \sum_{i-n-k}^{n-1} a_{n-i}u^i = \sum_{i=n-2k}^{n-1} C_i u^i. \tag{4.21}$$

Proof. From Lemma 4.2.1 we know

$$\begin{aligned}\sum_{i=n-2k}^{n} C_i &= \sum_{i=n-k}^{n} a_{n-i} \sum_{j=i-k}^{i} a_{i-j} u^j \\ &= \sum_{i=n-k}^{n-1} a_{n-i} \sum_{j=i-k}^{i} a_{i-j} u^j + a_0 \sum_{j=i-k}^{n-1} a_{i-j} u^j + a_0 a_0 u^n.\end{aligned} \tag{4.22}$$

Subtracting $a_0 a_0 u^n \equiv C_n u^n$ from each side demonstrates the identity, concluding the proof. QED

Applying a general backward difference method equations to the vector potential, scalar potential, gauge condition and continuity equation yields:

$$\frac{1}{\Delta c^2}\frac{1}{\Delta t^2} \sum_{i=n-k}^{n} a_{n-i} \sum_{j=i-k}^{i} a_{i-j} \phi^j - \Delta \phi^n = \frac{\rho^n}{\epsilon_0}, \tag{4.23}$$

$$\frac{1}{\Delta c^2}\frac{1}{\Delta t^2} \sum_{i=n-k}^{n} a_{n-i} \sum_{j=i-k}^{i} a_{i-j} \mathbf{A}^j - \Delta \mathbf{A}^n = \mu_0 \mathbf{J}^n, \tag{4.24}$$

$$\frac{1}{c^2}\frac{1}{\Delta t} \sum_{i=n-k}^{n} a_{n-i} \phi^i + \nabla \cdot \mathbf{A}^n = 0, \tag{4.25}$$

$$\frac{1}{\Delta t} \sum_{i=n-k}^{n} a_{n-i} \rho^i + \nabla \cdot \mathbf{J}^n = 0. \tag{4.26}$$

where here we assume $\mathbf{J}^n$ is given and compute ρ^n and the fields for the particle update. Additionally, we define the residuals

$$\epsilon_1^n \coloneqq \frac{1}{c^2}\frac{1}{\Delta t} \sum_{i=n-k}^{n} a_{n-i} \phi^i + \nabla \cdot \mathbf{A}^n, \tag{4.27}$$

$$\epsilon_2^n \coloneqq \frac{1}{\Delta t} \sum_{i=n-k}^{n} a_{n-i} \rho^i + \nabla \cdot \mathbf{J}^n. \tag{4.28}$$

We now prove an additional lemma which will link the residuals of the semi-discrete continuity equation and semi-discrete gauge condition.

Lemma 4.2.2. *In the system* (4.23) - (4.24)*, the residual ϵ_1^n is a linear combination of ϵ_2^n and ϵ_2^i, where $n - 2k \leq i < n$.*

Proof. From (4.23) and (4.24), we get the update schemes

$$\phi^n = \mathcal{L}^{-1}\left[\frac{1}{\alpha^2}\frac{\rho^n}{\epsilon_0} - \sum_{i=n-k}^{n-1} a_{n-i} \sum_{j=i-k}^{i} a_{i-j}\phi^j - a_0 \sum_{i=n-k}^{n-1} a_{n-i}\phi^i\right], \tag{4.29}$$

$$\mathbf{A}^n = \mathcal{L}^{-1}\left[\frac{1}{\alpha^2}\frac{\rho^n}{\epsilon_0} - \sum_{i=n-k}^{n-1} a_{n-i} \sum_{j=i-k}^{i} a_{i-j}\mathbf{A}^j - a_0 \sum_{i=n-k}^{n-1} a_{n-i}\mathbf{A}^i\right]. \tag{4.30}$$

We plug these into the definition of ϵ_1^n, (4.27), and see

$$\begin{aligned}
\epsilon_1^n &= \frac{1}{c^2}\frac{1}{\Delta t}\sum_{i=n-k}^{n} a_{n-i}\phi^i + \nabla\cdot\mathbf{A}^n \\
&= \frac{1}{c^2}\frac{1}{\Delta t}\sum_{i=n-k}^{n} a_{n-i}\mathcal{L}^{-1}\left[\frac{1}{\alpha^2}\frac{\rho^i}{\epsilon_0} - \sum_{j=i-k}^{i-1} a_{i-j}\sum_{l=j-k}^{j} a_{j-l}\phi^l - a_0\sum_{j=i-k}^{i-1} a_{i-j}\phi^j\right] \\
&+ \mathcal{L}^{-1}\left[\frac{\mu_0}{\alpha^2}\mathbf{J}^n - \sum_{i=n-k}^{n-1} a_{n-i}\sum_{j=i-k}^{i} a_{i-j}\nabla\cdot\mathbf{A}^j - a_0\sum_{i=n-k}^{n-1} a_{n-i}\nabla\cdot\mathbf{A}^i\right]
\end{aligned} \tag{4.31}$$

This becomes

$$= \mathcal{L}^{-1}\left[\frac{\mu_0}{\alpha^2}\left(\frac{1}{\Delta t}\sum_{i=n-k}^{n} a_{n-i}\rho^i + \nabla\cdot\mathbf{J}^n\right)\right] \tag{4.32a}$$

$$- \frac{1}{c^2}\frac{1}{\Delta t}\sum_{i=n-k}^{n} a_{n-i}\mathcal{L}^{-1}\left[\sum_{j=i-k}^{i-1} a_{i-j}\sum_{l=j-k}^{j} a_{j-l}\phi^l + a_0\sum_{j=i-k}^{i-1} a_{i-j}\phi^j\right] \tag{4.32b}$$

$$- \mathcal{L}^{-1}\left[\sum_{i=n-k}^{n-1} a_{n-i}\sum_{j=i-k}^{i} a_{i-j}\nabla\cdot\mathbf{A}^i + a_0\sum_{i=n-k}^{n-1} a_{n-i}\nabla\cdot\mathbf{A}^i\right]. \tag{4.32c}$$

The first term is clearly $\mathcal{L}^{-1}\left[\frac{\mu_0}{\alpha^2}\epsilon_2^n\right]$. Disregarding the $\frac{1}{c^2}\frac{1}{\Delta t}$ coefficient and the $\mathcal{L}^{-1}$, we apply

Corollary 4.2.1 to the argument passed to $\mathcal{L}^{-1}$, and, breaking up the outermost summation, we see:

$$\begin{aligned}
&a_0\left(\sum_{j=n-k}^{n-1} a_{n-j}\sum_{l=j-k}^{j} a_{j-l}\phi^l + a_0\sum_{j=n-k}^{n-1} a_{n-j}\phi^j\right)\\
&+a_1\left(\sum_{j=n-k-1}^{n-2} a_{n-1-j}\sum_{l=j-k}^{j} a_{j-l}\phi^l + a_0\sum_{j=n-k-1}^{n-2} a_{n-1-j}\phi^j\right)\\
&+a_2\left(\sum_{j=n-k-2}^{n-3} a_{n-2-j}\sum_{l=j-k}^{j} a_{j-l}\phi^l + a_0\sum_{j=n-k-2}^{n-3} a_{n-2-j}\phi^j\right)\\
&+\cdots\\
&+a_k\left(\sum_{j=n-2k}^{n-k-1} a_{n-k-j}\sum_{l=j-k}^{j} a_{j-l}\phi^l + a_0\sum_{j=n-2k}^{n-k-1} a_{n-k-j}\phi^j\right).
\end{aligned} \tag{4.33}$$

We apply Corollary 4.2.1 to each nested summation, and we see

$$\begin{aligned}
&a_0\left(C_{n-2k}\phi^{n-2k} + C_{n-2k+1}\phi^{n-2k+1} + \cdots + C_{n-k}\phi^{n-k} + \cdots + C_{n-1}\phi^{n-1}\right)\\
&+a_1\left(C_{n-2k}\phi^{n-2k-1} + C_{n-2k+1}\phi^{n-2k} + \cdots + C_{n-k}\phi^{n-k-1} + \cdots + C_{n-1}\phi^{n-2}\right)\\
&+\cdots\\
&+a_k\left(C_{n-2k}\phi^{n-3k} + C_{n-2k+1}\phi^{n-3k+1} + \cdots + C_{n-k}\phi^{n-k-2} + \cdots + C_{n-1}\phi^{n-k}\right)
\end{aligned} \tag{4.34}$$

We then group like terms with like, and find that we have a linear combination of first order BDF-k derivatives.

$$
\begin{aligned}
&C_{n-1}\left(a_0\phi^{n-1}+a_1\phi^{n-2}+\cdots+a_k\phi^{n-k-1}\right)\\
&+C_{n-2}\left(a_0\phi^{n-2}+a_1\phi^{n-3}+\cdots+a_k\phi^{n-k-2}\right)\\
&+\cdots\\
&+C_{n-k+1}\left(a_0\phi^{n-k+1}+a_1\phi^{n-k}+\cdots+a_k\phi^{n-2k+1}\right)\\
&+C_{n-k}\left(a_0\phi^{n-k}+a_1\phi^{n-k-1}+\cdots+a_k\phi^{n-2k}\right)\\
&+C_{n-k-1}\left(a_0\phi^{n-k-1}+a_1\phi^{n-k-2}+\cdots+a_k\phi^{n-2k-1}\right)\\
&+\cdots\\
&+C_{n-2k+1}\left(a_0\phi^{n-2k+1}+a_1\phi^{n-2k}+\cdots+a_k\phi^{n-3k+1}\right)\\
&+C_{n-2k}\left(a_0\phi^{n-2k}+a_1\phi^{n-2k-1}+\cdots+a_k\phi^{n-3k}\right).
\end{aligned}
\tag{4.35}
$$

This may be more compactly written as

$$
\sum_{i=n-2k}^{n-1} C_i \sum_{j=0}^{k} a_j \phi^{i-j} \tag{4.36}
$$

A simpler process of applying Corollary 4.2.1 to the argument in (4.32c), gives similar results:

$$
\sum_{i=n-2k}^{n-1} C_i \nabla \cdot \mathbf{A}^i \tag{4.37}
$$

Multiplying the $\frac{1}{c^2}\frac{1}{\Delta t}$ coefficients we left out from (4.32b) against (4.36), we add this to (4.37) and see (4.32b) + (4.32c) becomes

$$
\mathcal{L}^{-1}\left[\sum_{i=n-2k}^{n-1} C_i\left(\frac{1}{c^2}\frac{1}{\Delta t}\sum_{j=0}^{k}\left(a_j\phi^{i-j}\right)+\nabla\cdot\mathbf{A}^i\right)\right]. \tag{4.38}
$$

This contains the exact definitions for the gauge residuals (4.27), ϵ_1^i. Thus we see combining (4.32a), (4.32b), and (4.32c) yields

$$
\begin{aligned}
&\epsilon_1^n = \mathcal{L}^{-1}\left[\frac{\mu_0}{\alpha^2}\epsilon_2^n+\sum_{i=n-2k}^{n-1} C_i\epsilon_1^i\right],\\
&C_i \coloneqq \begin{cases}\sum_{j=0}^{i} a_j a_{i-j}, i \le k,\\ \sum_{j=0}^{r} a_{k-j}a_{k-r+j}, i > k, r \coloneqq 2k-i.\end{cases}
\end{aligned}
\tag{4.39}
$$

We have demonstrated ϵ_1^n is a linear combination of ϵ_2^n and previous steps of the gauge residual.

QED

Having proven this lemma, we now can prove that any BDF method satisfies the semi-discrete continuity equation satisfies the semi-discrete gauge condition and vice versa.

Theorem 4.2.1. *Under the system* (4.23)-(4.24)*,* (4.26) *is satisfied if* (4.25) *is, and, assuming the initial conditions of* (4.25) *are satisfied,* (4.25) *is satisfied if* (4.26) *is satisfied.*

Proof. Assume (4.25) is satisfied, that is, $\epsilon_1^i = 0 \, \forall \, i$. From Lemma 4.2.2 we have

$$\begin{aligned} \epsilon_1^n &= \mathcal{L}^{-1}\left[\epsilon_2^n + \sum_{i=n-k-1}^{n-1} C_i \epsilon_1^i\right], \\ \implies 0 &= \mathcal{L}^{-1}\left[\epsilon_2^n + \sum_{i=n-k-1}^{n-1} C_i \, (0)\right], \\ \implies 0 &= \mathcal{L}^{-1}\left[\epsilon_2^n\right]. \end{aligned} \tag{4.40}$$

Clearly $\mathcal{L}^{-1}$ is invertible, so $\epsilon_2^n = 0$.

Assume both (4.26) and the initial conditions of (4.25) are satisfied. That is, $\epsilon_2^i = 0 \forall i$ and $\epsilon_1^n = 0$ $\forall \, n \leq 0$. We have

$$\begin{aligned} \epsilon_1^n &= \mathcal{L}^{-1}\left[\epsilon_2^n + \sum_{i=n-k-1}^{n-1} C_i \epsilon_1^i\right], \\ \implies \epsilon_1^n &= \mathcal{L}^{-1}\left[(0) + \sum_{i=n-k-1}^{n-1} C_i \epsilon_1^i\right], \\ \implies \epsilon_1^n &= \mathcal{L}^{-1}\left[\sum_{i=n-k-1}^{n-1} C_i \epsilon_1^i\right]. \end{aligned} \tag{4.41}$$

Given the initial conditions are all zero, we know ϵ_1^1 is zero, as is ϵ_1^2, and so on. This logic can be stepped to arbitrary n.

We have demonstrated (4.25) $\implies$ (4.26) if (4.25) is satisfied initially, and (4.26) $\implies$ (4.25).

QED

We have linked the semi-discrete continuity equation with the semi-discrete gauge condition for arbitrary order BDF methods. Now we will show Gauss's law for electricity follows from the satisfaction of the semi-discrete gauge condition (4.25).

Theorem 4.2.2. *If the semi-discrete gauge condition* (4.25) *is satisfied for time level* $n+1$*, then* $\nabla \cdot \boldsymbol{E}^{n+1} = \frac{\rho^{n+1}}{\epsilon_0}$.

Proof. We assume (4.25):

$$\frac{1}{c^2}\frac{1}{\Delta t}\sum_{i=n-k}^{n} a_{n-i}\phi^i + \nabla \cdot \mathbf{A}^n = 0. \tag{4.42}$$

By definition we have $\mathbf{E} = -\nabla\phi - \frac{\partial \mathbf{A}}{\partial t}$, whose BDF-k time discrete form is as follows:

$$\mathbf{E}^n = -\nabla\phi^n - \frac{1}{\Delta t}\sum_{i=n-k}^{n} a_{n-i}\mathbf{A}^i. \tag{4.43}$$

We take the divergence, which yields

$$\nabla \cdot \mathbf{E}^n = -\Delta\phi^n - \frac{1}{\Delta t}\sum_{i=n-k}^{n} a_{n-i}\nabla \cdot \mathbf{A}^i \tag{4.44}$$

Using (4.25), we replace $\nabla \cdot \mathbf{A}^i$ with the BDF-k of ϕ^i:

$$\begin{aligned}
\nabla \cdot \mathbf{E}^n &= -\Delta\phi^n - \frac{1}{\Delta t}\sum_{i=n-k}^{n} a_{n-i}\left(-\frac{1}{c^2}\frac{1}{\Delta t}\sum_{j=i-k}^{i} a_{i-j}\phi^j\right) \\
&= \frac{1}{c^2}\frac{1}{\Delta t^2}\sum_{i=n-k}^{n} a_{n-i}\sum_{j=i-k}^{i} a_{i-j}\phi^j - \Delta\phi^n \\
&= \frac{\rho^n}{\epsilon_0}.
\end{aligned} \tag{4.45}$$

The last step was taken by definition of the scalar potential wave equation (4.23).

We have demonstrated Gauss's Law for electricity is satisfied, completing the proof. QED

Remark 4.2.1. *We note that all BDF methods satisfy this theorem. However, while first and second order BDF methods are A-stable, third order BDF methods and above are Aα-stable. In practice, this means that using first and second order BDF methods can be used with any CFL one wants, while third order BDF and above need to take time steps that are greater than t_{min} to be stable when solving a wave equation, which has eigenvalues on the imaginary axis. This is because third order*

BDF and above have stability diagrams that slightly move into the left half of the plane of the region of absolute stability and then back out again. A large enough CFL will avoid this issue.

Remark 4.2.2. *For our numerical experiments we use the second order BDF method, BDF-2. The semi-discrete wave equations, Lorenz gauge condition, and continuity equation take the following form:*

$$\begin{aligned}
\frac{1}{c^2}\frac{\phi^{n+1} - \frac{8}{3}\phi^n + \frac{22}{9}\phi^{n-1} - \frac{8}{9}\phi^{n-2} + \frac{1}{9}\phi^{n-3}}{\left((2/3)\Delta t\right)^2} - \Delta\phi^{n+1} &= \frac{\rho^{n+1}}{\epsilon_0}, \\
\frac{1}{c^2}\frac{\boldsymbol{A}^{n+1} - \frac{8}{3}\boldsymbol{A}^n + \frac{22}{9}\boldsymbol{A}^{n-1} - \frac{8}{9}\boldsymbol{A}^{n-2} + \frac{1}{9}\boldsymbol{A}^{n-3}}{\left((2/3)\Delta t\right)^2} - \Delta\boldsymbol{A} &= \mu_0\boldsymbol{J}^{n+1}, \\
\frac{1}{c^2}\frac{\phi^{n+1} - \frac{4}{3}\phi^n + \frac{1}{3}\phi^{n-1}}{(2/3)\,\Delta t} + \nabla\cdot\boldsymbol{A}^{n+1} &= 0, \\
\frac{\rho^{n+1} - \frac{4}{3}\rho^n + \frac{1}{3}\rho^{n-1}}{(2/3)\,\Delta t} + \nabla\cdot\boldsymbol{J}^{n+1} &= 0.
\end{aligned}$$

4.2.2 A Semi-discrete Time-centered Method for the Lorenz Gauge Formulation

To start, consider the semi-discrete treatment of the Lorenz gauge formulation, as in Chapter 3, in which second-order approximations are used for ∂_t and ∂_{tt}. As we will prove in this section, the satisfaction of the semi-discrete gauge condition as well as the involutions, (4.5) and (4.6), can be ensured using the time-centered difference approximations

$$\partial_t u^{n+\frac{1}{2}} = \frac{u^{n+1} - u^n}{\Delta t} + O(\Delta t^2), \quad \partial_{tt} u^n = \frac{u^{n+1} - 2u^n + u^{n-1}}{\Delta t^2} + O(\Delta t^2).$$

A critical observation is that two applications of the first difference approximation to a discrete data set produces the discrete second order discrete second difference in time, i.e.,

$$\partial_{tt} u = \frac{\partial_t u^{n+\frac{1}{2}} - \partial_t u^{n-\frac{1}{2}}}{\Delta t} + O(\Delta t^2) = \frac{\dfrac{u^{n+1} - u^n}{\Delta t} - \dfrac{u^n - u^{n-1}}{\Delta t}}{\Delta t} + O(\Delta t^2).$$

This leads to the semi-discrete system in an implicit form

$$\begin{cases}
\dfrac{\phi^{n+\frac{3}{2}} - 2\phi^{n+\frac{1}{2}} + \phi^{n-\frac{1}{2}}}{c^2\Delta t^2} - \Delta\left(\dfrac{\phi^{n+\frac{3}{2}} + \phi^{n-\frac{1}{2}}}{2}\right) = \dfrac{1}{\epsilon_0}\dfrac{\rho^{n+\frac{3}{2}} + \rho^{n-\frac{1}{2}}}{2}, & (4.46) \\
\dfrac{\mathbf{A}^{n+1} - 2\mathbf{A}^n + \mathbf{A}^{n-1}}{c^2\Delta t^2} - \Delta\left(\dfrac{\mathbf{A}^{n+1} + \mathbf{A}^{n-1}}{2}\right) = \mu_0\dfrac{\mathbf{J}^{n+1} + \mathbf{J}^{n-1}}{2}, & (4.47) \\
\dfrac{\phi^{n+\frac{3}{2}} - \phi^{n+\frac{1}{2}}}{c^2\Delta t} + \nabla\cdot\mathbf{A}^{n+1} = 0, & (4.48)
\end{cases}$$

a semi-implicit form

$$\begin{cases} \dfrac{\phi^{n+\frac{3}{2}} - 2\phi^{n+\frac{1}{2}} + \phi^{n-\frac{1}{2}}}{c^2\Delta t^2} - \Delta\left(\dfrac{\phi^{n+\frac{3}{2}} + \phi^{n-\frac{1}{2}}}{2}\right) = \dfrac{1}{\epsilon_0}\rho^{n+\frac{1}{2}}, & (4.49) \\ \dfrac{\mathbf{A}^{n+1} - 2\mathbf{A}^{n} + \mathbf{A}^{n-1}}{c^2\Delta t^2} - \Delta\left(\dfrac{\mathbf{A}^{n+1} + \mathbf{A}^{n-1}}{2}\right) = \mu_0\mathbf{J}^{n}, & (4.50) \\ \dfrac{\phi^{n+\frac{3}{2}} - \phi^{n+\frac{1}{2}}}{c^2\Delta t} + \nabla\cdot\mathbf{A}^{n+1} = 0, & (4.51) \end{cases}$$

and, alternatively, an explicit form

$$\begin{cases} \dfrac{\phi^{n+\frac{3}{2}} - 2\phi^{n+\frac{1}{2}} + \phi^{n-\frac{1}{2}}}{c^2\Delta t^2} - \Delta\phi^{n+\frac{1}{2}} = \dfrac{1}{\epsilon_0}\rho^{n+\frac{1}{2}}, & (4.52) \\ \dfrac{\mathbf{A}^{n+1} - 2\mathbf{A}^{n} + \mathbf{A}^{n-1}}{c^2\Delta t^2} - \Delta\mathbf{A}^{n} = \mu_0\mathbf{J}^{n}, & (4.53) \\ \dfrac{\phi^{n+\frac{3}{2}} - \phi^{n+\frac{1}{2}}}{c^2\Delta t} + \nabla\cdot\mathbf{A}^{n+1} = 0, & (4.54) \end{cases}$$

where here we assume $\mathbf{J}^{\{n,n+1\}}$ is given and use this to compute $\rho^{n+\frac{3}{2}}$ and the fields for the particle update. All examples we explore in section 4.3 are implicit and compute an approximation of $\mathbf{J}^{n+1}$ (see section 1.3.5 for more details).

Of particular relevance to this paper, much like Chapter 3, is a theorem that establishes an equivalence, at the semi-discrete level, between the continuity equation

$$\frac{\rho^{n+\frac{3}{2}} - \rho^{n+\frac{1}{2}}}{\Delta t} + \nabla\cdot\mathbf{J}^{n+1} = 0, \tag{4.55}$$

and the Lorenz gauge condition (4.48) (see Theorem 3.2.1). To establish similar results for these methods, we will need to identify groupings of terms. For convenience, we shall introduce the notation

$$\epsilon_1^k = \frac{\phi^{k+\frac{1}{2}} - \phi^{k-\frac{1}{2}}}{c^2\Delta t} + \nabla\cdot\mathbf{A}^{k}, \quad \epsilon_2^k = \frac{\rho^{k+\frac{1}{2}} - \rho^{k-\frac{1}{2}}}{\Delta t} + \nabla\cdot\mathbf{J}^{k}, \tag{4.56}$$

to simplify the presentation. Our first task is to establish the interdependence of satisfying the gauge condition with satisfying the continuity equation. Then we can establish that if our method is time-consistent, and the gauge condition is satisfied, then we will ensure that Gauss's law for electricity is satisfied. In the semi-discrete case, the derivatives are analytical, meaning Gauss's law

for magnetism is satisfied by definition. In the next section, we will examine how this looks in the fully-discrete case, and introduce the method for ensuring satisfaction of the continuity equation, and hence we will establish that the method preserves the gauge condition and the involutions.

We now define operator notation that will be used in the proofs of the semi-discrete theorem for the fully-implicit update. Consider now the linear wave equation

$$\frac{1}{c^2}\partial_{tt}u - \Delta u = S. \tag{4.57}$$

The coefficient $c > 0$ and assumed to be a constant. Additionally, we denote $S(\mathbf{x}, t)$ as the source function. An implicit second-order Crank-Nicolson method for u^{n+1} centered at $t = t^n$ is

$$\left(\mathcal{I} - \frac{1}{\alpha^2}\Delta\right)\left(u^{n+1} + u^{n-1}\right) = 2u^n + \frac{1}{\alpha^2}\Gamma^n, \tag{4.58}$$

where we use $\alpha = \sqrt{2}/(c\Delta t)$ and $\Gamma^n = S^{n+1} + S^{n-1}$. We define

$$\mathcal{L}(\cdot) = \left(\mathcal{I} - \frac{1}{\alpha^2}\Delta\right)(\cdot)$$

and denote the inverse as $\mathcal{L}^{-1}(\cdot)$. The inverse can be computed with any number of methods. For our purposes, we will compute the inverse using the FFT.

Lemma 4.2.3. *(Implicit method-Green's Function) For the implicit formulation in* (4.46)-(4.47)*, the semi-discrete Lorenz gauge condition* (4.48) *satisfies*

$$\epsilon_1^{n+1} = -\epsilon_1^{n-1} + \mathcal{L}^{-1}\left(2\epsilon_1^n + \frac{\mu_0}{\alpha^2}\left(\epsilon_2^{n+1} + \epsilon_2^{n-1}\right)\right). \tag{4.59}$$

Proof. This proof is a direct construction. We start with equation (4.46). Inverting the modified Helmholtz operator $\mathcal{L}$ gives the scalar potential as

$$\phi^{n+\frac{3}{2}} = -\phi^{n-\frac{1}{2}} + \mathcal{L}^{-1}\left(2\phi^{n+\frac{1}{2}} + \frac{1}{\alpha^2\epsilon_0}\left(\rho^{n+\frac{3}{2}} + \rho^{n-\frac{1}{2}}\right)\right), \tag{4.60}$$

which can be shifted to obtain

$$\phi^{n+\frac{1}{2}} = -\phi^{n-\frac{3}{2}} + \mathcal{L}^{-1}\left(2\phi^{n-\frac{1}{2}} + \frac{1}{\alpha^2\epsilon_0}\left(\rho^{n-\frac{1}{2}} + \rho^{n-\frac{3}{2}}\right)\right). \tag{4.61}$$

Next, we take the divergence of $\mathbf{A}$ in equation (4.47) and find that

$$\mathcal{L}\left(\nabla\cdot\mathbf{A}^{n+1}+\nabla\cdot\mathbf{A}^{n-1}\right)=2\nabla\cdot\mathbf{A}^{n}+\frac{\mu_0}{\alpha^2}\left(\nabla\cdot\mathbf{J}^{n+1}+\nabla\cdot\mathbf{J}^{n-1}\right).$$

Formally inverting the operator $\mathcal{L}$, we obtain the relation

$$\nabla\cdot\mathbf{A}^{n+1}=-\nabla\cdot\mathbf{A}^{n-1}+\mathcal{L}^{-1}\left(2\nabla\cdot\mathbf{A}^{n}+\frac{\mu_0}{\alpha^2}\left(\nabla\cdot\mathbf{J}^{n+1}+\nabla\cdot\mathbf{J}^{n-1}\right)\right). \tag{4.62}$$

With the aid of equations (4.60), (4.61), and (4.62), along with the linearity of the operator $\mathcal{L}$, a direct calculation reveals that the residual at time level is given by

$$\frac{\phi^{n+\frac{3}{2}}-\phi^{n+\frac{1}{2}}}{c^2\Delta t}+\nabla\cdot\mathbf{A}^{n+1}=-\epsilon_1^{n-1}+$$
$$\mathcal{L}^{-1}\left(2\epsilon_1^{n}+\left(\frac{1}{\alpha^2\epsilon_0}\left(\frac{\rho^{n+\frac{3}{2}}-\rho^{n+\frac{1}{2}}}{c^2\Delta t}\right)+\frac{\mu_0}{\alpha^2}\nabla\cdot\mathbf{J}^{n+1}\right)+\left(\frac{1}{\alpha^2\epsilon_0}\left(\frac{\rho^{n-\frac{1}{2}}-\rho^{n-\frac{3}{2}}}{c^2\Delta t}\right)+\frac{\mu_0}{\alpha^2}\nabla\cdot\mathbf{J}^{n-1}\right)\right).$$

From these calculations, we see that the above expression is the same (4.59), with the observation that we have used the following relation $c^2=1/(\mu_0\epsilon_0)$. We observe that the corresponding consistent semi-discrete continuity equation

$$\frac{\rho^{n+\frac{3}{2}}-\rho^{n+\frac{1}{2}}}{\Delta t}+\nabla\cdot\mathbf{J}^{n+1}=\epsilon_2^{n+1}, \tag{4.63}$$

acts as a source for the residual, which completes the proof. QED

With the aid of Lemma 4.2.3, we are now prepared to prove the following theorem that establishes the time-consistency of the semi-discrete system.

Theorem 4.2.3. *(Implicit method-Green's Function) Assuming* $\epsilon_1^n=\epsilon_2^n=0,\ \forall\, n\le 0$*, the semi-discrete Lorenz gauge formulation of Maxwell's equations* (4.46)-(4.48) *is time-consistent in the sense that the semi-discrete Lorenz gauge condition* (4.48) *is satisfied at any discrete time if and only if the corresponding semi-discrete continuity equation* (4.63) *is also satisfied.*

Proof. We use a simple inductive argument to prove both directions. In the case of the forward direction, we assume that the semi-discrete gauge condition is satisfied, so $\epsilon_1^n\equiv 0,\quad \forall n\ge 0$. From

our assumption $\epsilon_2^{-1} \equiv 0$. Combining this with equation (4.59) established by Lemma 4.2.3, it follows that the next time level satisfies

$$0 = \mathcal{L}^{-1}\left(\frac{\mu_0}{\alpha^2}\left(\frac{\rho^{\frac{1}{2}} - \rho^{-\frac{1}{2}}}{\Delta t} + \nabla \cdot \mathbf{J}^0\right)\right).$$

Applying the operator $\mathcal{L}$ to both sides leads to

$$\frac{\rho^{\frac{1}{2}} - \rho^{-\frac{1}{2}}}{\Delta t} + \nabla \cdot \mathbf{J}^0 = 0.$$

This argument can be iterated n times to show that

$$\frac{\rho^{n+\frac{1}{2}} - \rho^{n-\frac{1}{2}}}{\Delta t} + \nabla \cdot \mathbf{J}^n = 0,$$

also holds at any discrete time level n, which establishes the forward direction.

A similar argument can be used for the converse. Here, we show that if the semi-discrete continuity equation (4.63) is satisfied for any time level n, i.e., $\epsilon_2^n \equiv 0$, then the residual for the semi-discrete gauge condition also satisfies $\epsilon_1^{n+1} \equiv 0$. First, we assume that the initial data and starting values satisfy $\epsilon_1^{-1} \equiv \epsilon_1^0 \equiv 0$. Appealing to equation (4.59) with this initial data, it is clear that after a single time step, the residual in the gauge condition satisfies

$$\epsilon_1^1 = -\epsilon_1^{-1} + \mathcal{L}^{-1}\left(2\epsilon_1^0 + \frac{\mu_0}{\alpha^2}\left(\epsilon_2^1 + \epsilon_2^{-1}\right)\right) \equiv \mathcal{L}^{-1}(0).$$

This argument can also be iterated n more times to obtain the result, which finishes the proof. QED

Lemma 4.2.4. *(Semi-Implicit method-Green's Function) For the semi-implicit formulation in* (4.49)-(4.50)*, the semi-discrete Lorenz gauge condition* (4.51) *satisfies*

$$\epsilon_1^{n+1} = -\epsilon_1^{n-1} + \mathcal{L}^{-1}\left(2\epsilon_1^n + \frac{\mu_0}{\alpha^2}\epsilon_2^n\right). \tag{4.64}$$

Proof. The proof is nearly identical to that of Lemma 4.2.3, so we exclude it. QED

Theorem 4.2.4. *(Semi-Implicit method-Green's Function) Assuming* $\epsilon_1^n = \epsilon_2^n = 0, \quad \forall n \leq 0$*, the semi-discrete Lorenz gauge formulation of Maxwell's equations* (4.49)-(4.51) *is time-consistent in the sense that the semi-discrete Lorenz gauge condition* (4.51) *is satisfied at any discrete time if and only if the corresponding semi-discrete continuity equation* (4.63) *is also satisfied.*

Proof. The proof is nearly identical to that of Theorem 4.2.3, so we exclude it. QED

Lemma 4.2.5. *(Explicit method) For the explicit formulation in* (4.52)-(4.53)*, the semi-discrete Lorenz gauge condition* (4.54) *satisfies*

$$\epsilon_1^{n+1} = 2\epsilon_1^n - \epsilon_1^{n-1} + \left(c^2\Delta t^2\right)\Delta\epsilon_1^n + \left(c^2\Delta t^2\right)\mu_0\epsilon_2^n. \tag{4.65}$$

Proof. Start with

$$\epsilon_1^{n+1} = \frac{\phi^{n+\frac{3}{2}} - \phi^{n+\frac{1}{2}}}{c^2\Delta t} + \nabla\cdot\mathbf{A}^{n+1},$$

and substitute equation (4.52) in for $\phi^{n+\frac{3}{2}}$ and $\phi^{n+\frac{1}{2}}$, then substitute equation (4.53) in for $\mathbf{A}^{n+1}$. We have

$$\begin{aligned}\frac{\phi^{n+\frac{3}{2}} - \phi^{n+\frac{1}{2}}}{c^2\Delta t} = &\frac{2\phi^{n+\frac{1}{2}} - \phi^{n-\frac{1}{2}} - (c^2\Delta t^2)\Delta\phi^{n+\frac{1}{2}} + (c^2\Delta t^2)\frac{1}{\epsilon_0}\rho^{n+\frac{1}{2}}}{c^2\Delta t}\\ &- \frac{\left(2\phi^{n-\frac{1}{2}} - \phi^{n-\frac{3}{2}} - (c^2\Delta t^2)\Delta\phi^{n-\frac{1}{2}} + (c^2\Delta t^2)\frac{1}{\epsilon_0}\rho^{n-\frac{1}{2}}\right)}{c^2\Delta t},\end{aligned}$$

and

$$\nabla\cdot\mathbf{A}^{n+1} = 2\nabla\cdot\mathbf{A}^n - \nabla\cdot\mathbf{A}^{n-1} - c^2\Delta t^2\Delta\nabla\cdot\mathbf{A}^n + c^2\Delta t^2\mu_0\nabla\cdot\mathbf{J}^n.$$

After grouping terms in the form of ϵ_1^k and ϵ_2^k as in Lemma 4.2.3, we arrive at (4.65). This completes the proof. QED

Theorem 4.2.5. *(Explicit method) Assuming* $\epsilon_1^n = \epsilon_2^n = 0,\ \forall\, n \le 0$*, the explicit semi-discrete Lorenz gauge formulation of Maxwell's equations* (4.52)-(4.54) *is time-consistent in the sense that the semi-discrete Lorenz gauge condition* (4.54) *is satisfied at any discrete time if and only if the corresponding semi-discrete continuity equation* (4.63) *is also satisfied.*

Proof. The proof is an identical construction to that in Theorem 4.2.3. QED

Theorem 4.2.6. *Under the assumption that* $\epsilon_1^k = \epsilon_2^k = 0,\ \forall\, k \le n+1$*, the implicit semi-discrete methods* (4.46)-(4.48) *satisfy Gauss's Law*

$$\nabla\cdot\mathbf{E}^{n+\frac{1}{2}} = \frac{1}{\epsilon_0}\left(\frac{\rho^{n+\frac{3}{2}} + \rho^{n-\frac{1}{2}}}{2}\right). \tag{4.66}$$

Proof. Starting with the identity $\mathbf{E} = -\nabla\phi - \partial_t \mathbf{A}$, we have

$$\mathbf{E}^{n+\frac{1}{2}} = -\nabla\left(\frac{\phi^{n+\frac{3}{2}} + \phi^{n-\frac{1}{2}}}{2}\right) - \frac{\mathbf{A}^{n+1} - \mathbf{A}^n}{\Delta t}. \tag{4.67}$$

Taking the divergence, we obtain

$$\nabla \cdot \mathbf{E}^{n+\frac{1}{2}} = -\Delta\left(\frac{\phi^{n+\frac{3}{2}} + \phi^{n-\frac{1}{2}}}{2}\right) - \frac{\nabla \cdot \mathbf{A}^{n+1} - \nabla \cdot \mathbf{A}^n}{\Delta t}. \tag{4.68}$$

Then, from the assumption, we know that

$$\epsilon_1^n = 0 \implies \frac{1}{c^2}\frac{\phi^{n+\frac{1}{2}} - \phi^{n-\frac{1}{2}}}{\Delta t} + \nabla \cdot \mathbf{A}^n = 0.$$

From this, we see that

$$\begin{aligned}
\nabla \cdot \mathbf{E}^{n+\frac{1}{2}} &= -\Delta\left(\frac{\phi^{n+\frac{3}{2}} + \phi^{n-\frac{1}{2}}}{2}\right) - \frac{\left(-\frac{1}{c^2}\frac{\phi^{n+\frac{3}{2}} - \phi^{n+\frac{1}{2}}}{\Delta t}\right) - \left(-\frac{1}{c^2}\frac{\phi^{n+\frac{1}{2}} - \phi^{n-\frac{1}{2}}}{\Delta t}\right)}{\Delta t} \\
&= -\Delta\left(\frac{\phi^{n+\frac{3}{2}} + \phi^{n-\frac{1}{2}}}{2}\right) + \frac{1}{c^2}\frac{\phi^{n+\frac{3}{2}} - 2\phi^{n+\frac{1}{2}} + \phi^{n-\frac{1}{2}}}{\Delta t^2} \\
&= \frac{1}{\epsilon_0}\left(\frac{\rho^{n+\frac{3}{2}} + \rho^{n-\frac{1}{2}}}{2}\right).
\end{aligned} \tag{4.69}$$

The last step comes from the fully implicit CDF-2 scalar wave equation (4.46). We thus see Gauss's Law is satisfied. QED

Theorem 4.2.7. *Under the assumption that $\epsilon_2^k = 0$, for $k \leq n+1$, both the explicit and semi-implicit semi-discrete methods satisfy Gauss's law*

$$\nabla \cdot \mathbf{E}^{n+\frac{1}{2}} = \frac{\rho^{n+\frac{1}{2}}}{\epsilon_0}. \tag{4.70}$$

Proof. We start by noting, under the assumption that $\epsilon_2^k = 0$, we have $\epsilon_1^k = 0$, for $k = n+1$, from the previous theorems. We carry out the proof for the explicit case and note that the semi-implicit case is identical except for the fact that $\nabla\phi^{n+\frac{1}{2}}$ will be replaced by $\nabla\left(\frac{1}{2}(\phi^{n+\frac{3}{2}} + \phi^{n-\frac{1}{2}})\right)$ in the identity

$$\mathbf{E} = -\nabla\phi - \partial_t \mathbf{A}.$$

Evaluating this identity at time $t^{n+\frac{1}{2}}$ and making use of the semi-discrete potentials, we find

$$\mathbf{E}^{n+\frac{1}{2}} = -\nabla\phi^{n+\frac{1}{2}} - \frac{\mathbf{A}^{n+1} - \mathbf{A}^{n}}{\Delta t}.$$

Again, taking the divergence gives

$$\nabla \cdot \mathbf{E}^{n+\frac{1}{2}} = -\Delta\phi^{n+\frac{1}{2}} - \frac{\nabla \cdot \mathbf{A}^{n+1} - \nabla \cdot \mathbf{A}^{n}}{\Delta t}.$$

given that $\epsilon_1^{n+1} = 0$, then we can replace $\nabla \cdot \mathbf{A}^{n+1}$ with $-\frac{\phi^{n+\frac{3}{2}} - \phi^{n+\frac{1}{2}}}{c^2\Delta t}$ and $\nabla \cdot \mathbf{A}^{n}$ with $-\frac{\phi^{n+\frac{1}{2}} - \phi^{n-\frac{1}{2}}}{c^2\Delta t}$, so

$$\nabla \cdot \mathbf{E}^{n+\frac{1}{2}} = -\Delta\phi^{n+\frac{1}{2}} - \frac{\phi^{n+\frac{3}{2}} - 2\phi^{n+\frac{1}{2}} + \phi^{n-\frac{1}{2}}}{c^2\Delta t^2} = \frac{\rho^{n+\frac{1}{2}}}{\epsilon_0}.$$

Hence, we arrive at the conclusion of the theorem. QED

Remark 4.2.3. *The semi-discrete formulation method automatically satisfies* $\nabla \cdot \mathbf{B} = \nabla \cdot (\nabla \times \mathbf{A}) = 0$.

Remark 4.2.4. *All three time-consistent methods satisfy all of the involutions and the gauge condition, as long as the method satisfies the semi-discrete continuity condition.*

Remark 4.2.5. *For all the methods we discuss, we incorporate the improved asymmetric Euler method for our particle update method. A time-centered wave advance opens the door for time-centering the particle pusher, which increases the accuracy of the solver and can be used to explore aspects of symplecticity. This exploration is beyond the scope of this thesis but will be considered in future work.*

4.2.3 s-Stage Adams Bashforth

Consider the equation $y' = f(y, t)$. The s-stage Adams Bashforth method may be described as follows:

$$y^n = y^{n-1} + \Delta t \sum_{i=n-s}^{n-1} \left(c_i f\left(t^i, y^i\right)\right). \tag{4.71}$$

For $\frac{1}{c^2}\frac{\partial^2 u}{\partial t^2} - \Delta u = S$, defining $v \coloneqq \frac{\partial u}{\partial t}$, we rewrite it as the first order system

$$\frac{\partial}{\partial t}\begin{pmatrix} v \\ u \end{pmatrix} = \begin{pmatrix} c^2\left(S + \Delta u\right) \\ v \end{pmatrix}. \tag{4.72}$$

We then get the following update system

$$v^n = v^{n-1} + c^2\Delta t \sum_{i=n-s}^{n-1} c_i \left(S^i + \Delta u^i\right), \tag{4.73}$$

$$u^n = u^{n-1} + \Delta t \sum_{i=n-s}^{n-1} c_i v^i. \tag{4.74}$$

We apply this to our wave equations

$$\begin{aligned} v_\phi^n &= v_\phi^{n-1} + c^2\Delta t \sum_{i=n-s}^{n-1} c_i \left(\frac{\rho^i}{\epsilon_0} + \Delta\phi^i\right), \\ \phi^n &= \phi^{n-1} + \Delta t \sum_{i=n-s}^{n-1} c_i v_\phi^i. \end{aligned} \tag{4.75}$$

$$\begin{aligned} \mathbf{v}_\mathbf{A}^n &= \mathbf{v}_\mathbf{A}^{n-1} + c^2\Delta t \sum_{i=n-s}^{n-1} c_i \left(\mu_0\mathbf{J}^i + \Delta\mathbf{A}^i\right), \\ \mathbf{A}^n &= \mathbf{A}^{n-1} + \Delta t \sum_{i=n-s}^{n-1} c_i \mathbf{v}_\mathbf{A}^i. \end{aligned} \tag{4.76}$$

We define the following residuals:

$$\epsilon_L^n \coloneqq -\phi^n + \phi^{n-1} - c^2\Delta t \sum_{i=n-s}^{n-1} c_i \nabla\cdot\mathbf{A}^i, \tag{4.77}$$

$$\epsilon_V^n \coloneqq -v_\phi^n + v_\phi^{n-1} - c^2\Delta t \sum_{i=n-s}^{n-1} c_i \nabla\cdot\mathbf{v}_\mathbf{A}^i, \tag{4.78}$$

$$\epsilon_C^n \coloneqq -\rho^n + \rho^{n-1} - \Delta t \sum_{i=n-s}^{n-1} c_i \nabla\cdot\mathbf{J}^i. \tag{4.79}$$

We now prove two lemmas.

Lemma 4.2.6. *ϵ_V^n is a linear combination of ϵ_L, ϵ_C, and ϵ_V at previous timesteps.*

Proof. We take the definition of ϵ_V, (4.78), and plug in our update equations:

$$\begin{aligned}
\epsilon_V^n =& - v_\phi^n + v_\phi^{n-1} - c^2\Delta t \sum_{i=n-s}^{n-1} \nabla \cdot \mathbf{v}_\mathbf{A}^i \\
=& - \left(v_\phi^{n-1} + c^2\Delta t \sum_{i=n-s}^{n-1} c_i \left(\frac{\rho^i}{\epsilon_0} + \Delta\phi^i \right) \right) \\
&+ \left(v_\phi^{n-2} + c^2\Delta t \sum_{i=n-s-1}^{n-2} c_i \left(\frac{\rho^i}{\epsilon_0} + \Delta\phi^i \right) \right) \\
&- c^2\Delta t \sum_{i=n-s}^{n-1} c_i \nabla \cdot \left(\mathbf{v}_\mathbf{A}^{i-1} + c^2\Delta t \sum_{j=i-s}^{i-1} c_j \left(\mu_0 \mathbf{J}^j + \Delta \mathbf{A}^j \right) \right).
\end{aligned} \tag{4.80}$$

We rearrange

$$\begin{aligned}
& - v_\phi^{n-1} + v_\phi^{n-2} - c^2\Delta t \sum_{i=n-s}^{n-1} c_i \nabla \cdot \mathbf{v}_\mathbf{A}^{i-1} \\
& - c^2\Delta t \sum_{i=n-s}^{n-1} c_i \left(\frac{\rho^i}{\epsilon_0} + \Delta\phi^i \right) + c^2\Delta t \sum_{i=n-s-1}^{n-2} c_i \left(\frac{\rho^i}{\epsilon_0} + \Delta\phi^i \right) \\
& - c^2\Delta t \sum_{i=n-s}^{n-1} c_i c^2\Delta t \sum_{j=i-s}^{i-1} c_j \left(\mu_0 \nabla \cdot \mathbf{J}^j + \Delta \nabla \cdot \mathbf{A}^j \right) \\
=& - v_\phi^{n-1} + v_\phi^{n-2} - c^2\Delta t \sum_{i=n-s}^{n-1} c_i \nabla \cdot \mathbf{v}_\mathbf{A}^{i-1} \\
& c^2\Delta t \sum_{i=n-s}^{n-1} c_i \left(-\frac{\rho^i}{\epsilon_0} + \frac{\rho^{i-1}}{\epsilon_0} - c^2\Delta t \sum_{j=i-s}^{i-1} c_j \mu_0 \nabla \cdot \mathbf{J}^j + \Delta \left(-\phi^i + \phi^{i-1} - c^2\Delta t \sum_{j=i-s}^{i-1} c_j \nabla \cdot \mathbf{A}^j \right) \right) \\
=& \epsilon_V^{n-1} + c^2\Delta t \sum_{i=n-s}^{n-1} c_i \left(\frac{1}{\epsilon_0} \epsilon_C^i + \Delta \epsilon_L^i \right)
\end{aligned} \tag{4.81}$$

$\therefore$ ϵ_V^n is a linear combination of ϵ_L, ϵ_C, and ϵ_V at previous timesteps. QED

Lemma 4.2.7. *ϵ_L^n is a linear combination of ϵ_L and ϵ_V at previous timesteps.*

Proof. We write ϵ_L^n as follows

$$
\begin{aligned}
\epsilon_L^n &= -\phi^n + \phi^{n-1} - c^2\Delta t \sum_{i=n-s}^{n-1} c_i \nabla \cdot \mathbf{A}^i \\
&= -\left(\phi^{n-1} + \Delta t \sum_{i=n-s}^{n-1} c_i v_\phi^i\right) + \left(\phi^{n-2} + \Delta t \sum_{i=n-s-1}^{n-2} c_i v_\phi^i\right) - c^2\Delta t \sum_{i=n-s}^{n-1} c_i \nabla \cdot \left(\mathbf{A}^i + \Delta t \sum_{j=i-s}^{i-1} c_j \mathbf{v}_\mathbf{A}^j\right) \\
&= -\phi^{n-1} + \phi^{n-2} - c^2\Delta t \sum_{i=n-s}^{n-1} c_i \nabla \cdot \mathbf{A}^i + \Delta t \sum_{i=n-s}^{n-1} c_i \left(-v_\phi^i + v_\phi^{i-1} - c^2\Delta t \sum_{j=i-s}^{i-1} c_j \nabla \cdot \mathbf{v}_\mathbf{A}^j\right) \\
&= \epsilon_L^{n-1} + \Delta t \sum_{i=n-s}^{n-1} \epsilon_V^i.
\end{aligned}
\tag{4.82}
$$

$\therefore$ ϵ_L^n is a linear combination of ϵ_L and ϵ_v at previous timesteps. QED

We take the above lemmas and prove the following theorem:

Theorem 4.2.8. *If $\epsilon_V^i = \epsilon_L^i = \epsilon_C^i = 0$ for $i \leq 0$, then $\epsilon_L^n = \epsilon_V^n = \epsilon_C^n = 0 \,\forall\, n$.*

Proof. Assume $\epsilon_V^i = \epsilon_L^i = \epsilon_C^i = 0$ for $i \leq 0$.

We prove by induction. Using Lemma 4.2.6, we see

$$
\epsilon_V^1 = \epsilon_V^0 + c^2\Delta t \sum_{i=1-s}^{0} c_i \left(\frac{1}{\epsilon_0}\epsilon_C^i + \Delta\epsilon_L^i\right) = (0) + c^2\Delta t \sum_{i=1-s}^{0} c_i (\frac{1}{\epsilon_0}(0) + \Delta(0)) = 0. \tag{4.83}
$$

This may be clicked up to arbitrary n using the exact same logic. So $\epsilon_V^n = 0 \,\forall\, n$. From Lemma 4.2.7, we know

$$
\epsilon_L^1 = \epsilon_L^0 + \Delta t \sum_{i=1-s}^{0} \epsilon_V^i = (0) + \Delta t \sum_{i=n-s}^{n-1} (0) = 0. \tag{4.84}
$$

So $\epsilon_L^n = 0 \,\forall\, n$. Knowing that $\epsilon_L^n = \epsilon_V^n = 0 \,\forall\, n$, we again use Lemma 4.2.6 to see

$$
\begin{aligned}
&\epsilon_V^n = \epsilon_V^{n-1} + c^2\Delta t \sum_{i=n-s}^{n-1} c_i \left(\frac{1}{\epsilon_0}\epsilon_C^i + \Delta\epsilon_L^i\right) \\
\implies &(0) = (0) + c^2\Delta t \sum_{i=n-s}^{n-1} c_i \left(\frac{1}{\epsilon_0}\epsilon_C^i + \Delta(0)\right) \\
\implies &\epsilon_C^{n-1} = -\sum_{n-s}^{n-2} \frac{c_i}{c_{n-1}} \epsilon_C^i.
\end{aligned}
\tag{4.85}
$$

Given this result, we use the above logic to show that $\epsilon_C^i = 0 \,\forall\, i \leq 0 \implies \epsilon_C^1 = 0$ and so on to arbitrary n.

$\therefore$ if $\epsilon_V^i = \epsilon_L^i = \epsilon_C^i = 0$ for $i \leq 0$, then $\epsilon_L^n = \epsilon_V^n = \epsilon_C^n = 0 \,\forall\, n$. QED

Finally, we connect satisfaction of the semi-discrete continuity equation and the semi-discrete Lorenz gauge with satisfaction of Gauss's Law, $\nabla \cdot \mathbf{E} = \frac{\rho}{\epsilon_0}$.

Theorem 4.2.9. *Assuming the involution $\nabla \cdot \mathbf{E} = \frac{\rho}{\epsilon_0}$ at $t = 0$, if the residuals for the Lorenz gauge condition* (4.77) *and the semi-discrete continuity equation* (4.79) *are zero for time level n, then $\nabla \cdot \mathbf{E}^n = \frac{\rho^n}{\epsilon_0} \,\forall\, n$.*

Proof. We prove by induction. Assume $\epsilon_C^n = \epsilon_L^n = 0 \,\forall\, n$.

By our assumption, $\nabla \cdot \mathbf{E}^0 = \frac{\rho^0}{\epsilon_0}$.

Now we assume true for n, and consider the $n+1$ case. By definition we know $\mathbf{E} = -\nabla\phi - \frac{\partial \mathbf{A}}{\partial t}$. We recall $\mathbf{v_A} - \frac{\partial \mathbf{A}}{\partial t}$. So

$$
\begin{aligned}
\mathbf{E}^{n+1} &= -\nabla\phi^{n+1} - \mathbf{v}_\mathbf{A}^{n+1}, \\
\implies \nabla \cdot \mathbf{E}^{n+1} &= -\Delta\phi^{n+1} - \nabla \cdot \mathbf{v}_\mathbf{A}^{n+1} \\
&= -\Delta\phi^{n+1} - \nabla \cdot \left(\mathbf{v}_\mathbf{A}^n + c^2 \Delta t \sum_{i=n-s}^{n-1} c_i \left(\mu_0 \mathbf{J}^i + \Delta \mathbf{A}^i \right) \right) \\
&= -\Delta\phi^{n+1} - \nabla \cdot \mathbf{v}_\mathbf{A}^n + c^2 \Delta t \sum_{i=n-s}^{n-1} c_i \left(\mu_0 \nabla \cdot \mathbf{J}^i + \Delta \nabla \cdot \mathbf{A}^i \right) \\
&= -\Delta\phi^{n+1} - \nabla \cdot \mathbf{v}_\mathbf{A}^n - \mu_0 c^2 \Delta t \sum_{i=n-s}^{n-1} c_i \nabla \cdot \mathbf{J}^i - \Delta \left(c^2 \Delta t \sum_{i=n-s}^{n-1} c_i \nabla \cdot \mathbf{A}^i \right) \qquad (4.86) \\
&= -\Delta\phi^{n+1} - \nabla \cdot \mathbf{v}_\mathbf{A}^n + \frac{1}{\epsilon_0} \left(\rho^{n+1} - \rho^n \right) + \Delta \left(\phi^{n+1} - \phi^n \right) \\
&= -\Delta\phi^n - \nabla \cdot \mathbf{v}_\mathbf{A}^n + \frac{\rho^{n+1}}{\epsilon_0} - \frac{\rho^n}{\epsilon_0} \\
&= \nabla \cdot \mathbf{E}^n + \frac{\rho^{n+1}}{\epsilon_0} - \frac{\rho^n}{\epsilon_0} \\
&= \frac{\rho^{n+1}}{\epsilon_0}.
\end{aligned}
$$

The sixth line is justified by our assumption, $\epsilon_C^n = \epsilon_L^n = 0 \,\forall\, n$. The last step is justified by our inductive hypothesis. This concludes the proof. QED

Remark 4.2.6. *The properties of this method were proven after the production of our third paper, as such this remains theory and has yet to be confirmed by numerical results.*

4.2.4 The Generalized s-stage Diagonal Implicit Runge-Kutta Method

In this section we will first establish an s-stage method for solving the wave equations and continuity equation. We will then prove the properties this method, namely that conservation of charge implies satisfaction of the Lorenz gauge condition. As with the CDF and BDF methods, we will assume we are given $\mathbf{J}$ during the construction. In practice, $\mathbf{J}$ will come from a particle advance, and there are several ways to go about constructing $\mathbf{J}$ at stage values.

4.2.4.1 The s-stage DIRK Method

Consider $\frac{1}{c^2}\frac{\partial^2 u}{\partial t} - \Delta u = S$, which we rewrite as a first order system:

$$\frac{\partial}{\partial t}\begin{pmatrix} v \\ u \end{pmatrix} = \begin{pmatrix} c^2\left(S + \Delta u\right) \\ v \end{pmatrix}. \tag{4.87}$$

We apply an s-stage Runge-Kutta method, where defining $S^{(i)} \coloneqq S\left(x, t^n + c_i h\right)$, we arrive at

$$k_i^v = c^2\left(S^{(i)} + \Delta\left(u^n + h\sum_{j=1}^{i} a_{ij} k_j^u\right)\right), \tag{4.88}$$

$$k_i^u = v^n + h\sum_{j=1}^{i} a_{ij} k_j^v, \tag{4.89}$$

$$u^{n+1} = u^n + h\sum_{i=1}^{s} b_i k_i^u, \tag{4.90}$$

$$v^{n+1} = v^n + h\sum_{i=1}^{s} b_i k_i^v. \tag{4.91}$$

Here the a_{ij}, b_i, and c_i terms come from whatever Butcher tableau with which our Runge-Kutta method is working. When solving for k_i^v we use the definition of k_i^u and vice versa to arrive at,

$$\mathcal{L}_i\left[k_i^u\right] = v^n + h\sum_{j=1}^{i-1} a_{ij}k_j^v + ha_{ii}\left(c^2\left(S^{(i)} + \Delta\left(u^n + h\sum_{j=1}^{i-1} a_{ij}k_j^u\right)\right)\right), \tag{4.92}$$

$$\mathcal{L}_i\left[k_i^v\right] = c^2\left(S^{(i)} + \Delta\left(u^n + h\sum_{j=1}^{i-1} a_{ij}k_j^u\right)\right) + ha_{ii}c^2\Delta\left(v^n + h\sum_{j=1}^{i-1} a_{ij}k_j^v\right). \tag{4.93}$$

Here we have defined $\mathcal{L}_i \coloneqq \left(\mathcal{I} - \frac{1}{\alpha_i^2}\Delta\right)$ and $\alpha_i \coloneqq \frac{1}{ha_{ii}c}$. Note the k_j values are known for $j < i$.

We apply this to our system of wave equations, the Lorenz gauge, and the continuity equation. To ease the comparison, we define $v_\phi \coloneqq \frac{\partial\phi}{\partial t}$ and $v_{\mathbf{A}} \coloneqq \frac{\partial\mathbf{A}}{\partial t}$. Doing so, we see the update statements for ϕ and $\mathbf{A}$ are

$$\phi^{n+1} = \phi^n + h\sum_{i=1}^{s} b_i k_i^\phi, \tag{4.94}$$

$$\mathbf{A}^{n+1} = \mathbf{A}^n + h\sum_{i=1}^{s} b_i k_i^{\mathbf{A}}, \tag{4.95}$$

$$v_\phi^{n+1} = v_\phi^n + h\sum_{i=1}^{s} b_i k_i^{v_\phi}, \tag{4.96}$$

$$\mathbf{v}_{\mathbf{A}}^{n+1} = \mathbf{v}_{\mathbf{A}}^n + h\sum_{i=1}^{s} b_i k_i^{\mathbf{v}_{\mathbf{A}}}, \tag{4.97}$$

with the $i = 1, \cdots, s$ stage values computed according to

$$k_i^\phi = \mathcal{L}_i^{-1}\left[v_\phi^n + h\sum_{j=1}^{i-1} a_{ij}k_j^{v_\phi} + ha_{ii}c^2\frac{\rho^{(i)}}{\epsilon_0} + ha_{ii}c^2\Delta\left(\phi^n + h\sum_{j=1}^{i-1} a_{ij}k_j^\phi\right)\right], \tag{4.98}$$

$$k_i^{v_\phi} = \mathcal{L}_i^{-1}\left[\frac{\rho^{(i)}}{\epsilon_0} + \Delta\left(\phi^n + h\sum_{j=1}^{i-1} a_{ij}k_j^\phi\right) + ha_{ii}c^2\Delta\left(v_\phi^n + h\sum_{j=1}^{i-1} a_{ij}k_j^{v_\phi}\right)\right], \tag{4.99}$$

$$\mathbf{k}_i^{\mathbf{A}} = \mathcal{L}_i^{-1}\left[\mathbf{v}_{\mathbf{A}}^n + h\sum_{j=1}^{i-1} a_{ij}\mathbf{k}_j^{\mathbf{v}_{\mathbf{A}}} + ha_{ii}c^2\mu_0\mathbf{J}^{(i)} + ha_{ii}c^2\Delta\left(\mathbf{A}^n + h\sum_{j=1}^{i-1} a_{ij}\mathbf{k}_j^{\mathbf{A}}\right)\right], \tag{4.100}$$

$$\mathbf{k}_i^{\mathbf{v}_{\mathbf{A}}} = \mathcal{L}_i^{-1}\left[\mu_0\mathbf{J}^{(i)} + \Delta\left(\mathbf{A}^n + h\sum_{j=1}^{i-1} a_{ij}\mathbf{k}_j^{\mathbf{A}}\right) + ha_{ii}c^2\Delta\left(\mathbf{v}_{\mathbf{A}}^n + h\sum_{j=1}^{i-1} a_{ij}\mathbf{k}_j^{\mathbf{v}_{\mathbf{A}}}\right)\right]. \tag{4.101}$$

We do a much more straightforward update statement for the gauge and continuity update equations:

$$\phi^{n+1} = \phi^n - c^2 h \sum_{i=1}^{s} b_i \nabla \cdot \mathbf{A}^{(i)}, \tag{4.102}$$

$$\rho^{n+1} = \rho^n - h \sum_{i=1}^{s} b_i \nabla \cdot \mathbf{J}^{(i)}. \tag{4.103}$$

In the above updates we have defined $\{\mathbf{A}, \mathbf{J}, \rho\}^{(i)}$ as the i-th linear interpolation between time levels n and $n+1$ given by the Runge-Kutta method, i.e.,

$$X^{(i)} = (1 - c_i)\, X^n + c_i X^{n+1}. \tag{4.104}$$

So it follows

$$\begin{aligned} \sum_{i=1}^{r} b_i X^{(i)} &= \sum_{i=1}^{r} b_i \left((1 - c_i)\, X^n + c_i X^{n+1} \right) \\ &\equiv R^{r,n} X^n + R^{r,n+1} X^{n+1}. \end{aligned} \tag{4.105}$$

4.2.4.2 The Properties of the s-stage Method

We wish to link the satisfaction of the DIRK-s formulation of the Lorenz gauge condition (4.102) with the DIRK-s continuity equation (4.103). To do so, we define the following five residuals:

$$\epsilon_1^{n+1} \coloneqq -\phi^{n+1} + \phi^n - c^2 h \left(R^{s,n} \nabla \cdot \mathbf{A}^n + R^{s,n+1} \nabla \cdot \mathbf{A}^{n+1} \right) \tag{4.106}$$

$$\epsilon_2^{n+1} \coloneqq -v_\phi^{n+1} + v_\phi^n - c^2 h \left(R^{s,n} \nabla \cdot \mathbf{v}_\mathbf{A}^n + R^{s,n+1} \nabla \cdot \mathbf{v}_\mathbf{A}^{n+1} \right) \tag{4.107}$$

$$\epsilon_3^{n+1} \coloneqq -\rho^{n+1} + \rho^n - h \left(R^{s,n} \nabla \cdot \mathbf{J}^n + R^{s,n+1} \nabla \cdot \mathbf{J}^{n+1} \right) \tag{4.108}$$

$$\epsilon_4^{n+1} \coloneqq -k_i^{\phi,n+1} + k_i^{\phi,n} - c^2 h \left(R^{s,n} \nabla \cdot \mathbf{k}_i^{\mathbf{A},n} + R^{s,n} \nabla \cdot \mathbf{k}_i^{\mathbf{A},n+1} \right) \tag{4.109}$$

$$\epsilon_5^{n+1} \coloneqq -k_i^{v_\phi,n+1} + k_i^{v_\phi,n} - c^2 h \left(R^{s,n} \nabla \cdot \mathbf{k}_i^{\mathbf{v}_\mathbf{A},n} + R^{s,n+1} \nabla \cdot \mathbf{k}_i^{\mathbf{v}_\mathbf{A},n+1} \right) \tag{4.110}$$

We have a host of lemmas to prove that will assist with the main theorem. The first, Lemma 4.2.8, is partially related to the residual of the continuity equation (4.108) and will assist in proving Lemmas 4.2.9 and 4.2.10, which are concerned with the residuals of the k variables (4.109) and (4.110).

These lemmas assist in proving Lemmas 4.2.11 and 4.2.12, two additional lemmas concerned with the residuals of the gauge condition (4.106) and its time derivative (4.107), respectively, and these will finally assist in proving Theorem 4.2.10, that satisfaction of the semi-discrete continuity equation implies satisfaction of the semi-discrete gauge condition.

Lemma 4.2.8. *For any substep i, the following identity holds:*

$$-\frac{\rho^{(i),n}}{\epsilon_0}+\frac{\rho^{(i),n-1}}{\epsilon_0}-c^2h\mu_0\left(R^{s,n}\nabla\cdot\mathbf{J}^{(i),n-1}+R^{s,n+1}\nabla\cdot\mathbf{J}^{(i),n}\right)=\mu_0c^2\left(\left(1-c_i\right)\epsilon_3^n+c_i\epsilon_3^{n+1}\right). \tag{4.111}$$

Proof. We use the identity $c^2=\frac{1}{\mu_0\epsilon_0}$ and see

$$\begin{aligned}
&-\frac{\rho^{(i),n}}{\epsilon_0}+\frac{\rho^{(i),n-1}}{\epsilon_0}-c^2h\mu_0\left(R^{s,n}\nabla\cdot\mathbf{J}^{(i),n-1}+R^{s,n+1}\nabla\cdot\mathbf{J}^{(i),n}\right)\\
&=\mu_0\left(-\frac{\rho^{(i),n}}{\mu_0\epsilon_0}+\frac{\rho^{(i),n-1}}{\mu_0\epsilon_0}-c^2h\mu_0\left(R^{s,n}\nabla\cdot\mathbf{J}^{(i),n-1}+R^{s,n+1}\nabla\cdot\mathbf{J}^{(i),n}\right)\right)\\
&=\mu_0c^2\left(-\rho^{(i),n}+\rho^{(i),n-1}-h\left(R^{s,n}\nabla\cdot\mathbf{J}^{(i),n-1}+R^{s,n+1}\nabla\cdot\mathbf{J}^{(i),n}\right)\right).
\end{aligned} \tag{4.112}$$

Taking the interior portion, we further derive

$$\begin{aligned}
&-\left(\left(1-c_i\right)\rho^n+c_i\rho^{n+1}\right)+\left(\left(1-c_i\right)\rho^{n-1}+c_i\rho^n\right)\\
&\quad-h\left(R^{s,n}\nabla\cdot\left(\left(1-c_i\right)\mathbf{J}^{n-1}+c_i\mathbf{J}^n\right)+R^{s,n+1}\nabla\cdot\left(\left(1-c_i\right)\mathbf{J}^n+c_i\mathbf{J}^{n+1}\right)\right)\\
&=\left(1-c_i\right)\left(-\rho^n+\rho^{n-1}\right)+c_i\left(-\rho^{n+1}+\rho^n\right)\\
&\quad-h\left(\left(1-c_i\right)\left(R^{s,n}\nabla\cdot\mathbf{J}^{n-1}+R^{s,n+1}\nabla\cdot\mathbf{J}^n\right)+c_i\left(R^{s,n}\nabla\cdot\mathbf{J}^n+R^{s,n+1}\nabla\cdot\mathbf{J}^{n+1}\right)\right)\\
&=\left(1-c_i\right)\left(-\rho^n+\rho^{n-1}-h\left(R^{s,n}\nabla\cdot\mathbf{J}^{n-1}+R^{s,n+1}\nabla\cdot\mathbf{J}^n\right)\right)\\
&\quad+c_i\left(-\rho^{n+1}+\rho^n-h\left(R^{s,n}\nabla\cdot\mathbf{J}^n+R^{s,n+1}\nabla\cdot\mathbf{J}^{n+1}\right)\right)\\
&=\left(1-c_i\right)\epsilon_3^n+c_i\epsilon_3^{n+1}.
\end{aligned} \tag{4.113}$$

We have thus demonstrated the identity. QED

Lemma 4.2.9. *The* ϵ_4 *residual* (4.109) *at time level n is a linear combination of the residuals of the Lorenz gauge* (4.106) *at time level n, the time derivative of the Lorenz gauge* (4.107) *at time level n, and the continuity equation at time levels n and* $n+1$.

Proof. We prove by induction. For the base case, we see

$$\begin{aligned}
\epsilon_4^n &= -k_1^{\phi,n} + k_1^{\phi,n-1} - hc^2\left(R^n\nabla\cdot\mathbf{k}_1^{\mathbf{A},n-1} + R^{n+1}\nabla\cdot\mathbf{k}_1^{\mathbf{A},n}\right)\\
&= -\mathcal{L}_1^{-1}\left[v_\phi^n + ha_{11}c^2\left(\Delta\phi^n + \frac{\rho^{(1),n}}{\epsilon_0}\right)\right]\\
&+ \mathcal{L}_1^{-1}\left[v_\phi^{n-1} + ha_{11}c^2\left(\Delta\phi^{n-1} + \frac{\rho^{(1),n-1}}{\epsilon_0}\right)\right]\\
&- hc^2R^n\nabla\cdot\mathcal{L}_1^{-1}\left[\mathbf{v}_\mathbf{A}^{n-1} + ha_{11}c^2\left(\Delta\mathbf{A}^{n-1} + \mu_0\mathbf{J}^{(1),n-1}\right)\right]\\
&- hc^2R^{n+1}\nabla\cdot\mathcal{L}_1^{-1}\left[\mathbf{v}_\mathbf{A}^{n} + ha_{11}c^2\left(\Delta\mathbf{A}^{n} + \mu_0\mathbf{J}^{(1),n}\right)\right]\\
&= \mathcal{L}_1^{-1}\left[-v_\phi^n + v_\phi^{n-1} - hc^2\left(R^n\nabla\cdot\mathbf{v}_\mathbf{A}^{n-1} + R^{n+1}\nabla\cdot\mathbf{v}_\mathbf{A}^{n}\right)\right]\\
&+ ha_{11}c^2\mathcal{L}_1^{-1}\left[-\Delta\phi^n + \Delta\phi^{n-1} - hc^2\left(R^n\Delta\left(\nabla\cdot\mathbf{A}^{n-1}\right) + R^{n+1}\Delta\left(\nabla\cdot\mathbf{A}^{n}\right)\right)\right]\\
&+ ha_{11}c^2\mathcal{L}_1^{-1}\left[-\frac{\rho^{(1),n-1}}{\epsilon_0} + \frac{\rho^{(1),n}}{\epsilon_0} - hc^2\mu_0\left(R^n\nabla\cdot\mathbf{J}^{(1),n-1} + R^{n+1}\nabla\cdot\mathbf{J}^{(1),n}\right)\right]\\
&= \mathcal{L}_1^{-1}\left[\epsilon_2^n + ha_{11}c^2\Delta\epsilon_1^n + ha_{11}c^4\mu_0\left((1-c_1)\,\epsilon_3^n + c_1\epsilon_3^{n+1}\right)\right]
\end{aligned} \tag{4.114}$$

The last step is justified definitionally and by Lemma 4.2.8. We have shown the base case, now we wish to show the inductive step. Assuming true for $i = l-1$, we now consider $i = l$:

$$\begin{aligned}
&\epsilon_4^n = -k_l^{\phi,n} + k_l^{\phi,n-1} - hc^2\left(R^{s,n}\nabla\cdot\mathbf{k}_l^{\mathbf{A},n-1} + R^{s,n+1}\nabla\cdot\mathbf{k}_l^{\mathbf{A},n}\right)\\
&= -\mathcal{L}_l^{-1}\left[v_\phi^{n-1} + h\sum_{j=1}^{l-1}a_{lj}k_j^{v_\phi,n-1} + ha_{ll}c^2\frac{\rho^{(l),n-1}}{\epsilon_0} + ha_{ll}c^2\Delta\left(\phi^{n-1} + h\sum_{j=1}^{l-1}a_{lj}k_j^{\phi,n-1}\right)\right]\\
&+\mathcal{L}_l^{-1}\left[v_\phi^{n-2} + h\sum_{j=1}^{l-1}a_{lj}k_j^{v_\phi,n-2} + ha_{ll}c^2\frac{\rho^{(l),n-2}}{\epsilon_0} + ha_{ll}c^2\Delta\left(\phi^{n-2} + h\sum_{j=1}^{l-1}a_{lj}k_j^{\phi,n-2}\right)\right]\\
&-hc^2R^{s,n}\nabla\cdot\left(\mathcal{L}_l^{-1}\left[\mathbf{v}_\mathbf{A}^{n-2} + h\sum_{j=1}^{l-1}a_{lj}\mathbf{k}_j^{\mathbf{v}_\mathbf{A},n-2} + ha_{ll}c^2\mu_0\mathbf{J}^{(l),n-2} + ha_{ll}c^2\Delta\left(\mathbf{A}^{n-2} + h\sum_{j=1}^{l-1}a_{lj}\mathbf{k}_j^{\mathbf{A},n-2}\right)\right]\right)\\
&-hc^2R^{s,n+1}\nabla\cdot\left(\mathcal{L}_l^{-1}\left[\mathbf{v}_\mathbf{A}^{n-1} + h\sum_{j=1}^{l-1}a_{lj}\mathbf{k}_j^{\mathbf{v}_\mathbf{A},n-1} + ha_{ll}c^2\mu_0\mathbf{J}^{(l),n-1} + ha_{ll}c^2\Delta\left(\mathbf{A}^{n-1} + h\sum_{j=1}^{l-1}a_{lj}\mathbf{k}_j^{\mathbf{A},n-1}\right)\right]\right).
\end{aligned} \tag{4.115}$$

Grouping all of these inside $\mathcal{L}_l^{-1}$, we can break all these apart, rearrange, and either using definitions or

Lemma 4.2.8 to see the argument passed to this operator takes the form:

$$
\begin{aligned}
&- v_\phi^{n-1} + v_\phi^{n-2} - hc^2 \left(hc^2 R^{s,n} \mathbf{v}_\mathbf{A}^{n-1} + R^{s,n+1} \mathbf{v}_\mathbf{A}^{n-1} \right) \\
&+ ha_{ll} c^2 \left(-\frac{\rho^{(l),n-1}}{\epsilon_0} + \frac{\rho^{(l),n-2}}{\epsilon_0} - hc^2 \mu_0 \left(R^{s,n} \nabla \cdot \mathbf{J}^{(l),n-2} + R^{s,n+1} \nabla \cdot \mathbf{J}^{(l),n-1} \right) \right) \\
&+ h^2 a_{ll} c^2 \Delta \left(-\phi^{n-1} + \phi^{n-2} - hc^2 \left(R^{s,n} \nabla \cdot \mathbf{A}^{n-2} + R^{s,n+1} \nabla \cdot \mathbf{A}^{n-1} \right) \right) \\
&+ h^2 a_{ll} c^2 \Delta \sum_{j=1}^{l-1} a_{lj} \left(-k_j^{\phi,n-1} + k_j^{\phi,n-2} - hc^2 \left(R^{s,n} \nabla \cdot \mathbf{k}^{\mathbf{A},n-2} + R^{s,n+1} \nabla \cdot \mathbf{k}_j^{\mathbf{A},n-1} \right) \right) \\
&= \epsilon_2^{n-1} + ha_{ll} c^2 \mu_0 c^2 \left((1 - c_l) \epsilon_3^{n-1} + c_l \epsilon_3^n \right) + ha_{ll} c^2 \Delta \epsilon_1^{n-1} + h^2 a_{11} c^2 \Delta \sum_{j=1}^{l-1} a_{lj} \alpha_l^{n-1}.
\end{aligned}
\tag{4.116}
$$

We define α_l^{n-1} to be some residual that is a linear combination of ϵ_1^{n-1}, ϵ_2^{n-1}, and ϵ_3^{n-1}. This is justified by our inductive hypothesis. We have demonstrated ϵ_4^n is a linear combination of residuals of previous timesteps for any number of substeps. QED

Lemma 4.2.10. *The ϵ_5 residual* (4.110) *at time level n is a linear combination of the residuals of the Lorenz gauge* (4.106) *at time level n, the time derivative of the Lorenz gauge* (4.107) *at time level n, the continuity equation at time levels n and n + 1, and the ϵ_4 residual (itself a linear combination of the other three residuals) at time level n.*

Proof. We prove by induction. For the base case, we see

$$
\begin{aligned}
\epsilon_5^n &= -k_1^{v_\phi,n} + k_1^{v_\phi,n-1} - hc^2 \left(R^n \nabla \cdot \mathbf{k}_1^{\mathbf{v_A},n-1} + R^{n+1} \nabla \cdot \mathbf{k}_1^{\mathbf{v_A},n} \right) \\
&= -\mathcal{L}_1^{-1} \left[c^2 \left(\Delta \phi^n + \frac{\rho^{(1),n}}{\epsilon_0} + ha_{11} \Delta v_\phi^n \right) \right] + \mathcal{L}_1^{-1} \left[c^2 \left(\Delta \phi^{n-1} + \frac{\rho^{(1),n-1}}{\epsilon_0} + ha_{11} \Delta v_\phi^{n-1} \right) \right] \\
&- hc^2 R^n \nabla \cdot \mathcal{L}_1^{-1} \left[c^2 \left(\Delta \mathbf{A}^{n-1} + \mu_0 \mathbf{J}^{(1),n-1} + ha_{11} \Delta \mathbf{v}_\mathbf{A}^{n-1} \right) \right] \\
&- hc^2 R^{n+1} \nabla \cdot \mathcal{L}_1^{-1} \left[c^2 \left(\Delta \mathbf{A}^n + \mu_0 \mathbf{J}^{(1),n} + ha_{11} \Delta \mathbf{v}_\mathbf{A}^n \right) \right] \\
&= c^2 \mathcal{L}_1^{-1} \left[\Delta \left(-\phi^n + \phi^{n-1} - hc^2 \left(R^n \nabla \cdot \mathbf{A}^{n-1} + R^{n+1} \nabla \cdot \mathbf{A}^n \right) \right) \right] \\
&+ c^2 \mathcal{L}_1^{-1} \left[-\frac{\rho^{(1),n}}{\epsilon_0} + \frac{\rho^{(1),n-1}}{\epsilon_0} - hc^2 \mu_0 \left(R^n \nabla \cdot \mathbf{J}^{(1),n-1} + R^{n+1} \nabla \cdot \mathbf{J}^{(1),n} \right) \right] \\
&+ ha_{11} c^2 \mathcal{L}_1^{-1} \left[\Delta \left(-v_\phi^n + v_\phi^{n-1} - hc^2 \left(R^n \nabla \cdot \mathbf{A}_\mathbf{A}^n + R^{n+1} \nabla \cdot \mathbf{v}_\mathbf{A}^{n-1} \right) \right) \right] \\
&= c^2 \mathcal{L}_1^{-1} \left[\Delta \epsilon_1^n \right] + c^4 \mu_0 \mathcal{L}_1^{-1} \left[(1 - c_1) \epsilon_3^n + c_1 \epsilon_3^{n+1} \right] + ha_{11} c^2 \mathcal{L}_1^{-1} \left[\epsilon_2^n \right]
\end{aligned}
\tag{4.117}
$$

The last step is justified definitionally and by Lemma 4.2.8. We have proven the base case, now we assume true for $i = l - 1$ substeps. We consider $i = l$ and see

$$
\begin{aligned}
&- k_l^{v_\phi,n} + k_l^{v_\phi,n-1} - hc^2\left(R^{s,n}\nabla\cdot\mathbf{k}_l^{\mathbf{v_A},n-1} + R^{s,n+1}\nabla\cdot\mathbf{k}_l^{\mathbf{v_A},n}\right)\\
&= -\mathcal{L}_l^{-1}\left[\frac{\rho^{(l),n-1}}{\epsilon_0} + \Delta\left(\phi^{n-1} + h\sum_{j=1}^{l-1}a_{lj}k_j^{\phi,n-1}\right) + ha_{ll}c^2\Delta\left(v_\phi^{n-1} + h\sum_{j=1}^{l-1}a_{lj}k_j^{v_\phi,n-1}\right)\right]\\
&+ \mathcal{L}_l^{-1}\left[\frac{\rho^{(l),n-2}}{\epsilon_0} + \Delta\left(\phi^{n-2} + h\sum_{j=1}^{l-1}a_{lj}k_j^{\phi,n-2}\right) + ha_{ll}c^2\Delta\left(v_\phi^{n-2} + h\sum_{j=1}^{l-1}a_{lj}k_j^{v_\phi,n-2}\right)\right]\\
&- hc^2R^{s,n}\nabla\cdot\mathcal{L}_l^{-1}\left[\mu_0\mathbf{J}^{(l),n-2} + \Delta\left(\mathbf{A}^{n-2} + h\sum_{j=1}^{l-1}a_{lj}\mathbf{k}_j^{\mathbf{A},n-2}\right) + ha_{ll}c^2\Delta\left(\mathbf{v}_\mathbf{A}^{n-2} + h\sum_{j=1}^{l-1}a_{lj}\mathbf{k}_j^{\mathbf{v_A},n-1}\right)\right]\\
&- hc^2R^{s,n+1}\nabla\cdot\mathcal{L}_l^{-1}\left[\mu_0\mathbf{J}^{(l),n-1} + \Delta\left(\mathbf{A}^{n-1} + h\sum_{j=1}^{l-1}a_{lj}\mathbf{k}_j^{\mathbf{A},n-1}\right) + ha_{ll}c^2\Delta\left(\mathbf{v}_\mathbf{A}^{n-1} + h\sum_{j=1}^{l-1}a_{lj}\mathbf{k}_j^{\mathbf{v_A},n-1}\right)\right]
\end{aligned}
\tag{4.118}
$$

We can group all of this within the $\mathcal{L}_l^{-1}$ operator and, taking the entire argument, we rearrange and see

$$
\begin{aligned}
&- \frac{\rho^{(l),n-1}}{\epsilon_0} + \frac{\rho^{(l)},n-1}{\epsilon_0} - hc^2\mu_0\left(R^{s,n}\nabla\cdot\mathbf{J}^{(l),n-2} + R^{s,n+1}\nabla\cdot\mathbf{J}^{n-1}\right)\\
&+ \Delta\left(-\phi^{n-1} + \phi^{n-2} - hc^2\left(R^{s,n}\nabla\cdot\mathbf{A}^{n-2} + R^{s,n+1}\nabla\cdot\mathbf{A}^{n-1}\right)\right)\\
&+ h\Delta\sum_{j=1}^{l-1}a_{lj}\left(-k_j^{\phi,n-1} + k_j^{\phi,n-2} - hc^2\left(R^{s,n}\nabla\cdot\mathbf{k}_j^{\mathbf{A},n-2} + R^{s,n+1}\nabla\cdot\mathbf{k}_j^{\mathbf{A},n-1}\right)\right)\\
&+ ha_{ll}c^2\Delta\left(-v_\phi^{n-1} + v_\phi^{n-2} - hc^2\left(R^{s,n}\nabla\cdot\mathbf{v}_\mathbf{A}^{n-1} + R^{s,n+1}\nabla\cdot\mathbf{v}_\mathbf{A}^{n-1}\right)\right)\\
&+ h^2a_{ll}c^2\Delta\sum_{j=1}^{l-1}a_{lj}\left(-k_j^{v_\phi,n-1} + k_j^{v_\phi,n-2} - hc^2\left(R^{s,n}\nabla\cdot\mathbf{k}_j^{\mathbf{v_A},n-2} + R^{s,n+1}\nabla\cdot\mathbf{k}_j^{\mathbf{v_A},n-1}\right)\right)\\
&= \mu_0c^2\left((1-c_l)\,\epsilon_3^{n-1} + c_l\epsilon_3^n\right) + \Delta\epsilon_1 + h\Delta\sum_{j=1}^{l-1}\alpha_l^{n-1} + ha_{ll}c^2\Delta\epsilon_2^{n-1} + h^2a_{ll}c^2\Delta\sum_{j=1}^{l-1}\beta_l^{n-1}.
\end{aligned}
\tag{4.119}
$$

Here we have set β_l as some linear combination of ϵ_1^{n-1}, ϵ_2^{n-1}, and ϵ_3^{n-1}, justified by our inductive hypothesis. α_l^{n-1} is likewise a linear combination of these residuals and is justified by Lemma 4.2.9. We have demonstrated ϵ_5^n is a linear combination of residuals of previous timesteps for any amount of substeps. QED

With these two lemmas in hand, we will prove the following lemmas further relating the residuals.

Lemma 4.2.11. *The residual of the Lorenz gauge condition* (4.106) *at time level* $n+1$ *is a linear combination of the residuals of the Lorenz gauge* (4.106)*, the time derivative of the Lorenz gauge* (4.107)*, and the continuity equation* (4.108)*.*

Proof. Consider the Lorenz gauge at time $n+1$:

$$\epsilon_1^{n+1} = -\phi^{n+1} + \phi^n - c^2 h \left(R^{s,n} \nabla \cdot \mathbf{A}^n + R^{s,n+1} \nabla \cdot \mathbf{A}^{n+1} \right) \tag{4.120}$$

We plug in our update equations (4.94) and (4.95):

$$\begin{aligned}
\epsilon_1^{n+1} &= -\left(\phi^n + h \sum_{i=1}^{s} b_i k_i^{\phi,n} \right) + \left(\phi^{n-1} + h \sum_{i=1}^{s} b_i k_i^{\phi,n-1} \right) \\
&\quad - c^2 h \left(R^{s,n} \nabla \cdot \left(\mathbf{A}^{n-1} + h \sum_{i=1}^{s} b_i \mathbf{k}_i^{\mathbf{A},n-1} \right) + R^{s,n+1} \nabla \cdot \left(\mathbf{A}^n + h \sum_{i=1}^{s} b_i \mathbf{k}_i^{\mathbf{A},n} \right) \right) \\
&= -\phi^n + \phi^{n-1} - c^2 h \left(R^{s,n} \nabla \cdot \mathbf{A}^{n-1} + R^{s,n+1} \nabla \cdot \mathbf{A}^n \right) \\
&\quad + h \sum_{i=1}^{s} b_i \left(-k_i^{\phi,n} + k_i^{\phi,n-1} - c^2 h \left(R^{s,n} \mathbf{k}_i^{\mathbf{A},n-1} + R^{s,n+1} \nabla \cdot \mathbf{k}_i^{\mathbf{A},n} \right) \right)
\end{aligned} \tag{4.121}$$

The first term is by definition ϵ_1^n, the second term is a linear combination of ϵ_1^n, ϵ_2^n, ϵ_3^n, and ϵ_3^{n+1} by Lemma 4.2.9. QED

Lemma 4.2.12. *The residual of the time derivative of the Lorenz gauge condition* (4.107) *at time level* $n+1$ *is a linear combination of the residuals of the Lorenz gauge* (4.106) *at time level* n*, the time derivative of the Lorenz gauge* (4.107) *at time level* n*, the continuity equation* (4.108) *at time levels* n *and* $n+1$*.*

Proof. Consider the residual of the time derivative of the Lorenz gauge at time $n+1$:

$$\epsilon_2^{n+1} = -v_\phi^{n+1} + v_\phi^n - c^2 h \left(R^{s,n} \nabla \cdot \mathbf{v}_{\mathbf{A}}^n + R^{s,n+1} \nabla \cdot \mathbf{v}_{\mathbf{A}}^{n+1} \right) \tag{4.122}$$

We plug in our update equations (4.96) and (4.97):

$$\begin{aligned}
\epsilon_2^{n+1} &= -\left(v_\phi^n + h\sum_{i=1}^{s} b_i k_i^{v_\phi,n}\right) + \left(v_\phi^{n-1} + h\sum_{i=1}^{s} b_i k_i^{v_\phi,n-1}\right) \\
&\quad - c^2 h\left(R^{s,n}\nabla\cdot\left(\mathbf{v}_\mathbf{A}^{n-1} + h\sum_{i=1}^{s} b_i \mathbf{k}_i^{\mathbf{v}_\mathbf{A},n-1}\right) + R^{s,n+1}\nabla\cdot\left(\mathbf{v}_\mathbf{A}^{n} + h\sum_{i=1}^{s} b_i \mathbf{k}_i^{\mathbf{v}_\mathbf{A},n}\right)\right) \\
&= -v_\phi^n + v_\phi^{n-1} - c^2 h\left(R^{s,n}\nabla\cdot\mathbf{v}_\mathbf{A}^{n-1} + R^{s,n+1}\nabla\cdot\mathbf{v}_\mathbf{A}^{n}\right) \\
&\quad + h\sum_{i=1}^{s} b_i\left(-k_i^{v_\phi,n} + k_i^{v_\phi,n-1} - c^2 h\left(R^{s,n}\mathbf{k}_i^{\mathbf{v}_\mathbf{A},n-1} + R^{s,n+1}\nabla\cdot\mathbf{k}_i^{\mathbf{v}_\mathbf{A},n}\right)\right).
\end{aligned} \tag{4.123}$$

The first term is by definition ϵ_2^n, the second term is a linear combination of ϵ_1^n, ϵ_2^n, ϵ_3^n, ϵ_3^{n+1}, and ϵ_4^n by Lemma 4.2.10. The same lemma shows ϵ_4^n is a linear combination of the other four residuals. QED

With Lemmas 4.2.11 and 4.2.12 at hand, we are now ready to prove the following theorem.

Theorem 4.2.10. *Assuming the residuals of the continuity and gauge condition* (4.106)-(4.108) *are zero for timestep* $n = 0$*, the residuals of the Lorenz gauge condition* (4.106)-(4.107) *are zero for all time steps* $n > 0$ *if the residual of the continuity equation* (4.108) *is zero for all time* $n > 0$*.*

Proof. Assume the residuals are zero for the starting conditions. Additionally, assume the residual for the continuity equation is zero for all time. By Lemma 4.2.11, we know ϵ_1^{n+1} is a linear combination of ϵ_1^n, ϵ_2^n, ϵ_3^n, and ϵ_3^{n+1}. ie

$$\epsilon_1^{n+1} = \mathcal{L}_i^{-1}\left[A\epsilon_1^n + B\epsilon_2^n + C\epsilon_3^n + D\epsilon_3^{n+1}\right]. \tag{4.124}$$

By our assumption, $\epsilon_3^k = 0\,\forall\, k$. Thus

$$\epsilon_1^{n+1} = \mathcal{L}_i^{-1}\left[A\epsilon_1^n + B\epsilon_2^n\right]. \tag{4.125}$$

Clearly, if $\epsilon_1^0 = \epsilon_2^0 = 0$, then by induction we have $\epsilon_1^{n+1} = 0$. Thus $\epsilon_1^k = 0\,\forall\, k$.

Lemma 4.2.12 gives that ϵ_2^{n+1} is a linear combination of ϵ_1^n, ϵ_2^n, ϵ_3^n, and ϵ_3^{n+1}. Similar logic will show that our assumptions imply $\epsilon_2^k = 0\,\forall\, k$.

If the residual of the continuity equation (4.108) is zero for all time, then the residuals for the Lorenz gauge (4.106)-(4.107) are zero for all time. QED

Remark 4.2.7. *In this generalization we have proven only one direction of the "if and only if" relationship indicated by the above schemes. However, for our purposes we are only interested in satisfaction of the continuity equation implying satisfaction of the Lorenz gauge, and so this suffices for now. The other direction will be proven for DIRK-2, indicating generalization to s stages is possible, but this will require more work.*

Remark 4.2.8. *Given this unidirectional relation, we were able to prove the relationship using only a generic linear combination of residuals, we did not need any specifics as to the coefficients. To prove the other direction, these details will be necessary.*

Remark 4.2.9. *For neither DIRK-2 nor the generalized DIRK-s methods have we established that Gauss's law for electricity is satisfied if the semi-discrete Lorenz gauage condition is satisfied. Stages beyond the first involve compounded inverse linear operators that render such a property intractable to prove. This is not to suggest that Runge-Kutta methods exclude this property, for example the implicit midpoint rule gives this relationship. Further work needs to be done to design Runge-Kutta methods that demonstrably have this property.*

4.2.4.3 The 2-stage Diagonal Implicit Runge-Kutta Method

We can prove that satisfaction of the semi-discrete Lorenz gauge implies satisfaction of the semi-discrete continuity equation for the 2-stage DIRK method (DIRK-2), using some of the tools provided above. The DIRK-2 method for the wave equation is as follows:

$$\phi^{n+1} = \phi^n + h\left(b_1 k_1^{\phi} + b_2 k_2^{\phi}\right), \tag{4.126}$$

$$\mathbf{A}^{n+1} = \mathbf{A}^n + h\left(b_1 \mathbf{k}_1^{\mathbf{A}} + b_2 \mathbf{k}_2^{\mathbf{A}}\right). \tag{4.127}$$

The substep variables are

$$k_1^\phi = \mathcal{L}_1^{-1}\left[v_\phi^n + ha_{11}c^2\left(\Delta\phi^n + \frac{\rho^{(1)}}{\epsilon_0}\right)\right], \tag{4.128}$$

$$k_2^\phi = \mathcal{L}_2^{-1}\left[v_\phi^n + ha_{21}c^2 k_1^{v_\phi} + ha_{22}c^2\left(\Delta\phi^n + ha_{21}\Delta k_1^\phi + \frac{\rho^{(2)}}{\epsilon_0}\right)\right], \tag{4.129}$$

$$\mathbf{k}_1^{\mathbf{A}} = \mathcal{L}_1^{-1}\left[\mathbf{v}_{\mathbf{A}}^n + ha_{11}c^2\left(\Delta\mathbf{A}^n + \mu_0\mathbf{J}^{(1)}\right)\right], \tag{4.130}$$

$$\mathbf{k}_2^{\mathbf{A}} = \mathcal{L}_2^{-1}\left[\mathbf{v}_{\mathbf{A}}^n + ha_{21}c^2\mathbf{k}_1^{\mathbf{v}_\mathbf{A}} + ha_{22}c^2\left(\Delta\mathbf{A}^n + ha_{21}\Delta\mathbf{k}_1^{\mathbf{A}} + \mu_0\mathbf{J}^{(2)}\right)\right]. \tag{4.131}$$

As with DIRK-s, we have defined $\mathcal{L}_i \coloneqq \left(\mathcal{I} - \frac{1}{\alpha_i^2}\Delta\right)$, $\alpha_i \coloneqq \frac{1}{ha_{ii}c}$, $v_\phi \coloneqq \frac{\partial\phi}{\partial t}$, and $v_{\mathbf{A}} \coloneqq \frac{\partial\mathbf{A}}{\partial t}$.

We see the update statements for ϕ and $\mathbf{A}$ are

$$k_1^\phi = \mathcal{L}_1^{-1}\left[v_\phi^n + ha_{11}c^2\left(\Delta\phi^n + \frac{\rho^{(1)}}{\epsilon_0}\right)\right], \tag{4.132}$$

$$k_1^{v_\phi} = \mathcal{L}_1^{-1}\left[c^2\left(\Delta\phi^n + \frac{\rho^{(1)}}{\epsilon_0} + ha_{11}\Delta v_\phi^n\right)\right], \tag{4.133}$$

$$k_2^\phi = \mathcal{L}_2^{-1}\left[v_\phi^n + ha_{21}c^2 k_1^\phi + ha_{22}c^2\left(\Delta\phi^n + ha_{21}\Delta k_1^\phi + \frac{\rho^{(2)}}{\epsilon_0}\right)\right], \tag{4.134}$$

$$k_2^{v_\phi} = \mathcal{L}_2^{-1}\left[c^2\left(\frac{\rho^{(2)}}{\epsilon_0} + \Delta\phi^n + ha_{22}c^2\Delta k_1^\phi + ha_{22}\Delta\left(v_\phi^n + ha_{21}k_1^{v_\phi}\right)\right)\right]. \tag{4.135}$$

Likewise, for v_ϕ and $\mathbf{v}_{\mathbf{A}}$:

$$v_\phi^{n+1} = v_\phi^n + h\left(b_1 k_1^{v_\phi} + b_2 k_2^{v_\phi}\right), \tag{4.136}$$

$$\mathbf{v}_{\mathbf{A}}^{n+1} = \mathbf{v}_{\mathbf{A}}^n + h\left(b_1\mathbf{k}_1^{\mathbf{v}_\mathbf{A}} + b_2\mathbf{k}_2^{v_\mathbf{A}}\right). \tag{4.137}$$

These have substep variables:

$$k_1^{v_\phi} = \mathcal{L}_1^{-1}\left[c^2\left(\Delta\phi^n + \frac{\rho^{(1)}}{\epsilon_0} + ha_{11}\Delta v_\phi^n\right)\right], \tag{4.138}$$

$$k_2^{v_\phi} = \mathcal{L}_2^{-1}\left[c^2\left(\frac{\rho^{(2)}}{\epsilon_0} + \Delta\phi^n + ha_{22}c^2\Delta k_1^\phi + ha_{22}\Delta\left(v_\phi^n + ha_{21}k_1^{v_\phi}\right)\right)\right], \tag{4.139}$$

$$\mathbf{k}_1^{\mathbf{v}_\mathbf{A}} = \mathcal{L}_1^{-1}\left[c^2\left(\Delta\mathbf{A}^n + \mu_0\mathbf{J}^{(1)} + ha_{11}\Delta\mathbf{v}_{\mathbf{A}}^n\right)\right], \tag{4.140}$$

$$\mathbf{k}_2^{\mathbf{v}_\mathbf{A}} = \mathcal{L}_2^{-1}\left[c^2\left(\mu_0\mathbf{J}^{(2)} + \Delta\mathbf{A}^n + ha_{22}c^2\Delta\mathbf{k}_1^{\mathbf{A}} + ha_{22}\Delta\left(\mathbf{v}_{\mathbf{A}}^n + ha_{21}\mathbf{k}_1^{\mathbf{v}_\mathbf{A}}\right)\right)\right]. \tag{4.141}$$

Now, we can do a similar update statement for the gauge and continuity equations:

$$\phi^{n+1} = \phi^n - c^2 h \left(b_1 \nabla \cdot \mathbf{A}^{(1)} + b_2 \nabla \cdot \mathbf{A}^{(2)} \right), \tag{4.142}$$

$$\rho^{n+1} = \rho^n - h \left(b_1 \nabla \cdot \mathbf{J}^{(1)} + b_2 \nabla \cdot \mathbf{J}^{(2)} \right). \tag{4.143}$$

Here we have defined $\{A, J\}^{(i)}$ as the ith linear interpolation between n and $n+1$ given by the Runge-Kutta method, ie

$$X^{(i)} = (1 - c_i) X^n + c_i X^{n+1}. \tag{4.144}$$

So it follows

$$\begin{aligned} b_1 X^{(1)} + b_2 X^{(2)} &= (b_1 (1 - c_1) + b_2 (1 - c_1)) X^n + (b_1 c_1 + b_2 c_2) X^{n+1} \\ &\equiv R^n X^n + R^{n+1} X^{n+1}. \end{aligned} \tag{4.145}$$

4.2.4.4 Properties of DIRK-2

Having described the update method, we now wish to link the satisfaction of the DIRK-2 formulation of the Lorenz gauge condition (4.142) with the DIRK-2 continuity equation (4.143). To do so, we define the following three residuals:

$$\epsilon_1^{n+1} \coloneqq -\phi^{n+1} + \phi^n - c^2 h \left(R^n \nabla \cdot \mathbf{A}^n + R^{n+1} \nabla \cdot \mathbf{A}^{n+1} \right), \tag{4.146}$$

$$\epsilon_2^{n+1} \coloneqq -v_\phi^{n+1} + v_\phi^n - c^2 h \left(R^n \nabla \cdot \mathbf{v}_\mathbf{A}^n + R^{n+1} \nabla \cdot \mathbf{v}_\mathbf{A}^{n+1} \right). \tag{4.147}$$

$$\epsilon_3^{n+1} \coloneqq -\rho^{n+1} + \rho^n - h \left(R^n \nabla \cdot \mathbf{J}^n + R^{n+1} \nabla \cdot \mathbf{J}^{n+1} \right), \tag{4.148}$$

Additionally, we have the following identities, the first two established by Lemma 4.2.8 and the

last two by the base cases of Lemmas 4.2.9 and 4.2.10, respectively.

$$\begin{aligned} -\frac{\rho^{(1),n}}{\epsilon_0} + \frac{\rho^{(1),n-1}}{\epsilon_0} &- c^2 h\mu_0 \left(R^n \nabla \cdot \mathbf{J}^{(1),n-1} + R^{n+1} \nabla \cdot \mathbf{J}^{(1),n} \right) \\ &= \mu_0 c^2 \left((1 - c_1)\, \epsilon_3^n + c_1 \epsilon_3^{n+1} \right), \end{aligned} \tag{4.149}$$

$$\begin{aligned} -\frac{\rho^{(2),n}}{\epsilon_0} + \frac{\rho^{(2),n-1}}{\epsilon_0} &- c^2 h\mu_0 \left(R^n \nabla \cdot \mathbf{J}^{(2),n-1} + R^{n+1} \nabla \cdot \mathbf{J}^{(2),n} \right) \\ &= \mu_0 c^2 \left((1 - c_2)\, \epsilon_3^n + c_2 \epsilon_3^{n+1} \right), \end{aligned} \tag{4.150}$$

$$\begin{aligned} -k_1^{\phi,n} + k_1^{\phi,n-1} &- hc^2 \left(R^n \nabla \cdot \mathbf{k}_1^{\mathbf{A},n-1} + R^{n+1} \nabla \cdot \mathbf{k}_1^{\mathbf{A},n} \right) \\ &= \mathcal{L}_1^{-1} \left[\epsilon_2^n + h a_{11} c^2 \Delta \epsilon_1^n + h a_{11} c^4 \mu_0 \left((1 - c_1)\, \epsilon_3^n + c_1 \epsilon_3^{n+1} \right) \right], \end{aligned} \tag{4.151}$$

$$\begin{aligned} -k_1^{v_\phi,n} + k_1^{v_\phi,n-1} &- hc^2 \left(R^n \nabla \cdot \mathbf{k}_1^{\mathbf{v}_\mathbf{A},n-1} + R^{n+1} \nabla \cdot \mathbf{k}_1^{\mathbf{v}_\mathbf{A},n} \right) \\ &= c^2 \mathcal{L}_1^{-1} \left[\Delta \epsilon_1^n + c^2 \mu_0 \left((1 - c_1)\, \epsilon_3^n + c_1 \epsilon_3^{n+1} \right) + h a_{11} \epsilon_2^n \right]. \end{aligned} \tag{4.152}$$

With these in mind, we wish to prove the following lemmas.

Lemma 4.2.13. *The residual of the Lorenz gauge condition* (4.146) *at time level* $n+1$ *is a linear combination of the residuals of the Lorenz gauge* (4.146) *at time level* n*, the time derivative of the Lorenz gauge condition* (4.147) *at time level* n*, and the continuity equation* (4.148) *at time levels* n *and* $n+1$*.*

Proof. Consider the residual of the Lorenz gauge (4.146) at time $n+1$.

$$\epsilon_1^{n+1} = -\phi^{n+1} + \phi^n - c^2 h \left(R^n \nabla \cdot \mathbf{A}^n + R^{n+1} \nabla \cdot \mathbf{A}^{n+1} \right).$$

We plug in our update equations (4.126)-(4.127) and see

$$\begin{aligned} \epsilon_1^{n+1} = &- \left(\phi^n + h \left(b_1 k_1^{\phi,n} + b_2 k_2^{\phi,n} \right) \right) + \left(\phi^{n-1} + h \left(b_1 k_1^{\phi,n-1} + b_2 k_2^{\phi,n-1} \right) \right) \\ &- c^2 h \left(R^n \nabla \cdot \left(\mathbf{A}^{n-1} + h \left(b_1 \mathbf{k}_1^{\mathbf{A},n-1} + b_2 \mathbf{k}_2^{\mathbf{A},n-1} \right) \right) + R^{n+1} \nabla \cdot \left(\mathbf{A}^n + h \left(b_1 \mathbf{k}_1^{\mathbf{A},n} + b_2 \mathbf{k}_2^{\mathbf{A},n} \right) \right) \right) \end{aligned} \tag{4.153}$$

We note that the first variable in each parenthetical, if combined, forms the definition of residual (4.146) at time level n. We do so and then use the definition of the k variables (4.128)-(4.131) to

expand into the following:

$$
\begin{aligned}
\epsilon_1^{n+1} = & -\phi^n + \phi^{n-1} - c^2 h \left(R^n \nabla \cdot \mathbf{A}^{n-1} + R^{n+1} \nabla \cdot \mathbf{A}^n \right) \\
& - h b_1 \mathcal{L}_1^{-1} \left[v_\phi^n + h a_{11} c^2 \left(\Delta \phi^n + \frac{\rho^{(1)}}{\epsilon_0} \right) \right] \\
& - h b_2 \mathcal{L}_2^{-1} \left[v_\phi^n + h a_{21} c^2 k_1^{v_\phi, n} + h a_{22} c^2 \left(\Delta \phi^n + h a_{21} \Delta k_1^{\phi, n} + \frac{\rho^{(2)}}{\epsilon_0} \right) \right] \\
& + h b_1 \mathcal{L}_1^{-1} \left[v_\phi^{n-1} + h a_{11} c^2 \left(\Delta \phi^{n-1} + \frac{\rho^{(1),n-1}}{\epsilon_0} \right) \right] \\
& + h b_2 \mathcal{L}_2^{-1} \left[v_\phi^{n-1} + h a_{21} c^2 k_1^{v_\phi, n-1} + h a_{22} c^2 \left(\Delta \phi^{n-1} + h a_{21} \Delta k_1^{\phi, n-1} + \frac{\rho^{(2),n-1}}{\epsilon_0} \right) \right] \\
& - h^2 c^2 R^n b_1 \mathcal{L}_1^{-1} \left[\nabla \cdot \mathbf{v}_\mathbf{A}^{n-1} + h a_{11} c^2 \left(\Delta \left(\nabla \cdot \mathbf{A}^{n-1} \right) + \mu_0 \nabla \cdot \mathbf{J}^{(1),n-1} \right) \right] \\
& - h^2 c^2 R^n b_2 \mathcal{L}_2^{-1} \left[\nabla \cdot \mathbf{v}_\mathbf{A}^{n-1} + h a_{21} c^2 \nabla \cdot \mathbf{k}_1^{\mathbf{v_A}, n-1} \right] \\
& \quad - h^2 c^2 R^n b_2 \mathcal{L}_2^{-1} \left[h a_{22} c^2 \left(\Delta \left(\nabla \cdot \mathbf{A}^{n-1} \right) + h a_{21} \Delta \left(\nabla \cdot \mathbf{k}_1^{\mathbf{A}, n-1} \right) + \mu_0 \nabla \cdot \mathbf{J}^{(2),n-1} \right) \right] \\
& - h^2 c^2 R^{n+1} b_1 \mathcal{L}_1^{-1} \left[\nabla \cdot \mathbf{v}_\mathbf{A}^n + h a_{11} c^2 \left(\Delta \left(\nabla \cdot \mathbf{A}^n \right) + \mu_0 \nabla \cdot \mathbf{J}^{(1),n} \right) \right] \\
& - h^2 c^2 R^{n+1} b_2 \mathcal{L}_2^{-1} \left[\nabla \cdot \mathbf{v}_\mathbf{A}^n + h a_{21} c^2 \nabla \cdot \mathbf{k}_1^{\mathbf{v_A}, n} \right] \\
& \quad - h^2 c^2 R^{n+1} b_2 \mathcal{L}_2^{-1} \left[h a_{22} c^2 \left(\Delta \left(\nabla \cdot \mathbf{A}^n \right) + h a_{21} \Delta \left(\nabla \cdot \mathbf{k}_1^{\mathbf{A}, n} \right) + \mu_0 \nabla \cdot \mathbf{J}^{(2),n} \right) \right]
\end{aligned}
\tag{4.154}
$$

We already noted the first row is the definition of the first residual at time level n. For the rest of the rows, a pattern emerges in which every other line[1] all have operators and coefficients that allow their components to be grouped together. Doing so, a further pattern emerges such that the ith

[1] Consider indented lines as belonging to the line above.

component of each has the same coefficient and may be grouped together. If we do so, we see

$$\begin{aligned}
\epsilon_1^{n+1} &= -\phi^n + \phi^{n-1} - c^2 h \left(R^n \nabla \cdot \mathbf{A}^{n-1} + R^{n+1} \nabla \cdot \mathbf{A}^n \right) \\
&+ h b_1 \mathcal{L}_1^{-1} \left[-v_\phi^n + v_\phi^{n-1} - c^2 h \left(R^n \nabla \cdot \mathbf{v}_\mathbf{A}^{n-1} + R^{n+1} \mathbf{v}_\mathbf{A}^n \right) \right] \\
&+ h^2 a_{11} c^2 b_1 \mathcal{L}_1^{-1} \left[-\Delta\phi^n + \Delta\phi^{n-1} - c^2 h \left(R^n \Delta \left(\nabla \cdot \mathbf{A}^{n-1} \right) + R^{n+1} \Delta \left(\nabla \cdot \mathbf{A}^n \right) \right) \right] \\
&+ h^2 a_{11} c^2 b_1 \mathcal{L}_1^{-1} \left[-\frac{\rho^{(1),n}}{\epsilon_0} + \frac{\rho^{(1),n-1}}{\epsilon_0} - c^2 h \mu_0 \left(R^n \nabla \cdot \mathbf{J}^{(1),n-1} + R^{n+1} \nabla \cdot \mathbf{J}^{(1),n} \right) \right] \\
&+ h^2 b_2 a_{21} c^2 \mathcal{L}_2^{-1} \left[-k_1^{v_\phi,n} + k_1^{v_\phi,n-1} - h c^2 \left(R^n \nabla \cdot \mathbf{k}_1^{\mathbf{v}_\mathbf{A},n-1} + R^{n+1} \nabla \cdot \mathbf{k}_1^{\mathbf{v}_\mathbf{A},n} \right) \right] \\
&+ h^2 b_2 a_{22} c^2 \mathcal{L}_2^{-1} \left[-\Delta\phi^n + \Delta\phi^{n-1} - h c^2 \left(R^n \Delta \left(\nabla \cdot \mathbf{A}^{n-1} \right) + R^{n+1} \left(\nabla \cdot \mathbf{A}^n \right) \right) \right] \\
&+ h^2 b_2 a_{22} c^2 \mathcal{L}_2^{-1} \left[-\Delta k_1^{\phi,n} + \Delta k_1^{\phi,n-1} - h c^2 \left(R^n \Delta \left(\nabla \cdot \mathbf{k}_1^{\mathbf{A},n-1} \right) + R^{n+1} \Delta \left(\nabla \cdot \mathbf{k}_1^{\mathbf{A},n} \right) \right) \right] \\
&+ h^2 a_{22} c^2 b_2 \mathcal{L}_2^{-1} \left[-\frac{\rho^{(2),n}}{\epsilon_0} + \frac{\rho^{(2),n-1}}{\epsilon_0} - h c^2 \mu_0 \left(R^n \nabla \cdot \mathbf{J}^{(2),n-1} + R^{n+1} \nabla \cdot \mathbf{J}^{(2),n} \right) \right].
\end{aligned} \tag{4.155}$$

Utilizing the residual definitions (4.146)-(4.148) and the identities (4.149)-(4.152), we see finally

$$\begin{aligned}
\epsilon_1^{n+1} &= \epsilon_1^n \\
&+ h b_1 \mathcal{L}_1^{-1} \left[\epsilon_2^n \right] \\
&+ h^2 a_{11} c^2 b_1 \mathcal{L}_1^{-1} \left[\Delta \epsilon_1^n \right] \\
&+ h^2 a_{11} c^2 b_1 c^2 \mu_0 \mathcal{L}_1^{-1} \left[(1 - c_1) \epsilon_3^n + c_1 \epsilon_3^{n+1} \right] \\
&+ h^2 b_2 a_{21} c^2 \mathcal{L}_2^{-1} \left[c^2 \mathcal{L}_1^{-1} \left[\Delta \epsilon_1^n + c^2 \mu_0 \left((1 - c_1) \epsilon_3^n + c_1 \epsilon_3^{n+1} \right) + h a_{11} \epsilon_2^n \right] \right] \\
&+ h^2 b_2 a_{22} c^2 \mathcal{L}_2^{-1} \left[\Delta \epsilon_1^n \right] \\
&+ h^2 b_2 a_{22} c^2 \mathcal{L}_2^{-1} \left[\Delta \mathcal{L}_1^{-1} \left[\epsilon_2^n + h a_{11} c^2 \Delta \epsilon_1^n + h a_{11} c^4 \mu_0 \left((1 - c_1) \epsilon_3^n + c_1 \epsilon_3^{n+1} \right) \right] \right] \\
&+ h^2 b_2 a_{22} c^2 \mu_0 c^2 \mathcal{L}_2^{-1} \left[(1 - c_2) \epsilon_3^n + c_2 \epsilon_3^{n+1} \right].
\end{aligned} \tag{4.156}$$

Thus we see the residual for the gauge condition at $t = n + 1$, ϵ_1^{n+1}, is a linear combination of the three residuals at current or previous timesteps. QED

We now prove a similar lemma concerning the time derivative values update.

Lemma 4.2.14. *The residual of the time derivative of the Lorenz gauge condition* (4.147) *at time level* $n + 1$ *is a linear combination of the residuals of the Lorenz gauge* (4.146) *at time level n, the*

time derivative of the Lorenz gauge condition (4.147) *at time level n, and the continuity equation* (4.148) *at time levels n and n* + 1.

Proof. Consider the residual of time derivative of the Lorenz gauge at time $n+1$.

$$\epsilon_2^{n+1} = -v_\phi^{n+1} + v_\phi^n - c^2 h \left(R^n \nabla \cdot \mathbf{v}_\mathbf{A}^n + R^{n+1} \nabla \cdot \mathbf{v}_\mathbf{A}^{n+1} \right)$$

The components of the righthand side may be expanded using the update equations (4.136) and (4.137). We can further expand using the definitions of the k variables, and then by the logic of Lemma 4.2.13 we will find

$$\begin{aligned}
\epsilon_2^{n+1} = \epsilon_2^n & \\
&+ h b_1 c^2 \mathcal{L}_1^{-1} \left[\Delta \epsilon_1^n \right] \\
&+ h b_1 c^2 \mathcal{L}_1^{-1} \left[\mu_0 c^2 \left((1-c_1)\, \epsilon_3^n + c_1 \epsilon_3^{n+1} \right) \right] \\
&+ h^2 b_1 a_{11} c^2 \mathcal{L}_1^{-1} \left[\Delta \epsilon_2^n \right] \\
&+ h b_2 c^2 \mathcal{L}_2^{-1} \left[\epsilon_1^n \right] \\
&+ h b_2 c^2 \mathcal{L}_2^{-1} \left[\mu_0 c^2 \left((1-c_2)\, \epsilon_3^n + c_2 \epsilon_3^{n+1} \right) \right] \\
&+ h^2 b_2 a_{22} c^2 \mathcal{L}_2^{-1} \left[\Delta \left(\mathcal{L}_1^{-1} \left[\epsilon_2^n + h a_{11} c^2 \Delta \epsilon_1^n + h a_{11} c^4 \mu_0 \left((1-c_1)\, \epsilon_3^n + c_1 \epsilon_3^{n+1} \right) \right] \right) \right] \\
&+ h^2 b_2 a_{22} c^2 \mathcal{L}_2^{-1} \left[\Delta \epsilon_2^n \right] \\
&+ h^3 b_2 a_{22} a_{21} c^2 \mathcal{L}_2^{-1} \left[\Delta \left(c^2 \mathcal{L}_1^{-1} \left[\Delta \epsilon_1^n + c^2 \mu_0 \left((1-c_1)\, \epsilon_3^n + c_1 \epsilon_3^{n+1} \right) + h a_{11} \epsilon_2^n \right] \right) \right].
\end{aligned} \tag{4.157}$$

Thus we see the residual for the time derivative of the gauge condition at $t = n+1$, ϵ_2^{n+1}, is a linear combination of the three residuals at current or previous timesteps. QED

Having proven the above lemmas, we wish to connect the satisfaction of the gauge condition (4.146)-(4.147) with the continuity equation (4.148).

Theorem 4.2.11. *Assuming the residuals of the continuity equation and gauge condition* (4.146) - (4.148) *are zero for timesteps* $n \in \{-1, 0\}$*, the residual of the continuity equation* (4.148) *is zero for all time* $n > 0$ *if and only if the residuals of the Lorenz gauge condition* (4.146) - (4.147) *are zero for all time steps* $n > 0$*.*

Proof. Assume $\epsilon_3^k = 0 \,\forall\, k \in \mathbb{Z}$.

Then by Theorem 4.2.10 we know $\epsilon_1^k = \epsilon_2^k = 0$ for all time.

Now we prove the other direction. Suppose $\epsilon_1^k = \epsilon_2^k = 0 \,\forall\, k \in \mathbb{Z}$. By Lemma 4.2.13 ϵ_1^{n+1}'s update equation becomes

$$\begin{aligned} 0 = {} & h^2 b_1 a_{11} c^4 \mu_0 \mathcal{L}_1^{-1}\left[(1-c_1)\epsilon_3^n + c_1\epsilon_3^{n+1}\right] + h^2 b_2 a_{21} c^6 \mu_0 \mathcal{L}_2^{-1}\left[\mathcal{L}_1^{-1}\left[\left((1-c_1)\,\epsilon_3^n + c_1\epsilon_3^{n+1}\right)\right]\right] \\ & + h^2 b_2 a_{22} c^2 \mathcal{L}_2^{-1}\left[\Delta\mathcal{L}_1^{-1}\left[h a_{11} c^4 \mu_0 \left((1-c_1)\,\epsilon_3^n + c_1\epsilon_3^{n+1}\right)\right]\right] \\ & + h^2 b_2 a_{22} c^2 \mu_0 c^2 \mathcal{L}_2^{-1}\left[(1-c_2)\,\epsilon_3^n + c_2\epsilon_3^{n+1}\right] \end{aligned} \tag{4.158}$$

Likewise, by Lemma 4.2.14, we see ϵ_2^{n+1}'s update equation is

$$\begin{aligned} 0 = {} & h b_1 c^4 \mu_0 \mathcal{L}_1^{-1}\left[(1-c_1)\,\epsilon_3^n + c_1\epsilon_3^{n+1}\right] + h b_2 c^4 \mu_0 \mathcal{L}_2^{-1}\left[(1-c_2)\,\epsilon_3^n + c_2\epsilon_3^{n+1}\right] \\ & + h^3 b_2 a_{22} a_{11} c^6 \mu_0 \mathcal{L}_2^{-1}\left[\Delta\mathcal{L}_1^{-1}\left[(1-c_1)\,\epsilon_3^n + c_1\epsilon_3^{n+1}\right]\right] \\ & + h^3 b_2 a_{22} a_{21} c^6 \mu_0 \mathcal{L}_2^{-1}\left[\Delta\mathcal{L}_1^{-1}\left[(1-c_1)\,\epsilon_3^n + c_1\epsilon_3^{n+1}\right]\right] \end{aligned} \tag{4.159}$$

We set $\epsilon_3^n = 0$ given our assumption that it is zero at the start. Thus we have two linear combinations of $\epsilon_3^{n+1} \equiv \epsilon_3$. They are as follows

$$\begin{aligned} & h^2 b_1 a_{11} c^4 \mu_0 c_1 \mathcal{L}_1^{-1}\left[\epsilon_3\right] + h^2 b_2 a_{21} c^6 \mu_0 c_1 \mathcal{L}_2^{-1}\left[\mathcal{L}_1^{-1}\left[\epsilon_3\right]\right] \\ & + h^3 b_2 a_{22} a_{21} c^6 \mu_0 c_1 \mathcal{L}_2^{-1}\left[\Delta\mathcal{L}_1^{-1}\left[\epsilon_3\right]\right] + h^2 b_2 a_{22} c^4 \mu_0 c_2 \mathcal{L}_2^{-1}\left[\epsilon_3\right] = 0 \end{aligned} \tag{4.160}$$

$$\begin{aligned} & h b_1 c^4 \mu_0 c_1 \mathcal{L}_1^{-1}\left[\epsilon_3\right] + h b_2 c^4 \mu_0 c_2 \mathcal{L}_2^{-1}\left[\epsilon_3\right] \\ & + h^3 b_2 a_{22} a_{11} c^6 \mu_0 c_1 \mathcal{L}_2^{-1}\left[\Delta\mathcal{L}_1^{-1}\left[\epsilon_3\right]\right] + h^3 b_2 a_{22} a_{21} c^6 \mu_0 c_1 \mathcal{L}_2^{-1}\left[\Delta\mathcal{L}_1^{-1}\left[\epsilon_3\right]\right] = 0 \end{aligned} \tag{4.161}$$

If we apply the $\mathcal{L}_1$ and $\mathcal{L}_2$ operators and then divide out common factors, these become

$$b_1 a_{11} \mu_0 c_1 \mathcal{L}_2\left[\epsilon_3\right] + b_2 a_{21} c^2 \mu_0 c_1 \epsilon_3 + h b_2 a_{22} a_{21} c^2 \mu_0 c_1 \Delta\epsilon_3 + b_2 a_{22} \mu_0 c_2 \mathcal{L}_1\left[\epsilon_3\right] = 0, \tag{4.162}$$

$$b_1 \mu_0 c_1 \mathcal{L}_2\left[\epsilon_3\right] + b_2 \mu_0 c_2 \mathcal{L}_1\left[\epsilon_3\right] + h^2 b_2 a_{22} a_{11} c^2 \mu_0 c_1 \Delta\epsilon_3 + h^2 b_2 a_{22} a_{21} c^2 \mu_0 c_1 \Delta\epsilon_3 = 0. \tag{4.163}$$

We define some coefficients for convenience, $A_1 \coloneqq b_1 a_{11} \mu_0 c_1$, $B_1 \coloneqq b_2 a_{21} c^2 \mu_0 c_1$, $C_1 \coloneqq h b_2 a_{22} a_{21} c^2 \mu_0 c_1$, $D_1 \coloneqq b_2 a_{22} \mu_0 c_2$, $A_2 \coloneqq b_1 \mu_0 c_1$, $B_2 \coloneqq b_2 \mu_0 c_2$, $C_2 \coloneqq h^2 b_2 a_{22} a_{11} c^2 \mu_0 c_1$,

$D_2 \coloneqq h^2 b_2 a_{22} a_{21} c^2 \mu_0 c_1$. Using these, along with the definition of the $\mathcal{L}_{\{1,2\}}$ operators and grouping like terms, we get

$$(\mathcal{I} + \Gamma_1 \Delta)\, \epsilon_3 = 0, \tag{4.164}$$

$$(\mathcal{I} + \Gamma_2 \Delta)\, \epsilon_3 = 0, \tag{4.165}$$

where we have defined

$$\Gamma_1(h) \coloneqq (A_1 + B_1 + D_1)^{-1} \left(hC_1 - (ha_{22}c)^2 A_1 - (ha_{11}c)^2 D_1 \right), \tag{4.166}$$

$$\Gamma_2(h) \coloneqq (A_2 + B_2)^{-1} \left(h^2 C_2 + h^2 D_2 - (ha_{11}c)^2 A_2 - (ha_{22}c)^2 B_2 \right). \tag{4.167}$$

Note we have assumed $A_1 + B_1 + D_1 \neq 0$ and $A_2 + B_2 \neq 0$. Were either of these zero, we would have Laplace's equation, and this under periodic boundary conditions only permits $\epsilon_3 = 0$. Additionally, under periodic boundary conditions, these have nontrivial solutions if Γ_1, Γ_2 are positive, otherwise $\epsilon_3 = 0$. The nontrivial solution of a Helmholtz equation $u + k^2 \partial_{xx} u = 0$ has the form $u = A \cos\left(\frac{1}{k}x\right) + B \sin\left(\frac{1}{k}x\right)$, if $k = \frac{L}{n\pi}$ (assuming a domain $[0, L)$). The derivatives with respect to whatever spatial dimensions are all associated with the same Γ value, so we know that the dimensions must all be the same. With this in mind, we are operating in a domain of length $L_x = L_y = \cdots = L$. Now, say $\Gamma_1 \neq \Gamma_2$. This would imply ϵ_3 would potentially satisfy one of the equations, but certainly would not satisfy the other. Thus the solutions we are looking for exist if $\Gamma_1(h) = \Gamma_2(h) = \left(\frac{L}{n\pi}\right)^2$, where $n \in \mathbb{Z}$. If either Γ values are not this, then $\epsilon_3 = 0$. We thus assume they both take this value and must find the h values such that this is the case.

$$\Gamma_1(h) = (A_1 + B_1 + D_1)^{-1} C_1 h - c^2 (A_1 + B_1 + D_1)^{-1} \left(a_{22}^2 A_1 + a_{11}^2 D_1 \right) h^2 = \left(\frac{L}{n\pi} \right)^2, \tag{4.168}$$

$$\Gamma_2(h) = (A_2 + B_2)^{-1} \left(C_2 + D_2 - a_{11}^2 c^2 A_2 - a_{22}^2 c^2 B_2 \right) h^2 = \left(\frac{L}{n\pi} \right)^2. \tag{4.169}$$

The above expressions give rise to the following two quadratic polynomials: (4.168) yields $\mathcal{A}_1 h^2 + \mathcal{B}_1 h + C_1 = 0$ and (4.169) yields $\mathcal{A}_2 h^2 + \mathcal{B}_2 h + C_2 = 0$. For there to be a nontrivial solution to ϵ_3, the coefficients of these two identities must be identical. Note $C_1 = C_2 = -\left(\frac{L}{n\pi}\right)^2$. We next consider $\mathcal{B}_1 = \mathcal{B}_2$, ie given $\mathcal{B}_2 = 0$, we need $\mathcal{B}_1 = 0$, ie

$$\frac{C_1}{A_1 + B_1 + D_1} = 0. \tag{4.170}$$

This can only happen if $C_1 = 0$, ie $b_2 a_{22} a_{21} c^2 \mu_0 c_1 = 0$. Given this is a DIRK method, we know the diagonal values are nonzero, so the only way this is achieved is for $a_{21} = 0$.

If we set $\mathcal{A}_1 = \mathcal{A}_2$, we would find that SDIRK methods (methods for which all a_{ii} are the same value) do not permit this to be the case, but that DIRK methods for which $a_{21} = 0$ and $c_1 < c_2$ allow for these values to be the same, in other words, there are DIRK methods for which ϵ_3 may have a nontrivial solution. However, to rule this out as a possibility, consider (4.170) and the difference (or lack thereof) between Γ_1 and Γ_2. We again know $\Gamma_1 = \Gamma_2$, thus $\Gamma_1 - \Gamma_2 = 0$, and so we move everything into one quadratic equation to solve:

$$(\mathcal{A}_1 + \mathcal{A}_2)\, h^2 - \mathcal{B}_1 h = 0 \tag{4.171}$$

From (4.170), we know $\mathcal{B}_2$ is zero. This implies the only possible timestep is $h = 0$, hardly a timestep in which we are interested. Thus, there does not exist a nontrivial solution for ϵ_3 for $h > 0$. QED

4.2.5 Conclusion

In Section 3.3.1 we proved that satisfaction of the semi-discrete Lorenz gauge implies satisfaction of the semi-discrete continuity equation and vice versa, as well as satisfaction of the semi-discrete Lorenz gauge implies satisfaction of Gauss's Law. In this section we extended this theory to encompass not only arbitrary BDF-k methods, but also for a family of second-order time centered methods, and Adams-Bashforth methods. Additionally we have proven that satisfaction of the semi-discrete continuity equation implies satisfaction of the semi-discrete Lorenz gauge for arbitrary DIRK-s methods, showing that the converse holds as well for DIRK-2, implying the possibility for the property holding for higher order DIRK as well. We now have the theory, we move on to see if this will yield numerical fruit.

4.3 Numerical Results

This section contains the numerical results for our PIC method using several wave solvers described above. We consider two different test problems with dynamic and steady state qualities. We first consider the Weibel instability [280], which is a streaming instability that occurs in a periodic domain. The second example is a simulation of a non-relativistic drifting cloud of electrons in

a periodic domain. For each example, we compare the performance of the different methods by inspecting the fully discrete Lorenz gauge condition and tracking its behavior as a function of time. Our exploration concentrates on the BDF-1, BDF-2, CDF-2, and DIRK-2 methods, typically with a mesh refinement of 128×128. The DIRK-2 method's weights are those explored by Qin and Zhang [290] and has the following Butcher tableau:

$$\begin{array}{c|cc} 1/4 & 1/4 & 0 \\ 3/4 & 1/2 & 1/4 \\ \hline & 1/2 & 1/2 \end{array}$$

All methods use a spectral solve to invert the $\mathcal{L}$ operator and compute gradients spectrally as well. We make use of quadratic particle weighting as in [286, 287, 291, 292, 293, 294] (see Appendix F for more details on interpolants), and we compute $\mathbf{J}^{n+1}$ using $\mathbf{x}_i^{n+1}$ as the location of the interpolant point and $\mathbf{v}_i^n$ and q_i as the value that is interpolated.

We conclude the section by summarizing the key results of the experiments.

4.3.1 Weibel Instability

In the preceeding chapter, Section 3.4.1, we considered the Weibel instability for the BDF-1 wave solver coupled with the IAEM. The full description of the problem and the setup can be found there. For convenience we repeat the table in in Table 4.2.

Parameter	Value
Average number density ($\bar{n}$) [m^{-3}]	1.0×10^{10}
Average electron temperature ($\bar{T}$) [K]	1.0×10^{4}
Electron angular plasma period (ω_{pe}^{-1}) [s/rad]	1.772688×10^{-7}
Electron skin depth (c/ω_{pe}) [m]	5.314386×10^{1}
Electron drift velocity in x ($v_\perp$) [m/s]	$c/2$
Maximum electron velocity in y ($v_\parallel$) [m/s]	$c/100$

Table 4.2 Plasma parameters used in the simulation of the Weibel instability. All simulation particles are prescribed a drift velocity corresponding to $v_\perp$ in the x direction while the y component of their velocities are sampled from a uniform distribution scaled to the interval $[-v_\parallel, v_\parallel)$.

Weibel Instability Magnetic Magnitude vs Angular Plasma Period, Mesh Resolution: 128×128

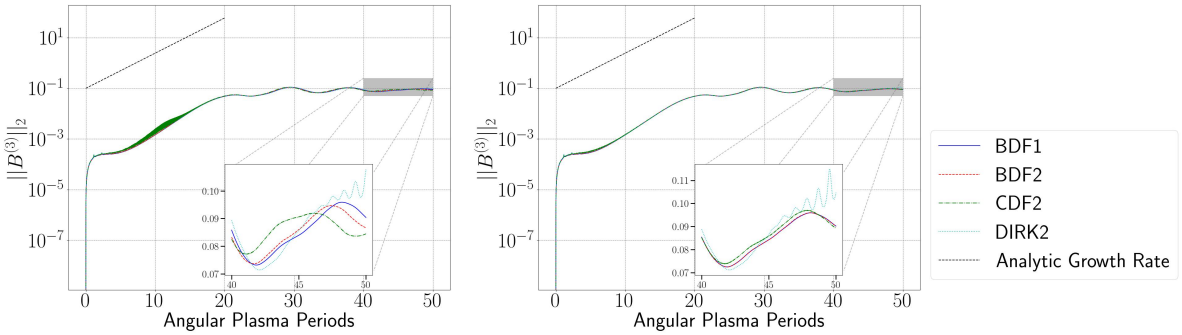

(a) Naive Update, Quadratic Weighting (b) Charge Conserving Update, Quadratic Weighting

Figure 4.1 The growth rate of the magnetic magnitude under the four methods under consideration. We note that both the naive update (left) and charge conserving update (right) follow the theoretical linear growth rate well, though the naive exhibits nonphysical oscillations and is clearly not as smooth. The naive update, unlike the charge conserving update, does not use the continuity equation to update ρ, but rather maps both $\mathbf{J}$ and ρ to the mesh using quadratic particle weighting. When we enforce continuity, the oscillations observed in not only the growth period, but also the final state, are removed for all methods except DIRK-2, which triggers small two-stream instabilities (see Remark 4.3.3).

Weibel Instability Gauge Error vs Angular Plasma Period, Mesh Resolution: 128×128

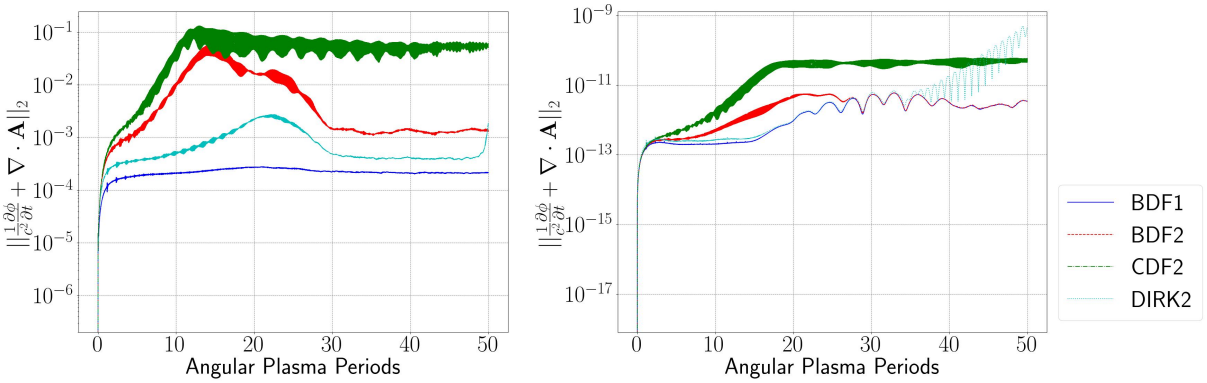

(a) Naive Update, Quadratic Weighting (b) Charge Conserving Update, Quadratic Weighting

Figure 4.2 The error in the Lorenz gauge condition for the Webeil Instability on a 128×128 grid. On the left we scatter charge and current density in a naive manner, on the right we have the setup in which we scatter current and update charge from the continuity equation. We see the error in the gauge is drastically reduced when we enforce continuity.

As noted earlier, we make use of higher order particle weighting as we are using a spectral solver. We see not only good alignment with the linear growth rate predicted by theory (Figures 4.1), but we also see good preservation of the Gauge condition (Figure 4.2) and Gauss's Law (Figure 4.3) in

all cases other than DIRK-2, which as we have previously described in Remark 4.2.9 does not have the latter property. In Figure 4.1 we show the growth rate of the magnetic magnitude as a function of angular plasma period. Figure 4.1a is the growth rate when using the ‘‘naive” weight where both charge density and current density are mapped to a mesh using the same weighting scheme on the collocated mesh. Figure 4.1b is the result of making use of the conservative method proposed in this paper. This shows the physical benefits quite nicely, as we see the oscillations in the growth rate eliminated and the change in the magnetic magnitude over time become much smoother. Likewise we exhibit the significant improvement in the Gauge condition and Gauss's law by comparing the naive weighting (Figures 4.2a and 4.3a, respectively) with the conserving scheme (Figures 4.2b and 4.3b, respectively).

Remark 4.3.1. *BDF-*1*, BDF-*2*, and CDF-*2 *with Crank-Nicolson all have diffusion, and as such this removes high frequencies, whereas the high frequencies are resolved by the Green's function solver used in Chapter 2.*

Remark 4.3.2. *DIRK-*2 *behaves dispersively, and as such high frequencies will remain when we use a spectral solver.*

Remark 4.3.3. *We note that DIRK-*2 *exhibits oscillations towards the end that eventually saturate (Figure 4.4). Due to its dispersive nature (Remark 4.3.2) it perturbs the cold direction ($v_\perp$) and triggers small two stream instabilities. Higher order particle weighting reduces the effect but does not eliminate it.*

All methods, BDF-1, BDF-2, CDF-2, and DIRK-2, capture the Weibel instability, which is a more challenging problem due to the care needed in setting up the problem, and additionally, once we enforce the semi-discrete continuity equation, they exhibit excellent gauge error and agreement with Gauss's Law (again, except DIRK-2 for Gauss). The DIRK-2 method gives results that merit some comment. Figure 4.4 shows the gauge error increasing in an oscillatory fashion at around the thirtieth plasma period, eventually stabilizing around the end of the run. DIRK-2 has no diffusion and cannot resolve high frequencies, as such it triggers nonphysical two stream instabilities in the

cold direction (Remark 4.3.3). Refining the interpolation scheme mitigates this effect, but does not entirely remove it. We see the downstream effects of this in the magnetic magnitude growth in the quadratic scheme (Figure 4.4b), though this matches the linear growth rate theory just as well as the other methods, towards the end the magnetic magnitude begin oscillating slightly.

There are a variety of ways we can approach this problem, the simplest of which would be adding numerical diffusion. Additionally, moving to a fully finite element basis based on C^1 elements or a new version of the Green's function solvers (eg [295]) would mitigate the issue, and will be the subject of future work. We are interested in developing Runge-Kutta methods that have the property of satisfying Gauss's Law if they satisfy the Gauge condition, and this too shall be the subject of future inquiry.

Weibel Instability Error in Gauss's Law vs Angular Plasma Period, Mesh Resolution: 128×128

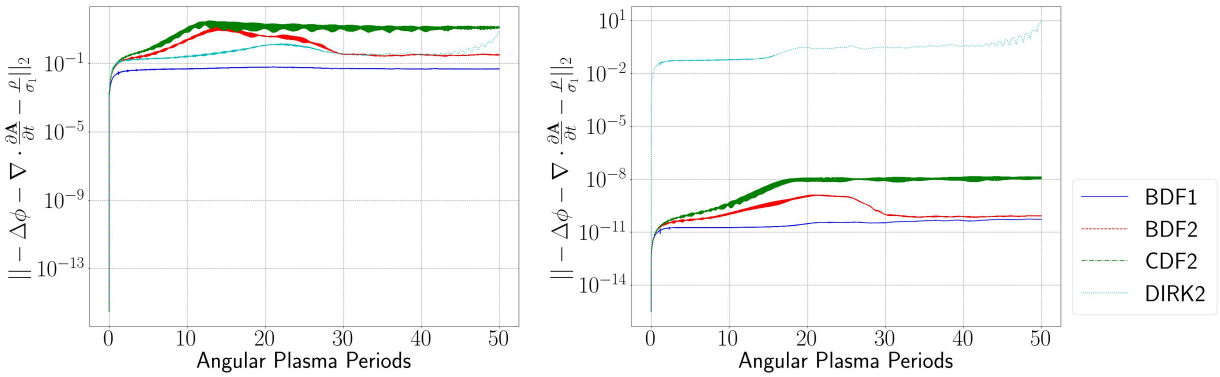

(a) Naive Update, Quadratic Weighting

(b) Charge Conserving Update, Quadratic Weighting

Figure 4.3 The error in Gauss's Law on a 128×128 grid. On the left we have scatter charge and current density in a naive manner, on the right we have the setup in which we scatter current and update charge from the continuity equation. We see the error in Gauss's law is drastically reduced with the exception of DIRK-2 (see Remark 4.2.9).

4.3.2 Drifting Cloud of Electrons

In a plasma that is macroscopically neutral, errors in Gauss's law may be mitigated, as an error in one direction caused by a negative particle may very well be cancelled by a likewise error from a positive particle nearby. In Section 3.4.2 we introduced the $2D - 2V$ problem of a drifting cloud of electrons. A stationary group of ions are distributed in a Gaussian about the center of the periodic

Weibel Instability, Charge Conserving DIRK-2, Mesh Resolution: 128×128

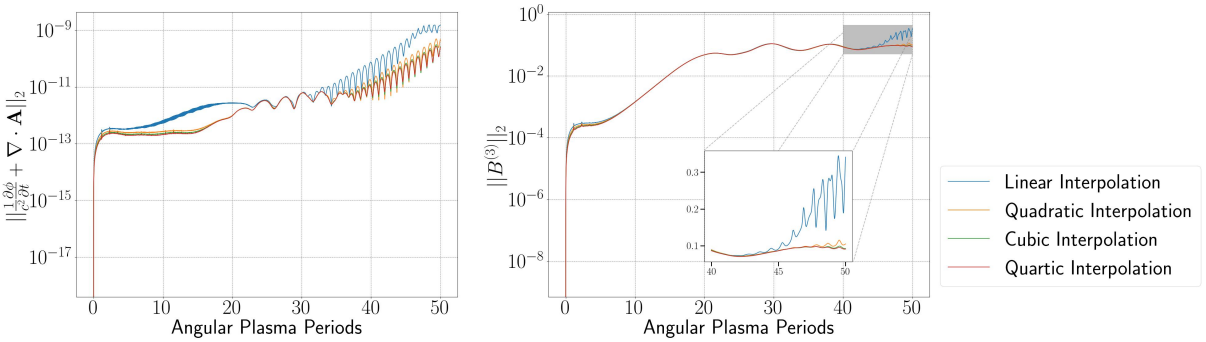

(a) Gauge Error vs Angular Plasma Period

(b) Magnetic Magnitude vs Angular Plasma Period

Figure 4.4 We refine interpolation schemes by increasing the order of spline basis functions for the DIRK-2 method. We see above excellent satisfaction for the gauge condition (left) until around the thirtieth plasma period, after which oscillations begin forming for around twenty plasma periods, eventually themselves stabilizing. This is unlike BDF-1, BDF-2, or CDF-2. Increasing the order of interpolation reduces this phenomenon, but does not remove it. This is a two-stream instability triggered by the DIRK-2 method's dispersive nature (see Remarks 4.3.2 and 4.3.3).

domain, $\left[-\frac{L_x}{2}, -\frac{L_y}{2}\right) \times \left[\frac{L_x}{2}, \frac{L_y}{2}\right)$, with a mobile group of electrons distributed in the exact same manner. This group of electrons is given a drift of $c/100$ in the x and y direction, which is enough for some of them to escape the potential well of the ions, while the bulk of the electrons falls back in the well (see Figure 4.7 for a visualization). Over time they move into the more neutral spaces, spreading apart as they go, and as they do there is ample opportunity for violations in Gauss' law and the Lorenz gauge condition. In this section we modify the dimensions slightly from those in Section 3.4.2, increasing the domain from $[-.5, .5]^2$ to $[-8, 8]^2$, where the units are in Debye lengths, to increase the amount of space that is traversed and make the problem more sensitive to errors in Gauss's Law. We increase the length of the run of the simulation to 100 angular plasma periods. A summary of the plasma parameters may be found in Table 4.3.

In Figure 4.5 we observe significant improvement in the gauge error when we compare the naive scatter method to the method enforcing charge conservation. Likewise when we compare satisfaction of Gauss's Law in Figure 4.6 between the naive scatter and charge conserving methods we find many orders of magnitude of improvement, confirming our theory.

In this section we examined two numerical experiments. First we simulated the well known Weibel Instability, showing our numerical simulations have good agreement with the known analytic

Parameter	Value
Average number density ($\bar{n}$) [m^{-3}]	1.0×10^{13}
Average electron temperature ($\bar{T}$) [K]	1.0×10^{5}
Electron angular plasma period (ω_{pe}^{-1}) [s/rad]	5.6057×10^{-9}
Electron skin depth (c/ω_{pe}) [m]	1.6806
Electron drift velocity in x and y [m/s]	$c/100$

Table 4.3 Plasma parameters used in the simulation of the Moving Cloud of Electrons problem. All simulation particles are prescribed a drift velocity corresponding to $v_x = v_y = \frac{c}{100}$ with a thermal velocity corresponding to a Maxwellian.

Moving Cloud Gauge Error vs Angular Plasma Period, Mesh Resolution: 128×128

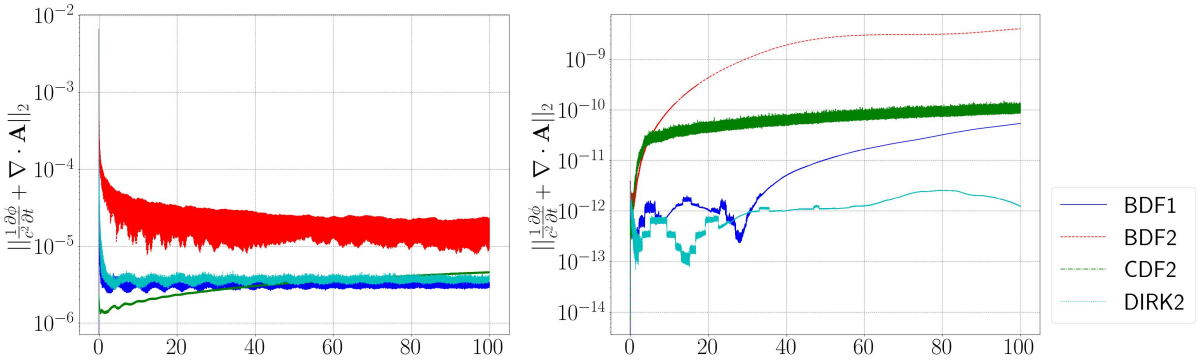

(a) Naive Conserving Update, Quadratic Weighting

(b) Charge Conserving Update, Quadratic Weighting

Figure 4.5 The error in the Lorenz gauge for the Moving Cloud of Electrons problem. We see on the left side relatively high errors in Gauss, whereas the right side shows significantly less.

solutions. We then simulated a non-relativistic cloud of electrons, an experiment particularly sensitive to gauge errors. Both problems showed negligible variation in the semi-discrete Lorenz gauge and significant improvement in Gauss's Law. The results of both of these experiments are in line with the theoretical results we presented in section 4.2.

4.4 Conclusion

In Chapter 3 we noted a number of ways of preserving the Lorenz gauge under the BDF-1 scheme. In particular, Section 3.2.1 we noted that if the time and spatial derivative was applied consistently to the continuity equation and the wave equations, we not only satisfied the semi-discrete Lorenz gauge condition if and only if we satisfied the semi-discrete continuity equation, but we additionally satisfied Gauss's Law if we satisfied the semi-discrete Lorenz gauge. In this chapter we have extended this property to a variety of wave solvers, generalizing to BDF-k and extending

Moving Cloud Error in Gauss's Law vs Angular Plasma Period, Mesh Resolution: 128×128

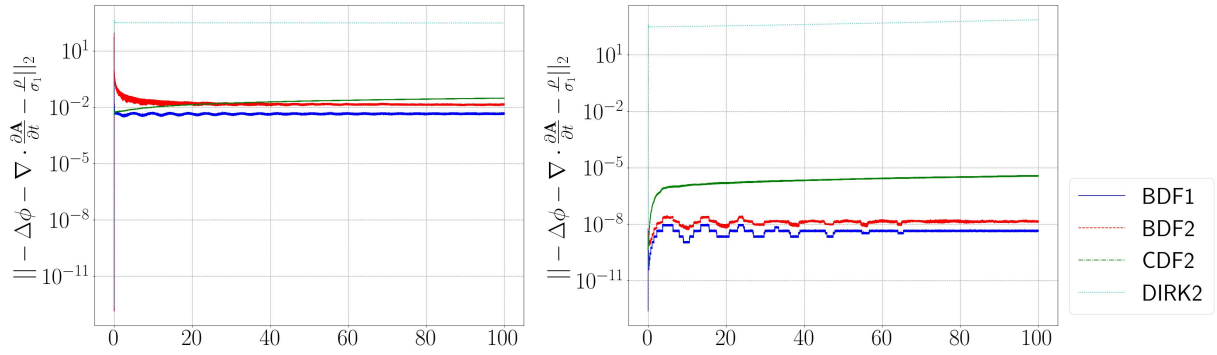

(a) Naive Conserving Update, Quadratic Weighting

(b) Charge Conserving Update, Quadratic Weighting

Figure 4.6 The error in Gauss's law for the Moving Cloud of Electrons problem. We see on the left side relatively high errors in Gauss, whereas the right side shows significantly less. As previously discussed, because the Runge-Kutta method is not a nested operator in time in a similar manner to the CDF or BDF methods, so there is no straightforward way to enable DIRK methods to satisfy Gauss's Law, as we would need to apply a DIRK time difference to a time difference to get the second time derivative. See Remark 4.2.9.

this property to a family of second order time-centered methods as well as arbitrary stage DIRK-s methods, though the DIRK-s methods lacked the desireable property of satisfying Gauss's Law if the semi-discrete continuity equation was satisfied. We then gave numerical evidence to confirm the theory.

This is what was to be shown.

We now turn to future inquiries.

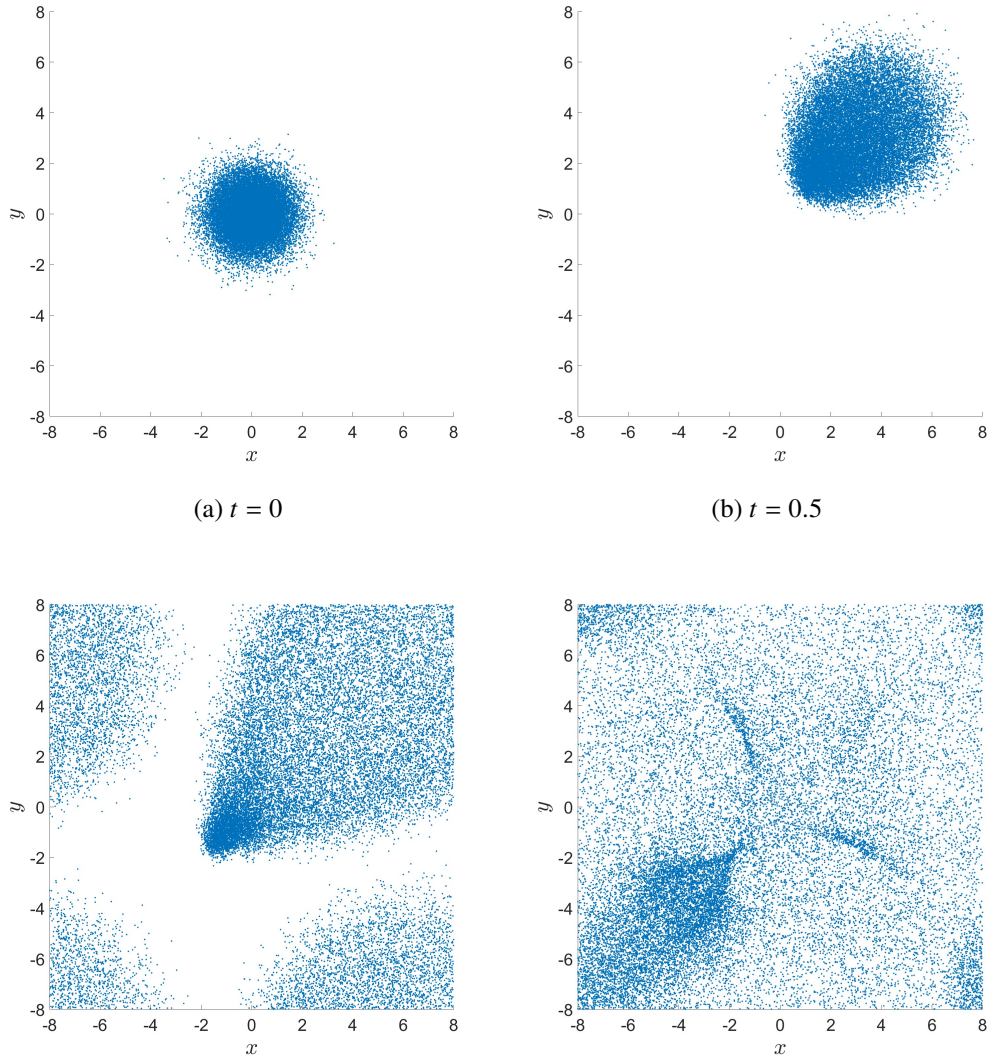

(a) $t = 0$ (b) $t = 0.5$

(c) $t = 1.0$ (d) $t = 2.0$

Figure 4.7 A Gaussian distribution of electrons and ions are placed on a periodic domain at $t = 0.0$. The electrons are given a drift velocity (see Table 4.3) in addition to their standard thermal Maxwellian velocity. Unlike the previous work's moving cloud of electrons problem in Section 3.4.2, only some electrons escape the well ($t = .5$), the rest are pulled back in ($t = 1.0$), causing a unique pattern to emerge as electrons are now travelling in opposing directions ($t = 2.0$).

CHAPTER 5

FUTURE WORK

The above work has seen the development of a PIC method that displays a number of properties. Chapter 2 showcases solving the modified Helmholtz equation using a Green's function, exhibiting the ability to retain physical characteristics, a resilience to numerical heating, close adherence to theory, and flexibility with regards to boundary conditions and geometries (though this component remains underexplored). Chapters 3 and 4 take this method and show the circumstances under which the Lorenz gauge and Gauss's law will be satisfied, solving the modified Helmholtz equation using either the FFT or sixth order finite difference method. This method, too, exhibits close adherence to theory. This PIC method, though still in its infancy, has much potential, and in this chapter we will briefly consider some future lines of inquiry to develop this promising method. First, in Section 5.1, we will consider the addition of particle source and sink terms, observing how this may change the theory linking the continuity equation with the Lorenz gauge. In Section 5.3 We will then consider developing kernel based derivatives and how that may enable us to return to our use of one dimensional Green's functions against a dimensionally split spatial operator. In Section 5.4 we will explore extending this theory to a Finite Element framework. Finally, in Section 5.5, we will consider adding a collision operator to our method. It should be emphasized that these are thumbnail sketches attempting to show the feasibility of what is being proposed.

5.1 Source Terms

In Section 2.4 one of the numerical experiments considered was an expanding beam, in which particles were injected into the domain on the left side of the box and removed upon contacting a boundary. Similar to this, a sheath problem was also considered, which had no particles injected but still removed particles upon contact with a boundary. Continuity is obviously violated here, as charge is showing up out of nowhere. In other words, our continuity equation now has a source term

$$\frac{\partial \rho}{\partial t} + \nabla \cdot \mathbf{J} = \sigma. \tag{5.1}$$

How this impacts the theory developed by Chapters 3 and 4 remains to be explored. Under the

BDF-1 scheme, we see the discretization of the continuity equation becomes

$$\frac{\rho^{n+1} - \rho^n}{\Delta t} + \nabla \cdot \mathbf{J}^{n+1} = \sigma^{n+1}. \tag{5.2}$$

So the residuals would form something akin to

$$\epsilon_1^{n+1} = \frac{1}{c^2}\frac{\phi^{n+1} - \phi^n}{\Delta t} + \nabla \cdot \mathbf{A}^{n+1}, \tag{5.3}$$

$$\epsilon_2^{n+1} = \frac{\rho^{n+1} - \rho^n}{\Delta t} + \nabla \cdot \mathbf{J}^{n+1} - \sigma^{n+1}. \tag{5.4}$$

We have the standard update equations

$$\phi^{n+1} = \mathcal{L}^{-1}\left[2\phi^n - \phi^{n-1} + \frac{1}{\alpha^2}\frac{\rho^{n+1}}{\epsilon_0}\right], \tag{5.5}$$

$$\nabla \cdot \mathbf{A}^{n+1} = \mathcal{L}^{-1}\left[2\nabla \cdot \mathbf{A}^n - \nabla \cdot \mathbf{A}^{n-1} + \frac{\mu_0}{\alpha^2}\nabla \cdot \mathbf{J}\right]. \tag{5.6}$$

Considering the Lorenz gauge with this unknown source term

$$\begin{aligned}
\frac{1}{c^2}\frac{\phi^{n+1} - \phi^n}{\Delta t} + \nabla \cdot \mathbf{A}^{n+1} &= \frac{1}{c^2\Delta t}\mathcal{L}^{-1}\left[2\phi^n - \phi^{n-1} + \frac{1}{\alpha^2}\frac{\rho^{n+1}}{\epsilon_0}\right] \\
&\quad - \frac{1}{c^2\Delta t}\mathcal{L}^{-1}\left[2\phi^{n-1} - \phi^{n-2} + \frac{1}{\alpha^2}\frac{\rho^n}{\epsilon_0}\right] \\
&\quad + \mathcal{L}^{-1}\left[2\nabla \cdot \mathbf{A}^n - \nabla \cdot \mathbf{A}^{n-1} + \frac{\mu_0}{\alpha^2}\nabla \cdot \mathbf{J}^{n+1}\right] \\
&= 2\mathcal{L}^{-1}\left[\frac{1}{c^2}\frac{\phi^n - \phi^{n-1}}{\Delta t} + \nabla \cdot \mathbf{A}^n\right] - \mathcal{L}^{-1}\left[\frac{1}{c^2}\frac{\phi^{n-1} - \phi^{n-2}}{\Delta t} + \nabla \cdot \mathbf{A}^{n-1}\right] \\
&\quad + \frac{\mu_0}{\alpha^2}\mathcal{L}^{-1}\left[\frac{\rho^n - \rho^{n-1}}{\Delta t} + \nabla \cdot \mathbf{J}^n\right] \\
&= \mathcal{L}^{-1}\left[2\epsilon_1^n - \epsilon_1^{n-1} + \frac{\mu_0}{\alpha^2}\epsilon_2^{n+1} + \sigma^{n+1}\right].
\end{aligned} \tag{5.7}$$

In other words, the residual of the Lorenz gauge at $n+1$ is equal to a linear combination of the Lorenz gauge residuals from previous timesteps, the residual of the continuity equation at $n+1$, and the source term of the continuity equation at $n+1$. Said differently, it appears as though the Lorenz gauge itself now has a source term identical to that of the continuity equation. Modifying the residual term, we arrive at

$$\tilde{\epsilon}_1^{n+1} = \frac{1}{c^2}\frac{\phi^{n+1} - \phi^n}{\Delta t} + \nabla \cdot \mathbf{A}^{n+1} + \mathcal{L}^{-1}\left[\sigma^{n+1}\right] = \epsilon_1^{n+1} + \mathcal{L}^{-1}\left[\sigma^{n+1}\right]. \tag{5.8}$$

We now consider how the Lorenz gauge itself behaves with a source. Assuming $\epsilon_1^0 = 0$ (or $\tilde{\epsilon}_1^0 = \mathcal{L}^{-1}\left[\sigma^0\right]$) and $\epsilon_2^n = 0 \,\forall\, n$, we consider

$$\begin{aligned}\tilde{\epsilon}_1^{n+1} &= \mathcal{L}^{-1}\left[2\epsilon_1^n - \epsilon_1^{n-1} + \frac{\mu_0}{\alpha^2}\epsilon_2^{n+1} + \sigma^{n+1}\right] \\ &= \mathcal{L}^{-1}\left[2\epsilon_1^n - \epsilon_1^{n-1} + \frac{\mu_0}{\alpha^2}(0) + \sigma^{n+1}\right] \\ &= \mathcal{L}^{-1}\left[2\epsilon_1^n - \epsilon_1^{n-1} + \sigma^{n+1}\right].\end{aligned} \tag{5.9}$$

By assumption we know $\epsilon_1^n = \epsilon_1^{n-1} = 0$. So we see $\tilde{\epsilon}_1^{n+1} = \mathcal{L}^{-1}\left[\sigma_1^{n+1}\right] \implies \epsilon_1^{n+1} = 0$.

In short, there is good reason to suggest that the theory can absorb a source term in the continuity equation. There are several practical next steps that follow. First, this theory itself is somewhat speculative. What does it mean for the Lorenz gauge to have a source term, especially in argument of the $\mathcal{L}^{-1}$ operator? The physical explanation of a source term for the Lorenz gauge is also something of a vexed question and will need to be explored. This has not been experimentally tested, and numerical experiments need to follow theory.

5.2 Rotated Grid

In Section 1.4.4, the difficulties of rotating a Yee grid while retaining a cartesian set of coordinates were discussed. This difficulty is primarily due to the staggered nature of the mesh, and while work has been done to mitigate these errors (eg [174, 179]), the amount of effort to work around the Yee mesh while retaining a finite difference formulation is nontrivial. Yee's requirement to maintain a uniformity in its mesh makes it difficult to simulate a domain that is not in line with the coordinates of the simulation reference frame (Figure 5.1). The MOLT method's nonstaggered nature, combined with its ability to have nonuniform lines of integration, enables it to handle these sort of domains with greater ease (Figure 5.2). The MOLT method has already been demonstrated to have remarkable geometric flexibility, showcased in elliptical domains in [265, 266, 267, 268], and extended even to simulation of an A6 magnetron in [296].

Initial investigations into the ability of MOLT to simulate electromagnetic waves compared to the Yee scheme are promising. A simple square domain, $[L, L] \times [L, L]$ with $L = 4$ with PEC boundaries is set up. A Gaussian source is injected into the magnetic field centered at $\left(-\frac{1}{2}, \frac{1}{2}\right)$. The

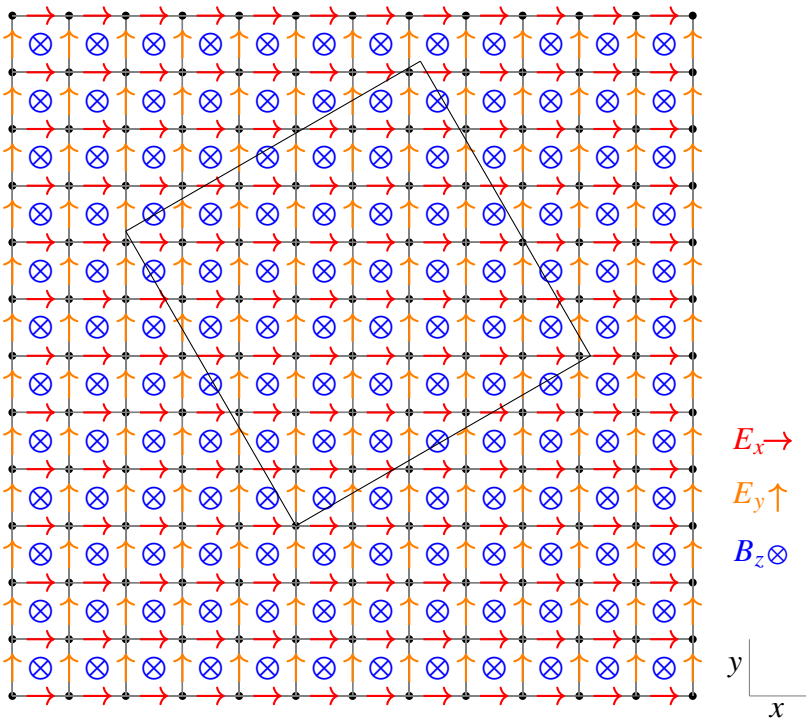

Figure 5.1 A 2D Yee grid in Transverse Electric (TE) mode. The domain itself is noted by the inscribed square.

Parameter	Value
τ	1
σ_x	$\frac{1}{20}$
σ_y	$\frac{1}{20}$
t_0	6τ
x_0	$-\frac{1}{2}$
y_0	$-\frac{1}{2}$
θ	$\frac{\pi}{6}$

Table 5.1 Table of parameter values for the source function.

root source, $\mathbf{S}$, is modified for both the Yee grid and the MOLT method to ensure the sources are physically the same:

$$\mathbf{S}(x,y,t) = \exp\left(-\left(\left(\frac{t-t_0}{\tau}\right)^2 + \left(\frac{x-x_0}{\sigma_x}\right)^2 + \left(\frac{y-y_0}{\sigma_y}\right)^2\right)\right)(\hat{\mathbf{x}}+\hat{\mathbf{y}}+\hat{\mathbf{z}}), \tag{5.10}$$

$$\mathbf{S}_{yee}(x,y,t) = \nabla \times \mathbf{S}, \tag{5.11}$$

$$\mathbf{S}_{MOLT}(x,y,t) = \frac{\partial \mathbf{S}}{\partial t}. \tag{5.12}$$

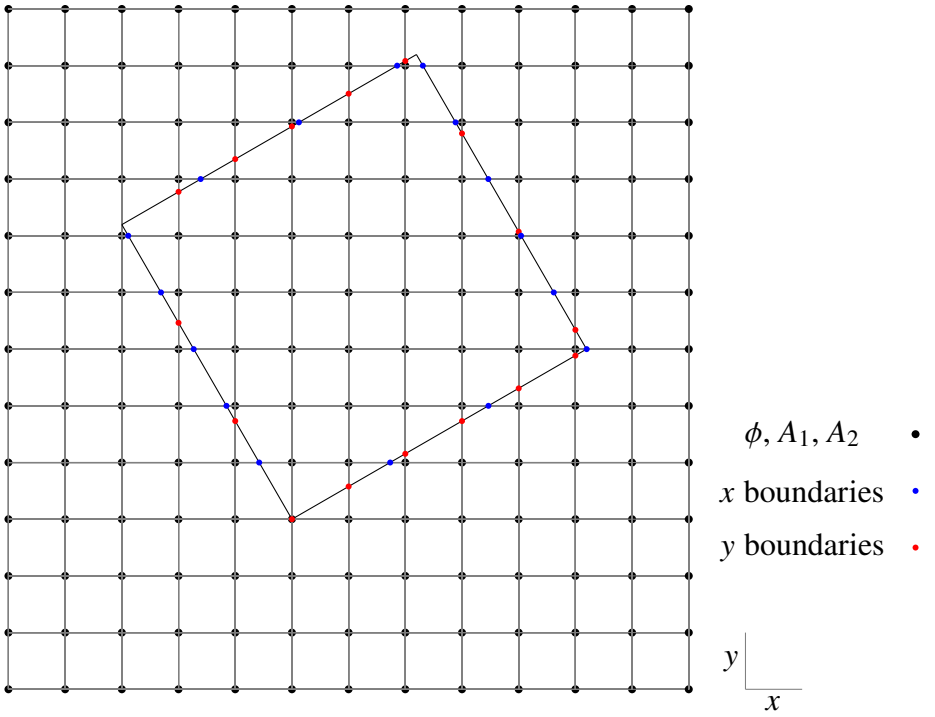

Figure 5.2 A 2D MOLT grid. The domain itself is noted by the inscribed square. The collocation of the nodes allow for easier coding as well as more consistent boundaries applied. Additionally, with a little extra coding, the staircases may be filled in (shown in the colored nodes, blue for x lines, red for y lines.

The parameters for $\mathbf{S}$ may be found in Table 5.1. The values of the magnetic field and the vector potentials at $(0, 0)$ are recorded. This was done with the standard Yee grid as well as the first and second order MOLT BDF methods.[1]

The aliasing associated with Yee [173] causes the electromagnetic structure of the rotated box to quickly deviate from that of the unrotated,[2] unlike MOLT, whose rotated box's values closely track

[1]It was observed that the amplitudes of the waves from BDF1 and BDF2, especially BDF1, were not matching that of Yee, given their dissipative nature. An alternative method discussed in [267, 268] that is purely dispersive (though artificial dissipation may be added if one wishes) was also tested. This is the basic MOLT method with an averaging parameter $\beta \in (0, 2]$. The semidiscretized form of the wave equation takes the following form

$$\frac{1}{c^2}\frac{u^{n+1} - 2u^n + u^{n-1}}{\Delta t^2} - \Delta\left(u^n + \frac{u^{n+1} - 2u^n + u^{n-1}}{\beta^2}\right) = S. \tag{5.13}$$

This is rearranged and solved using the standard MOLT wave solver with a Green's function discussed in Section 2.2. The β parameter makes this solver purely dispersive, and this non-dissipative method matched the amplitude of Yee at the start. As will be shown, the dissipative methods hold excellent agreement between their rotated and nonrotated components, unlike the Yee grid. Not shown is the dispersive β method holding equally well.

[2]This is a very naive implementation of the Yee mesh. If a node, that is, the bottom left corner of the Yee cell, was detected as being within the domain, then the full cell was included, even if the individual components were not within the domain. [173] does show some slight improvement in matching the modal content of the unroated mesh if a more

with that of the unrotated. Even B_z, whose values have to computed with numerical derivatives and interpolation of the rotated grid's values, has consistent values between rotated and unrotated grids. It should be emphasized, this is for a naively staircased grid, the edges have not been filled out yet, and we still see very close adherence to the nonrotated domain (Figures 5.6, 5.7, and 5.8). Shown also are the fields themselves at $t = 25$. The Yee grid (Figure 5.3) shows a completely different field once the domain is rotated, while the MOLT BDF1 and BDF2 fields (Figures 5.4 and 5.5, respectively) retain a close similarity between rotated and unrotated domains.

Yee computed B_z field at $t = 25$, Mesh Resolution: 256×256

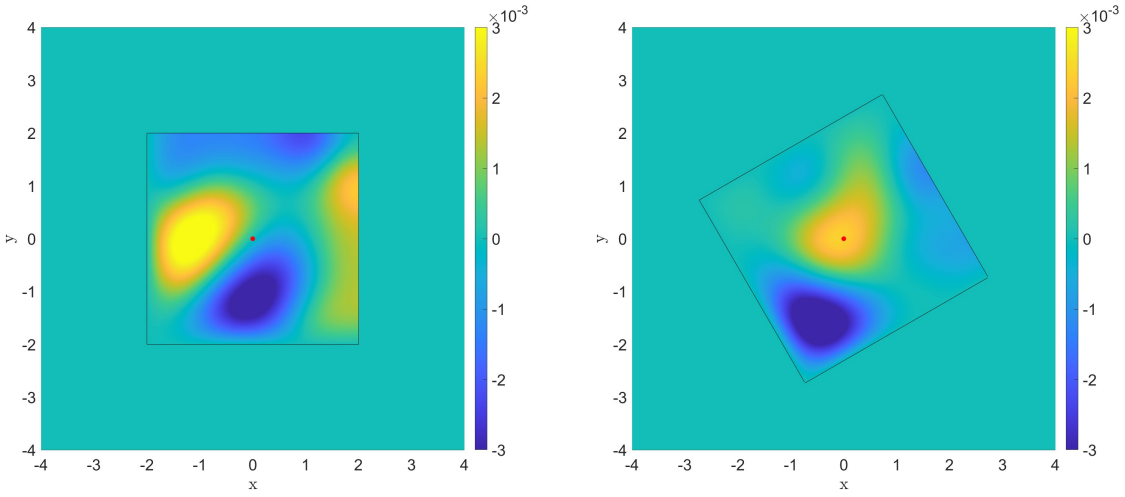

(a) Unrotated Domain

(b) Rotated Domain

Figure 5.3 B_z field at $t = 25$ as computed by the Yee method. The rotated domain is of a completely different nature than that of the unrotated. The red dot indicates the location of the listener node, whose values are recorded over time and displayed in Figure 5.6.

The next step for this process will be to incorporate macroparticles. The first stage is simple, noting the success of the naively staircased structure above, we can do a staircased domain with particles and observe the results. Once this is completed, the staircases will need to be filled in. From the wave's perspective this is simple and has already been accomplished by Causley,

careful selection of electric field points is made, but this improvement is rather small, around 2%. There are ways of improving this significantly, such as shown in [180] (see Section 1.4.4 for more discussion), but the main point here is that a naive implementation of both MOLT and Yee has very different results, the former retaining the structure of the waves, the latter losing it.

MOLT BDF1 computed B_z field at $t = 25$, Mesh Resolution: 256×256

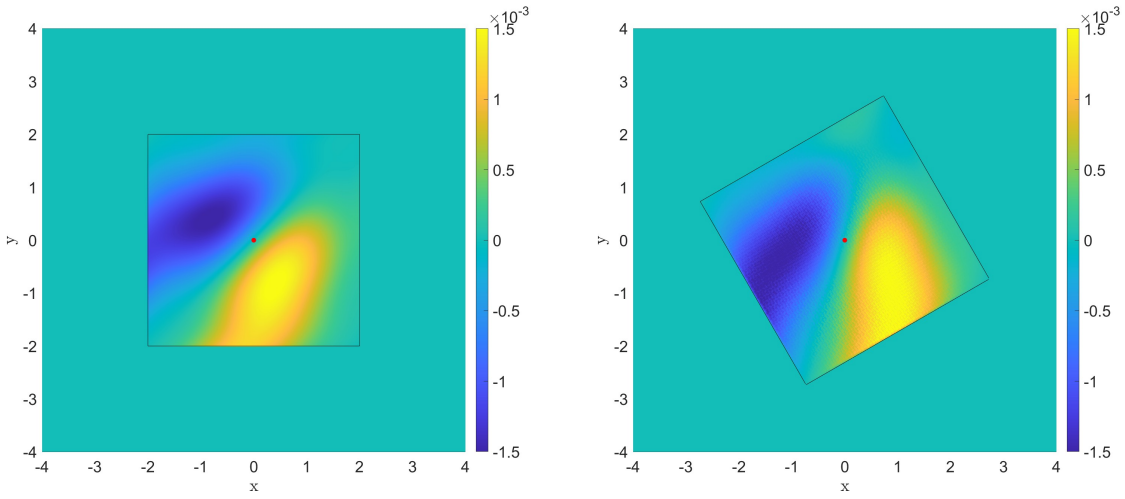

(a) Unrotated Domain

(b) Rotated Domain

Figure 5.4 B_z field at $t = 25$ as computed by the MOLT BDF1 method. The rotated domain is closely related to that of the unrotated. The red dot indicates the location of the listener node, whose values are recorded over time and displayed in Figure 5.6.

Thavappiragasam, and others. The particles will require more thought. Given the unstructured nature of the mesh near the edges, care will need to be made to interpolate the particles in such a way that will preserve charge.

5.3 Kernel Based Derivatives

The ability to handle complex geometries is certainly attractive. However, if the work of this thesis has hammered one point home, it is that preserving the involutions is important, and that the Green's function method, the one that is able to handle the nontrivial geometry described, does not preserve the involutions. This is due to the nature of the derivative of the potentials, the derivative of the continuity equation, and the Laplacian embedded in the modified Helmholtz operator, $\mathcal{L}$. Ultimately, if $\mathcal{L}$ is inverted using a Green's function, then we must use a similar method to compute the $\nabla \cdot \mathbf{J}$ term in the continuity equation.

[295] has begun exploration into a kernel based method for computing derivatives of arbitrary fields. In considering $\mathcal{L} = \mathcal{I} - \frac{1}{\alpha^2}\frac{\partial^2}{\partial x^2}$, they define an additional operator, $\mathcal{D} \coloneqq \mathcal{I} - \mathcal{L}^{-1}$, expanding

MOLT BDF2 computed B_z field at $t = 25$, Mesh Resolution: 256×256

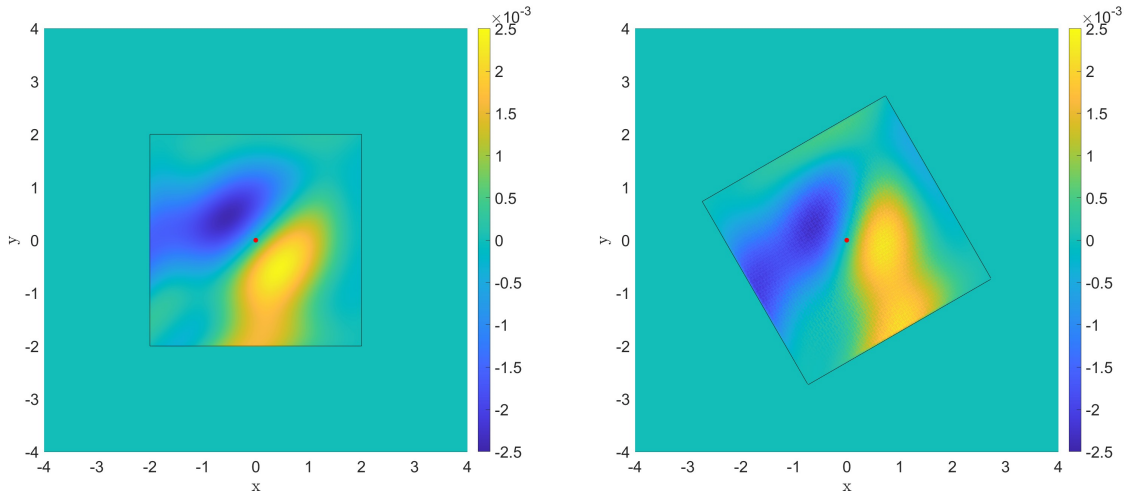

(a) Unrotated Domain

(b) Rotated Domain

Figure 5.5 B_z field at $t = 25$ as computed by the MOLT BDF2 method. The rotated domain is closely related to that of the unrotated. The red dot indicates the location of the listener node, whose values are recorded over time and displayed in Figure 5.6.

it into a Neumann series:[3]

$$\frac{1}{\alpha^2}\frac{\partial^2}{\partial x^2} = \mathcal{I} - \mathcal{L} = \mathcal{L}\left(\mathcal{L}^{-1} - \mathcal{I}\right) = -\mathcal{L}\left(\mathcal{I} - \mathcal{L}^{-1}\right) = -\mathcal{L}\mathcal{D} = -\left(\mathcal{I} - \mathcal{D}\right)^{-1}\mathcal{D} = -\sum_{p=1}^{\infty}\mathcal{D}^p. \tag{5.14}$$

We can do similar work to obtain a first order derivative operator, though it must be noted that these will be directional in nature. We consider the operators $\mathcal{L}_L \coloneqq \mathcal{I} - \frac{1}{\alpha}\frac{\partial}{\partial x}$ and $\mathcal{L}_R \coloneqq \mathcal{I} + \frac{1}{\alpha}\frac{\partial}{\partial x}$. Defining $\mathcal{D}_L \coloneqq \mathcal{I} - \mathcal{L}_L^{-1}$ and $\mathcal{D}_R \coloneqq \mathcal{I} - \mathcal{R}_R^{-1}$, we similarly find that the first order derivatives may be written in terms of Neumann series:

$$\frac{1}{\alpha}\frac{\partial^+}{\partial x} = \mathcal{I} - \mathcal{L}_L = \mathcal{L}_L\left(\mathcal{L}_L^{-1} - \mathcal{I}\right) = -\mathcal{D}_L\left(\mathcal{I} - \mathcal{D}_L\right)^{-1} = -\sum_{p=1}^{\infty}\mathcal{D}_L^p, \tag{5.15}$$

$$\frac{1}{\alpha}\frac{\partial^-}{\partial x} = \mathcal{L}_R - \mathcal{I} = \mathcal{L}_R\left(\mathcal{I} - \mathcal{L}_L^{-1}\right) = \mathcal{D}_R\left(\mathcal{I} - \mathcal{D}_R\right)^{-1} = \sum_{p=1}^{\infty}\mathcal{D}_R^p, \tag{5.16}$$

[3] A Neumann series considers a bounded linear operator $\mathcal{T} : X \to X$, where X is a Banach space. Assuming $\|\mathcal{T}\| < 1$ (with $\|\mathcal{T}\| = \inf_{\beta\in B}$, where $B = \{\beta | \|\mathcal{T}[x]\| \leq \beta\|x\| \; \forall\, x \in X\}$), the identity $(\mathcal{I} - \mathcal{T})^{-1} = \sum_{k=0}^{\infty}\mathcal{T}^k$ holds. This is the operator equivalent to the geometric series, $(1-x)^{-1} = \sum_{n=0}^{\infty}x^n$ for $|x| < 1$. For more details, see Chapters 1 and 2 of [297].

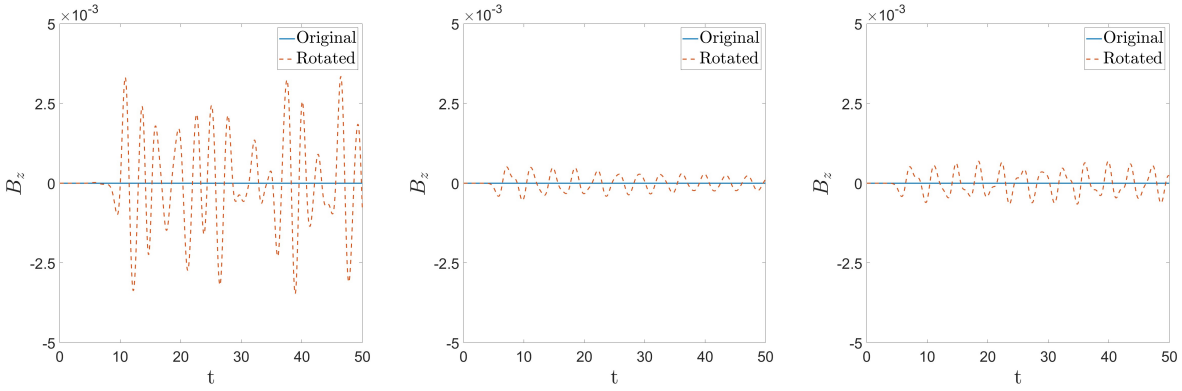

(a) Yee (b) MOLT BDF1 (c) MOLT BDF2

Figure 5.6 Value of $B_z(0,0)$ along time for Yee, MOLT BDF1, and MOLT BDF2. Both unrotated and rotated grids values are tracked. Both should be the same value, and MOLT's rotated grid is much closer to that of its unrotated grid. This is despite the fact that the magnetic field must be numerically derived, and that for the rotated grid this requires two interpolation steps resulting in a much more inaccurate magnetic field than the Yee grid would produce. It is also worth mentioning that the rotated Yee values are the order of magnitude of the waves themselves, unlike that of the MOLT BDF1 and BDF2 methods.

These differential operators, $\mathcal{D}_*$, are all defined in terms of identity operators and $\mathcal{L}_*^{-1}$ operators. The $\mathcal{L}_*^{-1}$ operators are known.

$$\mathcal{L}^{-1}[v](x) = \frac{\alpha}{2}\int_a^b e^{-\alpha|x-s|}v(s)ds + Ae^{-\alpha(x-a)} + Be^{-\alpha(b-x)}, \tag{5.17}$$

$$\mathcal{L}_L^{-1}[v](x) = \alpha\int_x^b e^{-\alpha(s-x)}v(s)ds + B_L e^{-\alpha(b-x)}, \tag{5.18}$$

$$\mathcal{L}_R^{-1}[v](x) = \alpha\int_a^x e^{-\alpha(x-s)}v(s)ds + A_R e^{-\alpha(x-a)}. \tag{5.19}$$

See Appendix G for derivation of $\mathcal{L}^{-1}$;[4] $\mathcal{L}_L^{-1}$ and $\mathcal{L}_R^{-1}$ are similarly derived.

[295] has already had success in simulating the 1D wave equation, 1D heat equation, and others using this method to approximate spatial derivative component of these equations to arbitrary accuracy. They were also able to do so for nonuniform meshes. Given the nature of this derivative and its direct relationship to the $\mathcal{L}$ operator, there is the promise of achieving the Gauge and Gauss's law accuracy displayed in chapters 3 and 4 while keeping the Green's function solution paradigm.

Given the success of [295], the next step will be applying this operator to compute the $\nabla \cdot \mathbf{J}$

[4] It is worth noting that $\mathcal{L} = \frac{1}{2}(\mathcal{L}_L + \mathcal{L}_R)$.

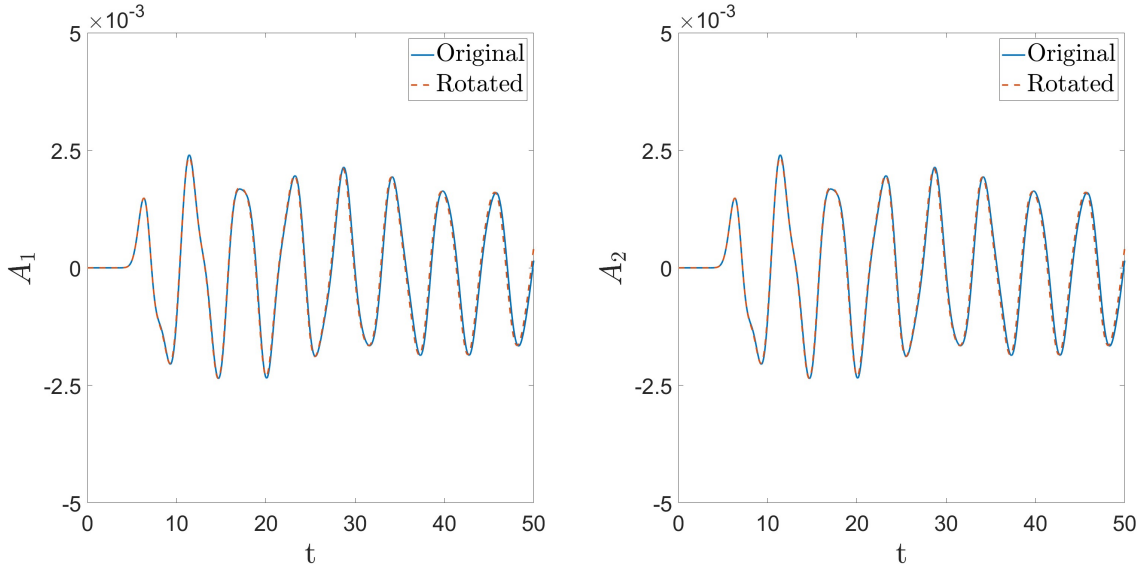

(a) MOLT BDF1 A_1 Values

(b) MOLT BDF1 A_2 Values

Figure 5.7 Value of $A_1(0,0)$ and $A_2(0,0)$ along time for MOLT. The adherence of the rotated grid's values to those of the unrotated is much closer than the magnetic field, indicating that the errors in the magnetic field between MOLT's rotated and unrotated likely stems from the numerical derivatives and two interpolation steps.

term in the continuity equation whilst in the context of the dimensionally split Green's function wave solver used in Chapter 2. If numerical experiments indicate success, theory will need to be developed in order to understand how the relationship between these two operators is formed.

5.4 Finite Element Method Formulation

There are three main approaches to mesh based numerical solutions of PDEs, Finite Difference, Finite Element, and Finite Volume. This thesis has been primarily interested in the first paradigm. Finite Element, though more involved, offers more rigor when it comes to error bounds, and gives even more flexibility with regards to geometry. The basic idea of the Finite Element Method (FEM) is to decompose the domain into a set of nonuniform elements. A common element shape is a triangle (2D) or tetrahedral (3D), though other shapes certainly exist. We can construct a finite element method for our wave equations as follows. First, we discretize in space using a triangularization $\mathcal{T}_h$

MOLT BDF2 A_1 and A_2 Values at Center of Domain, Mesh Resolution: 256×256

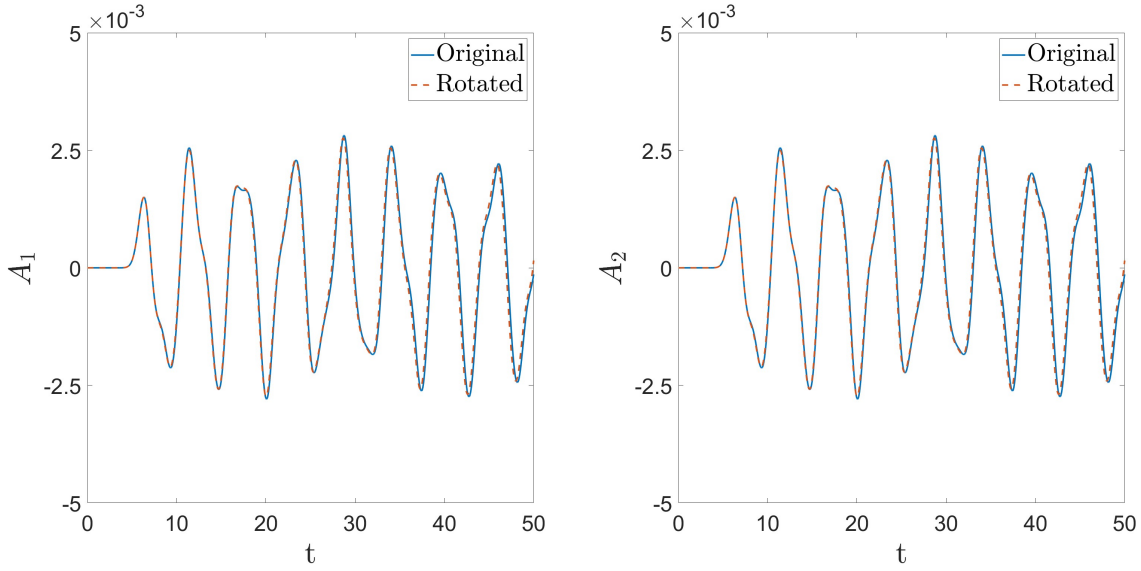

(a) MOLT BDF2 A_1 Values

(b) MOLT BDF2 A_2 Values

Figure 5.8 Value of $A_1(0,0)$ and $A_2(0,0)$ along time for MOLT BDF2. The adherence of the rotated grid's values to those of the unrotated is much closer than the magnetic field, indicating that the errors in the magnetic field between MOLT's rotated and unrotated likely stems from the numerical derivatives and two interpolation steps.

of the domain Ω such that $\Omega = \sum_{T \in \mathcal{T}_h} T$. We declare the following function spaces:

$$V_h^0 \coloneqq \left\{ v \in C^0(\Omega) \mid v|_T \in p^r(T) \right\} \subseteq H^1(\Omega), \tag{5.20}$$

$$V_h^1 \coloneqq \left\{ v \in C^1(\Omega) \mid v|_T \in p^r(T) \right\} \subseteq H^2(\Omega), \tag{5.21}$$

$$V_h^2 \coloneqq \left\{ v \in C^2(\Omega) \mid v|_T \in p^r(T) \right\} \subseteq H^3(\Omega). \tag{5.22}$$

All are equipped with the following inner product

$$(u, v)_{\mathcal{T}_h} \coloneqq \sum_{T \in \mathcal{T}_h} (u, v)_T \coloneqq \sum_{T \in \mathcal{T}_h} \int_T uv. \tag{5.23}$$

We wish to find $\phi_h, A_h^i \in V_h^0$, where $\mathbf{A}_h = \left(A_h^x, A_h^y, A_h^z \right)^T$ such that

$$\frac{1}{c^2} \left(\frac{\partial^2 \phi_h}{\partial t^2}, \eta_h \right)_{\mathcal{T}_h} + (\nabla \phi_h, \nabla \eta_h)_{\mathcal{T}_h} = \left(\frac{\rho}{\epsilon_0}, \eta_h \right)_{\mathcal{T}_h}, \ \forall \, \eta_h \in V_h^0, \tag{5.24}$$

$$\frac{1}{c^2} \left(\frac{\partial^2 A_h^i}{\partial t^2}, Z_h^i \right)_{\mathcal{T}_h} + \left(\nabla A_h^i, \nabla Z_h^i \right)_{\mathcal{T}_h} = \left(\mu_0 J^i, Z_h^i \right)_{\mathcal{T}_h}, \ \forall \, Z_h^i \in V_h^0. \tag{5.25}$$

If we consider the Lorenz gauge condition, $F_h \coloneqq \frac{1}{c^2}\frac{\partial \phi_h}{\partial t} + \nabla \cdot \mathbf{A}_h = 0$ as being satisfied at the start, we find that plugging it into the FEM formulation with test function $G_h \in V_h^0$ of the wave equation yields the following:

$$\left(\frac{1}{c^2}\frac{\partial^2 F_h}{\partial t^2}, G_h\right)_{\mathcal{T}_h} + (\nabla F_h, \nabla G_h)_{\mathcal{T}_h} = \cdots \tag{5.26a}$$

$$\left(\frac{1}{c^2}\frac{\partial}{\partial t}\left[\frac{\partial^2}{\partial t^2}\left[\phi_h\right]\right], G_h\right)_{\mathcal{T}_h} \tag{5.26b}$$

$$+\left(\frac{1}{c^2}\frac{\partial}{\partial t}\left[\nabla\phi_h\right], \nabla G_h\right)_{\mathcal{T}_h} \tag{5.26c}$$

$$+\left(\frac{1}{c^2}\frac{\partial^2}{\partial t^2}\left[\nabla \cdot \mathbf{A}_h\right], G_h\right)_{\mathcal{T}_h} \tag{5.26d}$$

$$+(\nabla\nabla \cdot \mathbf{A}_h, \nabla G_h)_{\mathcal{T}_h} \tag{5.26e}$$

(5.26b) combines with (5.26c) to acquire $\frac{1}{c^2}\left(\frac{\partial}{\partial t}\left[\frac{\rho}{\epsilon_0}\right], G_h\right)_{\mathcal{T}_h}$ by our wave equation setup. This is accomplished by simply pulling the time derivative out, which we can do given the inner product is an integral over space, not time. We would like to do the same with (5.26d) and (5.26e), however, (5.26e) is going to cause issues. We take (5.26e), decompose it, and using integration by parts we observe:

$$\begin{aligned}
(\nabla\nabla \cdot \mathbf{A}_h, \nabla G_h)_{\mathcal{T}_h} &= \sum_{T\in\mathcal{T}_h} (\nabla\nabla \cdot \mathbf{A}_h, \nabla G_h)_T \\
&= \sum_{T\in\mathcal{T}_h} \left[-(\Delta\nabla \cdot \mathbf{A}_h, G_h)_T + \langle(\nabla\nabla \cdot \mathbf{A}_h) \cdot \mathbf{n}, G_h\rangle_{\partial T}\right] \\
&= \sum_{T\in\mathcal{T}_h} \left[-(\nabla \cdot \Delta\mathbf{A}_h, G_h)_T + \langle(\nabla\nabla \cdot \mathbf{A}_h) \cdot \mathbf{n}, G_h\rangle_{\partial T}\right] \\
&= \sum_{T\in\mathcal{T}_h} \left[(\Delta\mathbf{A}_h, \nabla G_h)_T + \langle(\nabla\nabla \cdot \mathbf{A}_h) \cdot \mathbf{n}, G_h\rangle_{\partial T} - \langle\Delta\mathbf{A}_h \cdot \mathbf{n}, G_h\rangle_{\partial T}\right].
\end{aligned} \tag{5.27}$$

Were $A_h \in V_h^2$, then we have continuity along the second spatial derivative. Summing over all triangles would cancel each of these terms out. Low orders of smoothness prevent this from happening. Therefore, as the Lorenz gauge evolves over time under this framing, we observe the

two highlighted terms emerge.

$$\left(\frac{1}{c^2}\frac{\partial^2 F_h}{\partial t^2}, G_h\right)_{\mathcal{T}_h} + (\nabla F_h, \nabla G_h)_{\mathcal{T}_h} = \cdots \tag{5.28a}$$

$$= \frac{1}{c^2}\frac{\partial}{\partial t}\left(\left(\frac{1}{c^2}\frac{\partial^2 \phi_h}{\partial t^2}, G_h\right)_{\mathcal{T}_h} + (\nabla \phi_h, \nabla G_h)_{\mathcal{T}_h}\right) \tag{5.28b}$$

$$+ \left(\nabla \cdot \left(\frac{\partial^2 \mathbf{A}_h}{\partial t^2}\right), G_h\right)_{\mathcal{T}_h} + \left(\nabla \cdot (\nabla \mathbf{A}_h), \nabla G_h\right)_T \tag{5.28c}$$

$$+ \sum_{T \in \mathcal{T}_h} \left[\langle (\nabla\nabla \cdot \mathbf{A}_h) \cdot \mathbf{n}, G_h \rangle_{\partial T} - \langle \Delta \mathbf{A}_h \cdot \mathbf{n}, G_h \rangle_{\partial T}\right]. \tag{5.28d}$$

The two lines, (5.28b) and (5.28c), reduce to

$$\frac{1}{c^2}\left(\frac{\partial}{\partial t}\left[\frac{\rho}{\epsilon_0}\right], G_h\right)_{\mathcal{T}_h} + (\mu_0 \nabla \cdot \mathbf{J}, G_h)_{\mathcal{T}_h} = \mu_0 \left(\frac{\partial \rho}{\partial t} + \nabla \cdot \mathbf{J}, G_h\right)_{\mathcal{T}_h} = 0. \tag{5.29}$$

From (5.28d) there is possibly a nonzero remainder in the case of $A_h \notin V_h^2$. In other words, if the elements are not at least continuous up to the second derivative, the gauge will not be preserved.

What is to be done with this? The next steps are relatively straightforward. First, we could simply implement V_h^2 elements. This is certainly tractable if we use a very simple mesh and geometry. Under this assumption we can implement V_h^2 elements just to prove the theory plays out numerically. But V_h^2 elements are notoriously difficult to use in anything other than a very simple mesh, so assuming this works, for this method to gain any practical use, we would need to consider V_h^1 elements. A few approaches are considered.

We could consider constraints to the elements. It is important to note that it is not continuity per se that is eliminating those remainder terms, if the sums themselves cancel without continuity that works just as well. Additionally, There has also been good research done on boosting the smoothness of the elements to higher orders. SIAC filtering [298, 299, 300] or the lifting method recently introduced in [301]. If the elements are raised to higher levels of smoothness, then their derivatives will match on the boundaries, eliminating the offending remainder.

Dr. Sining Gong has suggested an alternative approach. Instead of smoothing the elements, what if we modified the $\mathbf{J}$ source term, projecting it onto V_h^2 in a particular way? This, too, will be explored.

Clearly $V_h^0 = V_h^2 + V_h^{2,\perp}$, where $V_h^{2,\perp}$ is the orthogonal complement to V_h^2, that is, $\forall\, v \in V_h^2, u \in V_h^{2,\perp}$, $(v,u) = 0$. We consider the bases of V_h^2 and $V_h^{2,\perp}$ as $\{\phi_i\}_{i=1}^M$ and $\{\phi_i\}_{i=M+1}^N$. We consider the following matrices, $B_{N\times N} = \left(\phi_i, \phi_j\right)$ and $C_{N\times N} = \left(\nabla\phi_i, \nabla\phi_j\right)$. We decompose these into block diagonal matrices as follows

$$B = \begin{pmatrix} B^{11} & B^{12} \\ B^{21} & B^{22} \end{pmatrix} \quad C = \begin{pmatrix} C^{11} & C^{12} \\ C^{21} & C^{22} \end{pmatrix}.$$

From now on we will drop the boldface for $\mathbf{J}$ and $\mathbf{A}$ given that we will be solving each of the vector components individually. Having defined these, we consider a projection of J onto V_h^2. We define a projection operator onto V^2 as $\mathbb{P}_{V_h^2} J = \sum_{i=1}^M L_i^J \phi_i$. Call the vector of coefficients $\mathbf{L}^J$. We further define

$$\tilde{J} \coloneqq \mathbb{P}_{V_h^2} J + \left(\left(C^{21}\left(\frac{1}{c^2}B^{11} + C^{11}\right)^{-1}\right)\mathbf{L}^J\right)^T (\phi_i)_{i=M+1}^N \,. \tag{5.30}$$

It is worth noting that $\mathbb{P}_{V_h^2} J = \mathbb{P}_{V_h^2}\tilde{J}$. It is also worth noting that we can annotate $\left(\mathbb{P}_{V_h^2} J, v\right)_{\mathcal{T}_h}$, which is equal to $\left(\tilde{J}, v\right)_{\mathcal{T}_h}$, as $B^{11}\mathbf{L}^J(\phi_i)_{i=1}^M$, where each index j in $\mathbf{L}^J$ corresponds to $v = \phi_j$ for $v \in V_h^2$. So if we set $v = \phi_j$, then this value is the jth row of B^{11} multiplied against $\mathbf{L}^J$.

We are now interested in solving the following variational problem for $A_h^i, J_h^i \in V_h^2$:

$$\frac{1}{c^2}\left(\frac{\partial^2 A_h^i}{\partial t^2}, w_h\right)_{\mathcal{T}_h} + \left(\nabla A_h^i, \nabla w_h\right)_{\mathcal{T}_h} = \mu_0\left(\tilde{J}^i, w_h\right)_{\mathcal{T}_h}, \ \forall\, w_h \in V_h^0. \tag{5.31}$$

From the above we know $w = v + u$, where $v \in V_h^2$ and $u \in V_h^{2,\perp}$. So we are really looking to satisfy the following system:

$$\frac{1}{c^2}\left(\frac{\partial^2 A_h^i}{\partial t^2}, v_h\right)_{\mathcal{T}_h} + \left(\nabla A_h^i, \nabla v_h\right)_{\mathcal{T}_h} = \mu_0\left(\tilde{J}_h^i, v_h\right)_{\mathcal{T}_h}, \ \forall\, v_h \in V_h^2. \tag{5.32}$$

$$\frac{1}{c^2}\left(\frac{\partial^2 A_h^i}{\partial t^2}, u_h\right)_{\mathcal{T}_h} + \left(\nabla A_h^i, \nabla u_h\right)_{\mathcal{T}_h} = \mu_0\left(\tilde{J}_h^i, u_h\right)_{\mathcal{T}_h}, \ \forall\, u_h \in V_h^{2,\perp}. \tag{5.33}$$

$$u_h + v_h = w_h. \tag{5.34}$$

To be more specific, we are looking to solve (5.32) while satisfying (5.33). When we do so, we by definition satisfy (5.31). First, as usual we semi-discretize this system in time. We are now

considering a BVP at some time level n. Given the plethora of indices already being annotated, we do not notate the time level, assuming they are all at the same time level. (We can also without loss of generality assume the source term $\tilde{J}$ contains the previous timesteps of A. With that bookkeeping out of the way, we see

$$(A_h, u_h) = \left(\sum_{i=0}^{M} a_i \phi_i, u_h \right)_{\mathcal{T}_h}, \tag{5.35}$$

$$(\nabla A_h, \nabla u_h) = \left(\sum_{i=0}^{M} a_i \nabla \phi_i, \nabla u_h \right)_{\mathcal{T}_h}. \tag{5.36}$$

Now, u_h may take any form. What if we had it take the form ϕ_1? Then clearly the results of these two inner products would be $\sum_i^M \phi_i a_i \phi_1$ or $\sum_i^M \nabla\phi_i a_i \nabla\phi_1$, respectively. And of course this logic works for arbitary ϕ_j. We can effectively anotate this as $B^{11}\mathbf{a}$ and $C^{11}\mathbf{a}$, respectively, with the jth index corresponding to u_h taking the value of ϕ_j. In other words, (5.32), when fully discretized, takes the form

$$\frac{1}{c^2} B^{11}\mathbf{a} + C^{11}\mathbf{a} = \mu_0 \mathbf{L}^J. \tag{5.37}$$

This, in turn, implies that $\mathbf{a} = \mu_0 \left(\frac{1}{c^2} B^{11} + C^{11} \right)^{-1} \mathbf{L}^J$.

Now, let us consider (5.33). First, it is clear, given $A_h^i \in V_h^2$, that $\left(A_h^i, u_h \right)_{\mathcal{T}_h} = 0$. Now we must consider $\left(\nabla A_h^i, \nabla u_h \right)_{\mathcal{T}_h}$.

Similar to the logic used above, we know (5.33) holds for all u_h, including $u_h = \phi_j$, though it is worth noting here that this ϕ_j is a member of $V_h^{2,\perp}$. The corresponding value of $\left(\nabla A_h^i, \nabla \phi_j \right)$ is then $\nabla \left(\sum_{i=1}^M a_i \phi_i \right) \nabla \phi_j$. We can effectively annotate this $C^{21}\mathbf{a}$. So it follows

$$\begin{aligned}
\left(\nabla A_h^i, \nabla v_h \right)_{\mathcal{T}_h} &= \left(\nabla \left(\sum_{i=0}^{M} a_i \phi_i \right), \nabla v_h \right)_{\mathcal{T}_h} \\
&= \left(\nabla \left(\mu_0 \left(\frac{1}{c^2} B^{11} + C^{11} \right)^{-1} (\phi_i)_{i=1}^{M} \right), \nabla v_h \right)_{\mathcal{T}_h} \\
&= \mu_0 C^{21} \left(\frac{1}{c^2} B^{11} + C^{11} \right)^{-1} \mathbf{L}^J \, (\phi_i)_{i=M+1}^{N}.
\end{aligned} \tag{5.38}$$

As we can see this is exactly what our source term $\tilde{J}$ is when we only consider the $V_h^{2,\perp}$ test functions. This proves that, with a little tweaking of the source term, we can satisfy the wave equation

using V_h^0 elements, ie

$$\left(A_h^i, v_h\right)_{\mathcal{T}_h} + \left(\nabla A_h^i, \nabla v_h\right)_{\mathcal{T}_h} = \mu_0 \left(\tilde{J}_h^i, v_h\right)_{\mathcal{T}_h}, \quad \forall\, v_h \in V_h^0. \tag{5.39}$$

This eliminates the spurious terms, (5.28d).

This has yet to be implemented in any code form, but provides a promising alternative to the above listed approaches to the problem.

5.5 Collisions

Collisions were briefly mentioned towards the end of Section 1.4.2. Our PIC method has so far only been interested in collisionless plasmas, as these are more straightforward, not to mentioned computationally cheaper, than collisional plasmas. There are a number of ways to approach this problem. First, it is worth noting how we can model collisions. [302] gives a good overview of the problem. We consider this by first adding a collision operator to the right hand side of the Vlasov equation:

$$\frac{\partial f_\alpha}{\partial t} + \mathbf{v} \cdot \nabla_x f_\alpha + \mathbf{F} \cdot \nabla_v f_\alpha = \sum_\beta a_{\alpha,\beta} Q\left(f_\alpha, f_\beta\right) \tag{5.40}$$

Here $a_{\alpha,\beta} = \frac{1}{\epsilon}$ represents the collision frequency between two species of elections, with ϵ being the Knudsen number, the ratio of the mean free path and the domain length. Sending $a_{\alpha,\beta} \to 0 \,\forall\, \alpha, \beta$ approaches the Vlasov equation. Q is the collision operator, in this case the Landau collision operator (see Section 1.4.2 for more details).

$$Q(f_\alpha, f_\beta) = \nabla_v \cdot \int_{\mathbb{R}^3} A(\mathbf{v} - \mathbf{v}_*) f_\beta(\mathbf{v}_*) \nabla_v f_\alpha(\mathbf{v}) - f_\alpha(\mathbf{v}) \nabla_{v_*} f_\beta(\mathbf{v}_*) d\mathbf{v}_*. \tag{5.41}$$

[7] derives both integral operators in Chapter 21. [302] also gives a good discussion on both from a more numerical perspective. Standard practice is to define $f \coloneqq f(\mathbf{v})$ and $f_* \coloneqq f(\mathbf{v}_*)$, so we will use this from here on out. A is the collision kernel, defined by

$$A(\mathbf{z}) \coloneqq C\|\mathbf{z}\|^\gamma \left(\|\mathbf{z}\|^2 I_d - \mathbf{z} \otimes \mathbf{z}\right) \equiv \|\mathbf{z}\|^{\gamma+2} \Pi(\mathbf{z}). \tag{5.42}$$

C is a constant (typically unity). $\Pi(\mathbf{z})$ is the projection matrix onto $\{\mathbf{z}\}^\perp$. I_d is the d dimensional identity matrix. $-d \leq \gamma \leq 1$ dictates the type of potential governing the system, hard potentials

for $\gamma > 0$, Maxwellian molecules for $\gamma = 0$, and $\gamma < 0$ corresponding to soft potentials. $\gamma = -3$ corresponds to Coulomb interactions.

Carrillo et al [303] developed a collision kernel for the Landau-Fokker-Plank equation, first for the homogenous Landau equation, then generalizing this to the Vlasov-Landau equation in [304]. These works conserve mass, momentum, and energy as well, with the added bonus of increasing a regularized entropy. The former's results have been replicated (Figure 5.9), the latter's will be as well, which will provide a good platform from which to launch.

In the former, they consider the spatially homogenous system, meaning only the time derivative on the lefthand side remains (homogeneity implies uniform spatial distribution, so $\nabla_x f = 0$, and homogeneity also implies no internal forces, so $\mathbf{F} \cdot \nabla_v f = 0$). The Landau collision operator is added to the righthand side:

$$\frac{\partial f}{\partial t} = Q\left(f, f\right) = \nabla_v \cdot \int_{\mathbb{R}^d} A(\mathbf{v} - \mathbf{v}_*) f f_* \left(\nabla_v \log\left(f\right) - \nabla_{v_*} \log\left(f_*\right)\right) d\mathbf{v}_*. \tag{5.43}$$

The Q term may be rewritten in terms of the variation of the entropy functional:

$$Q(f, f) = \nabla_v \cdot \left[\int_{\mathbb{R}^d} \left(A(\mathbf{v} - \mathbf{v}_*)\left(\nabla_v \frac{\delta E}{\delta f} - \nabla_{v_*} \frac{\delta E_*}{\delta f_*}\right) f_* d\mathbf{v}_*\right) f\right]. \tag{5.44}$$

This E and $\frac{\delta E}{\delta f}$ correspond to the entropy functional and its variational derivative:

$$E \coloneqq \int_{\mathbb{R}^d} f \log(f) d\mathbf{v}, \tag{5.45}$$

$$\implies \frac{\delta E}{\delta f} = \log(f). \tag{5.46}$$

They regularize the entropy functional and its variation by defining a mollifier function, ψ_ε:[5]

$$E_\varepsilon(f) \coloneqq \int_{\mathbb{R}^d} \left(f * \psi_\varepsilon\right) \log\left(f * \psi_\varepsilon\right) d\mathbf{v}, \tag{5.47}$$

$$\implies \frac{\delta E_\varepsilon}{\delta f} = \psi_\varepsilon * \log\left(f * \psi_\varepsilon\right), \tag{5.48}$$

$$F_\varepsilon(f) \coloneqq \nabla \frac{\delta E_\varepsilon}{\delta f}, \tag{5.49}$$

$$\psi_\varepsilon(\mathbf{v}) \coloneqq \frac{1}{(2\pi\varepsilon)^{\frac{d}{2}}} \exp\left(-\frac{\|\mathbf{v}\|^2}{2\varepsilon}\right). \tag{5.50}$$

[5]The F_ε term is a novelty introduced here to make a future step clearer.

This leaves us with the homogenous Landau equation defined by the regularized entropy functional

$$\frac{\partial f}{\partial t} = Q_\varepsilon(f,f) \coloneqq \nabla_v \cdot \left[\int_{\mathbb{R}^d} \left(A(\mathbf{v}-\mathbf{v}_*) \left(\nabla_v \frac{\delta E_\varepsilon}{\delta f} - \nabla_{v_*} \frac{\delta E_{\varepsilon,*}}{\delta f_*} \right) f_* d\mathbf{v}_* \right) f \right] \equiv -\nabla_v \cdot (U_\varepsilon(f) f) \,. \tag{5.51}$$

When we take the gradient of $\frac{\delta E_\varepsilon}{\delta f}$, we can immediately see the advantage of convolving f with ψ_ε. Exploiting the convolution property $\frac{d}{dx}\left(f(x) * g(x)\right) = \frac{df}{dx} * g$, we see $F_\varepsilon = \nabla\psi_\varepsilon * \log(f * \psi_\varepsilon)$.

Recalling that we are assuming homogeneity in space, we let the particle distribution function for N particles each with associated velocities at time t, v_i and associated weights w_i assume the following form

$$f^N(t,\mathbf{v}) = \sum_{i=1}^{N} w_i \delta(\mathbf{v} - \mathbf{v}_i(t)). \tag{5.52}$$

If we assume this form, we get the following

$$\begin{aligned}
\frac{\partial f^N}{\partial t} &= \sum_{i=0}^{N} w_i \frac{\partial}{\partial t} \delta\left(\mathbf{v} - \mathbf{v}_i(t)\right) \\
&= \sum_{i=0}^{N} w_i \left(\nabla_{\mathbf{v}_i} \delta\left(\mathbf{v} - \mathbf{v}_i(t)\right) \cdot \frac{d\mathbf{v}_i}{dt} \right) \\
&= \sum_{i=0}^{N} \left(w_i \left(-\nabla_{\mathbf{v}} \delta\left(\mathbf{v} - \mathbf{v}_i(t)\right) \right) \cdot \frac{d\mathbf{v}_i}{dt} \right) \\
&= -\nabla_{\mathbf{v}} \cdot \sum_{i=0}^{N} \left(w_i \delta\left(\mathbf{v} - \mathbf{v}_i(t)\right) \frac{d\mathbf{v}_i}{dt} \right) = -\nabla_{\mathbf{v}} \cdot \left(U_\varepsilon\left(f^N\right) f^N \right)
\end{aligned} \tag{5.53}$$

The second step is justified from a property of the Dirac delta function, $\frac{\partial}{\partial a}\delta(a-b) = -\frac{\partial}{\partial b}\delta(a-b)$. The last step is from (5.51), where we define U_ε. Now, before we take another step, it is important to note another property, that $f(\delta(x-y_1))\delta(x-y_2) = 0$ for $y_1 \neq y_2$, assuming $f(0) = 0$. The reasoning is simple, if $x = y_1$, then $f(y_1)$ may be nonzero, but $\delta(x-y_2) = 0$. Similarly, for $x = y_2$, the $f(0)$ resolves to 0. We see $U_\varepsilon(f)(t,\mathbf{v}_i)$ resolves to zero if $\mathbf{v}_i = 0$ due to the collision kernel A,

and so passing in $\delta(\mathbf{v} - \mathbf{v}_i)$ will have a similar effect. Now, by this logic,

$$\begin{aligned} U_\varepsilon\left(f^N\right) f &= U_\varepsilon\left(\sum_{i=0}^{N} w_i \delta(\mathbf{v} - \mathbf{v}_i(t))\right) \sum_{j=0}^{N} w_i \delta\left(\mathbf{v} - \mathbf{v}_i(t)\right) \\ &= \delta_{ij} U_\varepsilon\left(\sum_{i=0}^{N} w_i \delta(\mathbf{v} - \mathbf{v}_i(t))\right) \sum_{j=0}^{N} w_i \delta\left(\mathbf{v} - \mathbf{v}_i(t)\right) \\ &= \sum_{i=0}^{N} U_\varepsilon\left(w_i \delta\left(\mathbf{v} - \mathbf{v}_i\right)\right) w_i \delta\left(\mathbf{v} - \mathbf{v}_i\right). \end{aligned} \tag{5.54}$$

Combining (5.53) and (5.54), we observe

$$-\nabla_{\mathbf{v}} \cdot \sum_{i=0}^{N} \left(w_i \delta\left(\mathbf{v} - \mathbf{v}_i(t)\right) \frac{d\mathbf{v}_i}{dt}\right) = -\nabla_{\mathbf{v}} \cdot \sum_{i=0}^{N} U_\varepsilon\left(w_i \delta\left(\mathbf{v} - \mathbf{v}_i\right)\right) w_i \delta\left(\mathbf{v} - \mathbf{v}_i\right). \tag{5.55}$$

This implies

$$\frac{d\mathbf{v}_i}{dt} = U_\varepsilon\left(f^N\right)(t, \mathbf{v}_i). \tag{5.56}$$

$$-\nabla_{\mathbf{v}} \cdot \left(U_\varepsilon\left(f^N\right) f^N\right) = -\nabla_{\mathbf{v}} \cdot \left(U_\varepsilon\left(f^N\right) \sum_{i=0}^{N} w_i \delta\left(\mathbf{v} - \mathbf{v}_i(t)\right)\right) \tag{5.57}$$

Setting (5.53) equal to (5.57), we see

$$\begin{aligned} &-\nabla_{\mathbf{v}} \cdot \sum_{i=0}^{N} \left(w_i \delta(\mathbf{v} - \mathbf{v}_i(t)) \frac{d\mathbf{v}_i}{dt}\right) = -\nabla_{\mathbf{v}} \cdot \left(U_\varepsilon\left(f^N\right) \sum_{i=0}^{N} w_i \delta(\mathbf{v} - \mathbf{v}_i(t))\right), \\ \implies &\frac{d\mathbf{v}_i}{dt} = U_\varepsilon\left(f^N\right)(t, \mathbf{v}_i(t)). \end{aligned} \tag{5.58}$$

This gives us our velocity update equation

$$\frac{d\mathbf{v}_i}{dt} = U_\varepsilon(f^N)(t, \mathbf{v}_i(t)) = -\sum_{j}^{N} w_j A(\mathbf{v}_i - \mathbf{v}_j)\left[F_\varepsilon^N(\mathbf{v}_i) - F_\varepsilon^N(\mathbf{v}_j)\right] \tag{5.59}$$

The convolution of $f(\mathbf{v})$ and $\psi_\varepsilon(\mathbf{v})$ is $\sum_k w_k \psi_\varepsilon(\mathbf{v} - \mathbf{v}_k)$. Knowing this, we write

$$F_\varepsilon^N(\mathbf{v}) = \int_{\mathbb{R}^d} \nabla\psi_\varepsilon(\mathbf{v} - \mathbf{v}_*) \log\left(\sum_{k}^{N} w_k \psi_\varepsilon\left(\mathbf{v}_* - \mathbf{v}_k\right)\right) d\mathbf{v}_* \tag{5.60}$$

We can convert all of this to a discrete version. We see

$$\frac{d\bar{\mathbf{v}}_i}{dt} = \bar{U}_\varepsilon(\bar{f}^N)(t, \bar{v}_i) \coloneqq -\sum_{j}^{N} w_j A\left(\bar{\mathbf{v}}_i - \bar{\mathbf{v}}_j\right)\left[\bar{F}_\varepsilon^N\left(\bar{\mathbf{v}}_i\right) - \bar{F}_\varepsilon^N\left(\bar{\mathbf{v}}_j\right)\right]. \tag{5.61}$$

The discrete versions of E_ε^N and F_ε^N are shown to be

$$\bar{F}_\varepsilon(f)(\mathbf{v}_i) \coloneqq \sum_l \left[h^d \nabla \psi_\varepsilon \left(\bar{\mathbf{v}}_i - \mathbf{v}_l^c \right) \log \left(\sum_k w_k \psi_\varepsilon \left(\mathbf{v}_l^c - \bar{\mathbf{v}}_k \right) \right) \right] \tag{5.62}$$

$$\bar{E}_\varepsilon(f)(\mathbf{v}_i) \coloneqq \sum_l \left[h^d \left(\sum_i w_i \psi_\varepsilon \left(\mathbf{v}_l^c - \bar{\mathbf{v}}_i \right) \right) \log \left(\sum_k w_k \psi_\varepsilon \left(\mathbf{v}_l^c - \bar{\mathbf{v}}_k \right) \right) \right]. \tag{5.63}$$

Here, we have defined $\mathbf{v}_l^c$ to be the velocity cell centers and h to be the spacing between the centers. The summation comes from computing the integral according to the trapezoid rule. $\frac{d\mathbf{v}_i}{dt}$ may be computed using any difference scheme, this paper uses first order backward difference.

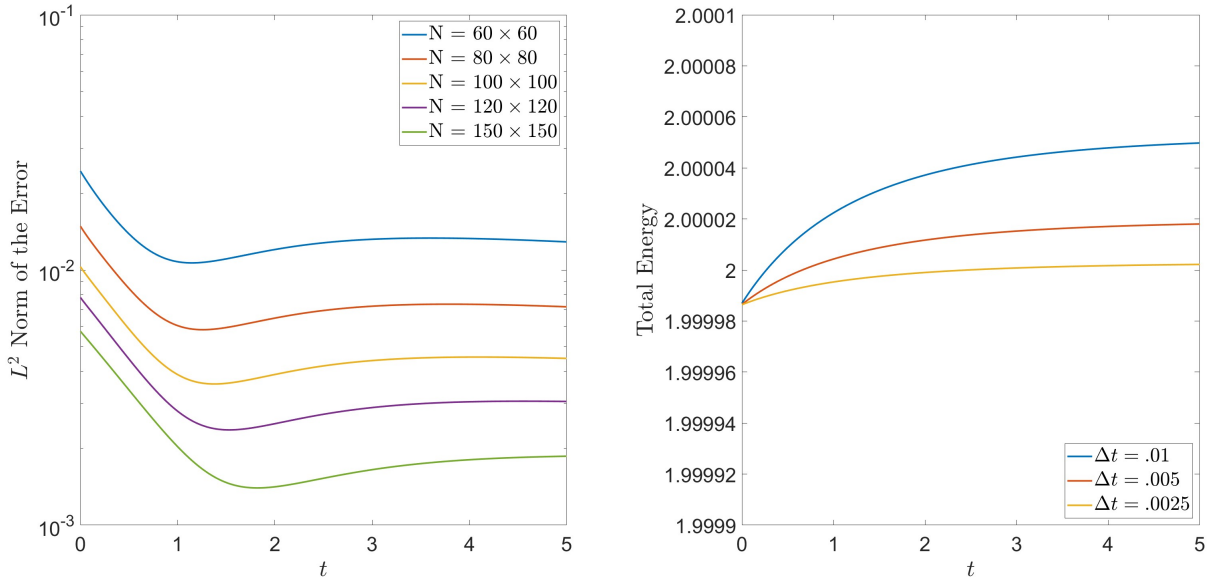

(a) Fractional Error, $\|f_{numerical} - f_{exact}\|_2 / \|f_{exact}\|_2$

(b) Total Energy Over Time

Figure 5.9 The fractional error between $f_{numerical}$ and f_{exact} refined over velocity space (left) and the total energy over time refined over time (right). This matches the results of [303], indicating our foundation is secure and the real work may begin.

A number of desirable properties are proven for the continuous case, with some of these properties transferring to the discrete. Of particular note is the preservation of the physical properties such as positivity, conservation of mass, momentum, and energy, and entropy decay.

Work has been done to replicate the results of this paper, which includes four sample problems, two of which have analytic solutions to compare to. We chose the first one, which gives the following

collision kernel and exact solution:

$$A(\mathbf{z}) = \frac{1}{16}\left(\|\mathbf{z}\|^2 I_d - \mathbf{z}\otimes\mathbf{z}\right), \tag{5.64}$$

$$f_{exact}(t,\mathbf{v}) = \frac{1}{2\pi K}\exp\left(\frac{-\|\mathbf{v}\|^2}{2K}\right)\left(\frac{2K-1}{K} + \frac{1-K}{2K^2}\|\mathbf{v}\|^2\right), \quad K \coloneqq 1 - \frac{1}{2}\exp\left(-\frac{t}{8}\right). \tag{5.65}$$

Having obtained our numerical update to our velocities, we obtain the numerical solution

$$f_{numerical}(t,\mathbf{v}) = \left(\psi_\varepsilon * \bar{f}^N(t,\mathbf{v})\right) = \sum_{i=1}^{N} w_i \psi_\varepsilon(v - \bar{v}_i(t)). \tag{5.66}$$

The comparisons of the numerical distribution with the exact are displayed in Figure 5.9. We notice that the norm is bound, though certainly not nontrivial. More importantly is the observation that the total energy hardly varies throughout the simulation. This is in direct agreement with the observations obtained by [303] (a comparison between the plots will show they are identical).

The next steps will be to extend this work to relativistic settings, as the current operator is accurate only for nonrelativistic settings. The ability to handle relativity is one of the benefits of our method brings to the table, so we need to develop a collision operator that can match. Discussions with Dr. Hu are already underway as of April 2025 to begin this work.

The first step will be to replace the standard nonrelativistic kernel with the relativistic kernel described in [305, 306, 307].[6] Once this is done, we will apply the same exact initial conditions given by [303] in their test problems, ensuring it reduces to the nonrelativistic. Given there are fewer extant relativistic collision test problems, we may need to extend one or more of these test problems to the relativistic setting.

Once this is done, we will use the more recent work of [304] where they extended to heterogeneous settings. Throughout all of this, it is worth noting that runtime becomes nontrivial. The computation of the macroparticles already composes the lion's share of the compute resources necessary in a PIC code. Implementing a collision operator installs an $O\left(N^2\right)$ operation, where N is the number of particles. This is extremely expensive. Work has been done to bring collision operators down to $O\left(N\log\left(N\right)\right)$, with Carrillo et al drawing special attention to the Fourier spectral methods

[6] All have a different way of formulating this kernel. Presumably they all reduce to the same form, but I have not tested this.

in particular given they can exploit the Landau operator's convolution components. Pareschi et al [308] considered a spectral solve, which they then combined with a splitting technique [309] which Zhang and Gamba [310, 311] built upon. They split the Fokker-Planck-Landau equation into two subproblems, the Vlasov-Poisson (They simplify Vlasov-Maxwell to Vlasov-Poisson) and the homogenous Landau problem via time-splitting. This, too, may be an avenue of advance.

5.6 Conclusion

Einstein once said, "As our circle of knowledge expands, so does the circumference of darkness surrounding it." And indeed, we see that having established a new PIC method that preserves involutions has only led to more questions surrounding it. There are a number of exciting lines of inquiry that this method has unlocked, only a few of which I have discussed in this chapter. We may consider how our theory extends to include source and sink terms, develop kernel based methods of taking derivatives that would enable the Green's function method to satisfy the involutions, extend our theory to a Finite Element formulation to push the geometric capabilities even further, or implement collision operators to better capture the physical phenomena of a system. Suffice to say, there is much to explore.

CHAPTER 6

CONCLUSION

In this dissertation we have covered a short sequence of projects concerning the development of a new Particle-in-Cell method. First, in Chapter 2 we hammered together Causley et al's the MOLT method of solving waves together with the Asymmetrical Euler Method particle pusher of Gibbon et al, modifying the pusher in order to better preserve physical properties. This forging resulted in a new PIC method that was shown to have a number of desirable properties. This method features an unconditionally stable wave solver, a particle pusher that displays volume preserving properties, features a mesh is collocated, is geometrically flexible, is able to handle a naive bilinear interpolation scheme while preserving physical properties of the system, is resilient to numerical heating, and refines at a rather fast rate.

In Chapter 3 we noted a lacuna within this method, that the Lorenz gauge and Gauss's laws had nontrivial errors that, while bound, were still concerning. We considered how to solve this problem, first developing theory to show that satisfaction of the continuity equation implied not only satisfaction of the Lorenz gauge (and vice versa), but that satisfaction of the Lorenz gauge in turn implied satisfaction of Gauss's laws. We additionally developed a gauge correction method that would manually enforce the Lorenz gauge. To do this we ceased solving the boundary value problems resulting from the method of lines transpose using a Green's function and instead employed either the Fast Fourier Transform or sixth order Finite Difference method.

In Chapter 4 we generalized the theory developed in Chapter 3 from the first order Backward Difference Formula to all Backward Difference Formulas, a family of time centered second order methods, and all Adams-Bashforth methods. All s-stage diagonally implicit Runge-Kutta methods were shown to satisfy the Lorenz gauge if they satisfied the continuity equation, with the two stage method being proven to hold the if and only if relationship, suggesting the possibility of extending this to arbitrary s stage methods.

Finally, in Chapter 5 we considered a number of possible lines of inquiry this work could lead to. These inquiries included adding source terms to the continuity equation while maintaining the

Lorenz gauge and Gauss's laws, developing kernel based methods for computing derivatives in order to implement the Green's function method described in Chapter 2 while keeping the theory explored in Chapters 3 and 4, extending from a Finite Difference formulation to a Finite Element formulation, and adding collision operators.

There is a quote attributed to the painter John Ruskin, "If you can paint one leaf you can paint the world." Certainly the contributions of this thesis compared with the ever widening domain of science are roughly proportional to a leaf compared with the vast complexity of the nature it inhabits. But it is my hope that this study tells us something not only about the simulation of charged particles in electromagnetic waves, but about this truly wonderful cosmos we inhabit.

Sit finis libri non finis quaerendi.

BIBLIOGRAPHY

[1] W.M. Miller. *A Canticle for Leibowitz*. Bantam Books, 1976. ISBN: 9780553379266.

[2] Andrew J. Christlieb, William A. Sands, and Stephen White. "A Particle-in-cell Method for Plasmas with a Generalized Momentum Formulation, Part I: Model Formulation". In: *Journal of Scientific Computing* 103.15 (Feb. 2025). DOI: 10.1007/s10915-025-02824-1.

[3] Andrew J. Christlieb, William A. Sands, and Stephen R. White. "A Particle-in-cell Method for Plasmas with a Generalized Momentum Formulation, Part II: Enforcing the Lorenz Gauge Condition". In: *Journal of Scientific Computing* 101.73 (Nov. 2024). DOI: 10.1007/s10915-024-02728-6.

[4] Andrew J. Christlieb, William A. Sands, and Stephen R. White. "A Particle-In-Cell Method for Plasmas with a Generalized Momentum Formulation, Part III: A Family of Gauge Conserving Methods". In: *Journal of Scientific Computing* 104.38 (June 2025). DOI: 10.1007/s10915-025-02953-7.

[5] Lewi Tonks and Irving Langmuir. "Oscillations in Ionized Gases". In: *Phys. Rev.* 33 (2 Feb. 1929), pp. 195–210. DOI: 10.1103/PhysRev.33.195.

[6] Lewi Tonks. "The Birth of 'Plasma'". In: *American Journal of Physics* 35.9 (Sept. 1967), pp. 857–858. ISSN: 0002-9505. DOI: 10.1119/1.1974266.

[7] J. A. Bittencourt. *Fundamentals of Plasma Physics*. Third. Springer-Verlag, 2010.

[8] Gábor Tóth et al. "Extended Magnetohydrodynamics with Embedded Particle-in-Cell Simulation of Ganymede's Magnetosphere". In: *Journal of Geophysical Research: Space Physics* 121 (Feb. 2016), n/a–n/a. DOI: 10.1002/2015JA021997.

[9] Xue-Ning Bai et al. "Magnetohydrodynamic Particle-in-cell Simulations of the Cosmic-Ray Streaming Instability: Linear Growth and Quasi-linear Evolution". In: *The Astrophysical Journal* 876.1 (May 2019), p. 60. DOI: 10.3847/1538-4357/ab1648.

[10] A. B. Zylstra et al. "Experimental achievement and signatures of ignition at the National Ignition Facility". In: *Phys. Rev. E* 106 (2 Aug. 2022), p. 025202. DOI: 10.1103/PhysRevE.106.025202.

[11] A. L. Kritcher et al. "Design of an inertial fusion experiment exceeding the Lawson criterion for ignition". In: *Phys. Rev. E* 106 (2 Aug. 2022), p. 025201. DOI: 10.1103/PhysRevE.106.025201.

[12] M. A. Lieberman and A. J. Lichtenberg. *Principles of Plasma Discharges and Materials Processing*. New York: Wiley-Interscience, 1994. ISBN: 978-0471005773.

[13] Nathan P. Brown and Mitchell L. R. Walker. "Review of Plasma-Induced Hall Thruster Erosion". In: *Applied Sciences* 10.11 (2020). ISSN: 2076-3417. DOI: 10.3390/app10113775.

[14] Dmitrii Andreev, Artem Kuskov, and Edl Schamiloglu. "Review of the relativistic magnetron". In: *Matter and Radiation at Extremes* 4.6 (Oct. 2019). 067201. ISSN: 2468-2047. DOI: 10.1063/1.5100028.

[15] Steven H. Gold and Gregory S. Nusinovich. "Review of high-power microwave source research". In: *Review of Scientific Instruments* 68.11 (Nov. 1997), pp. 3945–3974. ISSN: 0034-6748. DOI: 10.1063/1.1148382.

[16] Manfred Thumm and Lambert Feher. "Millimeter-Wave-Sources Development: Present and Future". In: *Advances in Microwave and Radio Frequency Processing*. Ed. by Monika Willert-Porada. Berlin, Heidelberg: Springer Berlin Heidelberg, 2006, pp. 15–23. ISBN: 978-3-540-32944-2.

[17] Jim Browning, C. Lester, and John Luginsland. "A crossed-field amplifier using a distributed field emission cathode". In: *Technical Digest - 2009 22nd International Vacuum Nanoelectronics Conference, IVNC 2009* (July 2009). DOI: 10.1109/IVNC.2009.5271588.

[18] Michael Faraday. *Experimental Researches in Electricity Volume I*. Richard and John Edward Taylor, 1839.

[19] Michael Faraday. *Experimental Researches in Electricity Volume II*. Richard and John Edward Taylor, 1844.

[20] Michael Faraday. *Experimental Researches in Electricity Volume III*. Richard Taylor and William Francis, 1855.

[21] Michael Faraday. "On the Physical Character of the Lines of Magnetic Force". In: *Philosophical Magazine and Journal of Science*. 4th ser. 3.20 (June 1852).

[22] Michael Faraday. "On Lines of Magnetic Force; their definite character; and their distribution within a Magnet and through Space". In: *Philosophical Transactions of the Royal Society of London*. 28th ser. 142 (142 Dec. 1852).

[23] James Clerk Maxwell. "On Faraday's Lines of Force". In: *Cambridge Philosophical Transactions* X.III (Dec. 1855), pp. 27–83.

[24] James Clerk Maxwell. "On Physical Lines of Force, Part I - The Theory of Molecular Vortices applied to Magnetic Phenomena". In: *Philosophical Magazine and Journal of Science*. 4th ser. 91.CXXXIX (Mar. 1861), pp. 161–175.

[25] James Clerk Maxwell. "On Physical Lines of Force, Part II - The Theory of Molecular Vortices applied to Electric Currents". In: *Philosophical Magazine and Journal of Science*.

4th ser. XXI.CXL (Apr. 1861), pp. 281–291.

[26] James Clerk Maxwell. "On Physical Lines of Force, Part III - The Theory of Molecular Vortices applied to Statical Electricity". In: *Philosophical Magazine and Journal of Science*. 4th ser. XXIII.CLI (Jan. 1862), pp. 12–24.

[27] James Clerk Maxwell. "On Physical Lines of Force, Part IV - The Theory of Molecular Vortices applied to the Action of Magnetism on Polarized Light". In: *Philosophical Magazine and Journal of Science*. 4th ser. XXIII.CLII (Feb. 1862), pp. 85–95.

[28] James Clerk Maxwell. "A Dynamical Theory of the Electromagnetic Field". In: *Philosophical Transactions of the Royal Society of London* 155 (1865), pp. 459–512.

[29] James Clerk Maxwell. *A Treatise on Electricity and Magnetism*. 3rd. New York: Dover Publications, 1954.

[30] James Clerk Maxwell. *The Scientific Papers of James Clerk Maxwell, Volume I*. Cambridge: C.J. Clay, M.A. and Sons, 1890.

[31] James Clerk Maxwell. *The Scientific Papers of James Clerk Maxwell, Volume II*. Cambridge: C.J. Clay, M.A. and Sons, 1890.

[32] John David Jackson. *Classical Electrodynamics*. 3rd ed. New York, NY: Wiley, 1999. ISBN: 9780471309321.

[33] Edmund Taylor Whittaker. *A History of the Theories of Aether and Electricity, Volume I*. New York: London: Thomas Nelson and Sons Ltd., 1910; New York: First Harper Torchbook, 1960, 1960.

[34] William A. Sands. "Numerical Methods for the Evolution of Fields with Applications to Plasmas". PhD thesis. "Michigan State University", 2022.

[35] Charles K. Birdsall and A. Bruce Langdon. *Plasma physics via computer simulation*. New York: Taylor and Francis, 2005. ISBN: 9781315275048.

[36] Matthew T. Bettencourt et al. "EMPIRE-PIC: A Performance Portable Unstructured Particle-in-Cell Code". In: *Communications in Computational Physics* 30.4 (June 2021). DOI: 10.4208/cicp.oa-2020-0261.

[37] John Villasenor and Oscar Buneman. "Rigorous charge conservation for local electromagnetic field solvers". In: *Computer Physics Communications* 69.2 (1992), pp. 306–316. ISSN: 0010-4655. DOI: https://doi.org/10.1016/0010-4655(92)90169-Y.

[38] J.P. Verboncoeur. "Symmetric Spline Weighting for Charge and Current Density in Particle Simulation". In: *Journal of Computational Physics* 174.1 (2001), pp. 421–427. ISSN:

0021-9991. DOI: https://doi.org/10.1006/jcph.2001.6923.

[39] David Foster Wallace. *Everything And More: A Compact History of Infinity*. W. W. Norton & Company, 2003. ISBN: 0393003388.

[40] Ludwig Boltzmann. "Some Errata in Maxwell's Paper 'On Faraday's Lines of Force'". In: *Nature*. 57th ser. (Nov. 1897), pp. 77–79.

[41] Alfred M. Bork. "Maxwell, Displacement Current, and Symmetry". In: *American Journal of Physics* 31.11 (Nov. 1963), pp. 854–859. ISSN: 0002-9505. DOI: 10.1119/1.1969140.

[42] David J Griffiths. *Introduction to Electrodynamics; 3rd ed.* Upper Saddle River, NJ: Prentice-Hall, 1999.

[43] John W. Arthur. "The Evolution of Maxwell's Equations from 1862 to the Present Day". In: *IEEE Antennas and Propagation Magazine* 55.3 (2013), pp. 61–81. DOI: 10.1109/MAP.2013.6586627.

[44] R.P. Feynman et al. *The Feynman Lectures on Physics; Vol. II*. Addison-Wesley Publishing Company, 1989.

[45] Oliver Heaviside. *Electrical Papers, Volume I*. London: Macmillan and Company, 1892.

[46] Josiah Willard Willard Gibbs. *Elements of Vector Analysis*. New York: Tuttle, Morehouse, and Taylor, 1881.

[47] Josiah Willard Willard Gibbs. *Vector Analysis*. New York: C. Scribner's Sons, 1901.

[48] Heinrich Hertz. *Electric waves : being researches on the propagation of electric action with finite velocity through space*. Trans. by D.E. Jones. London: Macmillan and co., 1893.

[49] Joseph Larmor. "Opening Address". In: *Nature* 62.1610 (1900), pp. 449–456.

[50] Oliver Heaviside. "XXXIX. On the electromagnetic effects due to the motion of electrification through a dielectric". In: *Philosophical Magazine Series 1* 27 (1889), pp. 324–339.

[51] Oliver Heaviside. *Electrical Papers, Volume II*. London: Macmillan and Company, 1894.

[52] Hendrik Lorentz. "Versuch einer Theorie der electrischen und optischen Erscheinungen in bewegten Körpern". In: *Royal Netherlands Academy* (1895).

[53] Albert Einstein. "On the electrodynamics of moving bodies". In: *Annalen Phys.* 17 (1905), pp. 891–921. DOI: 10.1002/andp.200590006.

[54] Sanborn C. Brown. “Chapter 1 - A Short History of Gaseous Electronics”. In: *Gaseous Electronics*. Ed. by Merle N. Hirsh and H.J. Oskam. New York: Academic Press, 1978, pp. 1–18. ISBN: 978-0-12-349701-7.

[55] Sir William Crookes. *On radiant matter a lecture delivered to the British Association for the Advancement of Science, at Sheffield, Friday, August 22, 1879*. London, [s.n.], 1879, 1879, p. 38.

[56] Sir William Crookes. “V. The Bakerian Lecture - On the illumination of lines of molecular pressure, and the trajectory of molecules”. In: *Philosophical Transactions of the Royal Society of London* 170 (1879), pp. 135–164.

[57] Irving Langmuir. “Electric discharges in gases at low pressures”. In: *Journal of the Franklin Institute* 214.3 (1932), pp. 275–298. ISSN: 0016-0032. DOI: https://doi.org/10.1016/S0016-0032(32)90932-6.

[58] Oliver Lodge. *Electrons or The Nature and Properties of Negative Electricity*. London: George Bell and Sons, 1906.

[59] Lord Rayleigh. “VII. On electrical vibrations and the constitution of the atom”. In: *The London, Edinburgh, and Dublin Philosophical Magazine and Journal of Science* 11.61 (1906), pp. 117–123. DOI: 10.1080/14786440609463428.

[60] E Hückel and P Debye. “The theory of electrolytes: I. lowering of freezing point and related phenomena”. In: *Physikalische Zeitschrift* 24 (1923), pp. 185–206.

[61] Ludwig Eduard Boltzmann. *Vorlesungen über Gastheorie*. Vol. 1. J.A.Barth, 1896.

[62] Ludwig Eduard Boltzmann. *Vorlesungen über Gastheorie*. Vol. 2. J.A.Barth, 1898.

[63] Ludwig Eduard Boltzmann. *Lectures on Gas Theory*. Trans. by Stephen G Brush. University of California Press, 1964.

[64] L.D. Landau. “Die kinetische gleichung für den fall Coulombscher wechselwirkung”. In: *Physikalische Zeitschrift Der Sowjetunion* 10 (1936).

[65] L.D. Landau. *Collected Papers of L.D. Landau*. Gordon, Breach, Science Publishers Inc., and Pergamon Press Ltd., 1965. ISBN: 978-0-08-010586-4.

[66] L.D. Landau. “Кинетическое Уравнение в случае кулоновского взаимодействия”. In: Журнал экспериментальной и теоретической физики 7 (1937).

[67] Matthew W. Kunz. *Lecture notes on Irreversible Processes in Plasmas*. Princeton, NJ 08543, Mar. 2024.

[68] A.V. Bobilev, I.F. Potapenko, and V.A. Chuyanov. “Kinetic equations of the Landau type as a model of the Boltzmann equation and completely conservative difference schemes”. In: *USSR Computational Mathematics and Mathematical Physics* 20.4 (1980), pp. 190–201. ISSN: 0041-5553. DOI: https://doi.org/10.1016/0041-5553(80)90281-5.

[69] A. A. Vlasov. “О вибрационных свойствах электронного газа”. Russian. In: Журнал экспериментальной и теоретической физики 8 (1938), pp. 291–318.

[70] A. A. Vlasov. “The Vibrational Properties of an Electron Gas”. In: *Soviet Physics Uspekhi* 10.6 (June 1968), p. 721. DOI: 10.1070/PU1968v010n06ABEH003709.

[71] Alan Turing. “On Computable Numbers, with an Application to the Entscheidungsproblem”. In: *Proceedings of the London Mathematical Society* 42.1 (1936), pp. 230–265. DOI: 10.2307/2268810.

[72] Alonzo Church. “An Unsolvable Problem of Elementary Number Theory”. In: *American Journal of Mathematics* 58 (1936), p. 345. DOI: 10.2307/2371045.

[73] C.K. Birdsall. “Particle-in-cell charged-particle simulations, plus Monte Carlo collisions with neutral atoms, PIC-MCC”. in: *IEEE Transactions on Plasma Science* 19.2 (Apr. 1991), pp. 65–85. ISSN: 1939-9375. DOI: 10.1109/27.106800.

[74] O Buneman and D.A. Dunn. “Computer Experiments in Plasma Physics”. In: *Science Journal* 2 (July 1966). Available at NASA Archives, pp. 34–43.

[75] D.R. Hartree. “Some Calculations of Transients in an Electronic Valve”. In: *Applied Scientific Research* 1 (1950), pp. 379–390. DOI: 10.1007/BF02919956.

[76] P. K. Tien and J. Moshman. “Monte Carlo Calculation of Noise Near the Potential Minimum of a High-Frequency Diode”. In: *Journal of Applied Physics* 27.9 (May 2004), pp. 1067–1078. ISSN: 0021-8979. DOI: 10.1063/1.1722543.

[77] R. W. Hockney and J. W. Eastwood. *Computer simulation using particles*. Bristol: Hilger, 1988, 1988.

[78] O. Buneman. “Dissipation of Currents in Ionized Media”. In: *Phys. Rev.* 115 (3 Aug. 1959), pp. 503–517. DOI: 10.1103/PhysRev.115.503.

[79] John Dawson. “One-Dimensional Plasma Model”. In: *The Physics of Fluids* 5.4 (Apr. 1962), pp. 445–459. ISSN: 0031-9171. DOI: 10.1063/1.1706638.

[80] J P Verboncoeur. “Particle simulation of plasmas: review and advances”. In: *Plasma Physics and Controlled Fusion* 47.5A (Apr. 2005), A231–A260.

[81] J Dawson and C Smith. *Some Investigations of Plasma Instabilities in One-Dimensional*

Plasmas. Tech. rep. Princeton Plasma Physics Lab, Nov. 1962.

[82] R.W. Hockney. In: *Quarterly Research Review* 4 (Apr. 1963), pp. 1–102.

[83] Peter Burger. "The Opposite-Stream Plasma Diode". PhD thesis. Stanford University, 1964.

[84] D.A. Dunn and I.T. Ho. *Computer Experiments on Ion-Beam Neutralization with Initially Cold Electrons*. Tech. rep. Stanford Electron Research Lab, Apr. 1963.

[85] A.B. Langdon and J.M. Dawson. "Investigations of a Sheet Model for a Bounded Plasma Field and Radiation". In: *Proceedings of 1st Conference for the Numerical Simulation of Plasmas*. Also available as a technical report in greater detail, Electronics Research Laboratory, University of Berkeley, 1969. Apr. 1967, pp. 39–40.

[86] Kane S. Yee. "Numerical solution of initial boundary value problems involving Maxwell's equations in isotropic media". In: *IEEE Transactions on Antennas and Propagation* 14 (3 1966), pp. 302–307.

[87] A.B. Langdon and J.M. Dawson. "Fast Numerical Procedures for Computer Experiments on Relativistic Plasmas". In: *Relativistic Plasmas: The Coral Gables Conference*. Ed. by O. Buneman and W. Pardo. Also available as a technical report in greater detail, Electronics Research Laboratory, University of Berkeley, 1969. New York: Benjamin, Apr. 1968, pp. 205–219.

[88] R. L. Morse and C. W. Nielson. "Numerical Simulation of the Weibel Instability in One and Two Dimensions". In: *The Physics of Fluids* 14.4 (Apr. 1971), pp. 830–840. ISSN: 0031-9171. DOI: 10.1063/1.1693518.

[89] A.B. Langdon. "Implicit Plasma Simulation". In: *Space Science Reviews* 42 (Oct. 1985), pp. 67–83.

[90] A. Bruce Langdon and Charles K. Birdsall. "Theory of Plasma Simulation Using Finite-Size Particles". In: *The Physics of Fluids* 13.8 (Aug. 1970), pp. 2115–2122. ISSN: 0031-9171. DOI: 10.1063/1.1693209.

[91] Jay P Boris et al. "Relativistic plasma simulation-optimization of a hybrid code". In: *Proc. Fourth Conf. Num. Sim. Plasmas*. 1970, pp. 3–67.

[92] Oscar Buneman. "Time-reversible difference procedures". In: *Journal of Computational Physics* 1.4 (1967), pp. 517–535. ISSN: 0021-9991. DOI: https://doi.org/10.1016/0021-9991(67)90056-3.

[93] Rodney J Mason. "Implicit moment particle simulation of plasmas". In: *Journal of Computational Physics* 41.2 (1981), pp. 233–244. ISSN: 0021-9991. DOI: https://doi.org/10.1016/0021-9991(81)90094-2.

[94] A.Bruce Langdon, Bruce I Cohen, and Alex Friedman. "A direct method for implicit particle-in-cell simulation". In: *Comments on Plasma Physics and Controlled Fusion* 6.6 (1981), pp. 225–236. ISSN: 0374-2806.

[95] J. Denavit. "Time-filtering particle simulations with $\omega_p e\Delta t >> 1$". In: *Journal of Computational Physics* 42.2 (1981), pp. 337–366. ISSN: 0021-9991. DOI: https://doi.org/10.1016/0021-9991(81)90249-7.

[96] A.Bruce Langdon, Bruce I Cohen, and Alex Friedman. "Direct implicit large time-step particle simulation of plasmas". In: *Journal of Computational Physics* 51.1 (1983), pp. 107–138. ISSN: 0021-9991. DOI: https://doi.org/10.1016/0021-9991(83)90083-9.

[97] Bruce I Cohen. "Multiple time scale methods in particle simulations of plasmas". In: *Part. Accel.* 19 (1986), pp. 227–236.

[98] J.U. Brackbill and B.I. Cohen. *Multiple Time Scales*. New York: Academic, 1985.

[99] William S Lawson. "Particle simulation of bounded 1D plasma systems". In: *Journal of Computational Physics* 80.2 (1989), pp. 253–276. ISSN: 0021-9991. DOI: https://doi.org/10.1016/0021-9991(89)90099-5.

[100] Peter Burger. "Elastic Collisions in Simulating One-Dimensional Plasma Diodes on the Computer". In: *The Physics of Fluids* 10.3 (Mar. 1967), pp. 658–666. ISSN: 0031-9171. DOI: 10.1063/1.1762162.

[101] Tomonor Takizuka and Hirotada Abe. "A binary collision model for plasma simulation with a particle code". In: *Journal of Computational Physics* 25.3 (1977), pp. 205–219. ISSN: 0021-9991. DOI: https://doi.org/10.1016/0021-9991(77)90099-7. URL: https://www.sciencedirect.com/science/article/pii/0021999177900997.

[102] M. Surendra, D. B. Graves, and I. J. Morey. "Electron heating in low-pressure rf glow discharges". In: *Applied Physics Letters* 56.11 (Mar. 1990), pp. 1022–1024. ISSN: 0003-6951. DOI: 10.1063/1.102604.

[103] M. Surendra and D.B. Graves. "Particle simulations of radio-frequency glow discharges". In: *IEEE Transactions on Plasma Science* 19.2 (1991), pp. 144–157. DOI: 10.1109/27.106808.

[104] V Vahedi et al. "Capacitive RF discharges modelled by particle-in-cell Monte Carlo simulation. II. Comparisons with laboratory measurements of electron energy distribution functions". In: *Plasma Sources Science and Technology* 2.4 (Nov. 1993), p. 273. DOI: 10.1088/0963-0252/2/4/007.

[105] V. Vahedi and M. Surendra. "A Monte Carlo collision model for the particle-in-cell method: applications to argon and oxygen discharges". In: *Computer Physics Communications*

87.1 (1995). Particle Simulation Methods, pp. 179–198. ISSN: 0010-4655. DOI: https://doi.org/10.1016/0010-4655(94)00171-W.

[106] B. Ripperda et al. "A Comprehensive Comparison of Relativistic Particle Integrators". In: *The Astrophysical Journal Supplement Series* 235.1 (Mar. 2018), p. 21. DOI: 10.3847/1538-4365/aab114.

[107] G. Chen, L. Chacón, and D.C. Barnes. "An energy- and charge-conserving, implicit, electrostatic particle-in-cell algorithm". In: *Journal of Computational Physics* 230.18 (2011), pp. 7018–7036. ISSN: 0021-9991. DOI: https://doi.org/10.1016/j.jcp.2011.05.031.

[108] Giovanni Lapenta and Stefano Markidis. "Particle acceleration and energy conservation in particle in cell simulations". In: *Physics of Plasmas* 18.7 (July 2011). ISSN: 1070-664X. DOI: 10.1063/1.3602216.

[109] Stefano Markidis and Giovanni Lapenta. "The energy conserving particle-in-cell method". In: *Journal of Computational Physics* 230.18 (Aug. 2011), pp. 7037–7052. DOI: 10.1016/j.jcp.2011.05.033.

[110] Barry Marder. "A method for incorporating Gauss' law into electromagnetic PIC codes". In: *Journal of Computational Physics* 68.1 (1987), pp. 48–55. ISSN: 0021-9991. DOI: https://doi.org/10.1016/0021-9991(87)90043-X.

[111] A. Bruce Langdon. "On enforcing Gauss' law in electromagnetic particle-in-cell codes". In: *Computer Physics Communications* 70.3 (1992), pp. 447–450. ISSN: 0010-4655. DOI: https://doi.org/10.1016/0010-4655(92)90105-8.

[112] P.J. Mardahl and J.P. Verboncoeur. "Charge conservation in electromagnetic PIC codes; spectral comparison of Boris/DADI and Langdon-Marder methods". In: *Computer Physics Communications* 106.3 (1997), pp. 219–229. ISSN: 0010-4655. DOI: https://doi.org/10.1016/S0010-4655(97)00094-5.

[113] G. Chen et al. "A semi-implicit, energy- and charge-conserving particle-in-cell algorithm for the relativistic Vlasov-Maxwell equations". In: *Journal of Computational Physics* 407 (2020), p. 109228. ISSN: 0021-9991. DOI: https://doi.org/10.1016/j.jcp.2020.109228.

[114] Giovanni Lapenta. "Exactly energy conserving semi-implicit particle in cell formulation". In: *Journal of Computational Physics* 334 (Apr. 2017), pp. 349–366. DOI: 10.1016/j.jcp.2017.01.002.

[115] H.X. Vu and J.U. Brackbill. "CELEST1D: an implicit, fully kinetic model for low-frequency, electromagnetic plasma simulation". In: *Computer Physics Communications* 69.2 (1992), pp. 253–276. ISSN: 0010-4655. DOI: https://doi.org/10.1016/0010-4655(92)90165-U.

[116] Lorenzo Siddi, Giovanni Lapenta, and Paul Gibbon. "Mesh-free Hamiltonian implementation of two dimensional Darwin model". In: *Physics of Plasmas* 24 (Aug. 2017), p. 082103. DOI: 10.1063/1.4994705.

[117] D.A. Knoll and D.E. Keyes. "Jacobian-free Newton–Krylov methods: a survey of approaches and applications". In: *Journal of Computational Physics* 193.2 (2004), pp. 357–397. ISSN: 0021-9991. DOI: https://doi.org/10.1016/j.jcp.2003.08.010.

[118] Bruce I. Cohen, Robert P. Freis, and Vincent Thomas. "Orbit-averaged implicit particle codes". In: *Journal of Computational Physics* 45.3 (1982), pp. 345–366. ISSN: 0021-9991. DOI: https://doi.org/10.1016/0021-9991(82)90108-5.

[119] L. Chacón, G. Chen, and D.C. Barnes. "A charge- and energy-conserving implicit, electrostatic particle-in-cell algorithm on mapped computational meshes". In: *Journal of Computational Physics* 233 (2013), pp. 1–9. ISSN: 0021-9991. DOI: https://doi.org/10.1016/j.jcp.2012.07.042.

[120] G. Chen and L. Chacón. "An energy- and charge-conserving, nonlinearly implicit, electromagnetic 1D-3V Vlasov–Darwin particle-in-cell algorithm". In: *Computer Physics Communications* 185.10 (2014), pp. 2391–2402. ISSN: 0010-4655. DOI: https://doi.org/10.1016/j.cpc.2014.05.010.

[121] G. Chen and L. Chacón. "A multi-dimensional, energy- and charge-conserving, nonlinearly implicit, electromagnetic Vlasov–Darwin particle-in-cell algorithm". In: *Computer Physics Communications* 197 (2015), pp. 73–87. ISSN: 0010-4655. DOI: https://doi.org/10.1016/j.cpc.2015.08.008.

[122] L. Chacón and G. Chen. "A curvilinear, fully implicit, conservative electromagnetic PIC algorithm in multiple dimensions". In: *Journal of Computational Physics* 316 (2016), pp. 578–597. ISSN: 0021-9991. DOI: https://doi.org/10.1016/j.jcp.2016.03.070.

[123] L.F. Ricketson and L. Chacón. "An energy-conserving and asymptotic-preserving charged-particle orbit implicit time integrator for arbitrary electromagnetic fields". In: *Journal of Computational Physics* 418 (2020), p. 109639. ISSN: 0021-9991. DOI: https://doi.org/10.1016/j.jcp.2020.109639.

[124] Oleksandr Koshkarov et al. "Fast nonlinear iterative solver for an implicit, energy-conserving, asymptotic-preserving charged-particle orbit integrator". In: *Journal of Computational Physics* 459 (Mar. 2022). DOI: 10.1016/j.jcp.2022.111146.

[125] G. Chen and L. Chacón. "An implicit, conservative and asymptotic-preserving electrostatic particle-in-cell algorithm for arbitrarily magnetized plasmas in uniform magnetic fields". In: *Journal of Computational Physics* 487 (2023), p. 112160. ISSN: 0021-9991. DOI: https://doi.org/10.1016/j.jcp.2023.112160.

[126] L. Chacón and G. Chen. "Local conservation of energy in fully implicit PIC algorithms". In: *Journal of Computational Physics* 529 (2025), p. 113862. ISSN: 0021-9991. DOI: https://doi.org/10.1016/j.jcp.2025.113862.

[127] Charles Galton Darwin. "The dynamical motions of charged particles". In: *The london, edinburgh, and dublin philosophical magazine and journal of science* 39.233 (1920), pp. 537–551.

[128] Clair W. Nielson and H. Ralph Lewis. "Particle-Code Models in the Nonradiative Limit". In: *Controlled Fusion*. Ed. by John Kileen. Vol. 16. Methods in Computational Physics: Advances in Research and Applications. Elsevier, 1976, pp. 367–388. DOI: https://doi.org/10.1016/B978-0-12-460816-0.50015-4.

[129] Yingda Cheng et al. "An asymptotic preserving Maxwell solver resulting in the Darwin limit of electrodynamics". In: *Journal of Scientific Computing* 71.3 (2017), pp. 959–993.

[130] Pierre Degond and Pierre-Arnaud Raviart. "An analysis of the Darwin model of approximation to Maxwell's equations". In: *Forum Mathematicum* 4.Jahresband (1992), pp. 13–44. DOI: doi:10.1515/form.1992.4.13.

[131] Ernst Hairer, Christian Lubich, and Gerhard Wanner. *Geometric Numerical Integration: Structure Preserving Algorithms for Ordinary Differential Equations*. Springer Berlin, Heidelberg, 2006. ISBN: 978-3-540-30663-4.

[132] Ernst Hairer, Syvert Paul Nørsett, and Gerhard Wanner. *Solving Ordinary Differential Equations I: Nonstiff Problems*. Springer Berlin, Heidelberg, 1993. ISBN: 978-3-540-56670-0.

[133] Ernst Hairer and Gerhard Wanner. *Solving Ordinary Differential Equations II: Stiff and Differential-Algebraic Problems*. Springer Berlin, Heidelberg, 1997. ISBN: 978-3-540-60452-5.

[134] J.M. Sanz-Serna and M.P. Calvo. *Numerical Hamiltonian Problems*. Dover Publications, 2018. ISBN: 978-0-486-82410-9.

[135] Hermann Weyl. *The Classical Groups, their Invariants and Representations*. Princeton University Press, 1946. ISBN: 0-691-07923-4.

[136] J. Squire, H. Qin, and W. M. Tang. "Geometric integration of the Vlasov-Maxwell system with a variational particle-in-cell scheme". In: *Physics of Plasmas* 19.8 (Aug. 2012). ISSN: 1089-7674. DOI: 10.1063/1.4742985.

[137] Jianyuan Xiao et al. "A variational multi-symplectic particle-in-cell algorithm with smoothing functions for the Vlasov-Maxwell system". In: *Physics of Plasmas* 20 (Oct. 2013), pp. 2517–. DOI: 10.1063/1.4826218.

[138] Yang He et al. "Hamiltonian time integrators for Vlasov-Maxwell equations". In: *Physics of Plasmas* 22.12 (Dec. 2015), p. 124503. ISSN: 1070-664X. DOI: 10.1063/1.4938034.

[139] Yang He et al. "Explicit K-symplectic algorithms for charged particle dynamics". In: *Physics Letters A* 381.6 (2017), pp. 568–573. ISSN: 0375-9601. DOI: https://doi.org/10.1016/j.physleta.2016.12.031.

[140] Yang He et al. *Hamiltonian integration methods for Vlasov-Maxwell equations*. May 2015. arXiv: 1505.06076 [physics.comp-ph]. URL: https://arxiv.org/abs/1505.06076.

[141] Yang He et al. *Explicit non-canonical symplectic algorithms for charged particle dynamics*. Sept. 2015. arXiv: 1509.07794 [physics.comp-ph]. URL: https://arxiv.org/abs/1509.07794.

[142] Yang He et al. "Hamiltonian particle-in-cell methods for Vlasov-Maxwell equations". In: *Physics of Plasmas* 23.9 (Sept. 2016), p. 092108. ISSN: 1070-664X. DOI: 10.1063/1.4962573.

[143] Jianyuan Xiao et al. "Explicit high-order non-canonical symplectic particle-in-cell algorithms for Vlasov-Maxwell systems". In: *Physics of Plasmas* 22.11 (Nov. 2015). ISSN: 1089-7674. DOI: 10.1063/1.4935904.

[144] Jianyuan Xiao, Hong Qin, and Jian Liu. "Structure-preserving geometric particle-in-cell methods for Vlasov-Maxwell systems". In: *Plasma Science and Technology* 20.11 (Sept. 2018), p. 110501. ISSN: 1009-0630. DOI: 10.1088/2058-6272/aac3d1.

[145] Hong Qin et al. "Canonical symplectic particle-in-cell method for long-term large-scale simulations of the Vlasov–Maxwell equations". In: *Nuclear Fusion* 56.1 (2015), p. 014001.

[146] Jianyuan Xiao and Hong Qin. "Explicit structure-preserving geometric particle-in-cell algorithm in curvilinear orthogonal coordinate systems and its applications to whole-device 6D kinetic simulations of tokamak physics". In: *Plasma Science and Technology* 23.5 (Apr. 2021), p. 055102. DOI: 10.1088/2058-6272/abf125. URL: https://dx.doi.org/10.1088/2058-6272/abf125.

[147] Yulei Wang, Feng Yuan, and Jian Liu. "A relativistic canonical symplectic particle-in-cell method for energetic plasma analysis". In: *Plasma Science and Technology* 22.6 (Mar. 2020), p. 065001. DOI: 10.1088/2058-6272/ab770e.

[148] F. E. Low. "A Lagrangian Formulation of the Boltzmann-Vlasov Equation for Plasmas". In: *Proceedings of the Royal Society of London. Series A, Mathematical and Physical Sciences* 248.1253 (1958), pp. 282–287. ISSN: 00804630.

[149] E.G. Evstatiev and B.A. Shadwick. "Variational formulation of particle algorithms for

kinetic plasma simulations". In: *Journal of Computational Physics* 245 (2013), pp. 376–398. ISSN: 0021-9991. DOI: https://doi.org/10.1016/j.jcp.2013.03.006.

[150] B. A. Shadwick, A. B. Stamm, and E. G. Evstatiev. "Variational formulation of macroparticle plasma simulation algorithms)". In: *Physics of Plasmas* 21.5 (May 2014), p. 055708. ISSN: 1070-664X. DOI: 10.1063/1.4874338.

[151] Alexander B. Stamm, Bradley A. Shadwick, and Evstati G. Evstatiev. "Variational Formulation of Macroparticle Models for Electromagnetic Plasma Simulations". In: *IEEE Transactions on Plasma Science* 42.6 (2014), pp. 1747–1758. DOI: 10.1109/TPS.2014.2320461.

[152] A. B. Stamm and B. A. Shadwick. "Variational formulation of E & M particle simulation algorithms in cylindrical geometry using an angular modal decomposition". In: *AIP Conference Proceedings* 1777.1 (Oct. 2016), p. 050004. ISSN: 0094-243X. DOI: 10.1063/1.4965627.

[153] Alexander B. Stamm and B. A. Shadwick. "Comparison of Conservation Behavior in Several Variationally Derived Implementations for Simulating Electromagnetic Plasmas". In: *2018 IEEE Advanced Accelerator Concepts Workshop (AAC)*. 2018, pp. 1–5. DOI: 10.1109/AAC.2018.8659406.

[154] M. Kraus et al. "GEMPIC: Geometric electromagnetic particle-in-cell methods". In: *Journal of Plasma Physics* 83 (4 2017). DOI: 10.1017/S002237781700040X.

[155] K. Kormann and E. Sonnendrücker. "Energy-conserving time propagation for a structure-preserving particle-in-cell Vlasov–Maxwell solver". In: *Journal of Computational Physics* 425 (15 2021), p. 109890. DOI: 10.1016/j.jcp.2020.109890.

[156] Martin Campos Pinto, Katharina Kormann, and Eric Sonnendrücker. "Variational Framework for Structure-Preserving Electromagnetic Particle-in-Cell Methods". In: *Journal of Scientific Computing* 91 (May 2022). DOI: 10.1007/s10915-022-01781-3.

[157] Martin Campos Pinto and Valentin Pagès. "A semi-implicit electromagnetic FEM-PIC scheme with exact energy and charge conservation". In: *Journal of Computational Physics* 453 (2022), p. 110912. DOI: 10.1016/j.jcp.2021.110912.

[158] Alexander S. Glasser and Hong Qin. "The geometric theory of charge conservation in particle-in-cell simulations". In: *Journal of Plasma Physics* 86.3 (May 2020). ISSN: 1469-7807. DOI: 10.1017/s0022377820000434.

[159] Kang Feng and Qin Mengzhao. *Symplectic geometric algorithms for Hamiltonian systems.* Springer, Jan. 2010. ISBN: 978-3-642-01776-6. DOI: 10.1007/978-3-642-01777-3.

[160] Benedict Leimkuhler and Sebastian Reich. *Simulating Hamiltonian Dynamics*. Cambridge Monographs on Applied and Computational Mathematics. Cambridge University Press,

2005. DOI: 10.1017/CBO9780511614118.

[161] Molei Tao. "Explicit symplectic approximation of nonseparable Hamiltonians: Algorithm and long time performance". In: *Phys. Rev. E* 94 (4 Oct. 2016), p. 043303. DOI: 10.1103/PhysRevE.94.043303.

[162] Anna Lassen and Jonas Conneryd. "Explicit Symplectic Integrators for Non-Separable Hamiltonians in Molecular Dynamics". Degree Project in Technology. KTH Royal Institute of Technology School of Engineering Sciences, 2019.

[163] Ruili Zhang et al. "Explicit symplectic algorithms based on generating functions for charged particle dynamics". In: *Phys. Rev. E* 94 (1 July 2016), p. 013205. DOI: 10.1103/PhysRevE.94.013205.

[164] Ruili Zhang et al. "Explicit symplectic algorithms based on generating functions for relativistic charged particle dynamics in time-dependent electromagnetic field". In: *Physics of Plasmas* 25.2 (Feb. 2018), p. 022117. ISSN: 1070-664X. DOI: 10.1063/1.5012767. URL: https://doi.org/10.1063/1.5012767.

[165] Randall J. LeVeque. *Finite Difference Methods for Ordinary and Partial Differential Equations*. Society for Industrial and Applied Mathematics, 2007. DOI: 10.1137/1.9780898717839.

[166] Allen Taflove and S. Hagness. *Computational Electrodynamics: The Finite-Difference Time-Domain Method, 3rd edition.* Vol. 2062. June 2005. ISBN: 978-1-58053-832-9. DOI: 10.1016/B978-012170960-0/50046-3.

[167] Andrew D. Greenwood et al. "On the elimination of numerical Cerenkov radiation in PIC simulations". In: *Journal of Computational Physics* 201.2 (2004), pp. 665–684. ISSN: 0021-9991. DOI: https://doi.org/10.1016/j.jcp.2004.06.021.

[168] BB Godfrey. "Time-biased field solver for electromagnetic PIC codes". In: *Proceedings of the Ninth Conference on Numerical Simulation of Plasmas*. 1980.

[169] A. Friedman et al. "Damped Time Advance Methods for Particles and EM Fields". In: *Proceedings of the US-Japan workshop on advances in simulation techniques applied to plasmas and fusion*. 1990.

[170] Peter W. Rambo et al. "Temporal and spatial filtering remedies for dispersion in electromagnetic particle codes". In: *Presented at the 13th Conference on the Numerical Simulation of Plasmas*. July 1989, pp. 17–20.

[171] J.S. Hesthaven. "High-order accurate methods in time-domain computational electromagnetics: A review". In: ed. by Peter W. Hawkes. Vol. 127. Advances in Imaging and Electron Physics. Elsevier, 2003, pp. 59–123. DOI: https://doi.org/10.1016/S1076-5670(03)

80097-6.

[172] A.C. Cangellaris and Diana Wright. "Analysis of the Numerical Error Caused by the Stair-Stepped Approximation of a Conducting Boundary in FDTD Simulations of Electromagnetic Phenomena". In: *Antennas and Propagation, IEEE Transactions on* 39 (Nov. 1991), pp. 1518–1525. DOI: 10.1109/8.97384.

[173] J.P. Verboncoeur. "Aliasing of electromagnetic fields in stair step boundaries". In: *Computer Physics Communications* 164.1 (2004). Proceedings of the 18th International Conferene on the Numerical Simulation of Plasmas, pp. 344–352. ISSN: 0010-4655. DOI: https://doi.org/10.1016/j.cpc.2004.06.046.

[174] C.J. Railton and J.B. Schneider. "An analytical and numerical analysis of several locally conformal FDTD schemes". In: *IEEE Transactions on Microwave Theory and Techniques* 47.1 (1999), pp. 56–66. DOI: 10.1109/22.740077.

[175] Chris J. Railton and Ian James Craddock. "Analysis of general 3-D PEC structures using improved CPFDTD algorithm". In: *Electronics Letters* 31 (1995), pp. 1753–1754.

[176] J. Anderson, M. Okoniewski, and S.S. Stuchly. "Practical 3-D contour/staircase treatment of metals in FDTD". in: *IEEE Microwave and Guided Wave Letters* 6.3 (1996), pp. 146–148. DOI: 10.1109/75.481095.

[177] S. Dey, R. Mittra, and S. Chebolu. "A technique for implementing the FDTD algorithm on a nonorthogonal grid". In: *Microwave and Optical Technology Letters* 14.4 (1997), pp. 213–215.

[178] S. Dey and R. Mittra. "A locally conformal finite-difference time-domain (FDTD) algorithm for modeling three-dimensional perfectly conducting objects". In: *IEEE Microwave and Guided Wave Letters* 7.9 (1997), pp. 273–275. DOI: 10.1109/75.622536.

[179] Collin S. Meierbachtol et al. "Conformal Electromagnetic Particle in Cell: A Review". In: *IEEE Transactions on Plasma Science* 43.11 (2015), pp. 3778–3793. DOI: 10.1109/TPS.2015.2487522.

[180] Björn Engquist, Jon Häggblad, and Olof Runborg. "On energy preserving consistent boundary conditions for the Yee scheme in 2D". in: *BIT Numerical Mathematics* 52 (2012), pp. 615–637.

[181] Yann-Meing Law, Alexandre Noll Marques, and Jean-Christophe Nave. "Treatment of complex interfaces for Maxwell's equations with continuous coefficients using the correction function method". In: *Journal of Scientific Computing* 82.56 (2020).

[182] Alexandre Noll Marques, Jean-Christophe Nave, and Rodolfo Ruben Rosales. "A Correction Function Method for Poisson problems with interface jump conditions". In: *Journal of*

Computational Physics 230.20 (2011), pp. 7567–7597. ISSN: 0021-9991. DOI: https://doi.org/10.1016/j.jcp.2011.06.014.

[183] Yann-Meing Law and Jean-Christophe Nave. "FDTD schemes for Maxwell's equations with embedded perfect electric conductors based on the correction function method". In: *Journal of Scientific Computing* 88 (July 2021). DOI: https://doi.org/10.1007/s10915-021-01591-z.

[184] Jonathan Whiteley. *Finite Element Methods*. 1st ed. Springer, 2017. ISBN: 978-3-319-49970-3. DOI: 10.1007/978-3-319-49971-0.

[185] Richard True. "The deformable relaxation mesh technique for solution of electron optics problems". In: *1975 International Electron Devices Meeting*. Vol. 21. Feb. 1975, pp. 257–260. DOI: 10.1109/IEDM.1975.188873.

[186] Richard True. "Gridded Pierce gun design and the PPM focussing of beams from gridded electron guns". In: *1982 International Electron Devices Meeting*. 1982, pp. 32–35. DOI: 10.1109/IEDM.1982.190204.

[187] Richard True. "A theory for coupling gridded gun design with PPM focussing". In: *IEEE Transactions on Electron Devices* 31.3 (1984), pp. 353–362. DOI: 10.1109/T-ED.1984.21527.

[188] Richard True. "Calculation and design of grids in Pierce guns". In: *International Technical Digest on Electron Devices Meeting*. 1989, pp. 215–218. DOI: 10.1109/IEDM.1989.74264.

[189] Richard True. "A general purpose relativistic beam dynamics code". In: *AIP Conference Proceedings*. Vol. 297. 1. Dec. 1993, pp. 493–499. DOI: 10.1063/1.45348.

[190] Richard True. "Chapter 14 - Electron Beam Formation, Focusing, and Collection in Microwave Tubes". In: *Handbook of Microwave Technology*. Ed. by T. Koryu Ishii. San Diego: Academic Press, 1995, pp. 497–567. ISBN: 978-0-12-374695-5. DOI: https://doi.org/10.1016/B978-012374695-5/50016-X.

[191] J. Petillo et al. "The MICHELLE three-dimensional electron gun and collector modeling tool: theory and design". In: *IEEE Transactions on Plasma Science* 30.3 (2002), pp. 1238–1264.

[192] John Petillo et al. "A Survey of Advanced Features of the MICHELLE Beam Optics Simulation Code". In: *2024 Joint International Vacuum Electronics Conference and International Vacuum Electron Sources Conference (IVEC + IVESC)*. 2024, pp. 1–2. DOI: 10.1109/IVECIVESC60838.2024.10694906.

[193] S.I Zaki, L.R.T Gardner, and T.J.M Boyd. "A finite element code for the simulation of one-dimensional vlasov plasmas. I. Theory". In: *Journal of Computational Physics* 79.1 (1988),

pp. 184–199. ISSN: 0021-9991. DOI: https://doi.org/10.1016/0021-9991(88)90010-1.

[194] S.I Zaki, T.J.M Boyd, and L.R.T Gardner. "A finite element code for the simulation of one-dimensional vlasov plasmas. II. Applications". In: *Journal of Computational Physics* 79.1 (1988), pp. 200–208. ISSN: 0021-9991. DOI: https://doi.org/10.1016/0021-9991(88)90011-3.

[195] A. Cangellaris, Chung-Chi Lin, and Kenneth Mei. "Point-matched time domain finite element methods for electromagnetic radiation and scattering". In: *IEEE Transactions on Antennas and Propagation* 35.10 (1987), pp. 1160–1173. DOI: 10.1109/TAP.1987.1143981.

[196] K. Mei Andreas Cangellaris. "The Method of Conforming Boundary Elements for Transient Electromagnetics". In: *Progress In Electromagnetics Research* 02 (1990), pp. 249–285. DOI: 10.2528/PIER89010700.

[197] D.R. Lynch and K.D. Paulsen. "Time-domain integration of the Maxwell equations on finite elements". In: *IEEE Transactions on Antennas and Propagation* 38.12 (1990), pp. 1933–1942. DOI: 10.1109/8.60982.

[198] Eric Sonnendrücker, John J. Ambrosiano, and Scott T. Brandon. "A finite element formulation of the Darwin PIC model for use on unstructured grids". In: *Journal of Computational Physics* 121.2 (1995), pp. 281–297. ISSN: 0021-9991. DOI: https://doi.org/10.1016/S0021-9991(95)90119-1.

[199] C.-D. Munz et al. "Divergence Correction Techniques for Maxwell Solvers Based on a Hyperbolic Model". In: *Journal of Computational Physics* 161.2 (2000), pp. 484–511. ISSN: 0021-9991. DOI: https://doi.org/10.1006/jcph.2000.6507.

[200] J.W. Eastwood et al. "Body-fitted electromagnetic PIC software for use on parallel computers". In: *Computer Physics Communications* 87.1 (1995). Particle Simulation Methods, pp. 155–178. ISSN: 0010-4655. DOI: https://doi.org/10.1016/0010-4655(94)00165-X.

[201] T.C. Warburton et al. "Galerkin and discontinuous Galerkin spectral/hp methods". In: *Computer Methods in Applied Mechanics and Engineering* 175.3 (1999), pp. 343–359. ISSN: 0045-7825. DOI: https://doi.org/10.1016/S0045-7825(98)00360-0.

[202] David A. Kopriva, Stephen L. Woodruff, and M. Y. Hussaini. "Discontinuous Spectral Element Approximation of Maxwell's Equations". In: *Discontinuous Galerkin Methods*. Ed. by Bernardo Cockburn, George E. Karniadakis, and Chi-Wang Shu. Berlin, Heidelberg: Springer Berlin Heidelberg, 2000, pp. 355–361.

[203] J.S Hesthaven and T Warburton. "Nodal High-Order Methods on Unstructured Grids: I. Time-Domain Solution of Maxwell's Equations". In: *Journal of Computational Physics*

181.1 (2002), pp. 186–221. ISSN: 0021-9991. DOI: https://doi.org/10.1006/jcph.2002.7118.

[204] G.B. Jacobs and J.S. Hesthaven. "High-order nodal discontinuous Galerkin particle-in-cell method on unstructured grids". In: *Journal of Computational Physics* 214.1 (2006), pp. 96–121. ISSN: 0021-9991. DOI: https://doi.org/10.1016/j.jcp.2005.09.008.

[205] Gustaaf B. Jacobs, Jan S. Hesthaven, and Giovanni Lapenta. "Simulations of the Weibel instability with a High-Order Discontinuous Galerkin Particle-In-Cell Solver". In: 2006.

[206] M. Movahhedi et al. "Alternating-Direction Implicit Formulation of the Finite-Element Time-Domain Method". In: *Microwave Theory and Techniques, IEEE Transactions on* 55 (July 2007), pp. 1322–1331. DOI: 10.1109/TMTT.2007.897777.

[207] Yingda Cheng et al. "Discontinuous Galerkin Methods for the Vlasov-Maxwell Equations". In: *SIAM Journal on Numerical Analysis* 52.2 (2014), pp. 1017–1049. ISSN: 00361429.

[208] Yingda Cheng, Andrew J. Christlieb, and Xinghui Zhong. "Energy-conserving discontinuous Galerkin methods for the Vlasov–Ampère system". In: *Journal of Computational Physics* 256 (2014), pp. 630–655. ISSN: 0021-9991. DOI: https://doi.org/10.1016/j.jcp.2013.09.013.

[209] Yingda Cheng, Andrew J. Christlieb, and Xinghui Zhong. "Energy-conserving discontinuous Galerkin methods for the Vlasov–Maxwell system". In: *Journal of Computational Physics* 279 (Dec. 2014), pp. 145–173. DOI: 10.1016/j.jcp.2014.08.041.

[210] Martin Campos Pinto, Katharina Kormann, and Eric Sonnendrücker. "Variational Framework for Structure-Preserving Electromagnetic Particle-in-Cell Methods". In: *Journal of Scientific Computing* 91 (May 2022). DOI: 10.1007/s10915-022-01781-3.

[211] Omkar H. Ramachandran et al. "A Necessarily Incomplete Review of Electromagnetic Finite Element Particle-in-Cell Methods". In: *IEEE Transactions on Plasma Science* (2023), pp. 1–11. DOI: 10.1109/TPS.2023.3257165.

[212] Scott O'Connor et al. "A Set of Benchmark Tests for Validation of 3-D Particle in Cell Methods". In: *IEEE Transactions on Plasma Science* 49 (2021), pp. 1724–1731.

[213] Zane D. Crawford et al. "Rubrics for Charge Conserving Current Mapping in Finite Element Electromagnetic Particle in Cell Methods". In: *IEEE Transactions on Plasma Science* 49 (2021), pp. 3719–3732.

[214] F. Zheng, Z. Chen, and J. Zhang. "A finite-difference time-domain method without the Courant stability conditions". In: *IEEE Microwave and Guided Wave Letters* 9.11 (1999), pp. 441–443. DOI: 10.1109/75.808026.

[215] D. W. Peaceman and H. H. Rachford Jr. “The Numerical Solution of Parabolic and Elliptic Differential Equations”. In: *Journal of the Society for Industrial and Applied Mathematics* 3.1 (1955), pp. 28–41. DOI: 10.1137/0103003.

[216] Jim Douglas and Henry H Rachford. “On the numerical solution of heat conduction problems in two and three space variables”. In: *Transactions of the American mathematical Society* 82.2 (1956), pp. 421–439.

[217] Jim Douglas. “Alternating direction methods for three space variables”. In: *Numerische Mathematik* 4 (1962), pp. 41–63.

[218] Carl Pearcy. “On convergence of alternating direction procedures”. In: *Numeŕische Mathématik* 4.1 (1962), pp. 172–176.

[219] Jim Douglas Jr and Carl M Pearcy. “On convergence of alternating direction procedures in the presence of singular operators”. In: *Numeŕische Mathématik* 5.1 (1963), pp. 175–184.

[220] Jim Douglas and James E Gunn. “A general formulation of alternating direction methods: Part I. Parabolic and hyperbolic problems”. In: *Numérische mathématik* 6 (1964), pp. 428–453.

[221] F. Zhen, Z. Chen, and J. Zhang. “Toward the development of a three-dimensional unconditionally stable finite-difference time-domain method”. In: *IEEE Transactions on Microwave Theory and Techniques* 48.9 (2000), pp. 1550–1558. DOI: 10.1109/22.869007.

[222] Jongwoo Lee and Bengt Fornberg. “A split step approach for the 3-D Maxwell’s equations”. In: *Journal of Computational and Applied Mathematics* 158.2 (2003), pp. 485–505. ISSN: 0377-0427. DOI: https://doi.org/10.1016/S0377-0427(03)00484-9.

[223] Jongwoo Lee and Bengt Fornberg. “Some unconditionally stable time stepping methods for the 3D Maxwell’s equations”. In: *Journal of Computational and Applied Mathematics* 166.2 (2004), pp. 497–523. ISSN: 0377-0427. DOI: https://doi.org/10.1016/j.cam.2003.09.001.

[224] Q. Meng-Zhao and Z. Wen-Jie. “Construction of higher order symplectic schemes by composition”. In: *Computing* 47 (3 Sept. 1992), pp. 299–361.

[225] Lewis F. Richardson and J. Arthur Gaunt. “The Deferred Approach to the Limit. Part I. Single Lattice. Part II. Interpenetrating Lattices”. In: *Philosophical Transactions of the Royal Society of London. Series A, Containing Papers of a Mathematical or Physical Character* 226 (1927), pp. 299–361. ISSN: 02643952.

[226] Victor Pereyra. “Accelerating the Convergence of Discretization Algorithms”. In: *SIAM Journal on Numerical Analysis* 4.4 (1967), pp. 508–533. ISSN: 00361429.

[227] Raymond C. Rumpf. “Simple Implementation of Arbitrarily Shaped Total-Field/Scattered-Field Regions in Finite-Difference Frequency-Domain”. In: *Progress in Electromagnetics Research B* 36 (2012), pp. 221–248.

[228] Raymond Rumpf. *Electromagnetic and Photonic Simulation for the Beginner: Finite-Difference Frequency-Domain in MATLAB*. Artech, Jan. 2022. ISBN: 9781630819262.

[229] Erich H. Rothe. “Zweidimensionale parabolische Randwertaufgaben als Grenzfall eindimensionaler Randwertaufgaben”. In: *Mathematische Annalen* 102 (1930), pp. 650–670.

[230] E.N. Sarmin and L.A. Chudov. “On the stability of the numerical integration of systems of ordinary differential equations arising in the use of the straight line method”. In: *USSR Computational Mathematics and Mathematical Physics* 3.6 (1963), pp. 1537–1543. ISSN: 0041-5553. DOI: https://doi.org/10.1016/0041-5553(63)90256-8.

[231] H. Cho. “Method of Lines Transpose: High-Order Schemes for Parabolic Problems”. PhD thesis. Michigan State University, 2016.

[232] David J. Eyre. “An Unconditionally Stable One-Step Scheme for Gradient Systems”. In: *IEEE Transactions on Image Processing* (1997).

[233] Fei Liu and Jie Shen. “Stabilized semi-implicit spectral deferred correction methods for Allen–Cahn and Cahn–Hilliard equations”. In: *Mathematical Methods in the Applied Sciences* 38 (June 2013). DOI: 10.1002/mma.2869.

[234] Andrew Christlieb et al. “High accuracy solutions to energy gradient flows from material science models”. In: *Journal of Computational Physics* 257 (2014), pp. 193–215. ISSN: 0021-9991. DOI: https://doi.org/10.1016/j.jcp.2013.09.049.

[235] J. Jones. “Development of a Fast and Accurate Time Stepping Scheme for the Functionalized Cahn Hilliard Equation and Application to a Graphics Processing Unit”. PhD thesis. Michigan State University, 2013.

[236] S.M. Cox and P.C. Matthews. “Exponential Time Differencing for Stiff Systems”. In: *Journal of Computational Physics* 176.2 (2002), pp. 430–455. ISSN: 0021-9991. DOI: https://doi.org/10.1006/jcph.2002.6995.

[237] Si Yuan. “ODE-Oriented Semi-Analytical Methods”. In: *Computational Mechanics in Structural Engineering*. Ed. by Franklin Y. Cheng and Yuanxian Gu. Oxford: Elsevier Science Ltd, 1999, pp. 375–388. ISBN: 978-0-08-043008-9. DOI: https://doi.org/10.1016/B978-008043008-9/50067-3.

[238] S. Yuan. “A New Semidiscrete Method: The Finite Element Method of Lines”. In: *Proceedings of 1st National Conference on Analytical and Numerical Combined Methods*. Hunan, China, 1990, pp. 132–136.

[239] Jozef Kačur. "Application of Rothe's method to nonlinear evolution equations". In: *Matematický časopis* 25.1 (1975), pp. 63–81.

[240] Jozef Kačur. "Application of Rothe's Method to Nonlinear Parabolic Boundary Value Problems". In: *Nonlinear Evolution Equations and Potential Theory*. Ed. by Josef Král. Boston, MA: Springer US, 1975, pp. 89–93. ISBN: 978-1-4613-4425-4. DOI: 10.1007/978-1-4613-4425-4_6.

[241] Jozef Kačur. "Method of Rothe and nonlinear parabolic boundary value problems of arbitrary order". eng. In: *Czechoslovak Mathematical Journal* 28.4 (1978), pp. 507–524.

[242] Erich Martensen. "The convergence of the horizontal line method for Maxwell's equations". In: *Mathematical Methods in the Applied Sciences* 1.1 (1979), pp. 101–113. DOI: https://doi.org/10.1002/mma.1670010109.

[243] Erich Martensen. "The Rothe method for the wave equation in several space dimensions". In: *Proceedings of the Royal Society of Edinburgh Section A: Mathematics* 84.1-2 (1979), pp. 1–18. DOI: 10.1017/S0308210500016929.

[244] Marensen E. "The Rothe Method for Nonlinear Hyperbolic Problems". In: *Equadiff 6*. Ed. by Jaromír Vosmanský and Miloš Zlámal. Berlin, Heidelberg: Springer Berlin Heidelberg, 1986, pp. 387–392. ISBN: 978-3-540-39807-3.

[245] J. Kačur. "Method of Rothe in Evolution Equations". In: *Equadiff 6*. Ed. by Jaromír Vosmanský and Miloš Zlámal. Berlin, Heidelberg: Springer Berlin Heidelberg, 1986, pp. 23–34. ISBN: 978-3-540-39807-3.

[246] Oscar P. Bruno and Mark Lyon. "High-order unconditionally stable FC-AD solvers for general smooth domains I. Basic elements". In: *Journal of Computational Physics* 229.6 (2010), pp. 2009–2033. ISSN: 0021-9991. DOI: https://doi.org/10.1016/j.jcp.2009.11.020.

[247] Mark Lyon and Oscar P. Bruno. "High-order unconditionally stable FC-AD solvers for general smooth domains II. Elliptic, parabolic and hyperbolic PDEs; theoretical considerations". In: *Journal of Computational Physics* 229.9 (2010), pp. 3358–3381. ISSN: 0021-9991. DOI: https://doi.org/10.1016/j.jcp.2010.01.006.

[248] John P Boyd. "A comparison of numerical algorithms for Fourier extension of the first, second, and third kinds". In: *Journal of Computational Physics* 178.1 (2002), pp. 118–160.

[249] Oscar P Bruno, Youngae Han, and Matthew M Pohlman. "Accurate, high-order representation of complex three-dimensional surfaces via Fourier continuation analysis". In: *Journal of Computational Physics* 227.2 (2007), pp. 1094–1125.

[250] Oscar P. Bruno and Andrés Prieto. "Spatially Dispersionless, Unconditionally Stable FC–AD

Solvers for Variable-Coefficient PDEs". In: *Journal of Scientific Computing* 58 (2014), pp. 331–366. DOI: https://doi.org/10.1007/s10915-013-9734-8.

[251] Nathan Albin and Oscar P. Bruno. "A spectral FC solver for the compressible Navier–Stokes equations in general domains I: Explicit time-stepping". In: *Journal of Computational Physics* 230.16 (2011), pp. 6248–6270. ISSN: 0021-9991. DOI: https://doi.org/10.1016/j.jcp.2011.04.023.

[252] Thomas G. Anderson, Oscar P. Bruno, and Mark Lyon. "High-order, Dispersionless "Fast-Hybrid" Wave Equation Solver. Part I: O(1) Sampling Cost via Incident-Field Windowing and Recentering". In: *SIAM Journal on Scientific Computing* 42.2 (2020), A1348–A1379. DOI: 10.1137/19M1251953.

[253] Akash Anand and Prakash Singh Nainwal. *A modified FC-Gram approximation algorithm with provable error bounds*. Sept. 2024. DOI: 10.48550/arXiv.2409.00722.

[254] Alex Barnett, Leslie Greengard, and Thomas Hagstrom. "High-order discretization of a stable time-domain integral equation for 3D acoustic scattering". In: *Journal of Computational Physics* 402 (2020), p. 109047.

[255] Shravan K Veerapaneni et al. "A boundary integral method for simulating the dynamics of inextensible vesicles suspended in a viscous fluid in 2D". in: *Journal of Computational Physics* 228 (7 2009), pp. 2334–2353.

[256] Shang-Huan Chiu, M. N. J. Moore, and Bryan Quaife. "Viscous transport in eroding porous media". In: *Journal of Fluid Mechanics* 893 (2020), A3. DOI: 10.1017/jfm.2020.228.

[257] Ludvig af Klinteberg, Travis Askham, and Mary Catherine Kropinski. "A fast integral equation method for the two-dimensional Navier-Stokes equations". In: *Journal of Computational Physics* 409 (2020), p. 109353. ISSN: 0021-9991. DOI: https://doi.org/10.1016/j.jcp.2020.109353. URL: https://www.sciencedirect.com/science/article/pii/S0021999120301273.

[258] Mary Catherine A. Kropinski and Bryan D. Quaife. "Fast integral equation methods for Rothe's method applied to the isotropic heat equation". In: *Computers and Mathematics with Applications* 61 (9 2011), pp. 2436–2446.

[259] Matthew Causley, Hana Cho, and Andrew Christlieb. "Method of Lines Transpose: Energy Gradient Flows Using Direct Operator Inversion for Phase-Field Models". In: *SIAM Journal on Scientific Computing* 39.5 (2017), B968–B992.

[260] Felipe Vico et al. "The decoupled potential integral equation for time-harmonic electromagnetic scattering". In: *Communications on Pure and Applied Mathematics* 69 (4 2016), pp. 771–812.

[261] Leslie Greengard and Vladimir Rokhlin. "A fast algorithm for particle simulations". In: *Journal of Computational Physics* 73 (1987), pp. 325–348.

[262] Leslie F. Greengard and Jingfang Huang. "A New Version of the Fast Multipole Method for Screened Coulomb Interactions in Three Dimensions". In: *Journal of Computational Physics* 180.2 (2002), pp. 642–658. ISSN: 0021-9991. DOI: https://doi.org/10.1006/jcph.2002.7110.

[263] Mary Catherine A. Kropinski and Bryan D. Quaife. "Fast integral equation methods for the modified Helmholtz equation". In: *Journal of Computational Physics* 230.2 (2011), pp. 425–434. ISSN: 0021-9991. DOI: https://doi.org/10.1016/j.jcp.2010.09.030.

[264] Matthew F. Causley et al. "Method of Lines Transpose: High Order L-Stable O(N) Schemes for Parabolic Equations Using Successive Convolution". In: *SIAM Journal on Numerical Analysis* 54.3 (2016), pp. 1635–1652. DOI: 10.1137/15M1035094.

[265] Matthew F. Causley et al. "Method of lines transpose: An implicit solution to the wave equation". In: *Mathematics of Computation* 83 (2014), pp. 2763–2786.

[266] Matthew F. Causley et al. *Method of Lines Transpose: A Fast Implicit Wave Propagator*. 2013.

[267] Matthew F. Causley and Andrew J. Christlieb. "Higher Order A-Stable Schemes for the Wave Equation Using a Successive Convolution Approach". In: *SIAM Journal on Numerical Analysis* 52.1 (2014), pp. 220–235. DOI: 10.1137/130932685.

[268] Matthew F. Causley, Andrew J. Christlieb, and Eric M. Wolf. "Method of Lines Transpose: An Efficient Unconditionally Stable Solver for Wave Propagation". In: *Journal of Scientific Computing* 70 (2017), pp. 896–921.

[269] Andrew Christlieb et al. "Parallel Algorithms for Successive Convolution". In: *Journal of Scientific Computing* 86 (Jan. 2021). DOI: 10.1007/s10915-020-01359-x.

[270] Eric M. Wolf et al. "A particle-in-cell method for the simulation of plasmas based on an unconditionally stable field solver". In: *Journal of Computational Physics* 326 (2016), pp. 342–372. ISSN: 0021-9991. DOI: https://doi.org/10.1016/j.jcp.2016.08.006.

[271] E. Wolf. "A Particle-In-Cell Method for the Simulation of Plasmas Based on an Unconditionally Stable Wave Equation Solver". PhD thesis. Michigan State University, 2015.

[272] A.J. Christlieb, R. Krasny, and J.P. Verboncoeur. "A treecode algorithm for simulating electron dynamics in a Penning–Malmberg trap". In: *Computer Physics Communications* 164.1 (2004). Proceedings of the 18th International Conferene on the Numerical Simulation of Plasmas, pp. 306–310. ISSN: 0010-4655. DOI: https://doi.org/10.1016/j.cpc.2004.06.076.

[273] Andrew J. Christlieb, Robert Krasny, and John P. Verboncoeur. "Efficient Particle Simulation of a Virtual Cathode Using a Grid-Free Treecode Poisson Solver". In: *IEEE Transactions on Plasma Science* 32 (2 2004), pp. 384–389.

[274] Gerald B. Folland. *Introduction to Partial Differential Equations: Second edition*. Princeton University Press, 1995. ISBN: 978-0691213033.

[275] Dean Duffy. *Green's Functions with Applications*. 2nd ed. CRC Press, 2015. ISBN: 1482251027.

[276] M. Thavappiragasam, A. Viswanathan, and A. Christlieb. "MOLT based fast high-order three dimensional A-stable scheme for wave propagation". In: *Journal of Coupled Systems and Multiscale Dynamics* 5.2 (2017), pp. 151–163.

[277] Martin Campos Pinto et al. "Charge-conserving FEM–PIC schemes on general grids". In: *Comptes Rendus Mécanique* 342.10 (2014). Theoretical and numerical approaches for Vlasov-maxwell equations, pp. 570–582. ISSN: 1631-0721. DOI: https://doi.org/10.1016/j.crme.2014.06.011.

[278] J.E. Allen. "The plasma–sheath boundary: its history and Langmuir's definition of the sheath edge". In: *Plasma Sources Science and Technology* 18.1 (Nov. 2008), p. 014004. DOI: 10.1088/0963-0252/18/1/014004.

[279] Umran S. Inan and Robert A. Marshall. *Numerical Electromagnetics: The FDTD Method*. Cambridge University Press, 2011.

[280] E.S. Weibel. "Spontaneously Growing Transverse Waves in a Plasma Due to an Anisotropic Velocity Distribution". In: *Physical Review Letters* 2 (3 1959), pp. 83–84.

[281] Artem Bohdan et al. "Magnetic Field Amplification by the Weibel Instability at Planetary and Astrophysical Shocks with High Mach Number". In: *Phys. Rev. Lett.* 126 (9 Mar. 2021), p. 095101. DOI: 10.1103/PhysRevLett.126.095101.

[282] S. Atzeni et al. "Fluid and kinetic simulation of inertial confinement fusion plasmas". In: *Computer Physics Communications* 169.1 (2005), pp. 153–159. DOI: 10.1016/j.cpc.2005.03.036.

[283] R.A. Fonseca et al. "Three-dimensional Weibel instability in astrophysical scenarios". In: *Physics of Plasmas* 10.5 (2003), pp. 1979–1984.

[284] Roswell Lee and Martin Lampe. "Electromagnetic Instabilities, Filamentation, and Focusing of Relativistic Electron Beams". In: *Physical Review Letters* 31.3 (1973). DOI: 10.1103/PhysRevLett.31.1390.

[285] Peter H. Yoon and Ronald C. Davidson. "Exact analytical model of the classical Weibel

instability in a relativistic anisotropic plasma". In: *Physical Review A* 35.6 (1987), p. 2718.

[286] Carlo Benedetti et al. "*ALaDyn*: A High-Accuracy PIC Code for the Maxwell–Vlasov Equations". In: *IEEE Transactions on Plasma Science* 36.4 (2008), pp. 1790–1798. DOI: 10.1109/TPS.2008.927143.

[287] Mohamad Shalaby et al. "SHARP: A Spatially Higher-order, Relativistic Particle-in-cell Code". In: *The Astrophysical Journal* 841.1 (May 2017), p. 52. DOI: 10.3847/1538-4357/aa6d13.

[288] A. Davidson et al. "Implementation of a hybrid particle code with a PIC description in r–z and a gridless description in ϕ into OSIRIS". in: *Journal of Computational Physics* 281 (2015), pp. 1063–1077. ISSN: 0021-9991. DOI: https://doi.org/10.1016/j.jcp.2014.10.064.

[289] Alireza Sadeghirad. "B-spline convected particle domain interpolation method". In: *Engineering Analysis with Boundary Elements* 160 (2024), pp. 106–133. ISSN: 0955-7997. DOI: https://doi.org/10.1016/j.enganabound.2023.12.028.

[290] Qin Meng-zhao and Zhang Mei-qing. "Symplectic Runge-Kutta Algorithms for Hamiltonian Systems". In: *Journal of Computational Mathematics* 10 (1992), pp. 205–215. ISSN: 02549409, 19917139.

[291] Charles K Birdsall and A Bruce Langdon. "Particle simulation techniques". In: *Computer Applications in Plasma Science and Engineering*. Springer, 1991, pp. 7–41.

[292] Chengkun Huang et al. "QUICKPIC: A highly efficient particle-in-cell code for modeling wakefield acceleration in plasmas". In: *Journal of Computational Physics* 217.2 (2006), pp. 658–679.

[293] Estelle Cormier-Michel et al. "Unphysical kinetic effects in particle-in-cell modeling of laser wakefield accelerators". In: *Physical Review E—Statistical, Nonlinear, and Soft Matter Physics* 78.1 (2008), p. 016404.

[294] R Lehe et al. "Laser-plasma lens for laser-wakefield accelerators". In: *Physical Review Special Topics-Accelerators and Beams* 17.12 (2014), p. 121301.

[295] Andrew Christlieb, Sining Gong, and Hyoseon Yang. *Boundary corrections for kernel approximation to differential operators*. 2024.

[296] Mathialakan Thavappiragasam. "A-Stable Implicit Rapid Scheme and Software Solution for Electromagnetic Wave Propagation". PhD thesis. Michigan State University, 2019.

[297] Kôsaku Yosida. *Functional Analysis*. Heidelberg: Springer Berlin, 1995. ISBN: 978-3-642-61859-8.

[298] Vidar Thomée. "High Order Local Approximations to Derivatives in the Finite Element Method". In: *Mathematics of Computation* 31.139 (1977), pp. 652–660. ISSN: 00255718, 10886842.

[299] J. H. Bramble and A. H. Schatz. "Higher Order Local Accuracy by Averaging in the Finite Element Method". In: *Mathematics of Computation* 31.137 (1977), pp. 94–111. ISSN: 00255718, 10886842.

[300] James King et al. "Smoothness-Increasing Accuracy-Conserving (SIAC) Filtering for Discontinuous Galerkin Solutions: Improved Errors Versus Higher-Order Accuracy". In: *Journal of Scientific Computing* 53.1 (Oct. 2012), pp. 129–149. DOI: 10.1007/s10915-012-9593-8.

[301] Mark Ainsworth and Charles Parker. "Two and three dimensional H2-conforming finite element approximations without C1-elements". In: *Computer Methods in Applied Mechanics and Engineering* 431 (2024), p. 117267. ISSN: 0045-7825. DOI: https://doi.org/10.1016/j.cma.2024.117267.

[302] Cèdric Villani. "On a New Class of Weak Solutions to the Spatially Homogeneous Boltzmann and Landau Equations". In: *Archive for Rational Mechanics and Analysis* 143 (1998), pp. 273–307. DOI: https://doi.org/10.1007/s002050050106.

[303] José A. Carrillo et al. "A particle method for the homogeneous Landau equation". In: *Journal of Computational Physics: X* 7 (2020), p. 100066. ISSN: 2590-0552. DOI: https://doi.org/10.1016/j.jcpx.2020.100066.

[304] Rafael Bailo, José A. Carrillo, and Jingwei Hu. "The collisional particle-in-cell method for the Vlasov–Maxwell–Landau equations". In: *Journal of Plasma Physics* 90.4 (2024), p. 905900415. DOI: 10.1017/S0022377824001077.

[305] M. Lemou. "Linearized quantum and relativistic Fokker-Planck-Landau equations". In: *Mathematical Methods in the Applied Sciences* 23.12 (Aug. 2000), pp. 1093–1119. DOI: 10.1002/1099-1476(200008)23:12<1093::AID-MMA153>3.0.CO;2-8.

[306] Robert M. Strain and Maja Tasković. "Entropy dissipation estimates for the relativistic Landau equation, and applications". In: *Journal of Functional Analysis* 277.4 (Aug. 2019), pp. 1139–1201. DOI: 10.1016/j.jfa.2019.04.007. eprint: 1806.08720 (math).

[307] Zhimeng Ouyang, Lei Wu, and Qinghua Xiao. *Hilbert Expansion for Coulomb Collisional Kinetic Models*. 2023. arXiv: 2207.00126 [math.AP]. URL: https://arxiv.org/abs/2207.00126.

[308] L. Pareschi, G. Russo, and G. Toscani. "Fast Spectral Methods for the Fokker–Planck–Landau Collision Operator". In: *Journal of Computational Physics* 165.1 (2000), pp. 216–236. ISSN: 0021-9991. DOI: https://doi.org/10.1006/jcph.2000.6612.

[309] Francis Filbet and Lorenzo Pareschi. "A Numerical Method for the Accurate Solution of the Fokker–Planck–Landau Equation in the Nonhomogeneous Case". In: *Journal of Computational Physics* 179.1 (2002), pp. 1–26. ISSN: 0021-9991. DOI: https://doi.org/10.1006/jcph.2002.7010.

[310] Chenglong Zhang. "On Study of Deterministic Conservative Solvers for The Nonlinear Boltzmann and Landau Transport Equations". PhD thesis. "University of Texas at Austin", 2014.

[311] Chenglong Zhang and Irene M. Gamba. "A conservative scheme for Vlasov Poisson Landau modeling collisional plasmas". In: *Journal of Computational Physics* 340 (2017), pp. 470–497. ISSN: 0021-9991. DOI: https://doi.org/10.1016/j.jcp.2017.03.046.

[312] Allen Taflove and Morris E. Brodwin. "Numerical Solution of Steady-State Electromagnetic Scattering Problems Using the Time-dependent Maxwell's Equations". In: *IEEE Transactions on Microwave Theory and Techniques* MTT-23 (8 1975), pp. 623–630.

[313] Hong Qin et al. "Why is Boris algorithm so good?" In: *Physics of Plasmas* 20 (Aug. 2013). DOI: 10.1063/1.4818428.

[314] Carl de Boor. *A Practical Guide to Splines*. New York, NY: Springer, 1978. ISBN: 978-0-387-95366-3.

[315] George Green. *An Essay on the Application of Mathematical Analysis to the Theories of Electricity and Magnetism*. Nottingham: Printed for the author by T. Wheelhouse, 1828.

APPENDIX A

NONDIMENSIONALIZATION OF EQUATIONS

We nondimensionalize four sets of equations. The second may be found in Chapter 1 of [34], the last two may be found in the appendix of [2] as well as [34], and the first is no less in debt to Bill Sand's patient instruction in nondimensionalization.[1]

The setup for the non-dimensionalization used in all the following sections considers the following substitutions:

$$\begin{cases} \mathbf{x} \to L\tilde{\mathbf{x}}, \quad t \to T\tilde{t}, \\ \mathbf{v} \to V\tilde{\mathbf{v}} \equiv \dfrac{L}{T}\tilde{\mathbf{v}}, \quad \mathbf{P} \to P\tilde{\mathbf{P}} \equiv \dfrac{ML}{T}\tilde{\mathbf{P}}, \\ \phi \to \phi_0\tilde{\phi}, \quad \mathbf{A} \to A_0\tilde{\mathbf{A}}, \\ n \to \bar{n}\tilde{n}, \quad q_i \to Q\tilde{q}_i, \quad m_i \to M\tilde{m}_i, \\ \rho \to Q\bar{n}\tilde{\rho}, \quad \mathbf{J} \to Q\bar{n}V\tilde{\mathbf{J}} \equiv \dfrac{Q\bar{n}L}{T}\tilde{\mathbf{J}}, \\ \mathbf{E} \to E_0\tilde{\mathbf{E}}, \quad \mathbf{B} \to B_0\tilde{\mathbf{B}}. \end{cases}$$

Here, we use $\bar{n}$ to denote a reference number density $[\mathrm{m}^{-3}]$, Q is the scale for charge in [C], and we also introduce M, which represents the scale for mass [kg]. The values for Q and M are set according to the electrons, so that $Q = |q_e|$ and $M = m_e$. For reasons that will become clear in Section A.2, we choose the scales for the potentials ϕ_0 and A_0 to be

$$\phi_0 = \frac{L^2 M}{T^2 Q}, \quad A_0 = \frac{LM}{TQ}.$$

A natural choice of the scales for L and T are the Debye length and angular plasma period, which are defined, respectively, by

$$L = \lambda_D = \sqrt{\frac{\epsilon_0 k_B \bar{T}}{\bar{n} q_e^2}} \quad [\mathrm{m}], \quad T = \omega_{pe}^{-1} = \sqrt{\frac{m_e \epsilon_0}{\bar{n} q_e^2}} \quad [\mathrm{s/rad}],$$

where k_B is the Boltzmann constant, m_e is the electron mass, q_e is the electron charge, and $\bar{T}$ is an average macroscopic temperature for the plasma. We choose to select these scales for all test

[1] And honesty compels me to admit probably copied from a whiteboard tutorial by him.

problems considered in section 2.4.2 with the exception of the beam problems, in which the length scale L corresponds to the longest side of the simulation domain and T is the crossing time for a particle that is injected into the domain. In most cases, the user will need to provide a macroscopic temperature $\bar{T}$ [K] in addition to the reference number density $\bar{n}$ to compute λ_D and ω_{pe}^{-1}. Note that the plasma period can be obtained from the angular plasma period T after multiplying the latter by 2π.

A.1 Maxwell's Equations

We have Maxwell's equations:

$$\nabla \cdot \mathbf{E} = \frac{\rho}{\epsilon_0}, \tag{A.1a}$$

$$\nabla \cdot \mathbf{B} = 0, \tag{A.1b}$$

$$\nabla \times \mathbf{E} = -\frac{\partial \mathbf{B}}{\partial t}, \tag{A.1c}$$

$$\nabla \times \mathbf{B} = \mu_0 \mathbf{J} + \frac{1}{c^2}\frac{\partial \mathbf{E}}{\partial t}. \tag{A.1d}$$

Where $\mathbf{E}$ is the electric field, $\mathbf{B}$ is the magnetic field, $\mathbf{J}$ is the current density, ρ is the charge density, ϵ_0 and μ_0 are the vacuum permittivity and vacuum permeability, respectively.

We have the position vector $\mathbf{x}$, the velocity vector $\mathbf{v}$, time t, number density n, and charge q.

Now we get

$$\frac{E_0}{L}\tilde{\nabla} \cdot \tilde{\mathbf{E}} = \frac{Q\bar{n}}{\epsilon_0}\tilde{\rho}, \tag{A.2a}$$

$$\frac{B_0}{L}\tilde{\nabla} \cdot \tilde{\mathbf{B}} = 0, \tag{A.2b}$$

$$\frac{E_0}{L}\tilde{\nabla} \times \tilde{\mathbf{E}} = -\frac{B_0}{T}\frac{\partial \tilde{\mathbf{B}}}{\partial \tilde{t}}, \tag{A.2c}$$

$$\frac{B_0}{L}\tilde{\nabla} \times \tilde{\mathbf{B}} = \mu_0 Q\bar{n}\frac{L}{T}\tilde{\mathbf{J}} + \frac{1}{c^2}\frac{E_0}{T}\frac{\partial \tilde{\mathbf{E}}}{\partial \tilde{t}}. \tag{A.2d}$$

We set

$$E_0 = \frac{MV}{QT} = \frac{ML}{QT^2}, \quad B_0 = \frac{M}{QT}$$

which yields

$$\tilde{\nabla} \cdot \tilde{\mathbf{E}} = \frac{LQ\bar{n}}{E_0 \epsilon_0} \tilde{\rho}, \tag{A.3a}$$

$$\tilde{\nabla} \cdot \tilde{\mathbf{B}} = 0, \tag{A.3b}$$

$$\tilde{\nabla} \times \tilde{\mathbf{E}} = -\frac{L}{T}\frac{B_0}{E_0}\frac{\partial \tilde{\mathbf{B}}}{\partial \tilde{t}} = -\frac{L}{T}\frac{\frac{M}{QT}}{\frac{MV}{QT}}\frac{\partial \tilde{\mathbf{B}}}{\partial \tilde{t}} = -\frac{L}{T}\frac{1}{V}\frac{\partial \tilde{\mathbf{B}}}{\partial \tilde{t}} = -\frac{\partial \tilde{\mathbf{B}}}{\partial \tilde{t}}, \tag{A.3c}$$

$$\tilde{\nabla} \times \tilde{\mathbf{B}} = \mu_0 Q\bar{n}\frac{L^2}{T}\frac{1}{B_0}\tilde{\mathbf{J}} + \frac{1}{c^2}\frac{E_0}{B_0}\frac{L}{T}\frac{\partial \tilde{\mathbf{E}}}{\partial \tilde{t}}. \tag{A.3d}$$

For Gauss's Law:

$$\frac{LQ\bar{n}}{E_0\epsilon_0} = \frac{LQ\bar{n}}{\frac{MV}{QT}\epsilon_0} = \frac{LQ^2T\bar{n}}{MV\epsilon_0} = \frac{Q^2T^2\bar{n}}{M\epsilon_0}.$$

Call this $\sigma_1^{-1} := \frac{Q^2T^2\bar{n}}{M\epsilon_0}$. For Faraday's Law (A.1c):

$$\frac{L}{T}\frac{B_0}{E_0} = \frac{L}{T}\frac{\frac{M}{QT}}{\frac{MV}{QT}} = \frac{L}{T}\frac{1}{V} = 1$$

For Ampere's Law, the first term (A.1d):

$$\frac{\mu_0 Q\bar{n}L^2}{T}\frac{1}{B_0} = \frac{\mu_0 Q\bar{n}L^2}{T}\frac{1}{\frac{M}{QT}} = \frac{\mu_0 Q\bar{n}L^2}{T}\frac{QT}{M} = \frac{\mu_0 Q^2L^2\bar{n}}{M}$$

Call this $\sigma_2 := \frac{\mu_0 Q^2L^2\bar{n}}{M}$. For the second term:

$$\frac{1}{c^2}\frac{E_0}{B_0}\frac{L}{T} = \frac{1}{c^2}\frac{\frac{MV}{QT}}{\frac{M}{QT}}\frac{L}{T} = \frac{1}{c^2}\frac{VL}{T} = \frac{V^2}{c^2}.$$

Call this $\kappa := \frac{c}{V}$.

Thus we have

$$\tilde{\nabla} \cdot \tilde{\mathbf{E}} = \frac{\tilde{\rho}}{\sigma_1}, \tag{A.4a}$$

$$\tilde{\nabla} \cdot \tilde{\mathbf{B}} = 0, \tag{A.4b}$$

$$\tilde{\nabla} \times \tilde{\mathbf{E}} = -\frac{\partial \tilde{\mathbf{B}}}{\partial \tilde{t}}, \tag{A.4c}$$

$$\tilde{\nabla} \times \tilde{\mathbf{B}} = \sigma_2\tilde{\mathbf{J}} + \frac{1}{\kappa^2}\frac{\partial \tilde{\mathbf{E}}}{\partial \tilde{t}}. \tag{A.4d}$$

We can now drop the tildes for simplicity. This completes the nondimensionalization.

A.2 Equations of Motion in E-B form

We have the Newton-Lorenz equations

$$\frac{d\mathbf{x}_i}{dt} = \mathbf{v}_i, \tag{A.5}$$

$$\frac{d\mathbf{v}_i}{dt} = \frac{q_i}{m_i}\Big(\mathbf{E}(\mathbf{x}_i) + \mathbf{v}_i \times \mathbf{B}(\mathbf{x}_i)\Big). \tag{A.6}$$

We insert the scales into the position equation (A.5), we obtain the following non-dimensional form

$$\frac{L}{T}\frac{d\tilde{\mathbf{x}}_i}{d\tilde{t}} = \frac{L}{T}\tilde{\mathbf{v}}_i \implies \frac{d\tilde{\mathbf{x}}_i}{d\tilde{t}} = \tilde{\mathbf{v}}_i.$$

Following the same process for the velocity equation, after some rearrangement, we obtain

$$\begin{aligned}\frac{V}{T}\frac{d\tilde{\mathbf{v}}}{d\tilde{t}} &= \frac{Q}{M}\frac{\tilde{q}_i}{\tilde{m}_i}\left(E_0\mathbf{E} + B_0 V\tilde{\mathbf{v}} \times \tilde{\mathbf{B}}\right)\\ \implies \frac{d\tilde{\mathbf{v}}}{d\tilde{t}} &= \frac{\tilde{q}_i}{r_i}\left(\frac{TQ}{VM}E_0\mathbf{E} + \frac{TQ}{M}B_0\tilde{\mathbf{v}}_i \times \tilde{\mathbf{B}}\right).\end{aligned}$$

Here we have introduced the non-dimensional electric and magnetic fields $\tilde{\mathbf{E}}$ and $\tilde{\mathbf{B}}$, which are normalized by E_0 and B_0, respectively, and $r_i = m_i/M$ is a mass ratio . From the definitions $\mathbf{B} = \nabla \times \mathbf{A}$ and $\mathbf{E} = -\nabla\phi - \frac{\partial \mathbf{A}}{\partial t}$, we can express these scales in terms of ϕ_0 and A_0 as

$$E_0 = \frac{\phi_0}{L}, \quad B_0 = \frac{A_0}{L}.$$

Therefore,[2] the non-dimensionalized equation for the velocity can be expressed in terms of these scales as

$$\begin{aligned}\frac{d\tilde{\mathbf{v}}_i}{d\tilde{t}} &= \frac{\tilde{q}_i}{r_i}\Big(\frac{TQ}{VM}\frac{\phi_0}{L}\tilde{\mathbf{E}} + \frac{TQ}{M}\frac{A_0}{L}\tilde{\mathbf{v}}_i \times \tilde{\mathbf{B}}\Big),\\ &= \frac{\tilde{q}_i}{r_i}\Big(\frac{TQ}{(L/T)M}\frac{\phi_0}{L}\tilde{\mathbf{E}} + \frac{TQ}{M}\frac{A_0}{L}\tilde{\mathbf{v}}_i \times \tilde{\mathbf{B}}\Big),\\ &= \frac{\tilde{q}_i}{r_i}\Big(\frac{T^2Q\phi_0}{L^2M}\tilde{\mathbf{E}} + \frac{TQA_0}{ML}\tilde{\mathbf{v}}_i \times \tilde{\mathbf{B}}\Big),\\ &\equiv \frac{\tilde{q}_i}{r_i}\Big(\alpha_1\tilde{\mathbf{E}} + \alpha_2\tilde{\mathbf{v}}_i \times \tilde{\mathbf{B}}\Big),\end{aligned}$$

where we have introduced the parameters

$$\alpha_1 = \frac{T^2Q\phi_0}{L^2M}, \quad \alpha_2 = \frac{TQA_0}{ML}.$$

[2]The $\mathbf{E_0} = \frac{\phi_0}{\mathbf{L}}$ initially seems off, until you see $E_0\tilde{\mathbf{E}} = -\frac{\phi_0}{L}\nabla\tilde{\phi} - \frac{A_0}{T}\tilde{\mathbf{A}}$ inherently requires $\frac{\phi_0}{L} = \frac{A_0}{T}$.

We then select ϕ_0 and A_0 so that $\alpha_1 = \alpha_2 = 1$, i.e.,

$$\phi_0 = \frac{L^2 M}{T^2 Q}, \quad A_0 = \frac{ML}{TQ}, \tag{A.7}$$

which, happily, results in an the non-dimensional system

$$\frac{d\mathbf{x}_i}{dt} = \mathbf{v}_i, \tag{A.8}$$

$$\frac{d\mathbf{v}_i}{dt} = \frac{q_i}{r_i}\Big(\mathbf{E} + \mathbf{v}_i \times \mathbf{B}\Big), \tag{A.9}$$

where we have dropped the tildes for convenience of notation.

A.3 Maxwell's Equations under the Lorenz Gauge

We now consider the vector and scalar wave equations formed by converting the **E** and **B** fields of Maxwell's equations to vector and scalar potentials under the Lorenz gauge.

$$\begin{cases} \dfrac{1}{c^2}\dfrac{\partial^2 \phi}{\partial t^2} - \Delta\phi = \dfrac{\rho}{\epsilon_0}, & \text{(A.10a)} \\ \dfrac{1}{c^2}\dfrac{\partial^2 \mathbf{A}}{\partial t^2} - \Delta\mathbf{A} = \mu_0 \mathbf{J}, & \text{(A.10b)} \\ \dfrac{1}{c^2}\dfrac{\partial \phi}{\partial t} + \nabla \cdot \mathbf{A} = 0. & \text{(A.10c)} \end{cases}$$

We non-dimensionalize the field equations by substituting scales introduced at the beginning of the section into the equations (A.10a) - (A.10c), which gives

$$\begin{cases} \dfrac{1}{c^2}\dfrac{\phi_0}{T^2}\dfrac{\partial^2 \tilde{\phi}}{\partial \tilde{t}^2} - \dfrac{\phi_0}{L^2}\tilde{\Delta}\tilde{\phi} = \dfrac{Q\bar{n}}{\epsilon_0}\tilde{\rho}, \\ \dfrac{1}{c^2}\dfrac{A_0}{T^2}\dfrac{\partial^2 \tilde{\mathbf{A}}}{\partial \tilde{t}^2} - \dfrac{A_0}{L^2}\tilde{\Delta}\tilde{\mathbf{A}} = \dfrac{\mu_0 Q\bar{n}L}{T}\tilde{\mathbf{J}}, \\ \dfrac{1}{c^2}\dfrac{\phi_0}{T}\dfrac{\partial \tilde{\phi}}{\partial \tilde{t}} + \dfrac{A_0}{L}\tilde{\nabla} \cdot \tilde{\mathbf{A}} = 0. \end{cases}$$

The first equation can be rearranged to obtain

$$\frac{L^2}{c^2 T^2}\frac{\partial^2 \tilde{\phi}}{\partial \tilde{t}^2} - \tilde{\Delta}\tilde{\phi} = \frac{L^2 Q\bar{n}}{\epsilon_0 \phi_0}\tilde{\rho}.$$

Similarly, with the second equation we obtain

$$\frac{L^2}{c^2 T^2}\frac{\partial^2 \tilde{\mathbf{A}}}{\partial \tilde{t}^2} - \tilde{\Delta}\tilde{\mathbf{A}} = \frac{Q\bar{n}VL^2}{c^2 \epsilon_0 A_0}\tilde{\mathbf{J}},$$

where we have used $V = LT^{-1}$ as well as the fact that $c^2 = (\mu_0\epsilon_0)^{-1}$. Finally, the gauge condition becomes

$$\frac{\phi_0 V}{c^2 A_0}\frac{\partial\tilde{\phi}}{\partial\tilde{t}} + \tilde{\nabla}\cdot\tilde{\mathbf{A}} = 0.$$

Introducing the normalized speed of light $\kappa = c/V$, and selecting ϕ_0 and A_0 according to (A.7), we find that the above equations simplify to (dropping the tildes)

$$\begin{cases} \dfrac{1}{\kappa^2}\partial_{tt}\phi - \Delta\phi = \dfrac{1}{\sigma_1}\rho, & \text{(A.11)} \\ \dfrac{1}{\kappa^2}\partial_{tt}\mathbf{A} - \Delta\mathbf{A} = \sigma_2\mathbf{J}, & \text{(A.12)} \\ \dfrac{1}{\kappa^2}\partial_t\phi + \nabla\cdot\mathbf{A} = 0, & \text{(A.13)} \end{cases}$$

where we have introduced the new parameters

$$\sigma_1 = \frac{M\epsilon_0}{Q^2T^2\bar{n}}, \quad \sigma_2 = \frac{Q^2L^2\bar{n}\mu_0}{M}. \tag{A.14}$$

These are nothing more than normalized versions of the permittivity and permeability constants in the original equations (matching exactly the normalized constants in Section A.1).

A.4 Particle Equations of Motion

We now wish to non-dimensionalize the particle equations of motion under the Lorenz gauge. The generalized momentum equations are as follows:

$$\begin{cases} \dfrac{d\mathbf{x}_i}{dt} = \dfrac{c^2\left(\mathbf{P}_i - q_i\mathbf{A}\right)}{\sqrt{c^2\left(\mathbf{P}_i - q_i\mathbf{A}\right)^2 + \left(m_ic^2\right)^2}}, & \text{(A.15)} \\ \dfrac{d\mathbf{P}_i}{dt} = -q_i\nabla\phi + \dfrac{q_ic^2\left(\nabla\mathbf{A}\right)\cdot\left(\mathbf{P}_i - q_i\mathbf{A}\right)}{\sqrt{c^2\left(\mathbf{P}_i - q_i\mathbf{A}\right)^2 + \left(m_ic^2\right)^2}}. & \text{(A.16)} \end{cases}$$

Starting with the position equation (A.15), we substitute the scales introduced at the beginning of this section and obtain

$$\frac{L}{T}\frac{d\tilde{\mathbf{x}}_i}{d\tilde{t}} = \frac{c^2\left(P\tilde{\mathbf{P}}_i - QA_0\tilde{q}_i\tilde{\mathbf{A}}\right)}{\sqrt{c^2\left(P\tilde{\mathbf{P}}_i - QA_0\tilde{\mathbf{A}}\right)^2 + \left(m_ic^2\right)^2}}.$$

This equation can be simplified further by using the definition of A_0 from (A.7) and noting that the scale for momentum is $P = MLT^{-1}$. Defining the normalized mass $\tilde{m}_i = m_i/M$ and charge

$\tilde{q}_i = q_i/Q$, we obtain the non-dimensionalized position equation

$$\frac{d\tilde{\mathbf{x}}_i}{d\tilde{t}} = \frac{\kappa^2\left(\tilde{\mathbf{P}}_i - \tilde{q}_i\tilde{\mathbf{A}}\right)}{\sqrt{\kappa^2\left(\tilde{\mathbf{P}}_i - \tilde{q}_i\tilde{\mathbf{A}}\right)^2 + \left(\tilde{m}_i\kappa^2\right)^2}},$$

where $\kappa = c/V$ is, again, the normalized speed of light.

Following an identical treatment for the generalized momentum equation (A.16) and appealing to the definition of the scales (A.7), after some simplifications, we obtain

$$\frac{d\tilde{\mathbf{P}}_i}{d\tilde{t}} = -\tilde{q}_i\tilde{\nabla}\tilde{\phi} + \frac{\tilde{q}_i\kappa^2\left(\tilde{\nabla}\tilde{\mathbf{A}}\right)\cdot\left(\tilde{\mathbf{P}}_i - \tilde{q}_i\tilde{\mathbf{A}}\right)}{\sqrt{\kappa^2\left(\tilde{\mathbf{P}}_i - \tilde{q}_i\tilde{\mathbf{A}}\right)^2 + \left(\tilde{m}_i\kappa^2\right)^2}}.$$

Therefore, the non-dimensional form of the relativistic equations of motion is given by (dropping tildes)

$$\begin{cases} \dfrac{d\mathbf{x}_i}{dt} = \dfrac{\kappa^2\left(\mathbf{P}_i - q_i\mathbf{A}\right)}{\sqrt{\kappa^2\left(\mathbf{P}_i - q_i\mathbf{A}\right)^2 + \left(m_i\kappa^2\right)^2}}, \\ \dfrac{d\mathbf{P}_i}{dt} = -q_i\nabla\phi + \dfrac{q_i\kappa^2\left(\nabla\mathbf{A}\right)\cdot\left(\mathbf{P}_i - q_i\mathbf{A}\right)}{\sqrt{\kappa^2\left(\mathbf{P}_i - q_i\mathbf{A}\right)^2 + \left(m_i\kappa^2\right)^2}}. \end{cases}$$

Performing analogous manipulations in the non-relativistic limit leads to the system (again dropping tildes)

$$\begin{cases} \dfrac{d\mathbf{x}_i}{dt} = \dfrac{1}{m_i}\left(\mathbf{P}_i - q_i\mathbf{A}\right), \\ \dfrac{d\mathbf{P}_i}{dt} = -q_i\nabla\phi + \dfrac{q_i}{m_i}\left(\nabla\mathbf{A}\right)\cdot\left(\mathbf{P}_i - q_i\mathbf{A}\right). \end{cases}$$

APPENDIX B

DERIVING THE PARTICLE EQUATIONS OF MOTION FROM FIRST PRINCIPLES

We wish to derive the equations of motion in terms of the vector and scalar potentials. To do so, we begin with the relativistic Lagrangians for a free particle and a particle interacting in a field, obtained from Chapter 12 of [32][1] (see also [34]):

$$\mathcal{L}_{free} = -\frac{mc^2}{\gamma}, \tag{B.1}$$

$$\mathcal{L}_{int} = -q\phi + q\mathbf{v}\cdot\mathbf{A}. \tag{B.2}$$

We combine these to acquire the Lagrangian:

$$\mathcal{L} = -\frac{mc^2}{\gamma} + q\mathbf{v}\cdot\mathbf{A} - q\phi. \tag{B.3}$$

We define the canonical momentum as

$$\mathbf{P} \coloneqq \nabla_{\mathbf{v}}\mathcal{L}. \tag{B.4}$$

Knowing $\frac{d}{dv_i}\gamma^{-1} = -\frac{\gamma v_i}{c^2}$, ie $\nabla_{\mathbf{v}}\gamma^{-1} = -\frac{\gamma\mathbf{v}}{c^2}$ yields

$$\mathbf{P} = \gamma m\mathbf{v} + q\mathbf{A}. \tag{B.5}$$

What is $\gamma m\mathbf{v}$ other than momentum? Thus we define $\mathbf{p} \coloneqq \gamma m\mathbf{v}$ as the ordinary kinetic momentum. The Hamiltonian is written in terms of the Lagrangian as

$$\mathcal{H} \coloneqq \mathbf{P}\cdot\mathbf{v} - \mathcal{L}. \tag{B.6}$$

[1] Jackson uses Gaussian units, which we convert here to SI.

We note

$$\begin{aligned}
\gamma &= \left(1 - \frac{\mathbf{v}^2}{c^2}\right)^{-\frac{1}{2}} \\
&= \left(1 - \frac{\left(\frac{1}{\gamma m}\left(\mathbf{P} - q\mathbf{A}\right)\right)^2}{c^2}\right)^{-\frac{1}{2}} \\
\implies \gamma^{-2} &= 1 - \frac{1}{\left(\gamma mc\right)^2}\left(\mathbf{P} - q\mathbf{A}\right)^2 \\
\implies 1 &= \gamma^2 - \frac{1}{\left(\gamma mc\right)^2}\left(\mathbf{P} - q\mathbf{A}\right)^2 \\
\implies -\gamma^2 &= -1 - \frac{1}{\left(mc\right)^2}\left(\mathbf{P} - q\mathbf{A}\right)^2 \\
\implies \gamma &= \sqrt{1 + \frac{1}{\left(mc\right)^2}\left(\mathbf{P} - q\mathbf{A}\right)^2}
\end{aligned} \tag{B.7}$$

We may derive the following identity from (B.5) and (B.7):

$$\begin{aligned}
\mathbf{v} &= \frac{\mathbf{P} - q\mathbf{A}}{m\sqrt{\frac{1}{(mc)^2}\left(\mathbf{P} - q\mathbf{A}\right)^2 + 1}} \\
&= \frac{c^2\left(\mathbf{P} - q\mathbf{A}\right)}{\sqrt{c^2\left(\mathbf{P} - q\mathbf{A}\right)^2 + \left(mc^2\right)^2}}.
\end{aligned} \tag{B.8}$$

We substitute this into the Lagrangian to acquire

$$\begin{aligned}
\mathcal{H} &= \mathbf{P}\cdot\mathbf{v} - \mathcal{L} \\
&= \mathbf{P}\cdot\left(\frac{c^2\left(\mathbf{P} - q\mathbf{A}\right)}{\sqrt{c^2\left(\mathbf{P} - q\mathbf{A}\right)^2 + \left(mc^2\right)^2}}\right) - \left(-\frac{mc^2}{\gamma} + q\left(\frac{c^2\left(\mathbf{P} - q\mathbf{A}\right)}{\sqrt{c^2\left(\mathbf{P} - q\mathbf{A}\right)^2 + \left(mc^2\right)^2}}\right)\cdot\mathbf{A} - q\phi\right) \\
&= \left(c^2\left(\mathbf{P} - q\mathbf{A}\right)^2 + \left(mc^2\right)^2\right)^{-\frac{1}{2}}\left(\mathbf{P} - q\mathbf{A}\right)\cdot c^2\left(\mathbf{P} - q\mathbf{A}\right) + mc^2\left(1 + \frac{1}{(mc)^2}\left(\mathbf{P} - q\mathbf{A}\right)^2\right)^{-\frac{1}{2}} + q\phi \\
&= \left(c^2\left(\mathbf{P} - q\mathbf{A}\right)^2 + \left(mc^2\right)^2\right)^{-\frac{1}{2}} c^2\left(\mathbf{P} - q\mathbf{A}\right)^2 + \left(mc^2\right)^2\left(\left(mc^2\right)^2 + c^2\left(\mathbf{P} - q\mathbf{A}\right)^2\right)^{-\frac{1}{2}} + q\phi \\
&= \left(c^2\left(\mathbf{P} - q\mathbf{A}\right)^2 + \left(mc^2\right)^2\right)^{-\frac{1}{2}}\left(c^2\left(\mathbf{P} - q\mathbf{A}\right)^2 + \left(mc^2\right)^2\right) + q\phi \\
&= \sqrt{c^2\left(\mathbf{P} - q\mathbf{A}\right)^2 + \left(mc^2\right)^2} + q\phi.
\end{aligned} \tag{B.9}$$

We compute the Hamiltonian for a system of N particles by summing over the Hamiltonian of each particle. Given a particle i, and evaluating $\mathbf{A}$ and ϕ at $\mathbf{x}_i$, we know

$$\frac{d\mathbf{x}_i}{dt} = \frac{\partial \mathcal{H}}{\partial \mathbf{P}_i} = \frac{c^2(\mathbf{P}_i - q_i\mathbf{A})}{\sqrt{c^2\left(\mathbf{P}_i - q_i\mathbf{A}\right)^2 + \left(m_i c^2\right)^2}} \tag{B.10}$$

$$\frac{d\mathbf{P}_i}{dt} = -\frac{\partial \mathcal{H}}{\partial \mathbf{x}_i} = -q_i\nabla\phi + \frac{q_i c^2(\nabla\mathbf{A})\cdot(\mathbf{P}_i - q_i\mathbf{A})}{\sqrt{c^2\left(\mathbf{P}_i - q_i\mathbf{A}\right)^2 + \left(m_i c^2\right)^2}} \tag{B.11}$$

We can resimplify in terms of γ_i

$$\frac{d\mathbf{x}_i}{dt} = \frac{1}{\gamma_i m_i}\left(\mathbf{P}_i - q_i\mathbf{A}\right), \tag{B.12}$$

$$\frac{d\mathbf{P}_i}{dt} = -q_i\nabla\phi + \frac{q_i}{\gamma_i m_i}\left(\nabla\mathbf{A}\right)\cdot\left(\mathbf{P}_i - q_i\mathbf{A}\right). \tag{B.13}$$

If we let assume a nonrelativistic setting, ie $\gamma \approx 1$ then we see the system simplifies to

$$\frac{d\mathbf{x}_i}{dt} = \frac{1}{m_i}\left(\mathbf{P}_i - q_i\mathbf{A}\right), \tag{B.14}$$

$$\frac{d\mathbf{P}_i}{dt} = \frac{q_i}{m_i}\left(\nabla\mathbf{A}\right)\cdot\left(\mathbf{P}_i - q_i\mathbf{A}\right) - q_i\nabla\phi \tag{B.15}$$

Thus we have the particle equations of motion in terms of the vector and scalar potentials.

APPENDIX C

DERIVING THE BOLTZMANN EQUATION FROM FIRST PRINCIPLES

Matthew W. Kunz has a set of lecture notes [67] upon which this is based, and it was Dr. Shiping Zhou who walked the Christlieb group through them. The main difference between these lecture notes and this (other than the addition some steps to make things clearer) will be the units, this uses SI whereas the lecture notes uses Gaussian.

We first begin by considering the evolution of a system of particles of species α in phase space. This system may be described by the following function

$$F_\alpha\left(t, \mathbf{r}, \mathbf{v}\right) = \sum_{i=1}^{N_\alpha} \delta\left(\mathbf{r} - \mathbf{R}_{\alpha i}(t)\right) \delta\left(\mathbf{v} - \mathbf{V}_{\alpha i}(t)\right). \tag{C.1}$$

Here N_α is the number of particles of species α, $\mathbf{r}$ is physical space and $\mathbf{v}$ is velocity space. This model views the collection of particles as a summation of delta functions over phase space. Newton's law and the Lorentz force give us

$$\frac{d\mathbf{R}_{\alpha i}}{dt} = \mathbf{V}_{\alpha i}, \quad \frac{1}{m_\alpha}\mathbf{F}_{\alpha i} = -\frac{d\mathbf{V}_{\alpha i}}{dt} = \frac{q_\alpha}{m_\alpha}\left(\mathbf{E}_m + \mathbf{V}_{\alpha i} \times \mathbf{B}_m\right) \tag{C.2}$$

The m indicates "microphysical," meaning the electric and magnetic fields are the result of the particles themselves, nothing external. These are functions of $\mathbf{r}$ and t. These of course satisfy Maxwell's equations, and given the linearity, we can incorporate external fields without issue. Now, taking a time derivative will show how the system evolves over time. Before we do so, the following properties will be useful:

$$a\delta\left(a - b\right) = b\delta\left(b - a\right), \tag{C.3a}$$

$$\frac{\partial}{\partial a} f(a - b) = -\frac{\partial}{\partial b} f(a - b). \tag{C.3b}$$

The reasoning for these is straightforward enough, if $a \neq b$, then $\delta\left(a - b\right) = 0$, if $a = b$, then $\delta\left(a - b\right) = \infty$, but more importantly the integral of $\delta\left(a - b\right)$ will be $a = b$. In either case, the first identity holds. The second immediately follows from the chain rule. If $\xi \coloneqq a - b$, then $\frac{\partial f}{\partial a} = \frac{\partial f}{\partial \xi}\frac{\partial \xi}{\partial a} = \frac{\partial f}{\partial \xi}$. Similar reasoning yields $\frac{\partial f}{\partial b} = -\frac{\partial f}{\partial \xi}$. Now we take a derivation of the particle

distribution function:

$$
\begin{aligned}
\frac{\partial F_\alpha}{\partial t} &= \frac{\partial}{\partial t}\sum_{i=1}^{N_\alpha}\delta\left(\mathbf{r}-\mathbf{R}_{\alpha i}(t)\right)\delta\left(\mathbf{v}-\mathbf{V}_{\alpha i}(t)\right)\\
&= \sum_{i=1}^{N_\alpha}\left[\frac{d\mathbf{R}_{\alpha i}}{dt}\cdot\nabla_{\mathbf{R}_{\alpha i}}\delta\left(\mathbf{r}-\mathbf{R}_{\alpha i}(t)\right)\delta\left(\mathbf{v}-\mathbf{V}_{\alpha i}(t)\right)+\frac{d\mathbf{V}_{\alpha i}}{dt}\cdot\nabla_{\mathbf{V}_{\alpha i}}\delta\left(\mathbf{r}-\mathbf{R}_{\alpha i}(t)\right)\delta\left(\mathbf{v}-\mathbf{V}_{\alpha i}(t)\right)\right]\\
&= -\sum_{i=1}^{N_\alpha}\left[\frac{d\mathbf{R}_{\alpha i}}{dt}\cdot\nabla_{\mathbf{r}}\delta\left(\mathbf{r}-\mathbf{R}_{\alpha i}(t)\right)\delta\left(\mathbf{v}-\mathbf{V}_{\alpha i}(t)\right)+\frac{d\mathbf{V}_{\alpha i}}{dt}\cdot\nabla_{\mathbf{r}}\delta\left(\mathbf{r}-\mathbf{R}_{\alpha i}(t)\right)\delta\left(\mathbf{v}-\mathbf{V}_{\alpha i}(t)\right)\right]\\
&= -\sum_{i=1}^{N_\alpha}\left[\mathbf{V}_{\alpha i}\cdot\nabla_{\mathbf{r}}\delta\left(\mathbf{r}-\mathbf{R}_{\alpha i}(t)\right)\delta\left(\mathbf{v}-\mathbf{V}_{\alpha i}(t)\right)\right]\\
&\quad -\sum_{i=1}^{N_\alpha}\left[\left(\frac{q_\alpha}{m_\alpha}\left(\mathbf{E}_m\left(\mathbf{R}_{\alpha i},t\right)+\mathbf{V}_{\alpha i}\times\mathbf{B}_m\left(\mathbf{R}_{\alpha i},t\right)\right)\right)\cdot\nabla_{\mathbf{r}}\delta\left(\mathbf{r}-\mathbf{R}_{\alpha i}(t)\right)\delta\left(\mathbf{v}-\mathbf{V}_{\alpha i}(t)\right)\right]\\
&= -\sum_{i=1}^{N_\alpha}\left[\mathbf{v}\cdot\nabla_{\mathbf{r}}\delta\left(\mathbf{r}-\mathbf{R}_{\alpha i}(t)\right)\delta\left(\mathbf{v}-\mathbf{V}_{\alpha i}(t)\right)\right]\\
&\quad -\sum_{i=1}^{N_\alpha}\left[\left(\frac{q_\alpha}{m_\alpha}\left(\mathbf{E}_m\left(\mathbf{r},t\right)+\mathbf{v}\times\mathbf{B}_m\left(\mathbf{r},t\right)\right)\right)\cdot\nabla_{\mathbf{r}}\delta\left(\mathbf{r}-\mathbf{R}_{\alpha i}(t)\right)\delta\left(\mathbf{v}-\mathbf{V}_{\alpha i}(t)\right)\right]\\
&= -\mathbf{v}\cdot\nabla_{\mathbf{r}}F_\alpha-\frac{q_\alpha}{m_\alpha}\left(\mathbf{E}_m\left(\mathbf{r},t\right)+\mathbf{v}\times\mathbf{B}_m\left(\mathbf{r},t\right)\right)\cdot\nabla_{\mathbf{v}}F_\alpha
\end{aligned}
\tag{C.4}
$$

The move from the fourth and fifth line to the sixth and seventh is justified by the first identity, (C.3a), the move from the second to the third line is justified by the second identity (C.3b). Given this equality, it is clear

$$
\left[\frac{\partial}{\partial t}+\mathbf{v}\cdot\nabla_{\mathbf{r}}+\frac{q_\alpha}{m_\alpha}\left(\mathbf{E}_m+\mathbf{v}\times\mathbf{B}_m\right)\cdot\nabla_{\mathbf{v}}\right]F_\alpha=0. \tag{C.5}
$$

This is the Klimontovich equation. From this we can derive the Vlasov equation, which is useful given that simulating the Klimontovich equation is computationally intractable.[1] We define the ensemble average (basically a smoothing function)

$$
\left\langle G\left(F_\alpha,F_\beta,...,F_\gamma\right)\right\rangle \coloneqq \int d\mathbf{X}_{all}P_N G\left(F_\alpha,F_\beta,...,F_\gamma\right) \tag{C.6}
$$

[1] Rigorously speaking, simulation of the Klimontovich equation requires the simulation of every particle in the system, which is not PIC.

Here the P_N term is the probability of a particle having a certain set of initial conditions. We then define

$$f_\alpha(\mathbf{x}, t) \coloneqq \langle F_\alpha(\mathbf{x}, t)\rangle. \tag{C.7}$$

We consider this the number of particles of species α per unit phase space. We can then derive the time evolution for f_α. We first define a perturbation of the fields and F_α function by

$$F_\alpha = \langle F_\alpha\rangle + \delta F_\alpha, \quad \mathbf{E}_m = \langle \mathbf{E}_m\rangle + \delta\mathbf{E}, \quad \mathbf{B}_m = \langle \mathbf{B}_m\rangle + \delta\mathbf{B}, \tag{C.8}$$

$$f_\alpha \coloneqq \langle F_\alpha\rangle, \quad \mathbf{E} \coloneqq \langle \mathbf{E}_m\rangle, \quad \mathbf{B} \coloneqq \langle \mathbf{B}_m\rangle, \tag{C.9}$$

$$\langle \delta F_\alpha\rangle = \langle \delta\mathbf{E}\rangle = \langle \delta\mathbf{B}\rangle = 0. \tag{C.10}$$

The $\mathbf{E}$, $\mathbf{B}$, and F_α terms represent the smoother portions of the fields and distribution function. The fields in particular are now "macroscopic" fields, averaging out all of the plasma particles. the δ terms are the remainder, they represent the spiky and discrete nature of the particles. The last line is justified by definition. If we apply the ensemble average to an ensemble average, nothing happens. As such, applying the ensemble average to any of the terms in (C.8) necessitates the ensemble average of the δ term becoming zero. ie for some value T:

$$\begin{aligned} T &= \langle T\rangle + \delta T \\ \implies \langle T\rangle &= \langle\langle T\rangle + \delta T\rangle \\ \implies \langle T\rangle &= \langle\langle T\rangle\rangle + \langle\delta T\rangle \\ \implies \langle T\rangle &= \langle T\rangle + \langle\delta T\rangle \\ \implies \langle\delta T\rangle &= 0. \end{aligned}$$

We run the average over (C.5) and decompose its fields and distribution function as described above. When we do this, it becomes

$$\frac{\partial}{\partial t}\langle f_\alpha + \delta F_\alpha\rangle + \mathbf{v}\cdot\nabla_{\mathbf{r}}\langle f_\alpha + \delta F_\alpha\rangle + \left\langle \frac{q_\alpha}{m_\alpha}\left((\mathbf{E}+\delta\mathbf{E}) + \mathbf{v}\times(\mathbf{B}+\delta\mathbf{B})\right)\cdot\nabla_{\mathbf{v}}\left(f_\alpha + \delta F_\alpha\right)\right\rangle. \tag{C.11}$$

The third term we must be careful, the ensemble average falls upon the whole term, whereas the first two terms only F_α is a function of $\mathbf{r}$. We take a closer look at the third term, which upon multiplying,

we see becomes the sum of the following four terms:

$$\left\langle \frac{q_\alpha}{m_\alpha} \left(\mathbf{E} + \mathbf{v} \times \mathbf{B}\right) \cdot \nabla_{\mathbf{v}} f_\alpha \right\rangle, \tag{C.12a}$$

$$\left\langle \frac{q_\alpha}{m_\alpha} \left(\mathbf{E} + \mathbf{v} \times \mathbf{B}\right) \cdot \nabla_{\mathbf{v}} \delta F_\alpha \right\rangle, \tag{C.12b}$$

$$\left\langle \frac{q_\alpha}{m_\alpha} \left(\delta\mathbf{E} + \mathbf{v} \times \delta\mathbf{B}\right) \cdot \nabla_{\mathbf{v}} f_\alpha \right\rangle, \tag{C.12c}$$

$$\left\langle \frac{q_\alpha}{m_\alpha} \left(\delta\mathbf{E} + \mathbf{v} \times \delta\mathbf{B}\right) \cdot \nabla_{\mathbf{v}} \delta F_\alpha \right\rangle. \tag{C.12d}$$

Now, by definition $\langle \mathbf{E} \rangle = \mathbf{E}$, $\langle \mathbf{B} \rangle = \mathbf{B}$, and $\langle f_\alpha \rangle = f_\alpha$. Additionally, given $\mathbf{v}$ is not a function of space, we see $\langle \mathbf{v} \rangle = \mathbf{v}$. As such we may pull them out of the ensemble average, and, recalling the ensemble average of all of the delta terms is zero, we see these terms become

$$\frac{q_\alpha}{m_\alpha} \left(\mathbf{E} + \mathbf{v} \times \mathbf{B}\right) \cdot \nabla_{\mathbf{v}} f_\alpha, \tag{C.13a}$$

$$\frac{q_\alpha}{m_\alpha} \left(\mathbf{E} + \mathbf{v} \times \mathbf{B}\right) \cdot \nabla_{\mathbf{v}} \left\langle \delta F_\alpha \right\rangle = 0, \tag{C.13b}$$

$$\frac{q_\alpha}{m_\alpha} \left(\left\langle \delta\mathbf{E} \right\rangle + \mathbf{v} \times \left\langle \delta\mathbf{B} \right\rangle\right) \cdot \nabla_{\mathbf{v}} f_\alpha = 0, \tag{C.13c}$$

$$\left\langle \frac{q_\alpha}{m_\alpha} \left(\delta\mathbf{E} + \mathbf{v} \times \delta\mathbf{B}\right) \cdot \nabla_{\mathbf{v}} \delta F_\alpha \right\rangle. \tag{C.13d}$$

With these facts in mind, we see the Klimontovich equation under the ensemble average (C.11) becomes

$$\frac{\partial f_\alpha}{\partial t} + \mathbf{v} \cdot \nabla_{\mathbf{r}} f_\alpha + \frac{q_\alpha}{m_\alpha} \left(\mathbf{E} + \mathbf{v} \times \mathbf{B}\right) \cdot \nabla_{\mathbf{v}} f_\alpha = - \left\langle \frac{q_\alpha}{m_\alpha} \left(\delta\mathbf{E} + \mathbf{v} \times \delta\mathbf{B}\right) \cdot \nabla_{\mathbf{v}} \delta F_\alpha \right\rangle \tag{C.14}$$

This is the Boltzmann equation, which reduces to the Vlasov equation if the δ terms are negligible.

APPENDIX D

THE YEE AND BORIS METHOD

D.1 The Yee Grid

Named for the applied mathematician, Kane Yee (born 1934), the Yee scheme [86] is a clever numerical technique to model electromagnetic waves via the finite difference method. The brilliance of this technique lies in its staggering of the electric and magnetic fields (see figures D.1 and D.2). Where most solvers will collocate both the fields and their constituent components, the Yee grid staggers them, and in so doing enforces the involutions (Gauss's Law for both electricity and magnetism). It is derived as follows:[1]

We have Maxwell's equations, (1.7a) - (1.7d). We take the curl equations and view them in component form, first we will approach (1.7c).

$$\frac{\partial E_z}{\partial y} - \frac{\partial E_y}{\partial z} = -\frac{\partial B_x}{\partial t}, \tag{D.1a}$$

$$\frac{\partial E_x}{\partial z} - \frac{\partial E_z}{\partial x} = -\frac{\partial B_y}{\partial t}, \tag{D.1b}$$

$$\frac{\partial E_y}{\partial x} - \frac{\partial E_x}{\partial y} = -\frac{\partial B_z}{\partial t}, \tag{D.1c}$$

First, we stagger the electric and magnetic fields in time, with the magnetic field being on integer timesteps and the electric field being on half steps. We also stagger the fields in space as show in the diagram. We do so using the standard finite difference approach, Taylor expanding in both space and time:

$$\frac{E^{n+\frac{1}{2}}_{z,i,j+1,k+\frac{1}{2}} - E^{n+\frac{1}{2}}_{z,i,j,k+\frac{1}{2}}}{\Delta y} - \frac{E^{n+\frac{1}{2}}_{y,i,j+\frac{1}{2},k+1} - E^{n+\frac{1}{2}}_{y,i,j+\frac{1}{2},k}}{\Delta z} = -\frac{B^{n+1}_{x,i,j+\frac{1}{2},k+\frac{1}{2}} - B^{n}_{x,i,j+\frac{1}{2},k+\frac{1}{2}}}{\Delta t}, \tag{D.2a}$$

$$\frac{E^{n+\frac{1}{2}}_{x,i+\frac{1}{2},j,k+1} - E^{n+\frac{1}{2}}_{x,i+\frac{1}{2},j,k}}{\Delta z} - \frac{E^{n+\frac{1}{2}}_{z,i+1,j,k+\frac{1}{2}} - E^{n+\frac{1}{2}}_{z,i,j,k+\frac{1}{2}}}{\Delta x} = -\frac{B^{n+1}_{y,i+\frac{1}{2},j,k+\frac{1}{2}} - B^{n}_{y,i+\frac{1}{2},j,k+\frac{1}{2}}}{\Delta t}, \tag{D.2b}$$

[1] I am indebted to Dr. Raymond Rumpf at University of Texas at El Paso, who has an excellent Youtube series walking through the Yee grid and how it is derived.

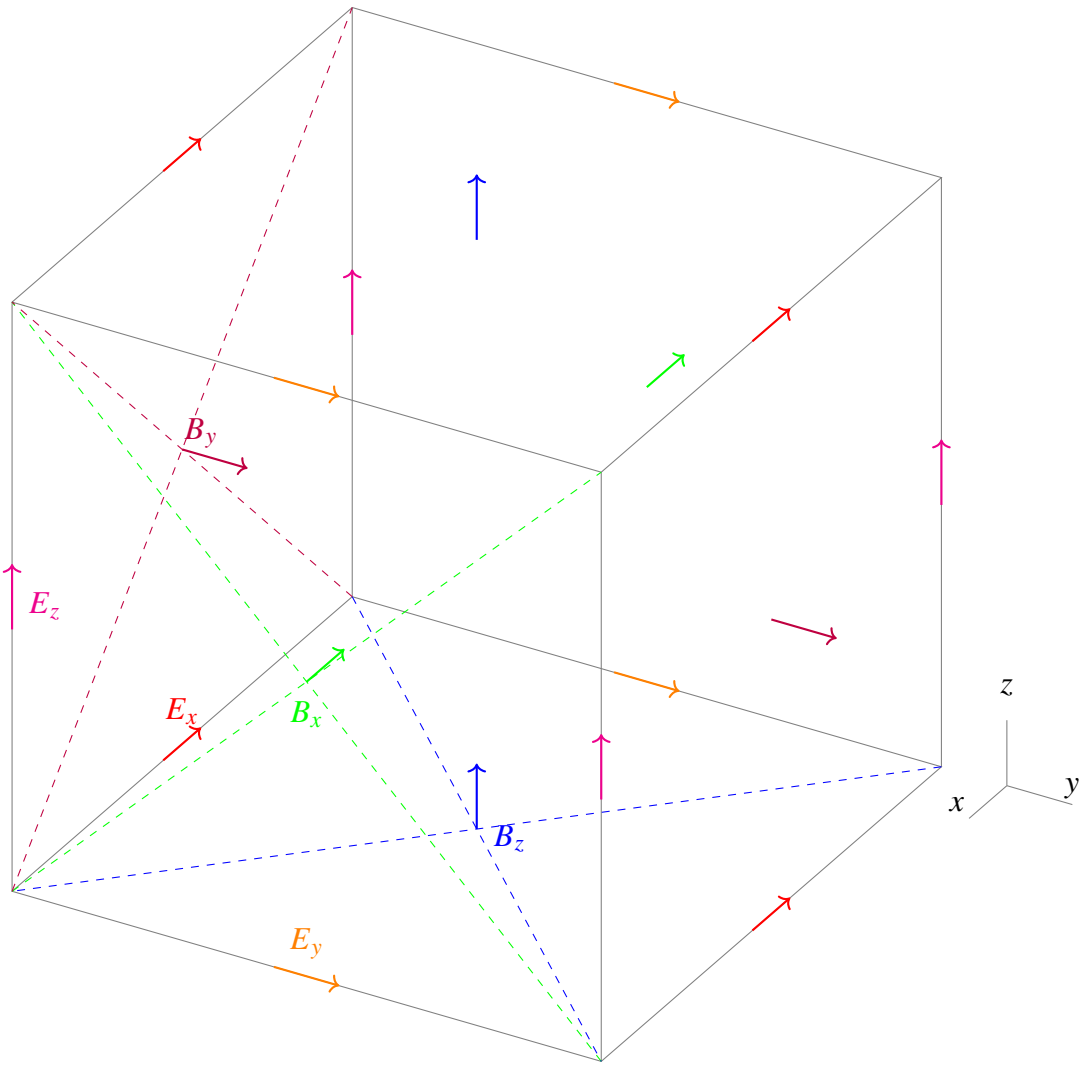

Figure D.1 A 3D Yee grid cell. Values are located on the arrows.

$$\frac{E^{n+\frac{1}{2}}_{y,i+1,j+\frac{1}{2},k} - E^{n+\frac{1}{2}}_{y,i,j+\frac{1}{2},k}}{\Delta x} - \frac{E^{n+\frac{1}{2}}_{x,i+\frac{1}{2},j+1,k} - E^{n+\frac{1}{2}}_{x,i+\frac{1}{2},j,k}}{\Delta y} = -\frac{B^{n+1}_{z,i+\frac{1}{2},j+\frac{1}{2},k} - B^{n}_{z,i+\frac{1}{2},j+\frac{1}{2},k}}{\Delta t}. \tag{D.2c}$$

We can then rearrange these to form update equations:

$$B^{n+1}_{x,i,j+\frac{1}{2},k+\frac{1}{2}} = B^{n}_{x,i,j+\frac{1}{2},k+\frac{1}{2}} - \Delta t \left(\frac{E^{n+\frac{1}{2}}_{z,i,j+1,k+\frac{1}{2}} - E^{n+\frac{1}{2}}_{z,i,j,k+\frac{1}{2}}}{\Delta y} - \frac{E^{n+\frac{1}{2}}_{y,i,j+\frac{1}{2},k+1} - E^{n+\frac{1}{2}}_{y,i,j+\frac{1}{2},k}}{\Delta z} \right), \tag{D.3a}$$

$$B^{n+1}_{y,i+\frac{1}{2},j,k+\frac{1}{2}} = B^{n}_{y,i+\frac{1}{2},j,k+\frac{1}{2}} - \Delta t \left(\frac{E^{n+\frac{1}{2}}_{x,i+\frac{1}{2},j,k+1} - E^{n+\frac{1}{2}}_{x,i+\frac{1}{2},j,k}}{\Delta z} - \frac{E^{n+\frac{1}{2}}_{z,i+1,j,k+\frac{1}{2}} - E^{n+\frac{1}{2}}_{z,i,j,k+\frac{1}{2}}}{\Delta x} \right), \tag{D.3b}$$

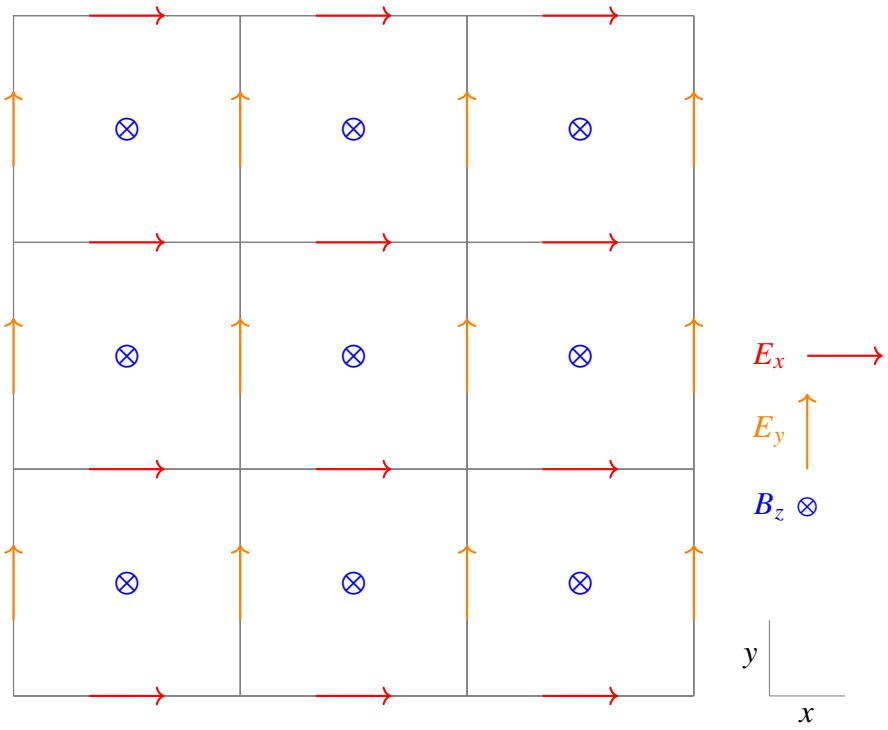

Figure D.2 A 2D Yee grid cell in Transverse Electric (TE) mode. The magnetic field is pointed out of the page.

$$B^{n+1}_{z,i+\frac{1}{2},j+\frac{1}{2},k} = B^{n}_{z,i+\frac{1}{2},j+\frac{1}{2},k} - \Delta t \left(\frac{E^{n+\frac{1}{2}}_{y,i+1,j+\frac{1}{2},k} - E^{n+\frac{1}{2}}_{y,i,j+\frac{1}{2},k}}{\Delta x} - \frac{E^{n+\frac{1}{2}}_{x,i+\frac{1}{2},j+1,k} - E^{n+\frac{1}{2}}_{x,i+\frac{1}{2},j,k}}{\Delta y} \right). \tag{D.3c}$$

We may now repeat the process with (1.7d). Taking it in component form:

$$\frac{\partial B_z}{\partial y} - \frac{\partial B_y}{\partial z} = \mu_0 J_x + \frac{1}{c^2}\frac{\partial E_x}{\partial t}, \tag{D.4a}$$

$$\frac{\partial B_x}{\partial z} - \frac{\partial B_z}{\partial x} = \mu_0 J_y + \frac{1}{c^2}\frac{\partial E_y}{\partial t}, \tag{D.4b}$$

$$\frac{\partial B_y}{\partial x} - \frac{\partial B_x}{\partial y} = \mu_0 J_x + \frac{1}{c^2}\frac{\partial E_z}{\partial t}, \tag{D.4c}$$

We then Taylor expand:

$$\frac{B^{n}_{z,i+\frac{1}{2},j+\frac{1}{2},k} - B^{n}_{z,i+\frac{1}{2},j-\frac{1}{2},k}}{\Delta y} - \frac{B^{n}_{y,i+\frac{1}{2},j,k+\frac{1}{2}} - B^{n}_{y,i+\frac{1}{2},j,k-\frac{1}{2}}}{\Delta z} = \mu_0 J^{n-\frac{1}{2}}_{x,i+\frac{1}{2},j,k} + \frac{1}{c^2}\frac{E^{n+\frac{1}{2}}_{x,i+\frac{1}{2},j,k} - E^{n-\frac{1}{2}}_{x,i+\frac{1}{2},j,k}}{\Delta t}, \tag{D.5a}$$

$$\frac{B^n_{x,i,j+\frac{1}{2},k+\frac{1}{2}} - B^n_{x,i,j+\frac{1}{2},k-\frac{1}{2}}}{\Delta z} - \frac{B^n_{z,i+\frac{1}{2},j+\frac{1}{2},k} - B^n_{z,i-\frac{1}{2},j+\frac{1}{2},k}}{\Delta x} = \mu_0 J^{n-\frac{1}{2}}_{y,i,j+\frac{1}{2},k} + \frac{1}{c^2}\frac{E^{n+\frac{1}{2}}_{y,i,j+\frac{1}{2},k} - E^{n-\frac{1}{2}}_{y,i,j+\frac{1}{2},k}}{\Delta t}, \tag{D.5b}$$

$$\frac{B^n_{y,i+\frac{1}{2},j,k+\frac{1}{2}} - B^n_{y,i-\frac{1}{2},j,k+\frac{1}{2}}}{\Delta x} - \frac{B^n_{x,i,j+\frac{1}{2},k+\frac{1}{2}} - B^n_{x,i,j-\frac{1}{2},k+\frac{1}{2}}}{\Delta y} = \mu_0 J^{n-\frac{1}{2}}_{z,i,j,k+\frac{1}{2}} + \frac{1}{c^2}\frac{E^{n+\frac{1}{2}}_{z,i,j,k+\frac{1}{2}} - E^{n-\frac{1}{2}}_{z,i,j,k+\frac{1}{2}}}{\Delta t}. \tag{D.5c}$$

And once more we rearrange these to form update equations

$$E^{n+\frac{1}{2}}_{x,i+\frac{1}{2},j,k} = E^{n-\frac{1}{2}}_{x,i+\frac{1}{2},j,k} + c^2\Delta t\left(\frac{B^n_{z,i+\frac{1}{2},j+\frac{1}{2},k} - B^n_{z,i+\frac{1}{2},j-\frac{1}{2},k}}{\Delta y} - \frac{B^n_{y,i+\frac{1}{2},j,k+\frac{1}{2}} - B^n_{y,i+\frac{1}{2},j,k-\frac{1}{2}}}{\Delta z} - \mu_0 J^{n-\frac{1}{2}}_{x,i+\frac{1}{2},j,k}\right), \tag{D.6a}$$

$$E^{n+\frac{1}{2}}_{y,i,j+\frac{1}{2},k} = E^{n-\frac{1}{2}}_{y,i,j+\frac{1}{2},k} + c^2\Delta t\left(\frac{B^n_{x,i,j+\frac{1}{2},k+\frac{1}{2}} - B^n_{x,i,j+\frac{1}{2},k-\frac{1}{2}}}{\Delta z} - \frac{B^n_{z,i+\frac{1}{2},j+\frac{1}{2},k} - B^n_{z,i-\frac{1}{2},j+\frac{1}{2},k}}{\Delta x} - \mu_0 J^{n-\frac{1}{2}}_{y,i,j+\frac{1}{2},k}\right), \tag{D.6b}$$

$$E^{n+\frac{1}{2}}_{z,i,j,k+\frac{1}{2}} = E^{n-\frac{1}{2}}_{z,i,j,k+\frac{1}{2}} + c^2\Delta t\left(\frac{B^n_{y,i+\frac{1}{2},j,k+\frac{1}{2}} - B^n_{y,i-\frac{1}{2},j,k+\frac{1}{2}}}{\Delta x} - \frac{B^n_{x,i,j+\frac{1}{2},k+\frac{1}{2}} - B^n_{x,i,j-\frac{1}{2},k+\frac{1}{2}}}{\Delta y} - \mu_0 J^{n-\frac{1}{2}}_{z,i,j,k+\frac{1}{2}}\right). \tag{D.6c}$$

From here we can begin reducing our dimensions. For example, let us say there is no change in the z direction. This reduces the above equations to

$$B^{n+1}_{x,i,j+\frac{1}{2},k+\frac{1}{2}} = B^n_{x,i,j+\frac{1}{2},k+\frac{1}{2}} - \Delta t\left(\frac{E^{n+\frac{1}{2}}_{z,i,j+1,k+\frac{1}{2}} - E^{n+\frac{1}{2}}_{z,i,j,k+\frac{1}{2}}}{\Delta y}\right), \tag{D.7a}$$

$$B^{n+1}_{y,i+\frac{1}{2},j,k+\frac{1}{2}} = B^n_{y,i+\frac{1}{2},j,k+\frac{1}{2}} - \Delta t\left(-\frac{E^{n+\frac{1}{2}}_{z,i+1,j,k+\frac{1}{2}} - E^{n+\frac{1}{2}}_{z,i,j,k+\frac{1}{2}}}{\Delta x}\right), \tag{D.7b}$$

$$B^{n+1}_{z,i+\frac{1}{2},j+\frac{1}{2},k} = B^{n}_{z,i+\frac{1}{2},j+\frac{1}{2},k} - \Delta t \left(\frac{E^{n+\frac{1}{2}}_{y,i+1,j+\frac{1}{2},k} - E^{n+\frac{1}{2}}_{y,i,j+\frac{1}{2},k}}{\Delta x} - \frac{E^{n+\frac{1}{2}}_{x,i+\frac{1}{2},j+1,k} - E^{n+\frac{1}{2}}_{x,i+\frac{1}{2},j,k}}{\Delta y} \right). \tag{D.7c}$$

$$E^{n+\frac{1}{2}}_{x,i+\frac{1}{2},j,k} = E^{n-\frac{1}{2}}_{x,i+\frac{1}{2},j,k} + c^2 \Delta t \left(\frac{B^{n}_{z,i+\frac{1}{2},j+\frac{1}{2},k} - B^{n}_{z,i+\frac{1}{2},j-\frac{1}{2},k}}{\Delta y} - \mu_0 J^{n-\frac{1}{2}}_{x,i+\frac{1}{2},j,k} \right), \tag{D.8a}$$

$$E^{n+\frac{1}{2}}_{y,i,j+\frac{1}{2},k} = E^{n-\frac{1}{2}}_{y,i,j+\frac{1}{2},k} + c^2 \Delta t \left(-\frac{B^{n}_{z,i+\frac{1}{2},j+\frac{1}{2},k} - B^{n}_{z,i-\frac{1}{2},j+\frac{1}{2},k}}{\Delta x} - \mu_0 J^{n-\frac{1}{2}}_{y,i,j+\frac{1}{2},k} \right), \tag{D.8b}$$

$$E^{n+\frac{1}{2}}_{z,i,j,k+\frac{1}{2}} = E^{n-\frac{1}{2}}_{z,i,j,k+\frac{1}{2}} + c^2 \Delta t \left(\frac{B^{n}_{y,i+\frac{1}{2},j,k+\frac{1}{2}} - B^{n}_{y,i-\frac{1}{2},j,k+\frac{1}{2}}}{\Delta x} - \frac{B^{n}_{x,i,j+\frac{1}{2},k+\frac{1}{2}} - B^{n}_{x,i,j-\frac{1}{2},k+\frac{1}{2}}}{\Delta y} - \mu_0 J^{n-\frac{1}{2}}_{z,i,j,k+\frac{1}{2}} \right). \tag{D.8c}$$

Notice now that this set of equations can be decoupled into what is known as Tranverse Magnetic (TM), or E_z and Transverse Electric (TE) B_z mode.

$$B^{n+1}_{x,i,j+\frac{1}{2},k+\frac{1}{2}} = B^{n}_{x,i,j+\frac{1}{2},k+\frac{1}{2}} - \Delta t \left(\frac{E^{n+\frac{1}{2}}_{z,i,j+1,k+\frac{1}{2}} - E^{n+\frac{1}{2}}_{z,i,j,k+\frac{1}{2}}}{\Delta y} \right), \tag{D.9a}$$

$$B^{n+1}_{y,i+\frac{1}{2},j,k+\frac{1}{2}} = B^{n}_{y,i+\frac{1}{2},j,k+\frac{1}{2}} - \Delta t \left(-\frac{E^{n+\frac{1}{2}}_{z,i+1,j,k+\frac{1}{2}} - E^{n+\frac{1}{2}}_{z,i,j,k+\frac{1}{2}}}{\Delta x} \right), \tag{D.9b}$$

$$E^{n+\frac{1}{2}}_{z,i,j,k+\frac{1}{2}} = E^{n-\frac{1}{2}}_{z,i,j,k+\frac{1}{2}} + c^2 \Delta t \left(\frac{B^{n}_{y,i+\frac{1}{2},j,k+\frac{1}{2}} - B^{n}_{y,i-\frac{1}{2},j,k+\frac{1}{2}}}{\Delta x} - \frac{B^{n}_{x,i,j+\frac{1}{2},k+\frac{1}{2}} - B^{n}_{x,i,j-\frac{1}{2},k+\frac{1}{2}}}{\Delta y} - \mu_0 J^{n-\frac{1}{2}}_{z,i,j,k+\frac{1}{2}} \right). \tag{D.9c}$$

$$E^{n+\frac{1}{2}}_{x,i+\frac{1}{2},j,k} = E^{n-\frac{1}{2}}_{x,i+\frac{1}{2},j,k} + c^2 \Delta t \left(\frac{B^{n}_{z,i+\frac{1}{2},j+\frac{1}{2},k} - B^{n}_{z,i+\frac{1}{2},j-\frac{1}{2},k}}{\Delta y} - \mu_0 J^{n-\frac{1}{2}}_{x,i+\frac{1}{2},j,k} \right), \tag{D.10a}$$

$$E^{n+\frac{1}{2}}_{y,i,j+\frac{1}{2},k} = E^{n-\frac{1}{2}}_{y,i,j+\frac{1}{2},k} + c^2 \Delta t \left(-\frac{B^{n}_{z,i+\frac{1}{2},j+\frac{1}{2},k} - B^{n}_{z,i-\frac{1}{2},j+\frac{1}{2},k}}{\Delta x} - \mu_0 J^{n-\frac{1}{2}}_{y,i,j+\frac{1}{2},k} \right), \tag{D.10b}$$

$$B^{n+1}_{z,i+\frac{1}{2},j+\frac{1}{2},k} = B^{n}_{z,i+\frac{1}{2},j+\frac{1}{2},k} - \Delta t \left(\frac{E^{n+\frac{1}{2}}_{y,i+1,j+\frac{1}{2},k} - E^{n+\frac{1}{2}}_{y,i,j+\frac{1}{2},k}}{\Delta x} - \frac{E^{n+\frac{1}{2}}_{x,i+\frac{1}{2},j+1,k} - E^{n+\frac{1}{2}}_{x,i+\frac{1}{2},j,k}}{\Delta y} \right). \tag{D.10c}$$

We can reduce down to one dimension by eliminating changes in the y direction. This will eliminate equations (D.9a) and (D.10a) and simplify equations (D.9c) and (D.10c).

$$B^{n+1}_{y,i+\frac{1}{2},j,k+\frac{1}{2}} = B^{n}_{y,i+\frac{1}{2},j,k+\frac{1}{2}} - \Delta t \left(-\frac{E^{n+\frac{1}{2}}_{z,i+1,j,k+\frac{1}{2}} - E^{n+\frac{1}{2}}_{z,i,j,k+\frac{1}{2}}}{\Delta x} \right), \tag{D.11a}$$

$$B^{n+1}_{z,i+\frac{1}{2},j+\frac{1}{2},k} = B^{n}_{z,i+\frac{1}{2},j+\frac{1}{2},k} - \Delta t \left(\frac{E^{n+\frac{1}{2}}_{y,i+1,j+\frac{1}{2},k} - E^{n+\frac{1}{2}}_{y,i,j+\frac{1}{2},k}}{\Delta x} \right). \tag{D.11b}$$

$$E^{n+\frac{1}{2}}_{y,i,j+\frac{1}{2},k} = E^{n-\frac{1}{2}}_{y,i,j+\frac{1}{2},k} + c^2 \Delta t \left(-\frac{B^{n}_{z,i+\frac{1}{2},j+\frac{1}{2},k} - B^{n}_{z,i-\frac{1}{2},j+\frac{1}{2},k}}{\Delta x} - \mu_0 J^{n-\frac{1}{2}}_{y,i,j+\frac{1}{2},k} \right), \tag{D.12a}$$

$$E^{n+\frac{1}{2}}_{z,i,j,k+\frac{1}{2}} = E^{n-\frac{1}{2}}_{z,i,j,k+\frac{1}{2}} + c^2 \Delta t \left(\frac{B^{n}_{y,i+\frac{1}{2},j,k+\frac{1}{2}} - B^{n}_{y,i-\frac{1}{2},j,k+\frac{1}{2}}}{\Delta x} - \mu_0 J^{n-\frac{1}{2}}_{z,i,j,k+\frac{1}{2}} \right). \tag{D.12b}$$

This is again decoupled into two sets of update equations.

$$E^{n+\frac{1}{2}}_{z,i,j,k+\frac{1}{2}} = E^{n-\frac{1}{2}}_{z,i,j,k+\frac{1}{2}} + c^2 \Delta t \left(\frac{B^{n}_{y,i+\frac{1}{2},j,k+\frac{1}{2}} - B^{n}_{y,i-\frac{1}{2},j,k+\frac{1}{2}}}{\Delta x} - \mu_0 J^{n-\frac{1}{2}}_{z,i,j,k+\frac{1}{2}} \right). \tag{D.13a}$$

$$B^{n+1}_{y,i+\frac{1}{2},j,k+\frac{1}{2}} = B^{n}_{y,i+\frac{1}{2},j,k+\frac{1}{2}} - \Delta t \left(-\frac{E^{n+\frac{1}{2}}_{z,i+1,j,k+\frac{1}{2}} - E^{n+\frac{1}{2}}_{z,i,j,k+\frac{1}{2}}}{\Delta x} \right), \tag{D.13b}$$

$$E^{n+\frac{1}{2}}_{y,i,j+\frac{1}{2},k} = E^{n-\frac{1}{2}}_{y,i,j+\frac{1}{2},k} + c^2 \Delta t \left(-\frac{B^{n}_{z,i+\frac{1}{2},j+\frac{1}{2},k} - B^{n}_{z,i-\frac{1}{2},j+\frac{1}{2},k}}{\Delta x} - \mu_0 J^{n-\frac{1}{2}}_{y,i,j+\frac{1}{2},k} \right), \tag{D.14a}$$

$$B^{n+1}_{z,i+\frac{1}{2},j+\frac{1}{2},k} = B^{n}_{z,i+\frac{1}{2},j+\frac{1}{2},k} - \Delta t \left(\frac{E^{n+\frac{1}{2}}_{y,i+1,j+\frac{1}{2},k} - E^{n+\frac{1}{2}}_{y,i,j+\frac{1}{2},k}}{\Delta x} \right). \tag{D.14b}$$

Thus we have our Yee grid for 1, 2, and 3 dimensions. This is an explicit update equation and is limited to timesteps of size [86, 312]:

$$\Delta t \leq \frac{1}{c\sqrt{\frac{1}{\Delta x^2} + \frac{1}{\Delta y^2} + \frac{1}{\Delta z^2}}}. \tag{D.15}$$

We now turn to derive this value.

D.1.1 CFL Condition

The following is based on [312].[2] To ensure stability we will derive the Courant–Friedrichs–Lewy (CFL) number for the Yee scheme.

Consider the two curl equations in vacuum without current:

$$\nabla \times \mathbf{E} = -\frac{1}{c}\frac{\partial \mathbf{B}}{\partial t}, \tag{D.16}$$

$$\nabla \times \mathbf{B} = \frac{1}{c}\frac{\partial \mathbf{E}}{\partial t}. \tag{D.17}$$

The $\frac{1}{c^2}$ term typically on the RHS of (D.17) has been spread over to (D.16) for reasons that will soon become apparent. This is justified by simply rescaling our system, or can be thought of as switching over to Gaussian units.

Multiplying (D.17) by the imaginary unit i and subtracting (D.16) from it yields:

$$\begin{aligned} i\nabla \times \mathbf{B} - \nabla \times \mathbf{E} &= \frac{1}{c}\left(i\frac{\partial \mathbf{E}}{\partial t} + \frac{\partial \mathbf{B}}{\partial t} \right) \\ \implies \nabla \times (i\mathbf{B} - \mathbf{E}) &= \frac{1}{c}\frac{\partial}{\partial t}(i\mathbf{E} + \mathbf{B}) \\ \implies i\nabla \times (\mathbf{B} + i\mathbf{E}) &= \frac{1}{c}\frac{\partial}{\partial t}(i\mathbf{E} + \mathbf{B}) \\ \implies i\nabla \times \mathbf{V} &= \frac{1}{c}\frac{\partial \mathbf{V}}{\partial t} \end{aligned} \tag{D.18}$$

[2] There are other ways of going about it in perhaps a more simple way, but Taflove and Brodwin have a really clever move where they separate the spatial and temporal components of the scheme and solve an eigenvalue problem for both. They do simplify things by setting $c = 1$ which I have generalized.

where $\mathbf{V} \coloneqq \mathbf{B} + i\mathbf{E}$. To assert stability we solve the following eigenvalue problem for the numerical derivatives:

$$i\nabla \times \mathbf{V} = \lambda \mathbf{V}. \tag{D.19}$$

$$\frac{1}{c}\frac{\partial \mathbf{V}}{\partial t} = \lambda \mathbf{V}, \tag{D.20}$$

First, we consider (D.19). Now, we assume $\mathbf{V}_{l,m,n} = V_0 e^{i(k_x l\Delta x + k_y m\Delta y + k_z n\Delta z)}$ as the "arbitrary lattice spatial mode." Taking the central difference scheme, we know

$$\frac{\partial \mathbf{V}_{l,m,n}}{\partial x} \approx \frac{\mathbf{V}_{l+\frac{1}{2},m,n} - \mathbf{V}_{l-\frac{1}{2},m,n}}{\Delta x}$$

with similar results for y and z. Let us consider the partial differential approximation on this particular vector field:

$$\begin{aligned}
\frac{\mathbf{V}_{l+\frac{1}{2},m,n} - \mathbf{V}_{l-\frac{1}{2},m,n}}{\Delta x} &= \frac{V_0 e^{i\left(k_x\left(l+\frac{1}{2}\right)\Delta x + k_y m\Delta y + k_z n\Delta z\right)} - V_0 e^{i\left(k_x\left(l-\frac{1}{2}\right)\Delta x + k_y m\Delta y + k_z n\Delta z\right)}}{\Delta x} \\
&= \frac{V_0 e^{i(k_x l\Delta x + k_y m\Delta y + k_z n\Delta z)} e^{\frac{1}{2}ik_x\Delta x} - V_0 e^{i(k_x l\Delta x + k_y m\Delta y + k_z n\Delta z)} e^{-\frac{1}{2}ik_x\Delta x}}{\Delta x} \\
&= \frac{V_0 e^{i(k_x l\Delta x + k_y m\Delta y + k_z n\Delta z)}}{\Delta x}\left(e^{\frac{1}{2}ik_x\Delta x} - e^{-\frac{1}{2}ik_x\Delta x}\right) \\
&= \frac{V_0 e^{i(k_x l\Delta x + k_y m\Delta y + k_z n\Delta z)}}{\Delta x}\left(2i\sin\left(\frac{1}{2}k_x\Delta x\right)\right) \\
&= \frac{2i\sin\left(\frac{1}{2}k_x\Delta x\right)}{\Delta x}\mathbf{V}_{l,m,n}
\end{aligned}$$

Therefore, we can simplify (D.19) to

$$-2\left(\frac{\sin\left(\frac{1}{2}k_x\Delta x\right)}{\Delta x}, \frac{\sin\left(\frac{1}{2}k_y\Delta y\right)}{\Delta y}, \frac{\sin\left(\frac{1}{2}k_z\Delta z\right)}{\Delta z}\right) \times \mathbf{V}_{l,m,n} = \lambda \mathbf{V}_{l,m,n} \tag{D.21}$$

Breaking into components yields

$$-2\left(\frac{\sin\left(\frac{1}{2}k_y\Delta y\right)}{\Delta y}V_{z,l,m,n} - \frac{\sin\left(\frac{1}{2}k_z\Delta z\right)}{\Delta z}V_{y,l,m,n}\right) = \lambda V_{x,l,m,n}, \tag{D.22a}$$

$$-2\left(\frac{\sin\left(\frac{1}{2}k_z\Delta z\right)}{\Delta z}V_{x,l,m,n}-\frac{\sin\left(\frac{1}{2}k_x\Delta x\right)}{\Delta x}V_{z,l,m,n}\right)=\lambda V_{y,l,m,n}, \tag{D.22b}$$

$$-2\left(\frac{\sin\left(\frac{1}{2}k_x\Delta x\right)}{\Delta x}V_{y,l,m,n}-\frac{\sin\left(\frac{1}{2}k_y\Delta y\right)}{\Delta y}V_{x,l,m,n}\right)=\lambda V_{z,l,m,n}. \tag{D.22c}$$

Now, we know the form $\mathbf{V}_{l,m,n}=\mathbf{V}_0e^{i\left(k_xl\Delta x+k_ym\Delta y+k_zn\Delta z\right)}$, so it follows the individual components will take this form. We substitute this into the (D.22) equations:

$$-2\left(\frac{\sin\left(\frac{1}{2}k_y\Delta y\right)}{\Delta y}V_{z,l,m,n}e^{i\left(k_xl\Delta x+k_ym\Delta y+k_zn\Delta z\right)}-\frac{\sin\left(\frac{1}{2}k_z\Delta z\right)}{\Delta z}V_{y,l,m,n}e^{i\left(k_xl\Delta x+k_ym\Delta y+k_zn\Delta z\right)}\right)$$
$$=\lambda V_{x,l,m,n}e^{i\left(k_xl\Delta x+k_ym\Delta y+k_zn\Delta z\right)}, \tag{D.23a}$$

$$-2\left(\frac{\sin\left(\frac{1}{2}k_z\Delta z\right)}{\Delta z}V_{x,l,m,n}e^{i\left(k_xl\Delta x+k_ym\Delta y+k_zn\Delta z\right)}-\frac{\sin\left(\frac{1}{2}k_x\Delta x\right)}{\Delta x}V_{z,l,m,n}e^{i\left(k_xl\Delta x+k_ym\Delta y+k_zn\Delta z\right)}\right)$$
$$=\lambda V_{y,l,m,n}e^{i\left(k_xl\Delta x+k_ym\Delta y+k_zn\Delta z\right)}, \tag{D.23b}$$

$$-2\left(\frac{\sin\left(\frac{1}{2}k_x\Delta x\right)}{\Delta x}V_{y,l,m,n}e^{i\left(k_xl\Delta x+k_ym\Delta y+k_zn\Delta z\right)}-\frac{\sin\left(\frac{1}{2}k_y\Delta y\right)}{\Delta y}V_{x,l,m,n}e^{i\left(k_xl\Delta x+k_ym\Delta y+k_zn\Delta z\right)}\right)$$
$$=\lambda V_{z,l,m,n}e^{i\left(k_xl\Delta x+k_ym\Delta y+k_zn\Delta z\right)}. \tag{D.23c}$$

Dividing by $e^{i\left(k_xl\Delta x+k_ym\Delta y+k_zn\Delta z\right)}$ yields

$$-2\left(\frac{\sin\left(\frac{1}{2}k_y\Delta y\right)}{\Delta y}V_{z,l,m,n}-\frac{\sin\left(\frac{1}{2}k_z\Delta z\right)}{\Delta z}V_{y,l,m,n}\right)=\lambda V_{x,l,m,n}, \tag{D.24a}$$

$$-2\left(\frac{\sin\left(\frac{1}{2}k_z\Delta z\right)}{\Delta z}V_{x,l,m,n}-\frac{\sin\left(\frac{1}{2}k_x\Delta x\right)}{\Delta x}V_{z,l,m,n}\right)=\lambda V_{y,l,m,n}, \tag{D.24b}$$

$$-2\left(\frac{\sin\left(\frac{1}{2}k_x\Delta x\right)}{\Delta x}V_{y,l,m,n} - \frac{\sin\left(\frac{1}{2}k_y\Delta y\right)}{\Delta y}V_{x,l,m,n}\right) = \lambda V_{z,l,m,n}. \tag{D.24c}$$

This can be rearranged

$$\lambda V_{x,l,m,n} - 2\frac{\sin\left(\frac{1}{2}k_z\Delta z\right)}{\Delta z}V_{y,l,m,n} + 2\frac{\sin\left(\frac{1}{2}k_y\Delta y\right)}{\Delta y}V_{z,l,m,n} = 0, \tag{D.25a}$$

$$2\frac{\sin\left(\frac{1}{2}k_z\Delta z\right)}{\Delta z}V_{x,l,m,n} + \lambda V_{y,l,m,n} - 2\frac{\sin\left(\frac{1}{2}k_x\Delta x\right)}{\Delta x}V_{z,l,m,n} = 0, \tag{D.25b}$$

$$-2\frac{\sin\left(\frac{1}{2}k_y\Delta y\right)}{\Delta y}V_{x,l,m,n} + 2\frac{\sin\left(\frac{1}{2}k_x\Delta x\right)}{\Delta x}V_{y,l,m,n} + \lambda V_{z,l,m,n} = 0. \tag{D.25c}$$

This takes the form

$$\begin{pmatrix} \lambda & -2\frac{\sin(\frac{1}{2}k_z\Delta z)}{\Delta z} & 2\frac{\sin(\frac{1}{2}k_y\Delta y)}{\Delta y} \\ 2\frac{\sin(\frac{1}{2}k_z\Delta z)}{\Delta z} & \lambda & -2\frac{\sin(\frac{1}{2}k_x\Delta x)}{\Delta x} \\ -2\frac{\sin(\frac{1}{2}k_y\Delta y)}{\Delta y} & 2\frac{\sin(\frac{1}{2}k_x\Delta x)}{\Delta x} & \lambda \end{pmatrix}\begin{pmatrix} V_{x,l,m,n} \\ V_{y,l,m,n} \\ V_{z,l,m,n} \end{pmatrix} = \begin{pmatrix} 0 \\ 0 \\ 0 \end{pmatrix} \tag{D.26}$$

We want the determinant to be zero to allow a nontrivial solution. Using software to compute the determinant yields:

$$\lambda^3 + 4\lambda\left(\sin^2\left(\frac{k_x\Delta x}{2}\right) + \sin^2\left(\frac{k_y\Delta y}{2}\right) + \sin^2\left(\frac{k_z\Delta z}{2}\right)\right) = 0. \tag{D.27}$$

One zero is obviously $\lambda = 0$, but the nontrivial zero is

$$\lambda^2 = -4\left(\frac{\sin^2(\frac{1}{2}k_x\Delta x)}{\Delta x} + \frac{\sin^2(\frac{1}{2}k_y\Delta y)}{\Delta y} + \frac{\sin^2(\frac{1}{2}k_z\Delta z)}{\Delta z}\right). \tag{D.28}$$

In other words, λ is purely imaginary. Furthermore, the largest magnitude it can have is for values of k_x, k_y, and k_z such that the numerator is 1. ie:

$$|\lambda| \leq 2\sqrt{\frac{1}{\Delta x} + \frac{1}{\Delta y} + \frac{1}{\Delta z}}. \tag{D.29}$$

Having established this, we next consider (D.20). Discretizing with respect to time yields

$$\frac{1}{c}\frac{\mathbf{V}^{n+\frac{1}{2}} - \mathbf{V}^{n-\frac{1}{2}}}{\Delta t} = \lambda \mathbf{V}^n. \tag{D.30}$$

Let $q \coloneqq \frac{\mathbf{V}^{n+\frac{1}{2}}}{\mathbf{V}^n}$ be the solution growth factor for all timesteps n. This yields the following:

$$\begin{aligned} &\frac{\mathbf{V}^{n+\frac{1}{2}} - \mathbf{V}^{n-\frac{1}{2}}}{\mathbf{V}^n} = \lambda \Delta t \\ \implies & q - \frac{1}{q} = c\lambda\Delta t \\ \implies & q^2 - c\lambda\Delta t q - 1 = 0. \end{aligned} \tag{D.31}$$

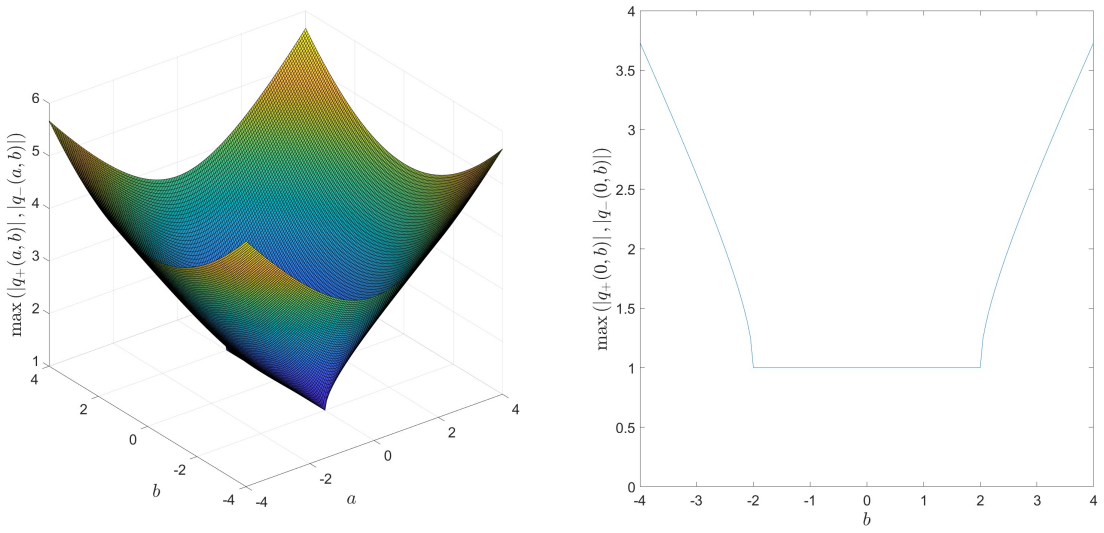

(a) Stability region over the complex plane

(b) Stability region over the imaginary axis

Figure D.3 The stability region over the complex plane with $\Delta t = c = 1$. The maximum absolute value between q_- and q_+ (solutions for polynomial's ± term) is plotted. We see that only values along the imaginary axis can satisfy $|q| \leq 1$, and these are for $\mathcal{I}[\lambda] \leq \frac{2c}{\Delta t}$.

Plugging this into the quadratic formula yields the result $q = \frac{c\lambda\Delta t}{2} \pm \sqrt{1 + \left(\frac{c\lambda\Delta t}{2}\right)^2}$. Note we need $|q| \leq 1$ for this to be stable. From (D.28) we know $\mathcal{R}[\lambda] = 0$.[3] So we know λ is purely imaginary.

[3]Taflove and Brodwin actually start out with this equation and just assert $\mathcal{R}[\lambda] = 0$ from only (D.31). This makes some intuitive sense. Say the imaginary component were zero. Any real component would immediately push $|q| > 1$. How this would shake out if λ were complex is somewhat more rickety, though plugging it into matlab (Figure D.3) does certainly indicate that the real component must be zero in order to satisfy $|q| \leq 1$. We get a much clearer view of this constraint from (D.29).

This means, letting $\lambda = \bar{\lambda} i$:

$$\begin{aligned} q &= \frac{\bar{\lambda} i \Delta t}{2} \pm \sqrt{1 + \left(\frac{\bar{\lambda} i \Delta t}{2}\right)^2} \\ &= \frac{\bar{\lambda} i \Delta t}{2} \pm \sqrt{1 - \left(\frac{\bar{\lambda} \Delta t}{2}\right)^2} \end{aligned}$$

$$\begin{aligned} qq^* &= \left(c\frac{\bar{\lambda} i \Delta t}{2} \pm \sqrt{1 - \left(\frac{c\bar{\lambda}\Delta t}{2}\right)^2}\right)\left(-\frac{c\bar{\lambda} i \Delta t}{2} \pm \sqrt{1 - \left(\frac{c\bar{\lambda}\Delta t}{2}\right)^2}\right) \\ &= -\left(\frac{c\bar{\lambda}\Delta t}{2}\right)^2 + 1 - \left(\frac{c\bar{\lambda}\Delta t}{2}\right)^2 \\ &= 1 - \frac{1}{2}\left(c\bar{\lambda}\Delta t\right)^2, \\ \implies |q| &= \sqrt{1 - \frac{1}{2}\left(c\bar{\lambda}\Delta t\right)^2}. \end{aligned} \tag{D.32}$$

This implies $\bar{\lambda} \leq \frac{2c}{\Delta t}$. We can therefore set up the following inequality, knowing $|\lambda| \leq \frac{2}{\Delta t}$ by stability requirement and $|\lambda| \leq 2\sqrt{\frac{1}{\Delta x} + \frac{1}{\Delta y} + \frac{1}{\Delta z}}$ by the nature of the grid:

$$2\sqrt{\frac{1}{\Delta x} + \frac{1}{\Delta y} + \frac{1}{\Delta z}} \leq \frac{2c}{\Delta t} \implies \Delta t \leq \frac{1}{c\sqrt{\frac{1}{\Delta x} + \frac{1}{\Delta y} + \frac{1}{\Delta z}}}. \tag{D.33}$$

D.1.2 Satisfaction of the Involutions

With the inevitable coding pains that come with bookkeeping a staggered mesh, inevitably we ask why the grid is staggered. This is due to the satisfaction of the involutions. Assuming a lack of charge, we wish to enforce $\nabla \cdot \mathbf{E} = \nabla \cdot \mathbf{B} = 0$, and the staggered nature of the Yee grid does exactly this.

Proof. Assume the involutions are satisfied at $t = n$ and $t = n + \frac{1}{2}$, ie $\nabla \cdot \mathbf{B}^n = \nabla \cdot \mathbf{E}^{n-\frac{1}{2}} = 0$. We now consider $\nabla \cdot \mathbf{E}^{n+\frac{1}{2}}$ under the Yee grid:

$$\frac{E^{n+\frac{1}{2}}_{x,i+\frac{1}{2},j,k} - E^{n+\frac{1}{2}}_{x,i-\frac{1}{2},j,k}}{\Delta x} + \frac{E^{n+\frac{1}{2}}_{y,i,j+\frac{1}{2},k} - E^{n+\frac{1}{2}}_{y,i,j-\frac{1}{2},k}}{\Delta y} + \frac{E^{n+\frac{1}{2}}_{z,i,j,k+\frac{1}{2}} - E^{n+\frac{1}{2}}_{x,i,j,k-\frac{1}{2}}}{\Delta z}. \tag{D.34}$$

Applying the update equations (D.3) and (D.6), we see the following:

$$\frac{\left(E^{n-\frac{1}{2}}_{x,i+\frac{1}{2},j,k} + c^2\Delta t\left(\frac{B^n_{z,i+\frac{1}{2},j+\frac{1}{2},k} - B^n_{z,i+\frac{1}{2},j-\frac{1}{2},k}}{\Delta y} - \frac{B^n_{y,i+\frac{1}{2},j,k+\frac{1}{2}} - B^n_{y,i+\frac{1}{2},j,k-\frac{1}{2}}}{\Delta z}\right)\right)}{\Delta x} \tag{D.35a}$$

$$- \frac{\left(E^{n-\frac{1}{2}}_{x,i-\frac{1}{2},j,k} + c^2\Delta t\left(\frac{B^n_{z,i-\frac{1}{2},j+\frac{1}{2},k} - B^n_{z,i-\frac{1}{2},j-\frac{1}{2},k}}{\Delta y} - \frac{B^n_{y,i-\frac{1}{2},j,k+\frac{1}{2}} - B^n_{y,i-\frac{1}{2},j,k-\frac{1}{2}}}{\Delta z}\right)\right)}{\Delta x} \tag{D.35b}$$

$$+ \frac{\left(E^{n-\frac{1}{2}}_{y,i,j+\frac{1}{2},k} + c^2\Delta t\left(\frac{B^n_{x,i,j+\frac{1}{2},k+\frac{1}{2}} - B^n_{x,i,j+\frac{1}{2},k-\frac{1}{2}}}{\Delta z} - \frac{B^n_{z,i+\frac{1}{2},j+\frac{1}{2},k} - B^n_{z,i-\frac{1}{2},j+\frac{1}{2},k}}{\Delta x}\right)\right)}{\Delta y} \tag{D.35c}$$

$$- \frac{\left(E^{n-\frac{1}{2}}_{y,i,j-\frac{1}{2},k} + c^2\Delta t\left(\frac{B^n_{x,i,j-\frac{1}{2},k+\frac{1}{2}} - B^n_{x,i,j-\frac{1}{2},k-\frac{1}{2}}}{\Delta z} - \frac{B^n_{z,i+\frac{1}{2},j-\frac{1}{2},k} - B^n_{z,i-\frac{1}{2},j-\frac{1}{2},k}}{\Delta x}\right)\right)}{\Delta y} \tag{D.35d}$$

$$+ \frac{\left(E^{n-\frac{1}{2}}_{z,i,j,k+\frac{1}{2}} + c^2\Delta t\left(\frac{B^n_{y,i+\frac{1}{2},j,k+\frac{1}{2}} - B^n_{y,i-\frac{1}{2},j,k+\frac{1}{2}}}{\Delta x} - \frac{B^n_{x,i,j+\frac{1}{2},k+\frac{1}{2}} - B^n_{x,i,j-\frac{1}{2},k+\frac{1}{2}}}{\Delta y}\right)\right)}{\Delta z} \tag{D.35e}$$

$$- \frac{\left(E^{n-\frac{1}{2}}_{z,i,j,k+\frac{1}{2}} + c^2\Delta t\left(\frac{B^n_{y,i+\frac{1}{2},j,k-\frac{1}{2}} - B^n_{y,i-\frac{1}{2},j,k-\frac{1}{2}}}{\Delta x} - \frac{B^n_{x,i,j+\frac{1}{2},k-\frac{1}{2}} - B^n_{x,i,j-\frac{1}{2},k-\frac{1}{2}}}{\Delta y}\right)\right)}{\Delta z}. \tag{D.35f}$$

This may be rearranged into two components. The first:

$$\frac{E^{n-\frac{1}{2}}_{x,i+\frac{1}{2},j,k} - E^{n-\frac{1}{2}}_{x,i-\frac{1}{2},j,k}}{\Delta x} + \frac{E^{n-\frac{1}{2}}_{y,i,j+\frac{1}{2},k} - E^{n-\frac{1}{2}}_{y,i,j-\frac{1}{2},k}}{\Delta y} + \frac{E^{n-\frac{1}{2}}_{z,i,j,k+\frac{1}{2}} - E^{n-\frac{1}{2}}_{x,i,j,k-\frac{1}{2}}}{\Delta z}, \tag{D.36}$$

and the second (with the common $c^2\Delta t$ left out for clarity):

$$\frac{\frac{B^n_{z,i+\frac{1}{2},j+\frac{1}{2},k} - B^n_{z,i+\frac{1}{2},j-\frac{1}{2},k}}{\Delta y} - \frac{B^n_{y,i+\frac{1}{2},j,k+\frac{1}{2}} - B^n_{y,i+\frac{1}{2},j,k-\frac{1}{2}}}{\Delta z}}{\Delta x} - \frac{\frac{B^n_{z,i-\frac{1}{2},j+\frac{1}{2},k} - B^n_{z,i-\frac{1}{2},j-\frac{1}{2},k}}{\Delta y} - \frac{B^n_{y,i-\frac{1}{2},j,k+\frac{1}{2}} - B^n_{y,i-\frac{1}{2},j,k-\frac{1}{2}}}{\Delta z}}{\Delta x}$$

$$+ \frac{\frac{B^n_{x,i,j+\frac{1}{2},k+\frac{1}{2}} - B^n_{x,i,j+\frac{1}{2},k-\frac{1}{2}}}{\Delta z} - \frac{B^n_{z,i+\frac{1}{2},j+\frac{1}{2},k} - B^n_{z,i-\frac{1}{2},j+\frac{1}{2},k}}{\Delta x}}{\Delta y} - \frac{\frac{B^n_{x,i,j-\frac{1}{2},k+\frac{1}{2}} - B^n_{x,i,j-\frac{1}{2},k-\frac{1}{2}}}{\Delta z} - \frac{B^n_{z,i+\frac{1}{2},j-\frac{1}{2},k} - B^n_{z,i-\frac{1}{2},j-\frac{1}{2},k}}{\Delta x}}{\Delta y}$$

$$+ \frac{\frac{B^n_{y,i+\frac{1}{2},j,k+\frac{1}{2}} - B^n_{y,i-\frac{1}{2},j,k+\frac{1}{2}}}{\Delta x} - \frac{B^n_{x,i,j+\frac{1}{2},k+\frac{1}{2}} - B^n_{x,i,j-\frac{1}{2},k+\frac{1}{2}}}{\Delta y}}{\Delta z} - \frac{\frac{B^n_{y,i+\frac{1}{2},j,k-\frac{1}{2}} - B^n_{y,i-\frac{1}{2},j,k-\frac{1}{2}}}{\Delta x} - \frac{B^n_{x,i,j+\frac{1}{2},k-\frac{1}{2}} - B^n_{x,i,j-\frac{1}{2},k-\frac{1}{2}}}{\Delta y}}{\Delta z}. \tag{D.37}$$

The first term goes to zero by our assumption. The second may be further rearranged to show all terms that have like components:

$$\frac{1}{\Delta x \Delta y}\left(\begin{array}{l} +\left(B^n_{z,i+\frac{1}{2},j+\frac{1}{2},k} - B^n_{z,i+\frac{1}{2},j-\frac{1}{2},k}\right) \\ -\left(B^n_{z,i-\frac{1}{2},j+\frac{1}{2},k} - B^n_{z,i-\frac{1}{2},j-\frac{1}{2},k}\right) \\ -\left(B^n_{z,i+\frac{1}{2},j+\frac{1}{2},k} - B^n_{z,i-\frac{1}{2},j+\frac{1}{2},k}\right) \\ +\left(B^n_{z,i+\frac{1}{2},j-\frac{1}{2},k} - B^n_{z,i-\frac{1}{2},j-\frac{1}{2},k}\right) \end{array}\right) + \frac{1}{\Delta x \Delta z}\left(\begin{array}{l} -\left(B^n_{y,i+\frac{1}{2},j,k+\frac{1}{2}} - B^n_{y,i+\frac{1}{2},j,k-\frac{1}{2}}\right) \\ +\left(B^n_{y,i-\frac{1}{2},j,k+\frac{1}{2}} - B^n_{y,i-\frac{1}{2},j,k-\frac{1}{2}}\right) \\ +\left(B^n_{y,i+\frac{1}{2},j,k+\frac{1}{2}} - B^n_{y,i-\frac{1}{2},j,k+\frac{1}{2}}\right) \\ -\left(B^n_{y,i+\frac{1}{2},j,k-\frac{1}{2}} - B^n_{y,i-\frac{1}{2},j,k-\frac{1}{2}}\right) \end{array}\right)$$
$$+\frac{1}{\Delta y \Delta z}\left(\begin{array}{l} +\left(B^n_{x,i,j+\frac{1}{2},k+\frac{1}{2}} - B^n_{x,i,j+\frac{1}{2},k-\frac{1}{2}}\right) \\ -\left(B^n_{x,i,j-\frac{1}{2},k+\frac{1}{2}} - B^n_{x,i,j-\frac{1}{2},k-\frac{1}{2}}\right) \\ -\left(B^n_{x,i,j+\frac{1}{2},k+\frac{1}{2}} - B^n_{x,i,j-\frac{1}{2},k+\frac{1}{2}}\right) \\ +\left(B^n_{x,i,j+\frac{1}{2},k-\frac{1}{2}} - B^n_{x,i,j-\frac{1}{2},k-\frac{1}{2}}\right) \end{array}\right) \tag{D.38}$$

The colors indicate which terms cancel out with which. Thus this term reduces to zero as well, leaving us with the conclusion that $\nabla \cdot \mathbf{E}^{\mathbf{n}+\frac{\mathbf{1}}{\mathbf{2}}} = 0$ under the Yee grid. A similar process shows the same for $\nabla \cdot \mathbf{B}^{n+1}$. QED

D.2 The Boris Push

Named after Jay Boris, who developed the method in the early 1970s [91], it is still one of the most popular particle methods owing to its volume preserving property, bound on energy error, and its simplicity [313]. We will consider both the nonrelativistic and slightly more complicated relativistic setup.[4]

D.2.1 Nonrelativistic Boris

We split our updates into two discrete times, Δt and $\frac{\Delta t}{2}$. We have velocity at the half timesteps and position at the full timesteps, and we will use the Newton-Lorentz equations of motion to do our updates

[4] Significantly, the Boris push handles relativity just fine, unlike other structure-preserving methods.

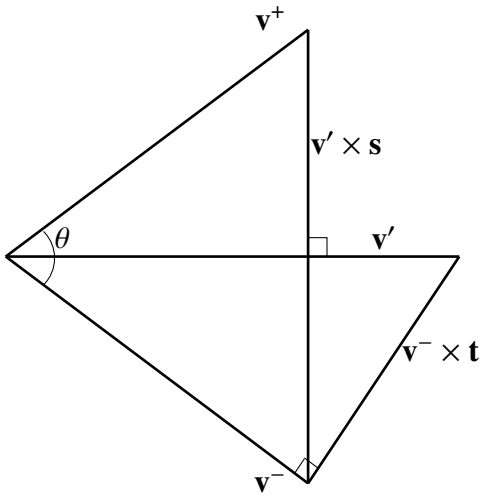

Figure D.4 The Boris Rotation

$$\frac{d}{dt}\gamma m\mathbf{v} = \mathbf{F} = q(\mathbf{E} + \mathbf{v} \times \mathbf{B}), \tag{D.39a}$$

$$\frac{d}{dt}\mathbf{x} = \mathbf{v}. \tag{D.39b}$$

Here γ is the relativistic factor $\gamma \coloneqq \left(\sqrt{1 - \frac{v^2}{c^2}}\right)^{-\frac{1}{2}}$. For simplicity we let $v << c$, and so $\gamma \approx 1$. Using the second-order accurate center difference scheme for the LHS of (D.39a) and (D.39b) and averaging the velocity value over two timesteps for the RHS of (D.39a) yields

$$\frac{\mathbf{v}^{n+\frac{1}{2}} - \mathbf{v}^{n-\frac{1}{2}}}{\Delta t} = \frac{q}{m}\left(\mathbf{E}^n + \frac{\mathbf{v}^{n+\frac{1}{2}} + \mathbf{v}^{n-\frac{1}{2}}}{\Delta t} \times \mathbf{B}^n\right), \tag{D.40a}$$

$$\frac{\mathbf{x}^{n+1} - \mathbf{x}^n}{\Delta t} = \mathbf{v}^{n+\frac{1}{2}}. \tag{D.40b}$$

We can solve this efficiently by the so-called Boris Push, first published in [91] but also described with simplicity in [80], [35] and many others.[5]

We rewrite the velocity vector $\mathbf{v}^{n\pm\frac{1}{2}} = \mathbf{v}^{\pm} \pm \frac{q\mathbf{E}}{m}\frac{\Delta t}{2}$. We put this back into (D.40a), which gives

[5]Also well described in https://www.particleincell.com/2011/vxb-rotation/

$$
\begin{aligned}
\frac{\mathbf{v}^+ - \mathbf{v}^-}{\Delta t} &= \frac{q}{2m}\left(\mathbf{v}^+ + \mathbf{v}^-\right) \times \mathbf{B} \\
\implies \mathbf{v}^+ - \mathbf{v}^- &= \frac{\Delta t}{2}\frac{q}{m}\left(\mathbf{v}^+ \times \mathbf{B} + \mathbf{v}^- \times \mathbf{B}\right) \\
\implies \mathbf{v}^+ - \frac{\Delta t}{2}\frac{q}{m}\mathbf{v}^+ \times \mathbf{B} &= \mathbf{v}^- + \frac{\Delta t}{2}\frac{q}{m}\mathbf{v}^- \times \mathbf{B} \\
\implies \mathbf{v}^+ - \mathbf{v}^+ \times \mathbf{t} &= \mathbf{v}^- + \mathbf{v}^- \times \mathbf{t}
\end{aligned}
\tag{D.41}
$$

Here we let $\mathbf{t} \coloneqq \frac{\Delta t}{2}\frac{q}{m}\mathbf{B}$. We know $\mathbf{v}^-$, to get from $\mathbf{v}^-$ to $\mathbf{v}^+$ is simply the vector $\mathbf{v}^+ - \mathbf{v}^-$. To begin doing so, we will construct a vector $\mathbf{v}'$ that is perpendicular to $\mathbf{v}^+ - \mathbf{v}^-$ and $\mathbf{B}$. To keep things perpendicular to $\mathbf{B}$ is straightforward, given $\mathbf{B}$ is pointing out of the page (in the z direction), we leave $\mathbf{v}'$ lying on the plane of the page (in the x, y plane). From geometry it is clear $\mathbf{v}'$ will bisect $\mathbf{v}^+$ and $\mathbf{v}^-$. We do this by incrementing $\mathbf{v}^-$ as such:

$$
\mathbf{v}' \coloneqq \mathbf{v}^- + \mathbf{v}^- \times \mathbf{t}. \tag{D.42}
$$

From D.41 we may safely conclude that $\mathbf{v}'$ bisects $\mathbf{v}^+$ and $\mathbf{v}^-$. ie this action is to rotate $\mathbf{v}^-$ halfway towards $\mathbf{v}^+$, though its magnitude is not guaranteed to match that of $\mathbf{v}^+$. Thus, we simply need to rotate it again by some vector $\mathbf{s}$.

$$
\mathbf{v}^+ = \mathbf{v}^- + \mathbf{v}' \times \mathbf{s}. \tag{D.43}
$$

We know $\mathbf{s}$ will point in the same direction as $\mathbf{t}$, but we need to pin down its magnitude. Recall that we require $\|\mathbf{v}^-\| = \|\mathbf{v}^+\|$. We can derive the magnitude of $\mathbf{s}$ as follows

$$
\begin{aligned}
\|\mathbf{v}^+\| &= \|\mathbf{v}^- + \mathbf{v}' \times \mathbf{s}\| \\
&= \|\mathbf{v}^- + (\mathbf{v}^- + \mathbf{v}^- \times \mathbf{t}) \times \mathbf{s}\| \\
&= \|\mathbf{v}^- + \mathbf{v}^- \times \mathbf{s} + (\mathbf{v}^- \times \mathbf{t}) \times \mathbf{s}\|.
\end{aligned}
\tag{D.44}
$$

Using the vector identity $(\mathbf{A} \times \mathbf{B}) \times \mathbf{C} = (\mathbf{A} \cdot \mathbf{C})\,\mathbf{B} - (\mathbf{B} \cdot \mathbf{C})\,\mathbf{A}$ gives us $(\mathbf{v}^- \times \mathbf{t}) \times \mathbf{s} = (\mathbf{v}^- \cdot \mathbf{s})\,\mathbf{t} - (\mathbf{t} \cdot \mathbf{s})\,\mathbf{v}^-$. This gives

$$
\|\mathbf{v}^+\| = \|\mathbf{v}^- + \mathbf{v}^- \times \mathbf{s} + (\mathbf{v}^- \cdot \mathbf{s})\,\mathbf{t} - (\mathbf{t} \cdot \mathbf{s})\,\mathbf{v}^-\|. \tag{D.45}
$$

Noting that $\mathbf{v}^-$ and $\mathbf{s}$ are orthogonal and $\mathbf{s}$ and $\mathbf{t}$ are parallel, and for clarity the letting $t \coloneqq \|\mathbf{t}\|$, etc. this yields

$$\begin{aligned} \|\mathbf{v}^+\| &= \|\mathbf{v}^- + \mathbf{v}^- \times \mathbf{s} - ts\mathbf{v}^-\| \\ &= \|(1 - ts)\,\mathbf{v}^- + \mathbf{v}^- \times \mathbf{s}\|. \end{aligned} \tag{D.46}$$

Noting again that $\mathbf{v}^-$ and $\mathbf{s}$ are orthogonal, we know $\|\mathbf{v}^- \times \mathbf{s}\| = \|\mathbf{s}\|\|\mathbf{v}^-\|$. We also know, if $\mathbf{a}$ and $\mathbf{b}$ are orthogonal vectors, then $\|\mathbf{a} - \mathbf{b}\|^2 = \|\mathbf{a} + \mathbf{b}\|^2 = \|\mathbf{a}\| + \|\mathbf{b}\|^2$. Therefore

$$\begin{aligned} \|\mathbf{v}^+\|^2 &= \|(1 - ts)\,\mathbf{v}^- + \mathbf{v}^- \times \mathbf{s}\|^2 \\ &= \|(1 - ts)\,\mathbf{v}^-\|^2 + \|\mathbf{v}^- \times \mathbf{s}\|^2 \\ &= (1 - ts)^2\,\|\mathbf{v}^-\|^2 + \|\mathbf{v}^-\|^2\|\mathbf{s}\|^2. \end{aligned} \tag{D.47}$$

Remembering our requirement that $\|\mathbf{v}^+\| = \|\mathbf{v}^-\|$, we may conclude

$$\begin{aligned} &(1 - ts)^2 + s^2 = 1 \\ \implies &1 - 2ts + t^2s^2 + s^2 = 1 \\ \implies &s^2\left(1 + t^2\right) - 2ts = 0 \\ \implies &s^2\left(1 + t^2\right) = 2ts \\ \implies &s^2 = \frac{2ts}{1 + t^2} \\ \implies &s = \frac{2t}{1 + t^2}. \end{aligned} \tag{D.48}$$

D.2.2 The Relativistic Boris Push

What if $\gamma \neq 1$? Consider time $t^n = n\Delta t$. Let m be the resting mass of a particle, and let $\mathbf{u} \coloneqq \gamma\mathbf{v}$, where $\gamma = \sqrt{1 + \frac{u^2}{c^2}}$. For convenience we again let boldface denote a vector, nonboldface denote the magnitude. The relativistic Lorentz force can be written

$$\frac{\mathbf{u}^{n+\frac{1}{2}} - \mathbf{u}^{n-\frac{1}{2}}}{\Delta t} = \frac{q}{m}\left[\mathbf{E}^n + \frac{1}{c}\frac{\mathbf{u}^{n+\frac{1}{2}} + \mathbf{u}^{n-\frac{1}{2}}}{2\gamma^n} \times \mathbf{B}^n\right]. \tag{D.49}$$

Similar to the nonrelativistic case, we let

$$\mathbf{u}^- \coloneqq \mathbf{u}^{n-\frac{1}{2}} + \frac{q\Delta t}{2m}\mathbf{E}^n, \tag{D.50}$$

$$\mathbf{u}^{+} \coloneqq \mathbf{u}^{n+\frac{1}{2}} - \frac{q\Delta t}{2m}\mathbf{E}^{n}. \tag{D.51}$$

This is plugged into D.49, which yields

$$\frac{\mathbf{u}^{+} - \mathbf{u}^{-}}{\Delta t} = \frac{q}{2\gamma^{n} mc}\left((\mathbf{u}^{+} + \mathbf{u}^{-}) \times \mathbf{B}^{n}\right). \tag{D.52}$$

Similar to the above, we define

$$\mathbf{u}' \coloneqq \mathbf{u}^{-} + \mathbf{u}^{-} \times \mathbf{t}. \tag{D.53}$$

And using similar logic, this yields

$$\mathbf{u}^{+} = \mathbf{u}^{-} + \mathbf{u}' \times \mathbf{s}. \tag{D.54}$$

Here we've defined

$$\mathbf{t} \coloneqq \frac{q\Delta t}{2\gamma^{n} mc}, \tag{D.55}$$

$$\mathbf{s} \coloneqq \frac{2t}{1 + t^{2}}. \tag{D.56}$$

We've averaged $\gamma^{n} \coloneqq \sqrt{1 + \left(\frac{u^{-}}{c}\right)^{2}} = \sqrt{1 + \left(\frac{u^{+}}{c}\right)^{2}}$ After acquiring the next velocity using D.51, we step the location using Newton's law

$$\frac{d}{dt}\mathbf{x} = \mathbf{v}, \tag{D.57}$$

which yields

$$\mathbf{x}^{n+1} = \mathbf{x}^{n} + \Delta t \mathbf{v}^{n+\frac{1}{2}} = \mathbf{x}^{n} + \Delta t \frac{\mathbf{u}^{n+\frac{1}{2}}}{\gamma^{n+\frac{1}{2}}}. \tag{D.58}$$

APPENDIX E

PROVING VILLASENOR AND BUNEMAN'S SCHEME CONSERVES CHARGE

We wish to prove that Villasenor and Buneman's scheme [37] is charge conserving, that is

$$\frac{\partial \rho}{\partial t} + \nabla \cdot \mathbf{J} = 0. \tag{E.1}$$

Proof. Consider a charge that has moved from one place to another, as displayed in Figure E.2. Without loss of generality, we only take the case in which the particle remains in the same cells. If it moves cells, simply take the subpaths (see figure E.3) that remain within their respective cells and repeat the following procedure. Defining the following:

$$\begin{aligned} \mathbf{w} &\coloneqq \mathbf{x} - \mathbf{X}_{j,k}, \\ \Delta\mathbf{w} &\coloneqq \mathbf{w}^{n+1} - \mathbf{w}^{n}, \\ \bar{\mathbf{w}} &\coloneqq \frac{\left(\mathbf{w}^{n+1} + \mathbf{w}^{n}\right)}{2}, \end{aligned} \tag{E.2}$$

It will be useful to note the following identity:

$$\Delta w_1 \bar{w}_2 + \Delta w_2 \bar{w}_1 = w_1^{n+1} w_2^{n+1} - w_2^{n} w_1^{n}. \tag{E.3}$$

So we have ρ at two points, ρ^n and ρ^{n+1}, and we can approximate the time derivative as

$$\frac{\partial \rho}{\partial t} = \frac{\rho_{j,k}^{n+1} - \rho_{j,k}^{n}}{\Delta t}. \tag{E.4}$$

We scatter ρ linearly, that is, for a particle of charge q, we have $\rho_{i,j} = \frac{1}{\Delta x \Delta y} q(1 - w_1)(1 - w_2)$, where w_1 and w_2 are the weights from our shape functions, and $\frac{1}{\Delta x \Delta y}$ is our volume. This is shown in figure E.1. So it follows

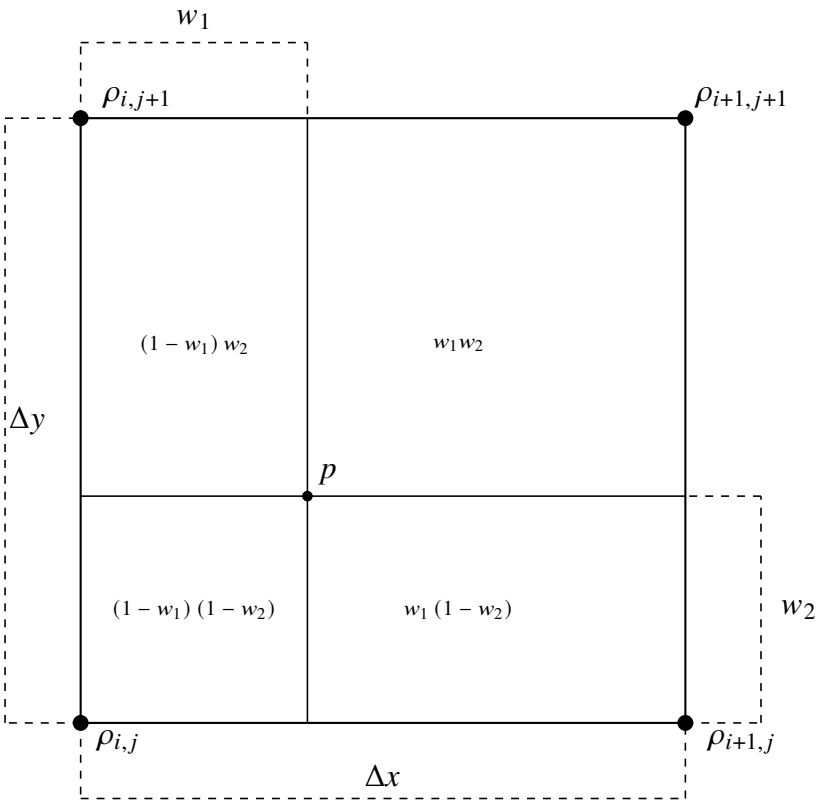

Figure E.1 A square with an interior point connected to the sides. The distances between the point and the square's sides are labeled.

$$\begin{aligned}
\frac{\rho_{j,k}^{n+1}-\rho_{j,k}^{n}}{\Delta t} &= \frac{1}{\Delta x \Delta y}\frac{q\left(1-w_1^{n+1}\right)\left(1-w_2^{n+1}\right)-q\left(1-w_1^{n}\right)\left(1-w_2^{n}\right)}{\Delta t} \\
&= \frac{1}{\Delta x \Delta y}\frac{q}{\Delta t}\left(1-w_1^{n+1}-w_2^{n+1}+w_1^{n+1}w_2^{n+1}-1+w_1^{n}+w_2^{n}-w_1^{n}w_2^{n}\right) \\
&= \frac{1}{\Delta x \Delta y}\frac{q}{\Delta t}\left(-\Delta w_1-\Delta w_2+w_1^{n+1}w_2^{n+1}-w_1^{n}w_2^{n}\right) \\
&= \frac{1}{\Delta x \Delta y}\frac{q}{\Delta t}\left(-\Delta w_1-\Delta w_2+\Delta w_1 \bar{w}_2+\Delta w_2 \bar{w}_1\right)
\end{aligned} \tag{E.5}$$

Now, considering $\nabla \cdot \mathbf{J}$, we expand using finite difference

$$\nabla \cdot \mathbf{J} = \frac{J_{1,j+\frac{1}{2},k}^{n+\frac{1}{2}}-J_{1,j-\frac{1}{2},k}^{n+\frac{1}{2}}}{\Delta x}+\frac{J_{1,j,k+\frac{1}{2}}^{n+\frac{1}{2}}-J_{1,j,k-\frac{1}{2}}^{n+\frac{1}{2}}}{\Delta y} \tag{E.6}$$

Noting $J_{1,j-\frac{1}{2},k} = J_{2,j,k-\frac{1}{2}} = 0$, given the shape functions we are using, we use Verbonceour's description of Villasenor and Buneman's scheme to scatter the particle [80]:

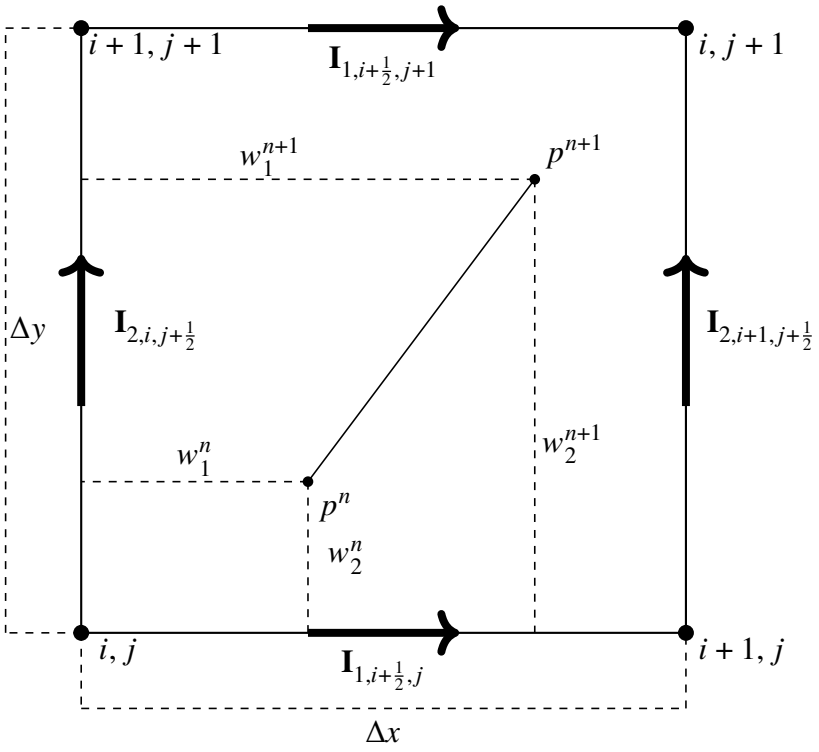

Figure E.2 A particle traversing within a single cell. Figure inspired by [80].

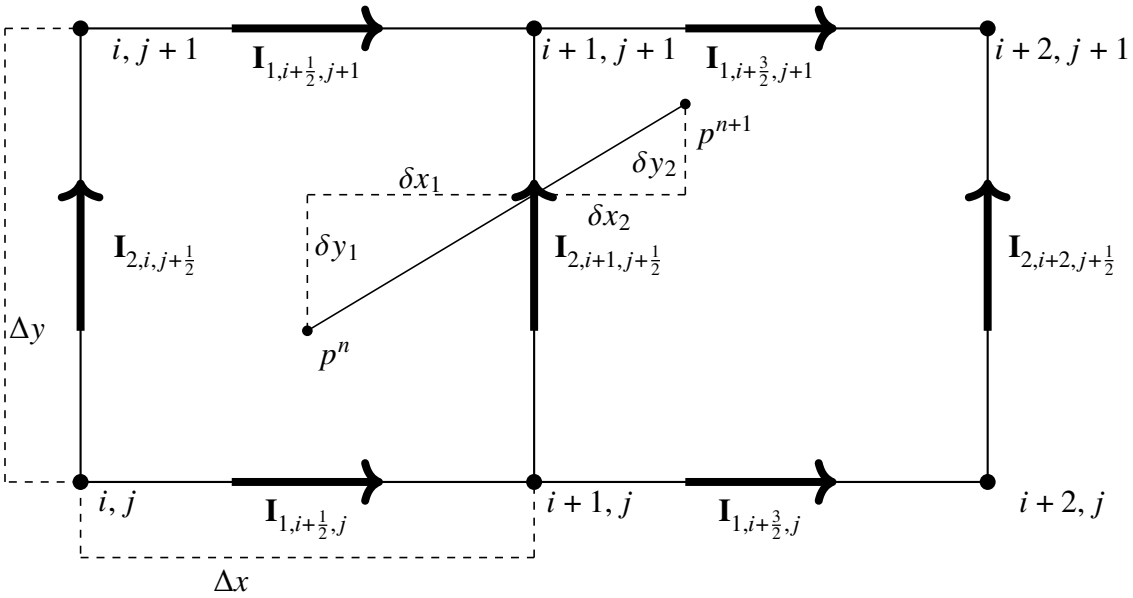

Figure E.3 A particle traversing across a cell boundary. Figure inspired by [80].

$$
\begin{aligned}
J_{1,j+\frac{1}{2},k} &= \frac{1}{\Delta y} I_{1,j+\frac{1}{2},k} = \frac{1}{\Delta y}\frac{q}{\Delta t}\left(\Delta w_1\left(1-\bar{w}_2\right)\right), \\
J_{1,j,k+\frac{1}{2}} &= \frac{1}{\Delta x} I_{2,j,k+\frac{1}{2}} = \frac{1}{\Delta x}\frac{q}{\Delta t}\left(\Delta w_2\left(1-\bar{w}_1\right)\right).
\end{aligned}
\tag{E.7}
$$

Plugging these into E.6, we get

$$
\begin{aligned}
\nabla \cdot \mathbf{J} &= \frac{q}{\Delta t}\left(\frac{\frac{1}{\Delta y}\Delta w_1\left(1-\bar{w}_2\right)}{\Delta x} + \frac{\frac{1}{\Delta x}\Delta w_2\left(1-\bar{w}_1\right)}{\Delta y}\right) \\
&= \frac{1}{\Delta x \Delta y}\frac{q}{\Delta t}\left(\Delta w_1\left(1-\bar{w}_2\right) + \Delta w_2\left(1-\bar{w}_1\right)\right) \\
&= \frac{1}{\Delta x \Delta y}\frac{q}{\Delta t}\left(\Delta w_1 - \Delta w_1 \bar{w}_2 + \Delta w_2 - \Delta w_2 \bar{w}_1\right) \\
&= \frac{1}{\Delta x \Delta y}\frac{q}{\Delta t}\left(\Delta w_1 + \Delta w_2 - \Delta w_1 \bar{w}_2 - \Delta w_2 \bar{w}_1\right).
\end{aligned}
\tag{E.8}
$$

Thus we see

$$
\frac{\partial \rho}{\partial t} = -\nabla \cdot \mathbf{J}.
$$

QED

APPENDIX F

SPLINES

The purpose of this is to make clearer how we derive multidimensional higher order particle weighting. The linear and quadratic schemes can be found in [35], with [80] giving a brief overview of linear and good visualizations of higher order schemes as well. A generalization using B-Splines, or Basis Splines, is discussed in detail by de Boor [314].[1]

F.1 Constructing Splines

Here we will go over some of the theoretical underpinnings of particle weighting. I am working primarily with the above footnoted pdf document and [289].

First, it's important to emphasize that, for our purposes, we are considering a node at the center of whatever spline we are considering. The particle we are interpolating to or from the node is relative to this center.

The zeroth order basis function is defined as follows

$$B^0_{j,j+1}(x) = \begin{cases} 1, & \text{if } K_j < x < K_{j+1}, \\ 0, & \text{otherwise.} \end{cases} \tag{F.1}$$

The higher order basis functions are defined as

$$B^k_{j,j+k+1}(x) = \frac{x - K_j}{K_{j+k} - K_j} B^{k-1}_{j,j+k}(x) + \frac{K_{j+k+1} - x}{K_{j+k+1} - K_{j+1}} B^{k-1}_{j+1,j+k+1}(x). \tag{F.2}$$

This is all one dimensional, but by taking a tensor product n times we can get $n + 1$ dimensions.

We can get a better idea of what this all means by building the first few layers. Consider the zeroth order basis which may be geometrically represented in as below:[2]

[1] This gitlab site is also very useful: https://gitlab.com/Makogan/mathproofs/blob/master/B-splines/b-splines.pdf

[2] Though this triangle representation is somewhat common, I'm particularly grateful for the gitlab site for making it more interpretable.

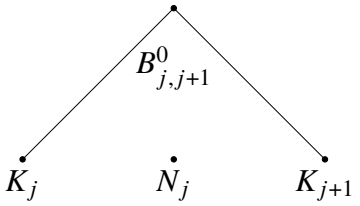

Assuming a uniform grid, this width of this spline is Δx, so if a particle is within a distance of $\frac{\Delta x}{2}$, ie $-\frac{\Delta x}{2} \leq x_p - K_j < \frac{\Delta x}{2}$, then N_j takes a value of 1. We can build a grid as follows, with a particle p falling between K_j and K_{j+1}:

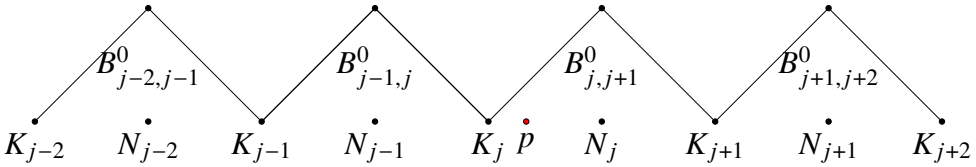

Clearly N_j will be assigned a value of 1 and the rest will be assigned a value of zero. This may be normalized by considering

$$B^0_{j,j+1}\left(\bar{x} \equiv \frac{x - K_j}{\Delta x}\right) = \begin{cases} 1, & \text{if } 0 < \bar{x} < 1, \\ 0, & \text{otherwise.} \end{cases} \tag{F.3}$$

Let's click things up to linear order. Now, instead of the node being between knots, we see the nodes as lining up with the knots (this will become a pattern, even splines have nodes between knots, odd splines line up). Our first order spline takes the following form:

$$B^1_{j,j+2} = \frac{x - K_j}{K_{j+1} - K_j} B^0_{j,j+1} + \frac{K_{i+2} - x}{K_{j+2} - K_{j+1}} B^0_{j+1,j+2} \tag{F.4}$$

The triangle diagram takes the following appearance, with a particle p falling between N_{j-1} and N_j again:

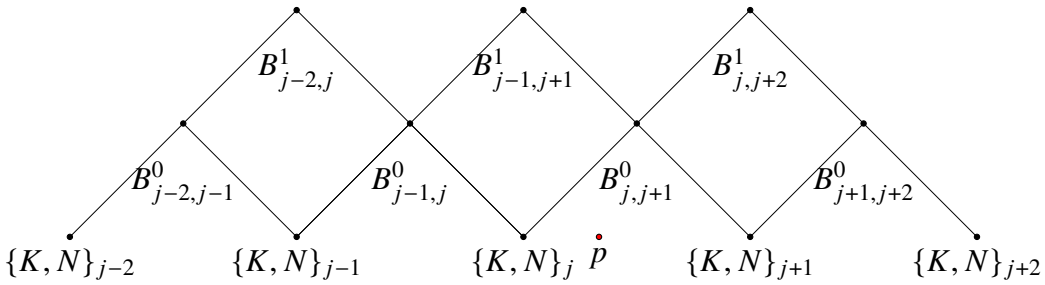

We therefore see that the value mapped to N_j is

$$B^1_{j-1,j+1}(p) = \frac{p - K_{j-1}}{K_j - K_{j-1}} B^0_{j-1,j}(p) + \frac{K_{j+1} - p}{K_{j+1} - K_j} B^0_{j,j+1}(p) \tag{F.5}$$

$$= \frac{p - K_{j-1}}{K_j - K_{j-1}}(0) + \frac{K_{j+1} - p}{K_{j+1} - K_j}(1) \tag{F.6}$$

$$= \frac{K_{j+1} - p}{\Delta x}. \tag{F.7}$$

This corresponds to how far away the particle is from N_j. Note it gets larger the closer p comes to N_j. Correspondingly, we see the value mapped to N_j is

$$B^1_{j,j+2}(p) = \frac{p - K_j}{K_{j+1} - K_j} B^0_{j,j+1}(p) + \frac{K_{j+2} - p}{K_{j+2} - K_{j+1}} B^0_{j+1,j+2}(p) \tag{F.8}$$

$$= \frac{p - K_j}{K_{j+1} - K_j}(1) + \frac{K_{j+2} - p}{K_{j+2} - K_{j+1}}(0) \tag{F.9}$$

$$= \frac{p - K_j}{\Delta x}. \tag{F.10}$$

This corresponds to how far away p is from N_{j+1}. It too gets larger the closer p comes to N_j. We can also rewrite it centered around the node it is to the right of (which has programmatic benefits). If K_j is the location of the node immediately to the left of p, then we write

$$B^1_{j-1,j+1}(p) = \frac{\left(K_j + \Delta x\right) - p}{\Delta x} = 1 - \frac{p - K_j}{\Delta x} \tag{F.11}$$

All other N values will be found to have nothing mapped to them due to the zeroth splines. We see adding the two nonzero values results in unity.

We again click up to second order splines.

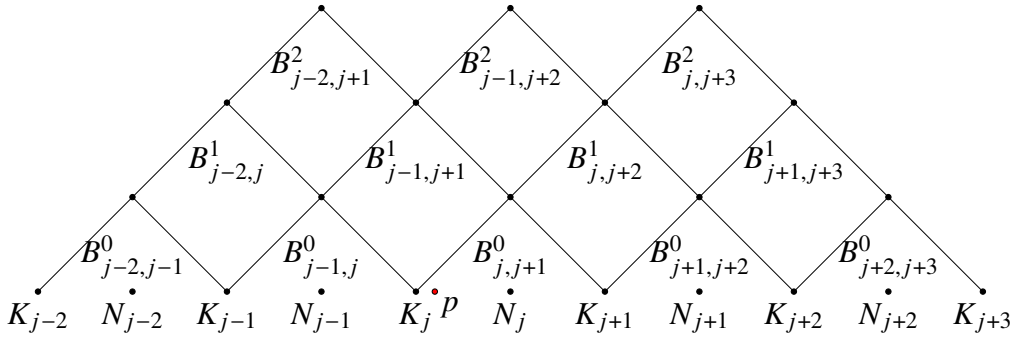

We see nodes N_{j-1}, N_j, and N_{j+1} will all receive values. The value of N_{j-1} is

$$
\begin{aligned}
B^2_{j-2,j+1}(p) &= \frac{p-K_{j-2}}{K_j-K_{j-2}}B^1_{j-2,j}(p) + \frac{K_j-p}{K_{j+1}-K_{j-1}}B^1_{j-1,j+1}(p) \\
&= \frac{p-K_{j-2}}{K_{j-1}-K_{j-2}}\left(\frac{p-K_{j-2}}{K_{j-1}-K_{j-2}}B^0_{j-2,j-1}(p) + \frac{K_j-p}{K_j-K_{j-1}}B^0_{j-1,j}(p)\right) \\
&+ \frac{K_{j+1}-p}{K_{j+1}-K_{j-1}}\left(\frac{p-K_{j-1}}{K_j-K_{j-1}}B^0_{j-1,j}(p) + \frac{K_{j+1}-p}{K_{j+1}-K_j}B^0_{j,j+1}(p)\right) \\
&= \frac{p-K_{j-2}}{K_{j-1}-K_{j-2}}\left(\frac{p-K_{j-2}}{K_{j-1}-K_{j-2}}(0) + \frac{K_j-p}{K_j-K_{j-1}}(0)\right) \\
&+ \frac{K_{j+1}-p}{K_{j+1}-K_{j-1}}\left(\frac{p-K_{j-1}}{K_j-K_{j-1}}(0) + \frac{K_{j+1}-p}{K_{j+1}-K_j}(1)\right) \\
&= \frac{K_{j+1}-p}{K_{j+1}-K_{j-1}}\frac{K_{j+1}-p}{K_{j+1}-K_j} = \frac{K_{j+1}-p}{2\Delta x}\frac{K_{j+1}-p}{\Delta x} \\
&= \frac{1}{2}\left(\frac{K_{j+1}-p}{\Delta x}\right)^2 = \frac{1}{2}\left(\frac{K_j+\Delta x-p}{\Delta x}\right)^2 = \frac{1}{2}\left(1-\frac{p-K_j}{\Delta x}\right)^2.
\end{aligned}
\tag{F.12}
$$

Similar, we consider the $B^2_{j,j+3}$ spline:

$$
\begin{aligned}
B^2_{j,j+3}(p) &= \frac{p-K_j}{K_{j+2}-K_j}B^1_{j,j+2}(p) + \frac{K_{j+3}-p}{K_{j+3}-K_j}B^1_{j+1,j+3}(p) \\
&= \frac{p-K_j}{K_{j+2}-K_j}\left(\frac{p-K_j}{K_{j+1}-K_j}B^0_{j,j+1}(p) + \frac{K_{j+1}-p}{K_{j+2}-K_{j+1}}B^0_{j+1,j+2}(p)\right) \\
&+ \frac{K_{j+3}-p}{K_{j+3}-K_{j+1}}\left(\frac{p-K_{j-1}}{K_{j+2}-K_{j+1}}B^0_{j+1,j+2}(p) + \frac{K_{j+3}-p}{K_{j+3}-K_{j+2}}B^0_{j+2,j+3}(p)\right) \\
&= \frac{p-K_j}{K_{j+2}-K_j}\left(\frac{p-K_j}{K_{j+1}-K_j}(1) + \frac{K_{j+1}-p}{K_{j+2}-K_{j+1}}(0)\right) \\
&+ \frac{K_{j+3}-p}{K_{j+3}-K_{j+1}}\left(\frac{p-K_{j-1}}{K_{j+2}-K_{j+1}}(0) + \frac{K_{j+3}-p}{K_{j+3}-K_{j+2}}(0)\right) \\
&= \frac{p-K_{j+1}}{K_{j+2}-K_j}\frac{p-K_{j+1}}{K_{j+1}-K_j} = \frac{p-K_{j+1}}{2\Delta x}\frac{p-K_{j+1}}{\Delta x} \\
&= \frac{1}{2}\left(\frac{p-K_{j+1}}{\Delta x}\right)^2 = \frac{1}{2}\left(\frac{p-(K_j+\Delta x)}{\Delta x}\right)^2 = \frac{1}{2}\left(-1+\frac{p-K_j}{\Delta x}\right)^2.
\end{aligned}
\tag{F.13}
$$

Lastly, we consider $B_{j-1,j+2}$:

$$
\begin{aligned}
B^2_{j-1,j+2}(p) &= \frac{p-K_{j-1}}{K_{j+1}-K_{j-1}} B^1_{j-1,j+1}(p) + \frac{K_{j+2}-p}{K_{j+2}-K_{j-1}} B^1_{j,j+2}(p) \\
&= \frac{p-K_{j-1}}{K_{j+1}-K_{j-1}} \left(\frac{p-K_{j-1}}{K_j-K_{j-1}} B^0_{j-1,j}(p) + \frac{K_{j+1}-p}{K_{j+1}-K_j} B^0_{j,j+1}(p) \right) \\
&+ \frac{K_{j+2}-p}{K_{j+2}-K_j} \left(\frac{p-K_j}{K_{j+1}-K_j} B^0_{j,j+1}(p) + \frac{K_{j+2}-p}{K_{j+2}-K_{j+1}} B^0_{j+1,j+2}(p) \right) \\
&= \frac{p-K_{j-1}}{K_{j+1}-K_{j-1}} \left(\frac{p-K_{j-1}}{K_j-K_{j-1}}(0) + \frac{K_{j+1}-p}{K_{j+1}-K_j}(1) \right) \\
&+ \frac{K_{j+2}-p}{K_{j+2}-K_j} \left(\frac{p-K_j}{K_{j+1}-K_j}(1) + \frac{K_{j+2}-p}{K_{j+2}-K_{j+1}}(0) \right) \\
&= \frac{p-K_{j-1}}{K_{j+1}-K_{j-1}} \frac{K_{j+1}-p}{K_{j+1}-K_j} + \frac{K_{j+2}-p}{K_{j+2}-K_j} \frac{p-K_j}{K_{j+1}-K_j} \\
&= \frac{p-K_{j-1}}{2\Delta x} \frac{K_{j+1}-p}{\Delta x} + \frac{K_{j+2}-p}{2\Delta x} \frac{p-K_j}{\Delta x} \\
&= \frac{p-(K_j-\Delta x)}{2\Delta x} \frac{(K_j+\Delta x)-p}{\Delta x} + \frac{(K_j+2\Delta x)-p}{2\Delta x} \frac{p-K_j}{\Delta x} \\
&= \frac{p-K_j+\Delta x}{2\Delta x} \frac{K_j+\Delta x-p}{\Delta x} + \frac{K_j+2\Delta x-p}{2\Delta x} \frac{p-K_j}{\Delta x} \\
&= \left(\frac{p-K_j}{2\Delta x} + \frac{1}{2} \right) \left(\frac{K_j-p}{\Delta x} + 1 \right) + \left(\frac{K_j-p}{2\Delta x} + 1 \right) \frac{p-K_j}{\Delta x} \\
&= \left(\frac{p-K_j}{2\Delta x} + \frac{1}{2} \right) \left(\frac{K_j-p}{\Delta x} + 1 \right) + \left(\frac{K_j-p}{2\Delta x} + 1 \right) \frac{p-K_j}{\Delta x} \\
&= \frac{1}{2} \left(\frac{p-K_j}{\Delta x} + 1 \right) \left(-\frac{p-K_j}{\Delta x} + 1 \right) + \left(-\frac{p-K_j}{2\Delta x} + 1 \right) \frac{p-K_j}{\Delta x} \\
&= -\frac{1}{2} \left(\frac{p-K_j}{\Delta x} \right)^2 + \frac{1}{2} - \frac{1}{2} \left(\frac{p-K_j}{\Delta x} \right)^2 + \frac{p-K_j}{\Delta x} \\
&= -\left(\frac{p-K_j}{\Delta x} \right)^2 + \frac{p-K_j}{\Delta x} + \frac{1}{2} = \frac{3}{4} - \left(\frac{p-K_j}{\Delta x} - \frac{1}{2} \right)^2 .
\end{aligned}
\tag{F.14}
$$

This is slightly different than the formula given in Chapter 8 of [35], which is

$$
S_2\left(X_j - x\right) = \frac{1}{\Delta x} \left[\frac{3}{4} - \left(\frac{x-X_j}{\Delta x} \right)^2 \right], \tag{F.15}
$$

$$
S_2\left(X_{j\pm1} - x\right) = \frac{1}{2\Delta x} \left(\frac{1}{2} \pm \frac{x-X_j}{\Delta x} \right)^2 . \tag{F.16}
$$

The $\frac{1}{\Delta x}$ coefficient is no problem, this is simply the authors considering the density rather than the value. A few pages prior they have the requirement $\Delta x \sum_j S(K_j - x) = 1$. In interests of generality

(for example if we want to interpolate a field to a particle, we are interested in its value, not its density), we have neglected this coefficient.

The second difference is more subtle. The location X_j of a node N_j is the halfway point between K_j and K_{j+1}, ie $X_j = \frac{K_j+K_{j+1}}{2} = K_j + \frac{\Delta x}{2}$. Let us consider what our formulas look like under this coordinate frame:

$$\begin{aligned}\frac{1}{2}\left(1-\frac{p-K_j}{\Delta x}\right)^2 &= \frac{1}{2}\left(1-\frac{p-\left(X_j-\frac{\Delta x}{2}\right)}{\Delta x}\right)^2 \\ &= \frac{1}{2}\left(\frac{1}{2}-\frac{p-X_j}{\Delta x}\right)^2,\end{aligned} \tag{F.17}$$

$$\begin{aligned}\frac{3}{4}-\left(\frac{p-K_j}{\Delta x}-\frac{1}{2}\right)^2 &= \frac{3}{4}-\left(\frac{p-\left(X_j-\frac{\Delta x}{2}\right)}{\Delta x}-\frac{1}{2}\right)^2 \\ &= \frac{3}{4}-\left(\frac{p-X_j}{\Delta x}\right)^2,\end{aligned} \tag{F.18}$$

$$\begin{aligned}\frac{1}{2}\left(-1+\frac{p-K_j}{\Delta x}\right)^2 &= \frac{1}{2}\left(-1+\frac{p-\left(X_j-\frac{\Delta x}{2}\right)}{\Delta x}\right)^2 \\ &= \frac{1}{2}\left(-\frac{1}{2}+\frac{p-X_j}{\Delta x}\right)^2 \\ &= \frac{1}{2}\left(\frac{1}{2}-\frac{p-X_j}{\Delta x}\right)^2.\end{aligned} \tag{F.19}$$

This is, without the $\frac{1}{\Delta x}$ prefactor, precisely the formulation of Birdsall and Langdon.

This covers the splines we have used in this paper. Of course, with sufficient tedium higher order splines may be constructed. All of these may be made d dimensional by taking the tensor product of the splines $d-1$ times. It is also worth noting that a spline of order n is equal to the convolution of the $(n-1)$th spline with the 0th order spline. As $n \to \infty$, the spline shape approaches a Gaussian [35] (see Figure F.1).

Birdsall and Langdon do not provide the variance, so we will show that it is $\frac{n+1}{12}$.

Proof. We do so by induction. First, consider the zeroth order spline $B_0(x)$. We see, from the

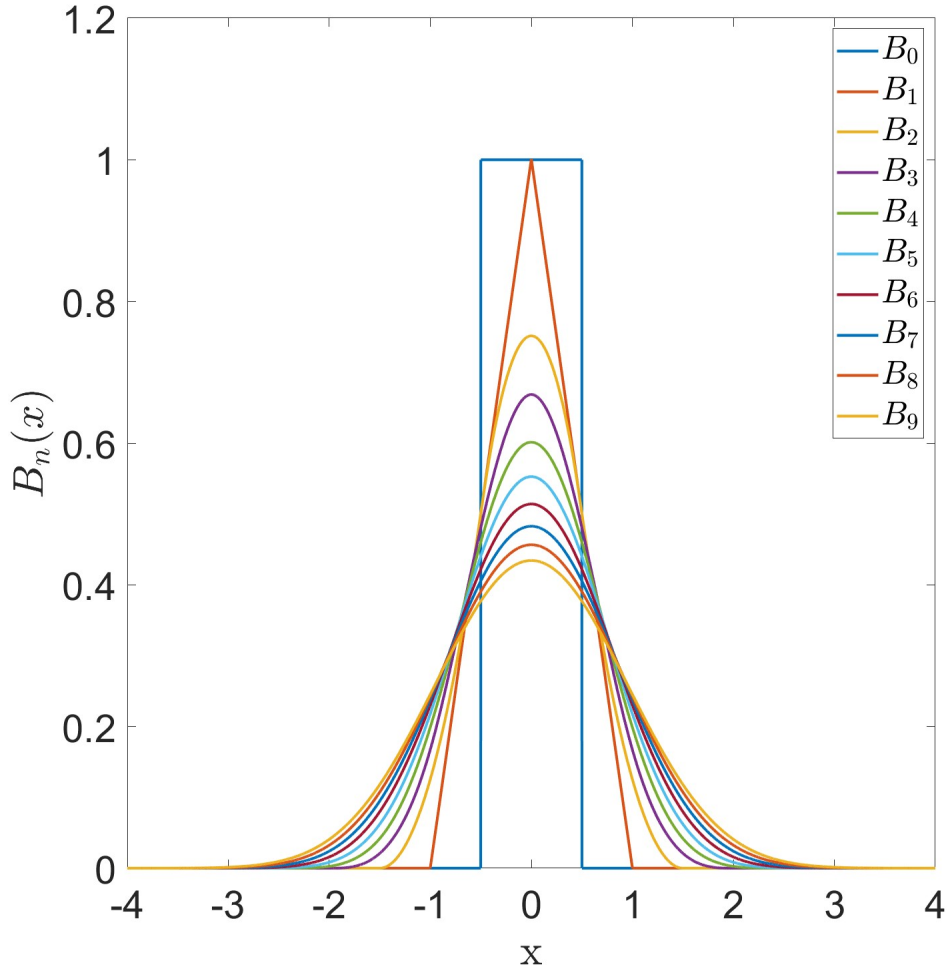

Figure F.1 The first 10 basis splines. B_n is generated by convolving B_0 against itself n times, eg $B_1 = B_0 * B_0$. As $n \to \infty$, B_n approaches a Gaussian with variance $\sigma_n^2 = \frac{n+1}{12}$.

standard definition of variance:

$$\int_{-\infty}^{\infty} x^2 B_0(x)dx = \frac{1}{3}x^3\Big|_{-\frac{1}{2}}^{\frac{1}{2}} = \frac{1}{24} - -\frac{1}{24} = \frac{1}{12}. \tag{F.20}$$

This shows our base case. We move on to the induction step. Assume true for $n-1$, we now consider n.

$$\begin{aligned}\int_{-\infty}^{\infty} x^2 B_n(x)dx &= \int_{-\infty}^{\infty} x^2 \left(B_{n-1} * B_0\right)(x)dx \\ &= \int_{-\infty}^{\infty} x^2 \left(\int_{-\infty}^{\infty} B_{n-1}(s-x)B_0(s)ds\right)dx \\ &= \int_{-\infty}^{\infty} B_0(s)\left(\int_{-\infty}^{\infty} x^2 B_{n-1}(s-x)dx\right)ds\end{aligned} \tag{F.21}$$

We consider the innermost integral. We will do a change of variables, $t = s - x$, $dt = ds$. The integration bounds are still infinity. It is also worth noting, as it will soon be relevant, that all basis spline functions are even, that their volume is always unity, and that an even function multiplied by an odd function is odd, so the integral over it is zero. Having said all this, we continue:

$$\begin{aligned}\int_{-\infty}^{\infty} (s-t)^2 B_{n-1}(t)dt &= \int_{-\infty}^{\infty} \left(s^2 - 2st + t^2\right) B_{n-1}(t)dt \\ &= \int_{-\infty}^{\infty} s^2 B_{n-1}(t)dt - \int_{-\infty}^{\infty} 2st B_{n-1}(t)dt + \int_{-\infty}^{\infty} t^2 B_{n-1}(t)dt \\ &= s^2 - 0 + \frac{n}{12}.\end{aligned} \tag{F.22}$$

The last step is justified by the aforementioned properties and the inductive hypothesis. We now see (F.21) becomes

$$\begin{aligned}\int_{-\infty}^{\infty} B_0(s) \left(\int_{-\infty}^{\infty} x^2 B_{n-1}(s-x)dx\right) ds &= \int_{-\infty}^{\infty} B_0(s) \left(s^2 + \frac{n}{12}\right) ds \\ &= \int_{-\infty}^{\infty} s^2 B_0(s)ds + \frac{n}{12}\int_{-\infty}^{\infty} B_0(s)ds \\ &= \frac{1}{2} + \frac{n}{12} = \frac{n+1}{12}.\end{aligned} \tag{F.23}$$

The last step is simply by definition of the variance, which was already proven, and the volume of B_0 being unity. We have shown the variance of the nth order B-spline, σ_n^2, is $\frac{n+1}{12}$, finishing the proof. QED

APPENDIX G

GREEN'S FUNCTIONS

The following is adapted and expanded out of Duffy's excellent textbook [275].

The PIC method laid out in chapter 2 relies on the concept of Green's functions, named after the mathematician George Green (1793-1841), who laid down the theoretical framework for them [315], motivated by finding a generic solution to Poisson's equation. Given how much Chapter 2 relies on them, it is a worthwhile exercise to consider what these functions are and how they work. Consider the linear differential equation $\mathcal{L}[u] = f(x)$, where $\mathcal{L}$ is a linear differential operator, f is a known source function, and u is the unknown solution. We let a and b be the left and right boundary conditions, respectively. Were we able to find an inverse operator, $\mathcal{L}^{-1}$, we would find the solution, $u(x) = \mathcal{L}^{-1}[f(x)]$. The discrete analog of this is finding the matrix $\mathcal{L}^{-1}$ for $\mathcal{L}$ such that $\mathcal{L}^{-1}\mathcal{L} = I$, where I is the identity matrix. The logic is as follows:

Note $\int_a^b \delta(x-s)f(s)ds = f(x)$. Now, let G be a function such that $\mathcal{L}[G(x;s)] = \delta(x-s)$. We multiply both sides by $f(s)$ and integrate, observing

$$\int_a^b \mathcal{L}[G(x;s)]f(s)ds = \int_a^b \delta(x-s)f(s)ds = f(x). \tag{G.1}$$

Noting that $\mathcal{L}$ is an operator on x, not s, we can pull it out of the integrand. $\mathcal{L}[\int_a^b G(x;s)f(s)ds] = f(x)$. Now, given $\mathcal{L}[u] = f(x)$, it immediately follows $\mathcal{L}[u] = \mathcal{L}[\int_a^b G(x;s)f(s)ds]$. Therefore, so long as $\mathcal{L}$ is invertible, we know

$$u = \int_a^b G(x;s)f(s)ds. \tag{G.2}$$

Correspondingly, we will find a function G such that $\mathcal{L}[G] = \delta(x)$, where $\delta(x)$ is the Dirac delta function.

Morse and Feshbach gave a list of properties of Green's functions $G(x;\xi)$ applied to Sturm-Liousville problems:

$$\frac{d}{dx}\left[f(x)\frac{dy}{dx}\right] + p(x)y = -q(x), \tag{G.3}$$

which are

- Satisfaction of homogenous equation, ie $q(x) = 0$, when $x \neq \xi$.
- Satisfies homogenous boundary conditions, ie $G(a;\xi) = G(b;\xi) = 0$ where a and b are the left and rightmost boundaries, respectively, or $\lim_{x\to\pm\infty} G(x;\xi) = 0$.
- Symmetry in x and ξ.
- Satisfaction of the following conditions $\left.\frac{dG}{dx}\right|_{x=\xi^+} - \left.\frac{dG}{dx}\right|_{x=\xi^-} = -\frac{1}{f(\xi)}$.

G.1 A Simple Example, Poisson's Equation in 1D

Duffy gives a good example in chapter 2 which will elucidate things. Consider the simple boundary value problem describing an elastic string along $[0, L]$ with uniform tensile force T:

$$T\frac{d^2u}{dx^2} = f(x), \tag{G.4a}$$

$$u(0) = u(L) = 0. \tag{G.4b}$$

Note this corresponds to a Sturm-Liousville problem with $f_{SL}(x) = -T$, $p(x) = 0$, and $q(x) = f_p(x)$ (f_p being the forcing function for the Poisson equation, f_{SL} being the f function in the canonical Sturm-Liousville equation (keeping notation as consistent with Duffy as possible)). We are interested in finding the displacement for a given point ξ and no more. In other words, we consider the force function $\delta(x - \xi)$, solving for the corresponding function $G(x, \xi)$. This yields

$$T\frac{d^2G}{dx^2} = \delta(x - \xi), \tag{G.5a}$$

$$G(0;\xi) = G(L;\xi) = 0. \tag{G.5b}$$

If $x \neq \xi$, then we get

$$\frac{d^2G}{dx^2} = 0, \tag{G.6}$$

Which yields

$$G(x;\xi) = \begin{cases} ax + b & \text{if x} < \xi \\ cx + d & \text{if x} > \xi \end{cases} \tag{G.7}$$

We can use the boundaries to get some of these values. If $G(0;\xi) = 0$, then surely $b = 0$. Likewise, if $G(L;\xi) = 0$, then surely $d = -cL$. Thus we get

$$G(x;\xi) = \begin{cases} ax & \text{if x} < \xi \\ c(x-L) & \text{if x} > \xi \end{cases} \tag{G.8}$$

But what of the case $x = \xi$? We know that the function must be continuous (Morse and Feshbach's second requirement, also intuitively makes sense, a broken string is unphyisical). So we know

$$a\xi = c(\xi - L). \tag{G.9}$$

Now, setting $x = \xi$, consider $\frac{d^2G}{dx^2}(\xi;\xi) = \delta(0)$. Using the property of the delta function, we integrate over an increasingly small boundary, $[\xi - \epsilon, \xi + \epsilon]$[1]

$$\lim_{\epsilon\to 0} T\frac{dG}{dx}\bigg|_{x=\xi-\epsilon}^{x=\xi+\epsilon} = 1. \tag{G.10}$$

This implies

$$\lim_{\epsilon\to 0}\left[\frac{dG}{dx}(\xi+\epsilon;\xi) - \frac{dG}{dx}(\xi-\epsilon;\xi)\right] = \frac{1}{T}. \tag{G.11}$$

Denote $\lim_{\epsilon\to 0}\xi \pm \epsilon$ as $\xi^{\pm}$ Now, we know what the derivatives of G are, above and below the ξ point.

$$\frac{dG}{dx}(\xi^-;\xi) = a \tag{G.12a}$$

$$\frac{dG}{dx}(\xi^+;\xi) = c \tag{G.12b}$$

Noting $c = \frac{a\xi}{\xi - L}$, we get

$$\begin{aligned} c - a &= \frac{1}{T} \\ \implies \frac{a\xi}{\xi - L} - a &= \frac{1}{T} \\ \implies \frac{aL}{\xi - L} &= \frac{1}{T} \\ \implies a &= \frac{\xi - L}{LT} \end{aligned} \tag{G.13}$$

[1]This gives another justification for the fourth requirement Morse and Feshbach give, which results in the same thing.

Defining $x_> \coloneqq \max(x, \xi)$ and $x_< \coloneqq \min(x, \xi)$, this finally gives us

$$G(x;\xi) = \frac{1}{TL}(x_> - L)x_< \tag{G.14}$$

Thus we know

$$\begin{aligned} u(x) &= \int_0^L f(\xi)G(x;\xi)d\xi \\ &= \frac{x-L}{TL}\int_0^x f(\xi)\xi d\xi + \frac{x}{TL}\int_x^L f(\xi)(\xi - L)d\xi. \end{aligned} \tag{G.15}$$

This is the solution for any source function f. How to compute the integral is of course another question, and most source functions will not give an analytic solution to these integrals, but we can apply any quadrature method we wish to arbitrary accuracy.

G.2 The Modified Helmholtz Equation in 1D

Duffy goes over the Helmholtz equation, $\Delta u + \lambda u = -f(x)$ in chapter 6 of [275]. We are interested in the modified Helmholtz function, $\Delta u - \lambda u = -S(x)$, which in the above work we notate as

$$\left(\mathcal{I} - \frac{1}{\alpha^2}\Delta\right)u = S(\mathbf{x}). \tag{G.16}$$

Given we dimensionally split the operator to one dimension, this reduces to

$$\left(\mathcal{I} - \frac{1}{\alpha^2}\frac{\partial^2}{\partial x^2}\right)u = f(x). \tag{G.17}$$

This corresponds to a Sturm-Liousville problem with $f(x) = -\frac{1}{\alpha^2}$, $p(x) = 1$, and $q(x) = -S(x)$. We now want to find the Green's function. We can use the roadmap Duffy gives in solving the Helmholtz equation to do so. Similar to solving for the Green's function for Poisson's equation,[2] we consider the following boundary value problem

$$\begin{cases} G - \frac{1}{\alpha^2}\frac{\partial^2 G}{\partial x^2} = \delta(x-\xi), \\ -\infty < x, \xi < \infty. \end{cases} \tag{G.18}$$

[2]Which is just a special case of the Helmholtz equation, modified or otherwise, where $\lambda = 0$.

This is slightly different than what we did with Poisson's equation, in that our boundaries here are infinite. This is a free space Green's function. The solutions are as follows

$$\begin{cases} G(x;\xi) &= Ae^{-\alpha(x-\xi)} + Be^{\alpha(x-\xi)}, \quad x < \xi, \\ G(x;\xi) &= Ce^{-\alpha(x-\xi)} + De^{\alpha(x-\xi)}, \quad x > \xi. \end{cases} \tag{G.19}$$

The solution must be zero at infinity (Morse and Freshbach's second requirement). This requires us to set $A = D = 0$. We now consider the continuity requirements. The continuity of the function G itself requires $B = C$. The last requirement listed by Morse and Feschbach yields

$$\left.\frac{dG}{dx}\right|_{x=\xi^+} - \left.\frac{dG}{dx}\right|_{x=\xi^-} = \alpha^2. \tag{G.20}$$

Using these requirements we see

$$\begin{aligned} &\frac{d}{dx}\left[Ce^{-\alpha(x-\xi)}\right]_{x=\xi^+} - \frac{d}{dx}\left[Be^{\alpha(x-\xi)}\right]_{x=\xi^-} = -\alpha^2 \\ \implies &-\alpha Ce^{-\alpha(x-\xi)}\Big|_{x=\xi^+} - \alpha Be^{\alpha(x-\xi)}\Big|_{x=\xi^-} = -\alpha^2 \\ \implies &Ce^{-\alpha(x-\xi)}\Big|_{x=\xi^+} + Be^{\alpha(x-\xi)}\Big|_{x=\xi^-} = \alpha \end{aligned} \tag{G.21}$$

If we consider $\xi^+ = \xi + \epsilon$ and $\xi^- = \xi - \epsilon$ and let $\epsilon \to 0$, we see this results in $C + B = \alpha$. W already know $C = B$, so it follows $C = B = \frac{\alpha}{2}$. Thus our Green's function is

$$G(x;\xi) = \frac{\alpha}{2}e^{-\alpha|x-\xi|}. \tag{G.22}$$

APPENDIX H

DERIVING THE QUADRATURE WEIGHTS

We want to derive the quadrature weights originally established in [268].

We are looking to compute the integral

$$\alpha \int_{x_{i-1}}^{x_i} e^{-\alpha(x_i-\xi)} v(\xi) d\xi. \tag{H.1}$$

To do so, we project v to a polynomial p. Given the set of polynomials is complete, we know any function $f(x) = \sum_{j=0}^{\infty} c_j x^j$. So we want to use this to get an approximation of v. First, we let $\xi = \Delta x \tau + x_{i-1}$. So the above integral (H.1), is equal to

$$\alpha \Delta x_i \int_0^1 e^{-\alpha \Delta x_i (1-\tau)} v(\Delta x_i \tau + x_{i-1}) d\tau. \tag{H.2}$$

Here we have defined $\Delta x_i \coloneqq x_i - x_{i-1}$. We want the polynomial p to interpolate through the points v_{i-1}, v_i, and v_{i+1}, where $v_j \coloneqq v(x_j)$. For simplicity of integration, we want to construct $p\,(x) = c_0 + c_1(x - x_{i-1}) + c_2(x - x_{i-1})^2$, as this gives $p\,(\Delta x_i \tau + x_{i-1}) = c_0 + c_1(\Delta x_i \tau) + c_2(\Delta x_i \tau)^2$. To do so, we need $p(x_j) = v_j \forall j \in \{i-1, i, i+1\}$. If we are centering around a particular point c, we acquire the linear system

$$\begin{pmatrix} 1 & x_{i-1} - c & (x_{i-1} - c)^2 \\ 1 & x_i - c & (x_i - c)^2 \\ 1 & x_{i+1} - c & (x_{i+1} - c)^2 \end{pmatrix} \begin{pmatrix} c_0 \\ c_1 \\ c_2 \end{pmatrix} = \begin{pmatrix} v_{i-1} \\ v_i \\ v_{i+1} \end{pmatrix}. \tag{H.3}$$

From our requirements listed above, we want to center this around $c = x_{i-1}$. For now we will assume a uniformly staggered grid. Ie $x_i - x_{i-1} = \Delta x \; \forall \; i$. This gives the system

$$\begin{pmatrix} 1 & 0 & 0 \\ 1 & \Delta x & \Delta x^2 \\ 1 & 2\Delta x & 4\Delta x^2 \end{pmatrix} \begin{pmatrix} c_0 \\ c_1 \\ c_2 \end{pmatrix} = \begin{pmatrix} v_{i-1} \\ v_i \\ v_{i+1} \end{pmatrix}. \tag{H.4}$$

Inverting yields

$$\begin{pmatrix} c_0 \\ c_1 \\ c_2 \end{pmatrix} = \frac{1}{2} \begin{pmatrix} 2 & 0 & 0 \\ -\frac{3}{\Delta x} & \frac{4}{\Delta x} & -\frac{1}{\Delta x} \\ \frac{1}{\Delta x^2} & -\frac{2}{\Delta x^2} & \frac{1}{\Delta x^2} \end{pmatrix} \begin{pmatrix} v_{i-1} \\ v_i \\ v_{i+1} \end{pmatrix}. \tag{H.5}$$

So, approximating $v(x)$ as $p(x) = c_0 + c_1(x - x_{i-1}) + c_2(x - x_{i-1})^2$, where the coefficients are defined as above, we note

$$\begin{aligned} p(\Delta x\tau + x_{i-1}) &= c_0 + c_1(\Delta x\tau + x_{i-1} - x_{i-1}) + c_2(\Delta x\tau + x_{i-1} - x_{i-1})^2 \\ &= c_0 + c_1\Delta x\tau + c_2\Delta x^2\tau^2. \end{aligned}$$

As such, (H.2) becomes

$$\alpha\Delta x \int_0^1 e^{-\alpha\Delta x(1-\tau)} \left(c_0 + c_1\Delta x\tau + c_2\Delta x^2\tau^2\right) d\tau \tag{H.6}$$

Defining $\nu \coloneqq \alpha\Delta x$ and $d \coloneqq e^{-\nu}$, (H.6) will be evaluated

$$\begin{aligned} &\nu \int_0^1 e^{-\nu(1-\tau)} \left(c_0 + c_1\Delta x\tau + c_2\Delta x^2\tau^2\right) d\tau \\ =&\nu c_0 \int_0^1 e^{-\nu(1-\tau)} d\tau + \nu\Delta x c_1 \int_0^1 \tau e^{-\nu(1-\tau)} d\tau + \nu\Delta x^2 c_2 \int_0^1 \tau^2 e^{-\nu(1-\tau)} d\tau \\ =&\nu c_0 \left[\frac{1}{\nu} e^{-\nu(1-\tau)}\right]_0^1 \\ &+c_1\nu\Delta x \left[\frac{1}{\nu^2}(\nu\tau - 1)e^{-\nu(1-\tau)}\right]_0^1 \\ &+c_2\nu\Delta x^2 \left[\frac{1}{\nu^3}(\nu^2\tau^2 - 2\nu\tau + 2)e^{-\nu(1-\tau)}\right]_0^1 \\ =&- c_0 \left[e^{-\nu(1-\tau)}\right]_0^1 \\ &+c_1\frac{\Delta x}{\nu}[(\nu\tau - 1)e^{-\nu(1-\tau)}]_0^1 \\ &+c_2\frac{\Delta x^2}{\nu^2}\left[(\nu^2\tau^2 - 2\nu\tau + 2)e^{-\nu(1-\tau)}\right]_0^1. \end{aligned} \tag{H.7}$$

This becomes

$$\begin{aligned} &c_0[1 - d] + c_1\frac{\Delta x}{\nu}[(\nu - 1) - -d] + c_2\frac{\Delta x^2}{\nu^2}[(\nu^2 - 2\nu + 2) - 2d] \\ =&c_0[1 - d] + c_1\frac{\Delta x}{\nu}[\nu - 1 + d] + c_2\frac{\Delta x^2}{\nu^2}[\nu^2 - 2\nu + 2 - 2d] \\ =&v_{i-1}[1 - d] + \left(\frac{1}{2\Delta x}(3v_{i-1} + 4v_i - v_{i+1})\right)\frac{\Delta x}{\nu}[\nu - 1 + d] \\ &+\frac{1}{2\Delta x^2}\left(v_{i-1} - 2v_i + \frac{1}{2}v_{i+1}\right)\frac{\Delta x^2}{\nu^2}[\nu^2 - 2\nu + 2 - 2d] \\ =&v_{i-1}[1 - d] + ((3v_{i-1} + 4v_i - v_{i+1}))\frac{1}{2\nu}[\nu - 1 + d] \\ &+(v_{i-1} - 2v_i + v_{i+1})\frac{1}{2\nu^2}[\nu^2 - 2\nu + 2 - 2d] \end{aligned} \tag{H.8}$$

We will sort these out by components. First, the v_{i-1} component:

$$
\begin{aligned}
& v_{i-1}\left(1-d-3\frac{\nu-1+d}{2\nu}+\frac{\nu^2-2\nu+2-2d}{2\nu^2}\right) \\
=& v_{i-1}\left(\frac{2\nu^2-2d\nu^2}{2\nu^2}-3\frac{\nu^2-\nu+d\nu}{2\nu^2}+\frac{\nu^2-2\nu+2-2d}{2\nu^2}\right) \\
=& v_{i-1}\left(\frac{2\nu^2-2d\nu^2-3\nu^2+3\nu-3d\nu+\nu^2-2\nu+2-2d}{2\nu^2}\right) \\
=& v_{i-1}\left(-\frac{2d\nu^2}{2\nu^2}+\frac{\nu-3d\nu}{2\nu^2}+\frac{2-2d}{2\nu^2}\right) \\
=& v_{i-1}\left(-d+\frac{2\nu-\nu-3d\nu}{2\nu^2}+\frac{1-d}{\nu^2}\right) \\
=& v_{i-1}\left(-d+\frac{-\nu-d\nu}{2\nu^2}+\frac{2\nu-2d\nu}{2\nu^2}+\frac{1-d}{\nu^2}\right) \\
=& v_{i-1}\left(-d+\frac{-\nu-d\nu}{2\nu^2}+\frac{1-d}{\nu}+\frac{1-d}{\nu^2}\right) \\
=& v_{i-1}\left(-d-\frac{1+d}{2\nu}+\frac{1-d}{\nu}+\frac{1-d}{\nu^2}\right) \\
=& v_{i-1}\left(-d+\frac{1-d}{\nu}+\frac{1-d}{\nu^2}-\frac{1+d}{2\nu}\right).
\end{aligned}
$$

We define $Q \coloneqq -d+\frac{1-d}{\nu}$ and $R \coloneqq \frac{1-d}{\nu^2}-\frac{1+d}{2\nu}$ for reasons that will become apparent, which gives us the final form of the v_{i-1} coefficient, $Q+R$.

Taking the v_i components:

$$
\begin{aligned}
& 4\frac{1}{2\nu}[\nu-1+d]-2\frac{1}{2\nu^2}[\nu^2-2\nu+2-2d] \\
=& \frac{2\nu^2-2\nu+2d\nu}{\nu^2}-\frac{\nu^2-2\nu+2-2d}{\nu^2} \\
=& \frac{2\nu^2-2\nu+2d\nu-\nu^2+2\nu-2+2d}{\nu^2} \\
=& \frac{\nu^2}{\nu^2}+\frac{2d-2}{\nu^2}+\frac{2d\nu}{\nu^2} \\
=& 1-2\frac{1-d}{\nu^2}+\frac{2d}{\nu} \\
=& 1-2\frac{1-d}{\nu^2}+\frac{d-1}{\nu}+\frac{d+1}{\nu} \\
=& 1-\frac{1-d}{\nu}-2\left(\frac{1-d}{\nu^2}-\frac{1+d}{2\nu}\right)
\end{aligned}
$$

We recognize the second component, we'll defined $P \coloneqq 1-\frac{1-d}{\nu}$. So the v_i component is $P-2R$.

Taking the v_{i+1} components:

$$\begin{aligned}
&-\frac{1}{2\nu}[\nu-1+d]+\frac{1}{2\nu^2}[\nu^2-2\nu+2-2d]\\
=&\frac{-\nu^2+\nu-d\nu}{2\nu^2}+\frac{\nu^2-2\nu+2-2d}{2\nu^2}\\
=&\frac{-\nu^2+\nu-d\nu+\nu^2-2\nu+2-2d}{2\nu}\\
=&\frac{-\nu-d\nu+2-2d}{2\nu^2}\\
=&\frac{-\nu-d\nu}{2\nu^2}+\frac{2-2d}{2\nu^2}\\
=&\frac{-1-d}{2\nu}+\frac{1-d}{\nu^2}\\
=&\frac{1-d}{\nu^2}-\frac{1+d}{2\nu}.
\end{aligned}$$

This is exactly R. Thus we have our quadrature weights for $\mathcal{J}$:

$$\mathcal{J}_j^L[v]=Pv(x_j)+Qv(x_{j-1})+R\left(v(x_{j+1})-2v(x_j)+v(x_{j-1})\right). \tag{H.9}$$

The quadrature weights for $\mathcal{J}^R$ may be similarly derived.